INTERNATIONAL DOCTORAL
SCHOOL OF THE USC

Iago
Fernández Llovo

PhD Thesis

CRITICAL PHENOMENA AND VORTEX DYNAMICS IN SUPERCONDUCTORS OF TECHNOLOGICAL INTEREST

Santiago de Compostela, 2023

Doctoral Programme in Materials Science

ESCOLA DE DOUTORAMENTO
INTERNACIONAL DA USC

DOCTORAL THESIS

CRITICAL PHENOMENA AND VORTEX DYNAMICS IN SUPERCONDUCTORS OF TECHNOLOGICAL INTEREST

Author:

Iago Fernández Llovo

Supervisor/s: Jesús Manuel Mosqueira Rey

PHD PROGRAMME IN MATERIAL SCIENCE

SANTIAGO DE COMPOSTELA

2023

Acknowledgements

I extend my heartfelt gratitude to the individuals and institutions who have played pivotal roles in the completion of this thesis. First and foremost, I would like to express my deepest appreciation to my thesis advisor, Prof. Jesús Mosqueira, whose unwavering guidance, expertise and support have been indispensable in conducting this research. I am deeply grateful to the rest of the members of QMatterPhotonics research group for their invaluable insight, collaboration and shared dedication to our collective pursuit of knowledge. The collective efforts and exchange of ideas within our research team have been instrumental in shaping the outcomes of this work.

I would also like to extend my immense appreciation to Dr. Thierry Grenet and Dr. Julien Delahaye for welcoming me (twice) into their team and for their invaluable participation as research collaborators, and to all the researchers at Institut Néel which I had the pleasure to meet, *merci de tout mon cur*. To our colleagues at Beijing National Laboratory for Condensed Matter Physics (China), Universidade Federal do Rio de Janeiro (Brazil) and Oak Ridge National Laboratory (USA), for the fruitful collaboration which has finally resulted in the completion of this doctoral thesis.

To my family, I owe a debt of gratitude for their unending encouragement and their understanding, especially with regards to missed gatherings and events. To my partner Holly, she has truly carried me through my thesis with love and emotional support, I could not have endured without her. To my closest friends Andrés, Antón, Christopher, Javi, Jesús, they have been a constant source of motivation and companionship throughout my life. To my officemate Martin, for all we have suffered together, remember it will be worth it! To the best flatmates David, Eliseo, Felipe, with whom I share some of the happiest memories from our early years of university.

To all those who contributed in various ways, although unnamed here, I am genuinely grateful for their collective support and encouragement. This thesis is the result of the collaborative efforts of many, and I am humbled by their contributions.

The University of Santiago de Compostela has provided essential resources, a conducive academic environment, and my sincerest thanks go to them. Financial support from Xunta de Galicia (grant no. ED481A-2020/149) was instrumental,

and I express my profound gratitude. This research has been funded by the Agencia Estatal de Investigación (AEI) and Fondo Europeo de Desarrollo Regional (FEDER) through projects FIS2016-79109-P and PID2019-104296GB-I00, and by Xunta de Galicia (grant GRC no. ED431C 2018/11).

Resumo

A descuberta da supercondutividade en 1911 por Kamerlingh Onnes marcou un importante fito na física do estado sólido. Este fenómeno, polo cal os materiais mostran resistencia eléctrica cero e expulsan os campos magnéticos do seu interior, foi observado inicialmente en fíos ultrapuros de mercurio. Descubertas sucesivas, como o efecto Meissner (diamagnetismo perfecto) e a formulación das ecuacións de London, ampliaron a comprensión da supercondutividade. Aínda que estas teorías iniciais explicaban a fenomenoloxía da supercondutividade, non abordaban a transición ao estado supercondutor, e o desenvolvemento da teoría de Ginzburg-Landau en 1950 proporcionou unha explicación máis completa coa introdución dun parámetro de orde, que representa a densidade de superportadores e que toma valores non nulos por debaixo da temperatura de transición supercondutora T_c. Esta teoría, que tamén foi crucial para describir os diferentes comportamentos observados en supercondutores de tipo I e tipo II, aínda carecía dunha explicación microscópica da supercondutividade, un fito que foi finalmente acadado pola teoría de Bardeen-Cooper-Schrieffer (BCS) en 1957, a cal explica os supercondutores convencionais a través de correlacións entre electróns mediadas por fonóns, levando ao emparellamento dos electróns en pares de Cooper. A teoría BCS foi capaz de explicar con éxito moitos fenómenos supercondutores, como a xanela de enerxías prohibidas que se abre no nivel de Fermi por debaixo de T_c, e o efecto isotópico, polo cal a T_c depende da masa dos isótopos que forman a rede. Máis tarde, a descuberta do efecto Josephson en 1962 abriu a porta a varias tecnoloxías baseadas en supercondutores, incluíndo SQUIDs e cúbits supercondutores. Esta tese céntrase en dúas familias de supercondutores de particular interese científico e tecnolóxico: os cupratos supercondutores e os supercondutores baseados en ferro, dúas familias que mostran propiedades como altos campos magnéticos críticos e correntes críticas, cruciais para aplicacións como o transporte eléctrico, a xeración de campos magnéticos e as tecnoloxías cuánticas.

Os cupratos supercondutores foron inicialmente descubertos en 1986, cando Karl Alexander Müller e Johannes Georg Bednorz acharon que o composto cerámico $Ba_xLa_{5-x}Cu_5O_{5(3-y)}$ se facía supercondutor a 30 K. A posterior descuberta de $(Y_{1-x}Ba_x)_2CuO_{4-\delta}$, supercondutor entre 80 e 93 K, superou por primeira vez o punto de ebulición do nitróxeno líquido (77 K), marcando un fito na consecución de supercondutores a temperaturas máis prácticas. Investigacións sucesivas nestes supercondutores cerámicos, con estrutura cristalográfica semellante ás perovskitas, levaron a acadar temperaturas críticas récord de 138 K a presión ambiental en

$Hg_{0.8}Tl_{0.2}Ba_2Ca_2Cu_3O_{8+\delta}$, que continúan sen ser superadas. No entanto, a aplicabilidade da teoría BCS para explicar o seu mecanismo de emparellamento segue sen resolverse. Por exemplo, experimentos ARPES (*Angle-Resolved Photoemission Spectroscopy*) mostran desviacións das predicións do emparellamento de tipo singlete, e propostas recentes suxiren que o emparellamento electrón-electrón podería ser mediado pola interacción de superintercambio nun estado illante con correlacións antiferromagnéticas, no canto da interacción electrón-fonón da teoría BCS. Ademais das súas altas temperaturas críticas, os cupratos teñen múltiples propiedades interesantes desde o punto de vista das aplicacións, como elevados campos críticos superiores e correntes críticas, necesarios para a fabricación de cables superconductores para o transporte eléctrico e a xeración de campos magnéticos, e cintas REBCO (Óxido de Cobre, Bario e Terras Raras) xa están dispoñibles comercialmente. Con todo, a súa alta anisotropía e a mala conectividade intergranular dos cristais, que requiren un aliñamento preciso, presentan desafíos para a súa aplicación a escala. Os cupratos superconductores tamén mostran outras propiedades inusuais e complexas que teñen desafiado os modelos teóricos convencionais, como a orixe da súa paracondutividade, a condutividade en exceso da esperada no estado normal por riba de T_c que os superconductores presentan. O traballo seminal de Bednorz e Müller en 1986 xa suxería que a diminución da resistencia preto de T_c en Ba-La-Cu-O podería ser resultado da combinación entre unha natureza percolativa e flutuacións superconductoras 2D. Os estudos iniciais usando a teoría do medio efectivo (EMT) en YBCO óptimamente dopado restaron importancia ao papel dos procesos percolativos emerxentes na paracondutividade, atribuíndo dita disminución de resistividade á presenza de flutuacións térmicas. En particular, os datos experimentais resultaron estar en bo acordo co modelo de Lawrence e Doniach (LD) na aproximación gaussiana do modelo de Ginzburg-Landau (GGL). Investigacións posteriores debateron se procesos percolativos emerxentes debidos a inhomoxeneidades intrínsecas puideran ser os únicos responsables do arredondamento nos cupratos superconductores, con algúns estudos suxerindo a coexistencia de flutuacións e percolación.

En 2008, outro avance significativo no eido da superconductividade foi a descuberta dos superconductores baseados en ferro (IBS). Os IBS teñen varias propiedades que os fan atractivos para aplicacións prácticas, como altos campos magnéticos críticos e de irreversibilidade, este último comparable ao dos cupratos a 4.2 K, mentres mostran un factor de anisotropía γ significativamente máis baixo, especialmente a familia 122 cun γ de aproximadamente 3, e maiores ángulos críticos de fronteira de gran (ata 9 graos), o cal axuda a mellorar a conectividade dos policristais. Isto fai que sexan potencialmente mellores ca os cupratos para producir fíos e cintas policristalinos, e para desenvolver dispositivos superconductores como imáns masivos ou nanocircuitos de filme delgado, incluíndo unións Josephson integradas e SQUIDs. Os IBS tamén teñen un interese fundamental debido ás súas semellanzas cos cupratos, como a súa estrutura lamelar, as súas altas temperaturas de transición (malia que inferiores ás dos cupratos) e a aparición da superconductividade a través da dopaxe, que interrompe a orde antiferromagnética do sistema precursor, suxerindo que o mecanismo de emparellamento nas dúas familias pode estar relacionado. Adicionalmente,

os IBS mostran unha estrutura electrónica multibanda, onde as xanelas de enerxía prohibida varían en función dos niveis de dopaxe e presión (externa ou química). Esta característica única causa dependencias coa temperatura non convencionais en varios observables, incluíndo a profundidade de penetración magnética, o coeficiente Seebeck, a calor específica e o campo magnético crítico superior.

Engadido ás aplicacións tradicionais dos supercondutores, o impulso dado polas tecnoloxías cuánticas renovou o interese dos supercondutores para a investigación aplicada. Principalmente, os circuitos supercondutores son actualmente o principal candidato para unha arquitectura escalable de computación cuántica, e xa se planificaron implementacións baseadas en supercondutores de computadores cuánticos ruidosos de tamaño intermedio (NISQ, *Noisy Intermediate Size Quantum*) cos que se prevé acadar máis de 4000 cúbits en 2025. Os sistemas supercondutores tamén se postulan para a futura implementación de memorias crioxénicas, tamén relevantes para a computación e comunicacións cuánticas e para as que a tecnoloxía CMOS actual non é axeitada. Simultaneamente, moitos avances tecnolóxicos en comunicacións cuánticas e ciencia fundamental dependen de detectores monofotón de alta eficiencia, para os cales os detectores monofotón baseados en nanofíos supercondutores (SNSPDs, *Superconductor Nanowire Single Photon Detectors*) son a tecnoloxía máis punteira, con eficiencias récord de máis do 90%. Dado que os cupratos e IBS son os únicos sistemas supercondutores que alcanzaron $T_c \gtrsim 30$ K a presión ambiente, algunhas das aplicacións dos supercondutores poderían beneficiarse enormemente da súa implementación en materiais de maior T_c, coa adición de campos críticos e correntes aumentadas que estes materiais poden soportar a temperaturas utilizables, e a investigación recente demostrou que os cupratos son prometedores para o seu uso por exemplo, en SNSPDs a temperaturas máis altas. Afondar nas propiedades dos cupratos supercondutores e IBS podería, polo tanto, axudar cara o obxectivo de maximizar certos parámetros relevantes para a súa aplicación industrial, así como axudar a dilucidar o seu mecanismo fundamental de emparellamento electrónico.

O obxectivo xeral da tese é o estudo dalgúns aspectos abertos da fenomenoloxía dos supercondutores de alta T_c, intrínsecamente nanoestruturados de forma lamelar, seguindo as liñas de investigación que o grupo QMatterPhotonics desenvolveu nos últimos anos no eido da supercondutividade. Esperamos que os resultados obtidos durante esta tese contribúan a unha mellor comprensión da nanoestruturación intrínseca dos supercondutores baseados en ferro e cupratos, e como a dimensionalidade reducida afecta as súas propiedades supercondutoras. Ademais, estes resultados teñen o potencial de axudar a mellorar algúns parámetros supercondutores interesantes, como a corrente crítica e o campo magnético de irreversibilidade, particularmente no caso dos supercondutores baseados en ferro, propiedades que están fortemente vencelladas á aplicación tecnolóxica destes supercondutores, así como os efectos precursores nos cupratos supercondutores. Estas cuestións son de importancia chave para a implementación tecnolóxico-industrial de aplicacións baseadas en supercondutores, ademais do seu interese inherente. Para cumprir con este obxectivo, o noso traballo levouse a cabo estudando os dous réximes nos que pode

estar un supercondutor: o estado normal a $T \gtrsim T_c(H)$, onde as propiedades dos supercondutores aínda poden diferir daquelas de materiais non supercondutores, e o estado propiamente supercondutor a $T < T_c(H)$. A temperaturas superiores a T_c, o noso estudo centrouse nos efectos precursores da supercondutividade, estudando múltiples observables, nomeadamente a paracondutividade por riba de T_c que arredonda a transición supercondutora, e a magnetocondutividade, a paracondutividade na presenza dun campo magnético externo aplicado. A temperaturas inferiores a T_c, o noso estudo centrouse en caracterizar as propiedades magnéticas dos supercondutores no chamado estado crítico, no que un supercondutor de tipo II ten a máxima cantidade de fluxo magnético atrapado que pode soportar para unha temperatura e un campo magnético aplicado dados. Isto dá lugar a unha histérese magnética, que pode proporcionar información útil sobre a ancoraxe do fluxo magnético atrapado dentro do supercondutor. Explicar a dependencia destes observables co campo magnético e a temperatura é crucial para a comprensión da supercondutividade nestes materiais.

Máis especificamente, con respecto aos supercondutores baseados en ferro, presentaremos os resultados de tres estudos diferentes centrados na fenomenoloxía dos IBS. Primeiramente, en *Multiband effects on the upper critical field angular dependence of 122family iron pnictide superconductors*, estudamos a dependencia angular anómala do campo crítico superior H_{c2} dun monocristal de alta calidade do IBS prototípico $Ba(Fe_{1-x}Co_x)_2As_2$. Este observable mostra unha desviación significativa con respecto ao cálculo baseado na teoría de Ginzburg-Landau para supercondutores 3D anisotrópicos (3D-aGL) esperado para campo magnético externo H orientado case en paralelo ás lamelas de FeAs, ao que proporcionamos con éxito unha explicación baseada na natureza multibanda destes materiais. Neste traballo, estudouse esta dependencia angular anómala medindo a resistividade eléctrica do monocristal ρ con diferentes orientacións dun campo magnético aplicado, con ángulo θ respecto do eixe c cristalográfico. Os datos de magnetocondutividade interpretáronse en termos do cálculo de Aslamazov-Larkin (AL) para fenómenos de flutuación no límite 3D (dada a pequena anisotropía do sistema), xeralizado ao réxime de campo magnético finito. Dos axustes da teoría aos datos, púidose facer unha determinación de $H_{c2}(\theta)$ libre de criterios, obtendo un perfil que se desvía significativamente do predito polo cálculo 3D-aGL. O perfil de $H_{c2}(\theta)$ explicouse mediante un cálculo teórico para supercondutores con dúas bandas que contribúen á supercondutividade no límite *sucio*, no cal o percorrido libre medio dos superportadores é moi inferior á lonxitude de coherencia supercondutora, evidenciando unha banda aproximadamente isotrópica ($\gamma \approx 1$) e outra banda moi anisotrópica ($\gamma \approx 9$). A partires destes resultados, suxerimos que o factor γ dependente da temperatura que algúns autores introducen para explicar o comportamento de $\rho(T, H, \theta)$ é un artefacto asociado ao uso do cálculo 3D-aGL, non aplicable a estes compostos. Tamén descubrimos que o campo de irreversibilidade non mostra tal comportamento anómalo e concorda plenamente co cálculo anisotrópico 3D, o que pode entenderse como se o mecanismo de ancoraxe non se vise moi afectado pola estrutura electrónica multibanda.

En segundo lugar, en *Vortex dynamics and second magnetization peak in the iron-pnictide superconductor* $Ca_{0.82}La_{0.18}Fe_{0.96}Ni_{0.04}As_2$ estudamos a dinámica de vórtices dun supercondutor baseado en ferro altamente anisotrópico, $Ca_{1-x}La_xFe_{1-y}Ni_yAs_2$, centrando especialmente o noso estudo no segundo pico de magnetización (SMP) que aparece nas curvas de histérese de magnetización isotérmica $M(H)$. Para este estudo da dinámica de vórtices, medíronse as curvas $M(H)$ para $H \parallel ab$ e $H \parallel c$, e curvas de relaxación magnética $M(t)_{H,T}$. Os nosos resultados suxiren un cambio na ancoraxe dos vórtices de plástica a colectiva ao cruzar H_p, o campo magnético para o cal se presenta o máximo do SMP. A baixas temperaturas, as curvas de $H_p(T)$ e $H_{on}(T)$, o campo magnético no cal muda a tendencia descendente da magnetización e comeza o SMP, achéganse seguindo curvaturas inversas e asemella que poderían chegar a aniquilarse, o que podería implicar un cambio na estrutura de ancoraxe a vórtices 2D acoplados por efecto Josephson. Con todo, esta unión non puido medirse a temperaturas superiores a 2 K. Adicionalmente, realizouse unha análise adicional da ancoraxe dos vórtices mediante o axuste das curvas de forza de ancoraxe normalizada fronte a campo magnético reducido $h = H/H_{irr}$ ao modelo de Dew-Hughes, que apunta a unha ancoraxe de tipo δl causado pola desorde puntual e defectos superficiais.

Finalmente, en *Enhancement of the critical current by surface irregularities in Fe-based superconductors* exploramos o efecto da introducción de irregularidades micrométricas na superficie de monocristais de $BaFe_2(As_{1-x}P_x)_2$, un composto atractivo de cara ás aplicacións dada a súa elevada J_c. As irregularidades superficiais xa foran previamente utilizadas para incrementar a corrente crítica en supercondutores convencionais de baixa T_c, e o seu efecto nos pnicturos de ferro nunca se estudara antes. Por iso, neste traballo estudouse o seu efecto nas propiedades críticas de $BaFe_2(As_{1-x}P_x)_2$ mediante o estudo do aumento da amplitude das curvas de histérese isotérmica $m(H)$ con $H \parallel c$ antes e despois de atacar as superficies dos cristais con area de sílice a baixas presións. Observouse un aumento significativo da corrente crítica para todas as mostras e para todas as curvas isotérmicas (é dicir, a todas as temperaturas), seguindo unhas dependencias coa temperatura e campo magnético apreciablemente diferentes das observadas para a corrente crítica volúmica antes do atacado con area. A partires destes datos, obtívose unha densidade estimada de corrente crítica superficial $K_c(T, H)$, que posteriormente se comparou cun cálculo teórico para a corrente non disipativa máxima que unha superficie rugosa pode soportar, baseado na teoría do continuo de Mathieu-Simon para o estado mixto, e que pode explicar cualitativamente o aumento da histérese observado. Das curvas de histérese, tamén se obtivo o campo de irreversibilidade H_{irr} para temperaturas próximas a T_c, observando un aumento da liña H_{irr} despois do tratamento. Ademais, observouse un aumento brusco de $K_c(T)$ xusto ao lado da liña $H_{irr}(T)$, un efecto que non está presente nas curvas de densidade de corrente crítica volúmica $J_c(T)$, o que podería axudar a clarexar a orixe da súa aparición noutros supercondutores.

En canto aos cupratos supercondutores, centrámonos no estudo da paracondutividade, a condutividade en exceso da esperada no estado normal por riba da tran-

sición supercondutora, $\Delta\sigma(T > T_c)$, para a cal múltiples propostas teóricas tentan explicar a súa dependencia coa temperatura e que, na súa maioría, son incompatibles entre si, e que son chave para a comprensión da natureza supercondutora destes materiais. Múltiples autores suxeriron que o arredondamento da transición superconductora nestes materiais podería ser causado só ou principalmente por procesos percolativos emerxentes, debido a unha distribución intrínseca de T_c. Con todo, moitos outros estudos atoparon que, en certos escenarios, as flutuacións térmicas por si soas poden producir suficiente aumento da condutividade para explicar os datos. Esta tese presenta dous artigos que discuten o arredondamento da resistividade nos planos de CuO_2 $\rho_{ab}(T)$ ao redor de T_c en cupratos óptimamente dopados. O primeiro artigo, titulado *Precursor superconducting effects in the optimally doped* $YBa_2Cu_3O_{7-\delta}$ *superconductor: the confrontation between superconducting fluctuations and percolative effects revisited*, céntrase en YBCO óptimamente dopado, mentres que o segundo artigo, con título *On the dilemma between percolation processes and fluctuating pairs as the origin of the enhanced conductivity above the superconducting transition in cuprates*, analiza cristais e filmes de alta calidade de $La_{2-x}Sr_xCuO_4$ (LaSCO), $Bi_2Sr_2CaCu_2O_{8+\delta}$ (Bi2212) e $Tl_2Ba_2Ca_2Cu_3O_{10}$ (Tl2223), máis anisotrópicos. Para isto, empregamos a teoría do medio efectivo (EMT, *Effective Medium Theory*) de Bruggeman para examinar se os efectos percolativos emerxentes, derivados de inhomoxeneidades microscópicas debidas a unha distribución de T_c, poderían explicar por si sós a paracondutividade nestes cupratos óptimamente dopados, considerando dominios cunha distribución de temperaturas críticas aproximada por unha distribución gaussiana. Con todo, este modelo non consegue reconstruír adecuadamente a dependencia experimental da paracondutividade para todos os compostos, especialmente para os máis anisotrópicos. Pola outra banda, mostramos que os cálculos de Lawrence-Doniach (LD) para materiais lamelares e de Aslamazov-Larkin para materiais bidimensionais (AL2D) reconstrúen máis fielmente a paracondutividade destes compostos ao seren estendidos a altas temperaturas reducidas mediante a inclusión dun corte na enerxía total que considera os modos de flutuación de onda curta. Por tanto, estes modelos teóricos baseados no escenario de flutuacións supercondutoras calculadas na teoría de Ginzburg-Landau en aproximación gaussiana mostran ser unha explicación máis axeitada para describir o comportamento da paracondutividade nestes supercondutores lamelares. O modelo LD, que foi previamente aplicado para explicar a paracondutividade de YBCO, aplicouse tamén con éxito a LaSCO, mentres que o modelo AL2D semella ser suficiente para explicar a paracondutividade de Bi2212 e Tl2223, mostrando que os datos experimentais están ben explicados dentro deste marco para todo o rango de temperaturas reducidas analizado, ata T_{onset}, a temperatura por debaixo da cal a resistividade dos compostos comeza a diverxer do comportamento no estado normal. Adicionalmente, analizouse un modelo percolativo proposto recentemente que suxire a percolación emerxente como única fonte de paracondutividade, en concreto para cupratos subdopados. Mostramos que este modelo, que predí un escalado universal da paracondutividade fronte a $T - T_c$, non logra explicar os datos dos cupratos óptimamente dopados. No entanto, o modelo GGL con corte na enerxía total si nos per-

mitiu reconstruir a paracondutividade dos compostos subdopados, salvo a inclusión dun parámetro multiplicativo (C_g), que pode ser debido ás incertezas na amplitude causadas pola xeometría das mostras ou o proceso de substración da resistividade normal, coñecidamente máis complexo en mostras subdopadas. Outro argumento chave contra os modelos de percolación emerxente son as amplas distribucións de T_c que se precisan para intentar explicar os datos con modelos percolativos, que contrastan marcadamente coas estreitas transicións diamagnéticas destes materiais, as cales son independentes da posible percolación. Esta discrepancia subliña a limitación do modelo percolativo e reafirma a relevancia das flutuacións supercondutoras para explicar a paracondutividade tanto en cupratos subdopados como óptimamente dopados. A nosa análise demostra a necesidade de considerar tanto as flutuacións térmicas como a estrutura lamelar dos cupratos para unha comprensión completa das súas propiedades supercondutoras. En conclusión, as predicións dos modelos baseados no escenario GGL, nos cales a paracondutividade é dependente da distancia efectiva entre lamelas d_{eff}, e o parámetro de acoplamento de Lawrence-Doniach B_{LD} para os cupratos menos anisotrópicos, aliñáronse ben cos datos experimentais, especialmente para temperaturas ben por encima de T_c e preto da rexión de corte. Estes achados mostran que os efectos percolativos son insuficientes para describir o comportamento xeral da paracondutividade en cupratos de alta T_c.

Summary

The discovery of superconductivity in 1911 by Kamerlingh Onnes marked a significant milestone in solid-state physics. This phenomenon, due to which materials exhibit zero electrical resistance and expel magnetic fields from their interior, was initially observed in ultra-pure mercury capillaries. Subsequent discoveries, such as the Meissner effect (perfect diamagnetism) and the formulation of the London equations, expanded the understanding of superconductivity. Although these initial theories explained the phenomenology of superconductivity, they did not address the superconducting transition, and the development of the Ginzburg-Landau theory in 1950 provided a more complete explanation with the introduction of an order parameter, representing the supercarrier density, which takes non-zero values below the superconducting transition temperature T_c. This theory, crucial for describing the different behaviors observed in type-I and type-II superconductors, could not yet provide a microscopic explanation for superconductivity, a feat finally achieved by the Bardeen-Cooper-Schrieffer (BCS) theory in 1957. This theory explains conventional superconductors through electron correlations mediated by phonons, leading to the pairing of electrons into Cooper pairs. The BCS theory successfully explained many superconducting phenomena, such as the energy gap that opens at the Fermi level below T_c, and the isotopic effect, whereby T_c depends on the mass of the isotopes forming the crystal lattice. Later, the discovery of the Josephson effect in 1962 opened the door to several superconductor-based technologies, including SQUIDs and superconducting qubits. This thesis focuses on two families of superconductors of particular scientific and technological interest: cuprate superconductors and iron-based superconductors, which exhibit properties such as high critical magnetic fields and critical currents, crucial for applications in electrical transport, magnetic field generation, and quantum technologies.

Cuprate superconductors were initially discovered in 1986, when Karl Alexander Müller and Johannes Georg Bednorz found that the ceramic compound $Ba_xLa_{5-x}Cu_5O_{5(3-y)}$ became superconducting at 30 K. The subsequent discovery of $(Y_{1-x}Ba_x)_2CuO_{4-\delta}$, superconducting between 80 and 93 K, surpassed for the first time the boiling point of liquid nitrogen (77 K), marking a milestone in achieving superconductors at more practical temperatures. Further research on these ceramic superconductors, with a crystallographic structure similar to perovskites, led to record critical temperatures of 138 K at ambient pressure in $Hg_{0.8}Tl_{0.2}Ba_2Ca_2Cu_3O_{8+\delta}$, which continue to be unsurpassed. However, the applicability of the BCS theory to

explain their pairing mechanism remains unresolved. For instance, ARPES (Angle-Resolved Photoemission Spectroscopy) experiments show deviations from the predictions of singlet-type pairing, and recent proposals suggest the electron-electron interaction may be mediated by the superexchange interaction in an antiferromagnetic correlated-insulator state, instead of electron-phonon interaction. Besides their high critical temperatures, cuprates have multiple interesting properties from the point of view of applications, such as high upper critical fields and critical currents, necessary for the manufacture of superconducting cables for electrical transport and magnetic field generation, and REBCO (Rare-earth Barium Copper Oxyde) tapes are already commercially available. However, their high anisotropy and poor intergranular connectivity of the crystals, which require precise alignment, present challenges for their application on a large scale. Cuprate superconductors also show other unusual and complex properties that have challenged conventional theoretical models, such as the origin of their paraconductivity, the excess conductivity in the normal state above T_c that superconductors exhibit. Bednorz and Müller's seminal work in 1986 already suggested that the decrease in resistance near T_c in Ba-La-Cu-O could be the result of a combination of a percolative nature and 2D superconducting fluctuations. Early studies using effective medium theory (EMT) in optimally doped YBCO downplayed the role of emerging percolative processes in paraconductivity, attributing the decrease in resistivity to the presence of thermal fluctuations. In particular, the experimental data were in good agreement with the Lawrence- Doniach (LD) model in the Gaussian-Ginzburg-Landau (GGL) scenario. Subsequent research has debated whether emerging percolative processes due to intrinsic inhomogeneities could be solely responsible for the rounding in cuprate superconductors, with some studies suggesting the coexistence of fluctuations and percolation.

In 2008, another significant advance in the field of superconductivity was the discovery of iron-based superconductors (IBS). IBS have several properties that make them attractive for practical applications, such as their high critical and irreversibility magnetic fields, the latter comparable to those of cuprates at 4.2 K, while showing a significantly lower anisotropy factor γ, especially the 122 family with a γ of approximately 3, and higher grain boundary critical angles (up to 9 degrees), improving polycrystal connectivity. These characteristics could make them more suitable than cuprates for mass manufacture of polycrystalline wires and tapes, and for the development of superconducting devices such as bulk magnets or thin-film nanocircuits including integrated Josephson junctions and SQUIDs. IBS also have fundamental interest given their similarities with cuprates, such as their laminar structure, their high transition temperatures (yet lower than those of cuprates), and the emergence of superconductivity with the introduction of dopants, which destroy the antiferromagnetic order of the parent system, suggesting that the pairing mechanism in the two families may be related. Additionally, IBS exhibit a multiband electronic structure, with energy gaps that depend on the doping level and on the pressure (external or chemical). This unique feature causes unconventional temperature dependencies in various observables, such as the magnetic penetration depth,

the Seebeck coefficient, the specific heat or the upper critical magnetic field.

Added to the traditional applications of superconductors, the impulse given by quantum technologies has renewed the interest of superconductors for applied research. Primarily, superconducting circuits are currently the main candidate for a scalable quantum computing architecture, and superconductor-based implementations of *Noisy Intermediate Size Quantum* (NISQ) computers are already planned to reach over 4000 qubits by 2025. Superconductors systems have been proposed for the future implementation of cryogenic memories for which current CMOS technology is not suitable, also relevant for quantum computing and communications. Simultaneously, many technological advances in quantum communications and fundamental science rely on high-efficiency single photon detectors, for which *Superconductor Nanowire Single Photon Detectors* (SNSPDs) are the most prominent technology with record-breaking efficiencies upwards of 90%. Given that cuprates and IBS are the only superconducting systems that have achieved $T_c \gtrsim 30$ K at room pressure, some of these applications could potentially benefit greatly of their implementation with higher-T_c systems, with the addition of increased critical fields and currents that these materials can withstand at usable temperatures, and recent research has demonstrated that cuprates are promising for their use for e.g., SNSPDs at higher temperatures. Determining the properties of cuprate superconductors and IBS could therefore help the aim of maximizing certain relevant parameters for their industrial application, as well as helping to shed light into their fundamental pairing mechanism.

The general aim of this thesis is the study of some open aspects of the phenomenology of high T_c superconductors, intrinsically nanostructured in a laminar form, following the lines of research that the QMatterPhotonics group has been developing in the past few years on the subject of superconductivity. We expect the results obtained during this thesis to contribute towards a better understanding of the intrinsic nanostructuration of iron-based and cuprate superconductors, and how reduced dimensionality affects their superconducting properties. Additionally, these results have the potential to help improve some interesting superconducting parameters, such as the critical current and the irreversibility magnetic field, particularly in the case of iron-based superconductors, properties that are strongly linked to the technological application of these superconductors, as well as the precursor effects in cuprate superconductors. These questions are of key importance to the technological-industrial implementation of applications based on superconductors, aside from their inherent interest. To fulfill this aim, our work was carried out by studying the two regimes in which a superconductor can be, the normal state at $T \gtrsim T_c(H)$, where the properties of superconductors can still differ from those of non-superconducting materials, and the proper superconducting state at $T < T_c(H)$. At temperatures higher than T_c, our study focused on the precursor effects of superconductivity, by studying multiple observables, namely the paraconductivity, i.e., the excess conductivity above T_c which rounds the superconducting transition, and the magnetoconductivity, the paraconductivity in presence of an external applied

magnetic field. At temperatures below T_c, our study focused on characterizing the magnetic properties of superconductors in the so-called critical state, in which a type-II superconductor has the maximum amount of trapped magnetic flux it can withstand for a given temperature and applied magnetic field. This gives rise to magnetic hysteresis, which can provide useful information about the pinning of the trapped flux inside the superconductor. Explaining the dependence of these observables with magnetic field and temperature is crucial to the understanding of the superconductivity in these materials.

More specifically, regarding iron-based superconductors, we will present the results of three different studies focused on the IBS phenomenology. Firstly, in *Multiband effects on the upper critical field angular dependence of 122-family iron pnictide superconductors*, we studied the anomalous angular dependence of the upper critical field H_{c2} of a high-quality single crystal of the prototypical IBS $Ba(Fe_{1-x}Co_x)_2As_2$. This observable has been shown to present a significant deviation from the expected 3D anisotropic Ginzburg-Landau (3D-aGL) approach for $\vec{H}$ oriented at angles almost parallel to the FeAs layers, to which we have successfully provided an explanation based on the multiband nature of these materials. In this work, this anomalous angular dependence was studied by measuring the electrical resistivity ρ of the single crystal with different orientations of an applied magnetic field, with angle θ with respect to the crystallographic c-axis. The excess magnetoconductivity data were interpreted in terms of the Aslamazov-Larkin (AL) calculation for fluctuation phenomena in the 3D limit (given the small anisotropy of the system), generalized to the finite magnetic field regime. From the best fits of this theory to the data, a criterion-free determination of $H_{c2}(\theta)$ could be made, obtaining a profile that deviates significantly from the one predicted by the 3D-aGL calculation. The profile of $H_{c2}(\theta)$ was then successfully explained by a theoretical calculation for dirty two-band superconductors in which one band is roughly isotropic ($\gamma \approx 1$) and another band is highly anisotropic ($\gamma \approx 9$). From these results, we suggest that the temperature-dependent γ that other authors introduce to account for the $\rho(T, H, \theta)$ behavior is an artifact associated to the use of the 3D-aGL calculation. We also found that the irreversibility field does not show such anomalous behavior and fully agrees with the 3D anisotropic calculation, which can be understood as if the pinning mechanism were not strongly affected by the the multiband electronic structure.

Secondly, in *Vortex dynamics and second magnetization peak in the iron-pnictide superconductor* $Ca_{0.82}La_{0.18}Fe_{0.96}Ni_{0.04}As_2$, we studied the vortex dynamics of a highly anisotropic iron-based superconductor, $Ca_{1-x}La_xFe_{1-y}Ni_yAs_2$, focusing our study on the second magnetization peak (SMP) that appears in the isothermal magnetization hysteresis curves $M(H)$. For this study of vortex dynamics, $M(H)$ curves for $H \parallel ab$ and $H \parallel c$, and magnetic relaxation curves $M(t)_{H,T}$ were measured. Our results suggest a crossover from plastic to collective pinning across H_p, the magnetic field at which the maximum of the SMP occurs. At low temperatures, the curves $H_p(T)$ and $H_{on}(T)$, the magnetic field above which the downward trend of

the magnetization changes marking the beginning of the SMP, close in following inverse curvatures and may eventually merge, which would imply a change in the pinning structure to 2D Josephson-coupled vortices. However, this merging could not be measured at temperatures above 2 K. Additional pinning analysis by fitting the normalized pinning force vs reduced magnetic field $h = H/H_{irr}$ curves to the Dew-Hughes model points towards a δl–type pinning caused by point disorder and surface defects.

Finally, in *Enhancement of the critical current by surface irregularities in Fe-based superconductors*, we explored the effect of introducing micrometric irregularities on the surface of $BaFe_2(As_{1-x}P_x)_2$ single crystals, an attractive compound for applications given its high J_c. Surface irregularities had previously been used to increase the critical current in conventional low T_c superconductors, and their effect on iron pnictides had never been studied before. Therefore, in this work, we studied their effect on the critical properties of $BaFe_2(As_{1-x}P_x)_2$ by studying the amplitude increase of the isothermal $m(H)$ hysteresis curves with $H \parallel c$ before and after sandblasting the crystal surfaces with silica sand at low pressures. A significant critical current increase was observed for all samples and for all isothermal curves (i.e., at all temperatures), following temperature and magnetic field dependence appreciably different from the bulk critical current before sandblasting. From these data, an estimated surface critical current density $K_c(T, H)$ was obtained, which was subsequently compared with a theoretical calculation for the maximum non-dissipative current that a rough surface can withstand, based on Mathieu-Simon continuum theory for the mixed state, and which can qualitatively explain the hysteresis increase. From the hysteresis curves, the irreversiblity field H_{irr} was also obtained for temperatures close to T_c, observing an increase in the H_{irr} line after treatment. Additionally, a sharp increase of $K_c(T)$ was observed right next to the $H_{irr}(T)$ line, an effect that is not present in the bulk critical current density curves $J_c(T)$, which could help shed light on the origin of its appearance in other superconductors.

Regarding cuprate superconductors, we will focus on the study of the paraconductivity $\Delta\sigma$, the excess conductivity above the superconducting transition, key to understanding the superconducting nature of these materials. Several theoretical proposals, which are for the most part incompatible with each other, attempt to explain its temperature dependence $\Delta\sigma(T > T_c)$. To this end, multiple authors have suggested that the rounding of the superconducting transition in these materials could be caused solely or primarily by emergent percolative processes, due to an intrinsic distribution of T_c. Nevertheless, many other studies have found that, in certain scenarios, thermal fluctuations alone can produce sufficient increased conductivity to explain the data. This thesis presents two articles where the rounding in the CuO_2-plane resistivity $\rho_{ab}(T)$ around T_c in optimally doped cuprates is discussed. The first article, titled *Precursor superconducting effects in the optimally doped $YBa_2Cu_3O_{7-\delta}$ superconductor: the confrontation between superconducting fluctuations and percolative effects revisited*, focuses on optimally doped YBCO, while the second article, titled *On the dilemma between percolation processes and*

fluctuating pairs as the origin of the enhanced conductivity above the superconducting transition in cuprates, analyzes high-quality crystals and films of $La_{2-x}Sr_xCuO_4$ (LaSCO), $Bi_2Sr_2CaCu_2O_{8+\delta}$ (Bi2212), and $Tl_2Ba_2Ca_2Cu_3O_{10}$ (Tl2223), which are more anisotropic. For this, we used Bruggeman's effective medium theory (EMT) to analyze whether emergent percolative effects arising from microscopic inhomogeneities due to a distribution of T_c could be the single source of paraconductivity in cuprates, considering domains with a critical temperature distribution, approximated by a Gaussian distribution. However, this model failed to reconstruct the experimental paraconductivity for all compounds, especially for the more anisotropic ones. On the other hand, we show that the calculations of Lawrence-Doniach (LD) for laminar materials and Aslamazov-Larkin for two-dimensional materials (AL2D) reproduce the paraconductivity of these compounds more faithfully, when extended to high reduced temperatures by including a total energy cutoff that considers short wavelength fluctuating modes. Therefore, these theoretical models based on the superconducting fluctuations scenario calculated in the Gaussian-Ginzburg-Landau framework prove to be a more appropriate explanation for describing the behavior of paraconductivity in these laminar superconductors. The LD model, previously used to explain the paraconductivity of YBCO, was also successfully applied to LaSCO, while the AL2D model seems sufficient to explain the paraconductivity of Bi2212 and Tl2223, showing that the experimental data are well described within this framework for the entire range of reduced temperatures analyzed, up to T_{onset}, the temperature below which the resistivity of the compounds begins to diverge from the normal state behavior. Additionally, a recently proposed percolative model which proposes emergent percolation as the sole source of paraconductivity, specifically for underdoped cuprates, was analyzed. We show that this model, which predicts a universal scaling of paraconductivity against $T - T_c$, fails to explain the data of optimally doped cuprates. However, the GGL model with a total energy cutoff did allow us to reconstruct the paraconductivity of the underdoped compounds, except for the inclusion of a multiplicative parameter (C_g), which may be due to uncertainties in the amplitude caused by the geometry of the samples or the process of subtracting the normal resistivity, knowingly more challenging in underdoped samples. Another key argument against emergent percolation models is the wide T_c distributions required to attempt to explain the data with percolative models, which markedly contrast with the much sharper diamagnetic transitions of these materials, which are not susceptible of percolation. This discrepancy underlines the limitation of the percolative model and reaffirms the relevance of superconducting fluctuations in explaining paraconductivity in both underdoped and optimally doped cuprates. Our analysis demonstrates the need to consider both thermal fluctuations and the laminar structure of cuprates for a complete understanding of their superconducting properties. In conclusion, the predictions of models based on the GGL scenario, in which paraconductivity is dependent on the effective interlayer distance d_{eff}, and the Lawrence-Doniach coupling parameter B_{LD} for the less anisotropic cuprates, aligned well with the experimental data, especially for temperatures well above T_c and near the cutoff region. These findings show that percolative effects are insufficient to

describe the overall behavior of paraconductivity in high T_c cuprates.

Contents

Introduction **1**
Objectives . . . 7
Outline of the manuscript . . . 9

1 Experimental Methods **11**
1.1 Thin film deposition and single crystal growth . . . 11
1.2 Resistivity measurements . . . 12
1.3 Magnetic moment measurements . . . 12
1.4 XRD . . . 13
1.5 T_c determination . . . 14
1.6 $\Delta\sigma$ determination . . . 14
1.7 AFM . . . 15
1.8 Sandblasting . . . 15

2 Multiband effects and vortex dynamics of iron-based superconductors **17**
2.1 The anomalous angular anisotropy of 122 family iron-based superconductors . . . 19
2.2 The mechanism behind the secondary magnetization peak . . . 20
2.3 Surface treatment to enhance the critical current of IBS . . . 21
2.4 Multiband effects on the upper critical field angular dependence of 122family iron pnictide superconductors . . . 23
2.5 Vortex dynamics and second magnetization peak in the iron-pnictide superconductor $Ca_{0.82}La_{0.18}Fe_{0.96}Ni_{0.04}As_2$ . . . 35
2.6 Enhancement of the critical current by surface irregularities in Fe-based superconductors . . . 51

3 Fluctuations vs percolation in cuprate superconductors **61**
3.1 Precursor superconducting effects in the optimally doped $YBa_2Cu_3O_{7-\delta}$ superconductor: the confrontation between superconducting fluctuations and percolative effects revisited . . . 65
3.2 On the dilemma between percolation processes and fluctuating pairs as the origin of the enhanced conductivity above the superconducting transition in cuprates . . . 71

4 Discussion **85**
4.1 Results on iron-based superconductors 85
4.1.1 On the multiband structure of $Ba(Fe_{1-x}Co_x)_2As_2$ 85
4.1.2 On the vortex dynamics of $Ca_{0.82}La_{0.18}Fe_{0.96}Ni_{0.04}As_2$ 89
4.1.3 On the increased surface pinning of $BaFe_2(As_{1-x}P_x)_2$ 91
4.2 Results on precursor effects of cuprate superconductors 94
4.2.1 Percolative analysis 94
4.2.2 Fluctuation analysis 95
4.2.3 Comparison with recent results 97

5 General conclusion **101**

List of publications and quality metrics **105**

References **111**

Introduction

The discovery of superconductivity in 1911 was possible thanks to the early work in cryogenics by Kamerlingh Onnes (Nobel Prize laureate in 1913) group at Leiden, the same group that first achieved the liquefaction of helium only three years prior. [1] Their finding was not completely accidental, albeit the experiment they were conducting was designed to explore the behavior of good conductors such as gold and platinum at low temperatures, for which the contemporary theories predicted two scenarios: Drude's 1900 kinetic theory of gases predicted a linear decrease of resistance with temperature so good conductors would have zero resistance at 0 K, and Lord Kelvin's 1901 calculation, which predicted that the conducting electrons would eventually become a "frozen solid", so no conduction at 0 K could be possible. [2] The Leiden team found that for most metals, the resistance of metals reached a residual value at low temperatures, which depended primarily on the purity of the metal. This motivated their experiment in mercury capillaries, as these can be made extremely pure by distillation, due to the low boiling point of mercury (356.7 °C). The team found that the resistance of the mercury capillaries dropped down to zero at 4.2 K, although suddenly instead of the progressive decrease predicted by Drude, [3] which marked the discovery of the first superconducting property: the *perfect conductivity*.

In 1933, the German physicists Walther Meissner and Robert Ochsenfeld discovered that superconductors also exhibited *perfect diamagnetism* ($\chi = -1$), characterized the complete expulsion of magnetic flux from their interior. This effect is known as Meissner-Ochsenfeld effect, or more commonly *Meissner effect*. [4, 5] Following this discovery, the British physicists Fritz and Heinz London managed to formulate the first theory of superconductivity, known as the *London equations*, which explained both the perfect conductivity and perfect diamagnetism of superconductors. [6] Albeit their theory cannot be obtained from first principles, [7] it was derived from well-known equations of electromagnetism under very simple assumptions. So, starting from the Drude theory of metals [8, 9] and assuming the superconducting charge carriers (*supercarriers*) do not suffer scattering processes (i.e., their relaxation time $\tau \to \infty$), it follows that

$$\frac{\partial \vec{J}}{\partial t} = \frac{n_s e^2}{m} \vec{E} \,, \tag{1}$$

known as the *first London equation*, where $\vec{J}$ is the superconducting current or

supercurrent, $\vec{E}$ is the applied electric field, n_s is the supercarrier density, and e, m are the charge and mass of the supercarriers, respectively. This equation reproduces the perfectly conducting behavior of superconductors: if the applied electric field $\vec{E} \to 0$, then the supercurrent does not decay (i.e., $\partial\vec{J}/\partial t = 0$). The perfectly diagmagnetic behavior can also be explained in this model. Eq. (1) predicts the presence of static supercurrents, due to which the charge carriers have a kinetic energy, so the total energy of the system is the sum of the kinetic energy plus the magnetic energy stored in the field. Minimizing this free energy with respect to the field distribution, the *second London equation* can be obtained, [10]

$$\left(\lambda^{-2} - \nabla^2\right)\vec{B} = 0\,, \tag{2}$$

where $\lambda = \sqrt{m/\mu_0 n_s e^2}$. This equation predicts an exponential-like decay of the magnetic field near the surface of the superconductor, so λ, known as the *London penetration length*, can be understood as the typical decay distance of the magnetic field inside of the superconductor. Well inside the superconductor, the second London equation correctly predicts that the magnetic induction must be $\vec{B} \to 0$, giving rise to the Meissner effect.

Nevertheless, the theory of superconductivity proposed by the London brothers could not explain the superconducting transition, i.e., the sudden drop to $\rho = 0$ and $\chi = -1$ at the superconducting transition temperature T_c, but only the phenomenology in the superconducting state. For this reason, a significant development in the formal characterization of superconductors was the formulation in 1950 of the Ginzburg-Landau theory of superconductors, by soviet physicists Vitaly Ginzburg and Lev Landau (Nobel Prize laureates in Physics, in 2003 and 1962, respectively). [11, 12] This theory is based on Landau's phenomenological theory of second-order phase transitions i.e., transitions that have no latent heat but whose free energy second derivatives are discontinuous. For this reason, an order parameter Ψ was introduced, understood as the supercarrier density, such that in the normal state $|\Psi| = 0$ and in superconducting phase $|\Psi| > 0$. A model that reconstructs this behavior is one whose free energy has the form

$$F[\Psi] = F_n + \int \left[\alpha(T)|\Psi|^2 + \frac{\beta(T)}{2}|\Psi|^4 + \frac{\hbar^2}{2m}|\nabla\Psi|^2\right] d^3x\,, \tag{3}$$

where F_n, α and β can we viewed as the order 0, 1 and 2 coefficients of the series expansion of F in $|\Psi|^2$ (so F_n corresponds to the free energy in the normal state), and the fourth term can be thought of as the kinetic energy of the charge carriers. [7] In first order approximation and in absence of gradients, a phase transition can be obtained from Eq. (3) if $\alpha \approx \alpha_0 \cdot (T - Tc)$, where $0 < \alpha_0 \neq \alpha(T)$, and $0 < \beta \neq \beta(T)$. So, at temperatures above T_c, the minimum of free energy is $F\left[\Psi = 0\right] = F_n$, but for $T < T_c$ this minimum is located at $|\Psi_0|^2 = -\alpha_0(T - T_c)/\beta$. However, we must include two more terms in Eq. (3) to account for the interaction with a magnetic field. Following the usual procedure in electrodynamics of replacing $\nabla \to \nabla - i\frac{e}{\hbar}\vec{A}$, and adding a term to account for the energy stored in the magnetic field, we finally

arrive to the Ginzburg-Landau free energy functional,

$$F[\Psi] = F_n + \int \left[\alpha_0 (T - T_c)|\Psi|^2 + \frac{\beta}{2}|\Psi|^4 + \frac{\hbar^2}{2m} \left| \left(\nabla - i\frac{e}{\hbar}\vec{A} \right) \Psi \right|^2 + \frac{\mu_0 H^2}{2} \right] d^3x \ . \tag{4}$$

From Eq. (4) and applying variational methods, the well-known Ginzburg-Landau (GL) equations are recovered, [7]

$$\alpha\Psi + \beta|\Psi|^2\Psi + \frac{\hbar^2}{2m}\left(i\nabla - \frac{e}{\hbar}\vec{A}\right)^2 \Psi = 0 \tag{5}$$

and

$$\vec{J} = i\frac{e\hbar}{2m}\left(\Psi\nabla\Psi^* - \Psi^*\nabla\Psi\right) - \frac{e^2}{m}\Psi^*\Psi\vec{A} \ . \tag{6}$$

The GL equations define the properties of superconductors from a thermodynamical perspective. One important characteristic length of superconductors that can be obtained from these equations is the *GL coherence length*. When no magnetic field is present, we can choose $\vec{A} = 0$, so all terms in Eq. (5) are real. In one dimension, we can solve for a normalized $\psi = \Psi/(-\alpha/\beta)^{-1/2}$, obtaining,

$$\xi^2(T)\frac{d^2\psi}{dx^2} + \psi - \psi^3 = 0 \ , \tag{7}$$

where $\xi(T) = \hbar/\sqrt{2m|\alpha(T)|}$ is the GL coherence length. ξ gives an idea of *how quickly* the variations of the superconducting order parameter can take place in space. The other characteristic length of superconductors, the London penetration depth λ, can also be obtained in terms of the GL parameters as $\lambda(T) = \sqrt{m\beta/\mu_0 e^2|\alpha(T)|}$.

The GL theory could also explain the different phenomenology observed for type-I and type-II superconductors. [7] Type-I superconductors are those that have an abrupt disappearance of superconductivity when a sufficient magnetic field $H < H_c$ is applied, where H_c is known as the *critical magnetic field*. However, a type-II superconductor does not experience such a sudden change in properties. Instead, it experiences Meissner effect i.e., $\chi \approx -1$ below a certain magnetic field H_{c1}, the *lower critical magnetic field*, and above this field an amount of magnetic flux can enter the superconductor, so $\chi > -1$ up to a its *upper critical magnetic field* H_{c2}. Nevertheless, the GL theory of superconductivity can account for these two different behaviors. In this theory, type-II superconductors are characterized for having negative domain energy when a sufficient magnetic field is applied ($H > H_{c1}$), but still having non-vanishing order parameter. The constant ratio between the penetration depth and the GL coherence length $\kappa = \lambda/\xi$ determines the type of superconductor, so for type-I $0 < \kappa < 1/\sqrt{2}$, and for type-II $\kappa > 1/\sqrt{2}$. [11, 12]

Despite the success of the GL theory to describe the phenomenology of superconductors, it could not provide a microscopic explanation for superconductivity. One decisive finding for this goal was the discovery of the isotope effect, the observation of the critical temperature of metallic superconductors being inversely

proportional to the square root of the mass of the isotope used. This effect, initially observed for mercury, indicated that the crystal lattice vibrations could have be relevant for the superconductivity of metals, as different isotopes normally have similar electrical properties. [13, 14] With this vital information at hand, and armed with Fröhlich's hamiltonian, which described the electron-phonon interaction in superconductors, [15] John Bardeen, Leon Cooper and Robert Schrieffer finally provided in 1957 a fundamental explanation of superconductivity from a microscopic perspective, a theory known by their initials as *BCS* and for which they won the 1972 Nobel Prize. [16] In their theory, superconductivity arises from correlations between electrons caused by an effective attractive force between pairs of electrons of the crystal lattice, mediated by phonons, the quantized normal modes of vibration of the lattice. This pairing mechanism was earlier introduced by Leon Cooper in 1956, and he described these correlations as electrons forming "paired" singlet systems of total spin zero (so they follow bosonic statistics), named *Cooper pairs* after him, which can condensate below a certain energy threshold as long as an attractive force exists, no matter how weak. [17] This theory predicted multiple superconducting phenomena, such as the appearance of an energy gap Δ at the Fermi level in the superconducting state, and a simple material-independent relationship of the gap with T_c, such that

$$\Delta(T = 0\ \mathrm{K}) = 1.764 k_B T_c\ . \tag{8}$$

Given the relevance and predictive capacity of the GL theory, Gor'kov proved in 1959 that this phenomenological theory can be directly derived from the BCS theory close to T_c, and that the electric charge and mass of the supercarriers in the GL theory correspond to twice those of the electron. [18]

However, the most significant breaktrough in the history of superconductivity towards applications was the 1962 discovery of the Josephson effect, [19] in honour of its discoverer Brian Josephson (yet another Nobel prize laureate, in 1973). The Josephson junction can be roughly described as the tunneling of Cooper pairs across a junction made of two superconducting electrodes, sandwiching a non superconducting interface, which gives rise to interesting phenomenology. The two possible manifestations of this effect are known as *DC Josephson effect* and *AC Josephson effect*. [7] The DC Josephson effect is characterized by the ability of the junction to establish a supercurrent between the two electrodes in absence of a voltage, being this current a function of the difference in phase of the Ginzburg-Landau order parameter $\Delta\phi$,

$$I_{\text{junction}} = I_c \sin \Delta\phi\ . \tag{9}$$

On the other hand, the AC Josephson effect describes how this phase difference evolves with time with the application of a constant voltage V,

$$\frac{d\Delta\phi}{dt} = \frac{2eV}{\hbar}\ . \tag{10}$$

The discovery of the Josephson effect was a stepping stone to the development of superconductor technology. A whole range of superconducting devices require Joseph-

son junctions for their core working principles, such as *Superconducting Quantum Interference Devices* (SQUID), among the most sensitive magnetometers available, [20] superconducting qubits, [21, 22] and ultra-fast [23] or ultra-low-power [24] logic.

Nevertheless, in recent years significant applied research has focused on two major superconducting families, known as *cuprate superconductors* and *iron-based superconductors*. The long-sought dream of higher temperature superconductors was finally achieved in 1986 by the hands of Karl Alexander Müller and Johannes Georg Bednorz with the discovery of $Ba_xLa_{5-x}Cu_5O_{5(3-y)}$, which became superconducting at 30 K. [25] The discovery of $(Y_{1-x}Ba_x)_2CuO_{4-\delta}$ the following year by Wu et al., which became superconducting between 80 and 93 K, proved that superconductivity could occur at temperatures higher than the boiling point of liquid nitrogen (77 K). [26] For their discovery, Bednorz and Müller were quickly awarded the 1987 Nobel Prize in Physics. These ceramic, perovskite-like superconducting cuprates opened a golden era of superconductivity, and record-high critical temperatures were obtained one after another, achieving a maximum T_c of 138 K at room pressure in $Hg_{0.8}Tl_{0.2}Ba_2Ca_2Cu_3O_{8+\delta}$ by Dai et al., still unbeaten to this day. [27] However, whether the BCS theory can explain the pairing mechanism for superconductivity in these compounds is an unresolved issue. ARPES experiments have shown gap nodes in hole-doped cuprates, which could indicate different pairing than the s–type pairing predicted by the BCS theory, [28] and recent proposals suggest the electron-electron interaction may be mediated by the superexchange interaction in an antiferromagnetic correlated-insulator state, instead of electron-phonon interaction. [29] Besides their high critical temperatures, cuprates have multiple interesting properties from the point of view of applications, such as high upper critical fields and critical currents, necessary for the manufacture of superconducting cables for electrical transport and magnetic field generation, and REBCO (Rare-earth Barium Copper Oxyde) tapes are already commercially available. [30, 31] However, certain considerations make their widespread application difficult and their implementation expensive. Primarily, cuprate superconductors are extremely anisotropic, being their anisotropy factor given by $\gamma = \sqrt{\rho_c/\rho_{ab}} \approx 5 - 100$, [32–34] and their crystal intergrain connectivity is poor, such that a misalignment of about $3 - 5°$ is enough to break the superconductivity in these materials. [34] In addition to their pairing mechanism, cuprate superconductors also exhibit several unusual and complex properties that have challenged conventional theoretical models, such as origin of their paraconductivity, excess conductivity above T_c that all superconductors present.

More recently, in 2008, a new family superconductor materials was discovered, which featured iron in their crystallographic structure, for which they are known as iron-based superconductors (IBS). [35] IBS present some properties that make them particularly interesting from the point of view of applications, such as high critical and irreversibility magnetic fields, similar to those of cuprates at 4.2 K, [36–40] albeit showing lower anisotropy (particularly in the 122 family, with $\gamma \approx 3$), and larger grain boundary critical angles (as high as 9°), improving polycrystal connectivity. [41] These characteristics could make them more suitable than cuprates

for mass manufacture of polycrystalline wires and tapes, [42, 43] and for the development of superconducting devices such as bulk magnets [44] or thin-film nanocircuits including integrated Josephson junctions and SQUIDs. [34] Furthermore, their fundamental interest is clear by their similitudes with cuprates, such as elevated transition temperatures (lower than those in cuprates but still considerable for usable applications) and the emergence of superconductivity with the introduction of dopants, which destroy the antiferromagnetic order of the parent system, [45–47] suggesting their pairing mechanism may be related. [48] On the other hand, they present a multiband electronic structure, with energy gaps that depend on the doping level and on the pressure (external or chemical). [45,46,46–51] This characteristic has been shown to be the cause of the unconventional temperature dependence of observables such as the magnetic penetration depth, [52,53] the Seebeck coefficient, [54] the specific heat, [55, 56] or the upper critical field. [57–59]

Added to the traditional applications of superconductors, the impulse given by quantum technologies has renewed the interest of superconductors for applied research. Primarily, superconducting circuits are currently the main candidate for a scalable quantum computing architecture, [60] and superconductor-based implementations of *Noisy Intermediate Size Quantum* (NISQ) computers are already planned to reach over 4000 qubits by 2025. [61] Superconductors systems have been proposed for the future implementation of cryogenic memories for which current CMOS technology is not suitable, also relevant for quantum computing and communications. [62] Simultaneously, many technological advances in quantum communications and fundamental science rely on high-efficiency single photon detectors, for which *Superconductor Nanowire Single Photon Detectors* (SNSPDs) are the most prominent technology with record-breaking efficiencies upwards of 90%. [63–66] Given that cuprates and IBS are the only superconducting systems that have achieved $T_c \gtrsim 30$ K at room pressure, some of these applications could potentially benefit greatly of their implementation with higher-T_c systems, with the addition of increased critical fields and currents that these materials can withstand at usable temperatures, [34] and recent research has demonstrated that cuprates are promising for their use for e.g., SNSPDs at higher temperatures. [67] Determining the properties of cuprate superconductors and IBS could therefore help the aim of maximizing certain relevant parameters for their industrial application, as well as shed light into their fundamental pairing mechanism. For this reason, during this thesis we will study the irreversibility field, the critical current, and the anisotropy factor of iron-based superconductors, properties which are strongly linked to the technological application of these superconductors, as well as the precursor effects in cuprate superconductors.

Objectives

The general aim of this thesis is the study of some open aspects of the phenomenology of intrinsically nanostructured, high T_c superconductors, including iron-based superconductors (IBS) and cuprates, following the lines of research that the QMatterPhotonics group has been developing in the past few years on the subject of superconductivity. We expect the results obtained during this thesis to contribute towards a better understanding of the intrinsic nanostructuration of iron-based and cuprate superconductors, and how reduced dimensionality affects their superconducting properties. Additionally, these results have the potential to help improve some interesting superconducting parameters, such as the critical current and the irreversibility magnetic field, particularly in the case of iron based superconductors. These questions are of key importance to the technological-industrial implementation of applications based on superconductors, aside from their inherent interest.

To fulfill this aim, our work was carried out by studying the two regimes in which a superconductor can be, the normal state at $T \gtrsim T_c(H)$, where the properties of superconductors can still differ from those of non-superconducting materials, and the proper superconducting state at $T < T_c(H)$. At temperatures higher than T_c, our study focused on the precursor effects of superconductivity, by studying multiple observables, namely the paraconductivity, i.e., the excess conductivity above T_c which rounds the superconducting transition, and the magnetoconductivity, the paraconductivity in presence of an external applied magnetic field. At temperatures below T_c, our study focused on characterizing the magnetic properties of superconductors in the so-called critical state, in which a type-II superconductor has the maximum amount of trapped magnetic flux it can withstand for a given temperature and applied magnetic field. This gives rise to magnetic hysteresis, which can provide useful information about the pinning of the trapped flux inside the superconductor. Explaining the dependence of these observables with magnetic field and temperature is crucial to the understanding of the superconductivity in these materials.

More specifically, regarding iron-based superconductors, we will present the results of three different studies focused on the IBS phenomenology. Firstly, we studied the anomalous angular dependence of the upper critical field H_{c2} of high-quality single crystal of the prototypical IBS $Ba(Fe_{1-x}Co_x)_2As_2$. This observable has been shown to present a significant deviation from the expected single-band 3D anisotropic Ginzburg-Landau (3D-aGL) approach for $\vec{H}$ oriented at angles almost parallel to the FeAs layers, [7, 68, 69] to which we have successfully provided an explanation based on the multiband nature of these materials. Secondly, we studied the vortex dynamics of the highly anisotropic compound $Ca_{0.82}La_{0.18}Fe_{0.96}Ni_{0.04}As_2$, particularly focusing our study in the second magnetization peak (SMP), which appears on the isothermal magnetization hysteresis loops $M(H)$. Finally, we explored the effect of increased surface roughness by sandblasting the surface of $BaFe_2(As_{1-x}P_x)_2$ single crystals, an attractive compound given its elevated T_c. This treatment has previously been observed to effectively enhance the critical current in conventional low-T_c superconductors, [70] and the effect on iron pnictides had never been studied

before.

Regarding cuprate superconductors, we will focus on the study of the paraconductivity, the excess conductivity above the superconducting transition, $\Delta\sigma(T > T_c)$. Multiple theoretical proposals attempt to explain its temperature dependence, which are for the most part incompatible with each other, and are key to understanding the superconducting nature of these materials. Multiple authors have suggested that the rounding of the superconducting transition in these materials could be caused solely or primarily by emergent percolative processes, due to an intrinsic distribution of T_c. [71–74] Nevertheless, many other studies have found that, in certain scenarios, thermal fluctuations alone can produce sufficient increased conductivity to explain the data. [75–84] For this reason, we have calculated the effect of a T_c distribution on high-quality samples of optimally-doped $YBa_2Cu_3O_{7-\delta}$ (YBCO), $La_{2-x}Sr_xCuO_4$ (LaSCO), $Bi_2Sr_2CaCu_2O_{8+\delta}$ (Bi2212) and $Tl_2Ba_2Ca_2Cu_3O_{10-\delta}$ (Tl2223) using effective medium theory (EMT) [85–87]. The results were compared with existing models based on the Ginzburg-Landau for thermodynamically induced superconducting fluctuations, which we will extend to cover the high temperature and high magnetic field regimes through the introduction of a total energy cutoff to the fluctuation modes.

Outline of the manuscript

This thesis is presented as a compilation of articles. The published papers that are part of this compilation are [88], [89], [90] and [91]. Additionally, a preprint of an article which is currently in peer review is also included, [92]. The outline of this manuscript is the following:

- In Chapter 1, the experimental methods followed for the achievement of results are described.
- Chapter 2 focuses on the phenomenology of IBS single crystals: 1) the anomalous dependency of the upper critical field of $Ba(Fe_{1-x}Co_x)_2As_2$; [88] 2) the vortex dynamics of $Ca_{1-x}La_xFe_{1-y}Ni_yAs_2$, particularly regarding the second magnetization peak (SMP); [89] 3) the impact of increased surface rugosity on $BaFe_2(As_{1-x}P_x)_2$ single crystals to enhance their critical current. [92]
- Chapter 3 deals with the comparison between calculations based on effective medium theory for emergent percolative effects and the superconducting fluctuations of thermodynamic origin as the cause of the rounding of the resistivity curves $\rho_{ab}(T)$ above T_c in cuprate superconductors. [90, 91]
- In Chapter 4, we present the main critical examination and interpretation of the data, and the implications of the results for the field.
- Finally, in Chapter 5, we provide a general conclusion of this manuscript, summarizing the main scientific contributions achieved during this doctoral thesis.

Chapter 1

Experimental Methods

1.1 Thin film deposition and single crystal growth

Multiple techniques can be used to grow thin films of superconducting (or non superconducting) materials. For thin film deposition, we will focus on the techniques commonly known as *Physical Vapour Deposition*, or PVD, in which the chemistry of the samples is not altered significantly, so most of the sample processing is of physical origin, such as evaporation, condensation and thermal annealing. We will briefly describe the PVD techniques that were used throughout the development of this doctoral thesis [93]:

- *Thermal evaporation*: this technique is the simplest PVD technique and it involves heating solid material in a high vacuum chamber until it undergoes vaporization. The resulting vaporized material condenses onto a substrate, commonly located above the target, to form a thin film. This method relies on controlled heating to create a vapor plume from the source material, which travels and adheres to a cooler substrate, allowing for precise control over film thickness and composition. Thermal evaporation is versatile and capable of depositing a wide range of materials, including metals, semiconductors and some organic compounds, albeit the high fusion point or low vapour pressure of some materials make their evaporation unfeasible even in ultra-high vacuum ($P \leq 10^{-8}$ mbar).
- *Electron-beam deposition* (EBD): by generating an electron beam within a vacuum chamber and focusing it on a solid source material, the target material can be locally vaporized, forming a vapor plume which, similarly to the case of thermal evaporation, condenses onto a substrate, creating a thin film. Electron-beam deposition is capable of depositing a wider range of materials, including metals and semiconductors, but also dielectrics and materials with high fusion point.
- *Sputtering deposition*: In this technique, high-energy ions are accelerated towards a solid target material within a vacuum chamber. The impact of these

ions on the target causes the ejection of atoms or molecules from its surface, creating a vaporized material, which condenses onto a substrate, forming a thin film. The slow growth of films with this technique provides excellent control over thickness, composition and uniformity, making it suitable for depositing a very wide range of materials, particularly superconductors such as cuprate perovskites, being the technique used in our laboratory to produce this type of samples.

For the growth of single crystal superconductor samples, the most widely used technique is known as *self-flux growth*. In this technique, the material to be grown also serves as the source and solvent (flux). This process occurs in a high-temperature furnace, where a mixture of the source material and a small amount of the desired single-crystal product or its precursors are heated above their melting point. As the temperature is gradually lowered, single crystals nucleate and grow from the molten flux, resulting in high-quality single crystals with minimal defects. This technique was used by our collaborators at Oak Ridge National Laboratory and Beijing National Laboratory for Condensed Matter Physics to manufacture the iron-based superconductor samples used throughout this thesis. [94]

1.2 Resistivity measurements

For the resistivity measurements, a 4-wire in-line method was used. Following this procedure, the contacts are set following the scheme $I^+ - V^+ - V^- - I^-$, where all contacts are parallel and across the sample. The I contacts can be set with a line of silver paint or conductive epoxy plus a conductive wire made of a good conductor such as copper or gold, and the V contacts should be well aligned (in a line parallel to the current lines) and as small as possible. [95] The distance between voltage contacts must be determined precisely to determine the geometrical factors to convert the resistance measurements into resistivity. A small current, determined as the one that maximizes the SNR (signal-to-noise ratio) while not producing any non-linear heating effects, is injected through the I contacts, and the voltage drop measured through the V contacts. The resistivity measurements made during this thesis were carried out in the Physical Property Measurement System (PPMS, Quantum Design), property of the General Services of the University of Santiago de Compostela. This device allows for temperature regulation ($1.9 - 400$ K), and magnetic field intensity (up to 9 T) and angle control ($0 - 360°$), to be carried out sequentially in a script.

1.3 Magnetic moment measurements

The magnetic moment measurements of single-crystals were carried out in two different orientations based on the angle θ between the applied magnetic field and the crystallographic c–axis, $H \parallel c$ ($\theta = 0°$) and $H \parallel ab$ ($\theta = 90°$). For the first type of measurements, the sample was introduced in a quartz cylinder with a slit

perpendicular to the symmetry axis, which acts as sample holder. The sample is introduced in this slit and glued with General Electric (GE) varnish. Both the quartz sample holder and the GE varnish have very small magnetic signal, making them ideal for this type of measurement. For the second type of measurements, a solid quartz cylinder (i.e, without slit) is used, and the sample is glued laterally to the cylinder. In both cases, the sample is aligned by rolling kapton tape around both ends of the quartz cylinder, ensuring the alignment is about 0.1 °. Before cooling down the samples, a degauss (demagnetizing the sample space cavity) and magnet reset (eliminating any current left in the superconducting magnet) were performed. The magnetization measurements made during this thesis were carried out in the Magnetic Property Measurement System (MPMS-XL, Quantum Design), property of the General Services of the University of Santiago de Compostela and located at the Faculty of Physics, in which the measurement of magnetic moment is carried out by a superconducting SQUID magnetometer, [95] with DC and RSO (improves sensitivity to 10^{-8} emu) measurement options. This device allows for temperature regulation ($1.9 - 400$ K, with optional accessories to go down to 0.5 K with ^{3}He and up to 800 K with oven) and magnetic field (up to 7 T) control to be carried out sequentially in a script.

1.4 XRD

X-ray diffraction (XRD) is a powerful analytical technique used to study the crystallographic structure and stoichiometry of materials. The interaction of x-rays of wavelength λ with the crystalline lattice of the samples can be used to determine the spacing d between crystal plane families, which provides information about the crystalline structure, following Bragg's law,

$$n\lambda = 2d\sin(\theta)\ , \tag{1.1}$$

being θ the angle between the incident beam and a certain crystal plane family. Multiple techniques can be used for this purpose, including but not only powder XRD, fiber XRD and $\theta - 2\theta$ XRD, small-angle x-ray scattering and grazing-incidence XRD. [96] To obtain crystallographic information about films and single crystals grown epitaxially in the c–direction (the case that will be used throughout this document), the usual procedure is $\theta - 2\theta$ XRD, in which the incident beam and the detector are rocked simultaneously with angles θ and 2θ respectively. As the normal is parallel to the c–direction, only the plane family perpendicular to the normal of the sample can fulfill the diffraction condition given by Eq. (1.1), with spacing $d = c$. The resulting $(00l)$ diffraction peaks are located at

$$\theta = \arcsin\left(\frac{l\lambda}{2c}\right)\ . \tag{1.2}$$

From the resulting diffractogram, multiple pieces of information can be obtained. Primarily, from the location of the peaks, the c–lattice parameter can be determined.

For many systems which have been doped to tune their electronic properties, this c–lattice parameter can be related to a certain doping level, providing information about the sample composition. The absence of certain peaks can also reveal information about symmetries, due to the structure factor of the specific crystallographic lattice cancelling out (e.g., if alternating equivalent planes diffracting x-rays out of phase). Additionally, the occurrence of multiple peaks (after filtering the data for a single λ) can indicate the presence of multiple phases present in a single sample. The appearance of peaks wider than the instrumental width, on the other hand, can be used to infer that the plane families are not located at well defined distances, which can indicate local non-stoichiometry, or the presence of a continuum of phases. The XRD measurements in this thesis were all made using a Rigaku Miniflex II benchtop diffractometer. f

1.5 T_c determination

The superconducting transition of type-II superconductors (like the ones studied in this work) is a second-order, or continuous, phase transition, so there is no latent heat. For this reason, close to the superconducting transition temperature, or critical temperature T_c, the system can microscopically be at a distribution of energies below and above the transition temperature, [76] and some of its properties can change gradually, not abruptly as it would occur in a first-order phase transition (with a latent heat). Therefore, the determination of the critical temperature of the samples is nontrivial and a criterion must be chosen for its determination. In this document, the criterion selected is the midpoint of the transition, which is determined as the maximum of the derivative $d\rho/dT$.

1.6 $\Delta\sigma$ determination

The paraconductivity $\Delta\sigma$ is the excess conductivity that superconductor materials evidence at temperatures above their superconducting transition at T_c, defined as

$$\Delta\sigma(T) = \frac{1}{\rho(T)} - \frac{1}{\rho_{\text{bkg}}(T)} \,. \tag{1.3}$$

This requires that the normal-state or *background resisitivity* $\rho_{\text{bkg}}(T)$ of the sample is determined. For some systems (i.e., optimally doped YBCO, Co-doped Ba-122, granular aluminium), the normal behavior well above T_c (i.e., $T > 2\,T_c$) recovers a linear dependency of $\rho(T)$, whilst for other systems the normal behavior is usually more complicated. In these cases, a suitable $\rho_{\text{bkg}}(T)$ must be chosen. An adequate background function must fit the data adequately well above T_c, where fluctuation effects are negligible, and then it must never cross the experimental data. The temperature at which this background function (or its derivative) begins to deviate from the experimental data is T_{onset}, the onset of the paraconductivity. For temperatures close to T_c, the resulting $\Delta\sigma$ is not strongly dependent on the specific functionality

of this background function, as it follows a power law dependency with the reduced temperature, such as [7]

$$\Delta\sigma \approx \frac{C}{(\log(T/T_c))^p} \ . \tag{1.4}$$

1.7 AFM

Atomic Force Microscopy is a technique which can be used to visualize surfaces at the nanoscale, providing high-resolution micrographs and detailed information about the topography and physical properties of materials at the atomic and molecular level. [97] The principle of operation is scanning a sharp tip located at the end of a cantilever over the surface of a sample, while measuring the interaction force between tip and sample. To calculate the force, the deflection of the cantilever must be measured using different techniques. Some of the most used AFM techniques are contact-mode AFM, in which the tip is gently touching the sample at a minimum of potential at all times; tapping-mode, in which the cantilever is harmonically forced up and down close to its resonance frequency so the force experienced by the tip strongly shifts the resonance frequency and hence the amplitude of the oscillation, and lateral-mode AFM, also known as Lateral Force Microsocopy (LFM), which can provide additional information about the surface of the sample, e.g., friction. The detection system is usually formed by two vertically aligned position-sensitive photodiodes (PSD), which measure the reflection of a laser beam by the cantilever, although more refined techniques such as using a crosshair of 4 photodiodes can also be used. Through a calibration of the voltages measured in the photodiodes, these deflection measurements can then be used to map the surface to a 3D micrograph. All AFM micrographs obtained during this thesis were obtained with a NanoScope E (Digital Instruments) LFM in contact mode.

1.8 Sandblasting

In order to introduce micrometric surface irregularities (about $\sim$ 5 µm wide and $\sim$ 1 µm deep) to the epitaxial sides of some samples, an abrasive sandblasting process was used. [98] For this purpose, a commercial sandblasting machine (Damglass E. Fexas, model DAM-1, property of the General Services of the University of Santiago de Compostela) was used with silica sand of diameter $\sim 50 - 100$ µm. The samples were kept centered in the ejection cone, with the nozzle-to-sample distance set to 8.5 cm. A 5 second burst at 1 bar nozzle pressure was used to etch one of the *ab* surfaces of the crystals. After the sandblasting, the samples were carefully cleaned from sand residue. The samples were characterized before and after sandblasting, including T_c determination, AFM surface imaging and weighing. No change in structural or stoichiometric quality was observed, T_c remained the same, and a very small amount of mass was lost ($\lesssim 2\%$).

Chapter 2

Multiband effects and vortex dynamics of iron-based superconductors

The following articles are part of this chapter:

- I. F. Llovo, C. Carballeira, D. Sóñora, A. Pereiro, J. J. Ponte, S. SalemSugui Jr., A. S. Sefat & J. Mosqueira. Multiband effects on the upper critical field angular dependence of 122family iron pnictide superconductors. *Sci. Rep.* **11**, 11526 (2021) dx.doi.org/10.1038/s41598-021-90858-4.
- I. F. Llovo, D. Sóñora, J. Mosqueira, S. Salem-Sugui Jr., S. Sundar, A. D. Alvarenga, Tao Xie, Chang Liu, Shiliang Li & Huiqian Luo. Vortex dynamics and second magnetization peak in the iron-pnictide superconductor $Ca_{0.82}La_{0.18}Fe_{0.96}Ni_{0.04}As_2$. *Supercond. Sci. Technol.*, **34**, 115010 (2021) dx.doi.org/10.1088/1361-6668/ac2556.
- (In peer review) I. F. Llovo, J. Mosqueira, Ding Hu, Huiqian Luo & Shiliang Li. Enhancement of the critical current by surface irregularities in Fe-based superconductors.

2.1 The anomalous angular anisotropy of 122 family iron-based superconductors

The angular dependence of the upper critical field $H_{c2}(\theta)$ of a single-band, anisotropic superconductor can be calculated in the framework of the Ginzburg-Landau theory for superconductors. If θ is defined as the angle of the applied magnetic field with the crystal c–axis, the so-called 3D anisotropic Ginzburg-Landau (3D-aGL) angular dependence can be expressed as

$$H_{c2}(\theta) = \left(\frac{\cos^2\theta}{H_{c2}^{\perp 2}} + \frac{\sin^2\theta}{H_{c2}^{\parallel 2}} \right)^{-1/2} , \tag{2.1}$$

where $H_{c2}^{\perp}$ and $H_{c2}^{\parallel}$ correspond to $\theta = 0°$ and $90°$ respectively. [7] For some compounds from the 122 family of IBS with a moderate anisotropy factor $\gamma \equiv H_{c2}^{\parallel}/H_{c2}^{\perp}$, $H_{c2}(\theta)$ has been reported to be roughly described by Eq. (2.1). [99–102] However, an anomalous angular dependence, which could be qualitatively described as similar to the two-band superconductor MgB_2 behavior, [103, 104] has instead been observed in these compounds in some detailed analyses. [68, 69]

The procedure used to determine the upper critical field can be a source of discrepancy towards the resulting $H_{c2}(\theta)$ curves. $H_{c2}(T)$ is generally estimated from the cuts of the transition at a given percentage of normal state resistivity ρ_{bkg}, i.e., T, H pairs are obtained from the point at which the electrical resistivity falls to this percentage of ρ_{bkg}. [68, 69, 99–102] However, this procedure is strongly dependent on the particular criterion used (e.g., 20%, 50% or 80% of ρ_{bkg}), due to different factors that *round* the $\rho(T)$ curves near the superconducting transition temperature $T_c(H)$. Firstly, due to the relatively high T_c and the small value of the coherence length (just a few nm), thermal fluctuation effects near $T_c(H)$ play an important role in these materials, [105] and contribute to the rounding of the resistive transition. [106–110] These effects are also strongly dependent on the amplitude and orientation of the applied magnetic field. [111] A second factor is the effect of T_c inhomogeneities, as these compounds are generally non-stoichiometric, and their T_c depends on the doping level. Due to the small values of their coherence lengths, even a random distribution of dopants could lead to nanoscale T_c variations, [112] and a consequent smoothing of the resistive transition. This effect is particularly important in non-optimally doped compounds. [106] Finally, the resistive transition is widened by vortex dynamics below $T_c(H)$, down to the irreversibility temperature, below which the vortices are pinned.

In the first article of this section, *Multiband effects on the upper critical field angular dependence of 122family iron pnictide superconductors*, we present measurements of the in-plane resistivity versus temperature under magnetic fields with different amplitudes and orientations with respect to the crystal c–axis, in an optimally doped $Ba(Fe_{1-x}Co_x)_2As_2$ (OP-BaFeCoAs) single crystal. In contrast with the percentage cuts method to estimate the upper critical field, we estimated the $\rho(T)_{H,\theta}$

rounding from fits to the an extension of the Aslamazov-Larkin (AL) fluctuation model, which is applicable in the region of high reduced temperatures and magnetic fields. [106] With this analysis, we were able to obtain a criterion-independent determination of the angular dependence of the upper critical field, and the resulting $H_{c2}(\theta)$ curve was then shown to agree with a theoretical prediction for multiband superconductors. [113, 114]

2.2 The mechanism behind the secondary magnetization peak

Another not-so-well understood feature of IBS is that many of these materials show the so-called *secondary magnetization peak* (SMP). This phenomenon is characterized by a sudden increase of the magnetization hysteresis observed in the critical-state, which appears above a certain *onset magnetic field* H_{on}. This increased magnetization observed in the SMP is directly correlated to an increase in the critical current density J_c. [115] Understanding the appearance of the SMP and externally modulating its magnitude could be of great fundamental relevance, as well as having important consequences from an applied point of view for applications that require high current densities, such as superconducting magnets. [34] The SMP phenomenon is not unique of IBS, as it has been observed in certain low-T_c conventional superconductors, [116, 117] in high-T_c superconductors, [118, 119] as well as in multiband superconductors such as MgB_2. [117] Nevertheless, it is worth mentioning that an SMP has been reported in most IBS, for magnetic field directions parallel ($H \parallel ab$) and perpendicular ($H \parallel c$) to the crystal ab-plane (see [120] and references therein).

Despite this commonplace occurrence in many superconductor families, the mechanism responsible for the SMP is not well understood, and some authors suggest the causes for this effect may even be material-dependent. [121] Since the discovery of IBS, [35] the SMP has been reported and explained in terms of a pinning-crossover in Ba(Fe-Co)$_2$As$_2$, (Ba-K)Fe$_2$As$_2$, Ba(Fe-Ni)$_2$As$_2$, Ca(Fe-Co)As and (Ca-La)(Fe-Co)As$_2$, [122–129] a phase transition in the vortex lattice in Ba(Fe-Co)$_2$As$_2$, LiFeAs, and BaFe$_2$(As-P)$_2$, [130–133] and an order-disorder transition. [134–136] All these systems share a similar structure, based on FeAs superconducting layers separated by a spacing layer. However, its occurrence is not universal in IBS, as some systems do not present it, even with $H \parallel c$–axis, e.g., in overdoped (Ba-K)Fe$_2$As$_2$, [137] (Li-Fe)OHFeSe, [138] La-doped CaFe$_2$As$_2$ [139] and La$_{0.34}$Na$_{0.66}$Fe$_2$As$_2$. [140] In the more anisotropic 1111 oxypnictide family, the SMP has been attributed to a 3D-order-to-2D-disorder phase transition. [141, 142] As the crystal structure in the 112 family has a larger spacing layer between FeAs superconducting layers compared to the 122 and 111 families, [143] the 112 family shows higher anisotropy, [108, 144, 145] making it more comparable to the 1111 oxypnictides. So, understanding the phenomenology of the SMP in this family of IBS could help shed light on the mechanism behind the SMP.

In the second article of this section, *Vortex dynamics and second magnetization peak in the iron-pnictide superconductor* $Ca_{0.82}La_{0.18}Fe_{0.96}Ni_{0.04}As_2$, we present isothermal $M(H)$ curves and extensive relaxation $M(t)$ measurements in a single crystal of the 112 iron pnictide $Ca_{0.82}La_{0.18}Fe_{0.96}Ni_{0.04}As_2$, with $T_c \sim 22$ K [146] and moderate anisotropy, [108] to study the possible origin of the SMP in this system. A well pronounced SMP was observed in all $M(H)$ curves with $H \parallel c$, even close to T_c, and for $H \parallel ab$ for temperatures above 14 K. The anisotropic nature of this system might lead to the possible emergence of two dimensional Josephson vortices at low temperatures and high magnetic fields, [119, 147] which make the SMP vanish for $H \parallel ab$ at lower temperatures (below 7.5 K), a feature that is not shared by most iron-pnictides. [148–150] For $H \parallel ab$, magnetic relaxation data were within the noise level of the measurements, which prevented us from studying the vortex dynamics for this direction. The behavior of the relaxation rate, $R = d\ln(M)/d\ln(t)$, with field and temperature, as well as the dependence of the activation energy U_0 with the critical current J_c [151] and of $U(M)$, [152–154] allowed us to study the vortex dynamics in the magnetic phase diagram of the system, and also to address the mechanism responsible for the SMP. A crossover from collective (elastic) to plastic pinning was observed across the SMP, accompanied with a possible phase transition of the vortex lattice near the maximum of the SMP, H_p.

2.3 Surface treatment to enhance the critical current of IBS

As we have mentioned before, IBS present some properties that make them particularly interesting to their potential implementation as polycrystalline wires and tapes, bulk magnets, integrated Josephson junctions, SQUIDs and more superconductor-based devices. [34, 42–44] Two such properties are, precisely, their high critical and irreversibility magnetic fields, [36–40] which in many cases are comparable or even higher than those of cuprates at usable temperatures, e.g., at 4.2 K, the boiling point of helium. [34] For these reasons, much attention has been put on enhancing the critical current density J_c in these materials. Multiple techniques have been shown to serve this purpose, such as proton, neutron and heavy ion irradiation to produce point-like [155–157] or columnar [155, 156, 158, 159] defects, self-assembled oxygen-rich impurities addition, [160] and the artificial generation of compositionally modulated superlattices, e.g. $BaFe_2As_2/Ba(Fe_{1-x}Co_x)_2As_2$. [161]

In addition to bulk pinning, surface irregularities have also been shown to be effective at enhancing the critical current in conventional low-T_c superconductors. [70] Among the procedures used to create surface defects in these materials are sandblasting, [70] mechanical abrasion, [162] buffered chemical or electrolytic polishing, [163] and low temperature bakeout. [164] More recent work in metallic niobium sheets has shown that laser-induced periodic structuration can make the irreversibility field H_{irr} to increase [165] or decrease when using a femtosecond-pulsed laser. [166] Nevertheless, no similar studies have been conducted on IBS so far.

In the third and final article of this section, *Enhancement of the critical current by surface irregularities in Fe-based superconductors*, we present our study on the effect of surface irregularities on the critical current of IBS single crystals. For this study, we chose the 122 family, the most studied among the IBS in applied research due to its lower anisotropy and higher J_c. [34] In particular, optimally doped $BaFe_2(As_{1-x}P_x)_2$ (P-doped 122) was used, for which crystals of considerable dimensions and high stoichiometric quality can be grown. [94, 107, 167] The results were compared with a theoretical estimate for the critical current density that a rough surface can sustain, based on Mathieu-Simon continuum theory for the mixed state. [70, 168]

scientific reports

Check for updates

OPEN

Multiband effects on the upper critical field angular dependence of 122-family iron pnictide superconductors

I. F. Llovo[1], C. Carballeira[1], D. Sóñora[1], A. Pereiro[1], J. J. Ponte[2], S. Salem-Sugui Jr.[3], A. S. Sefat[4] & J. Mosqueira[1]✉

Detailed measurements of the in-plane resistivity were performed in a high-quality $Ba(Fe_{1-x}Co_x)_2As_2$ ($x = 0.065$) single crystal, in magnetic fields up to 9 T and with different orientations θ relative to the crystal c axis. A significant $\rho(T)_{H,\theta}$ rounding is observed just above the superconducting critical temperature T_c due to Cooper pairs created by superconducting fluctuations. These data are analyzed in terms of a generalization of the Aslamazov-Larkin approach, that extends its applicability to high reduced-temperatures and magnetic fields. This method allows us to carry out a criterion-independent determination of the angular dependence of the upper critical field, $H_{c2}(\theta)$. In spite of the relatively small anisotropy of this compound, it is found that $H_{c2}(\theta)$ presents a significant deviation from the single-band 3D anisotropic Ginzburg-Landau (3D-aGL) approach, particularly for large θ (typically above $\sim 60^o$). These results are interpreted in terms of the multiband nature of these materials, in contrast with other proposals for similar $H_{c2}(\theta)$ anomalies. Our results are also consistent with an *effective* anisotropy factor almost temperature independent near T_c, a result that differs from the ones obtained by using a single-band model.

Since the discovery of superconductivity at relatively high temperatures in Fe-based superconductors (FeSC)[1] in 2008, intensive research on these materials has been taking place. On the one hand, these materials present high critical magnetic fields and low anisotropies, for which they have received great attention towards their potential applications in electric transport under high magnetic fields[2,3]. On the other hand, there is a fundamental interest in discovering the pairing mechanism responsible for their high critical temperature, which could be related to the one of cuprates. They also present unconventional superconducting properties associated to their multiband electronic structure, with energy gaps that depend on the doping level and on the pressure (external or chemical)[4–8]. An example of this would be the anomalous temperature dependences of the magnetic penetration depth[9], the specific heat[10,11], or the upper critical field[12–14], that have been interpreted in terms of theoretical models with two effective superconducting gaps[15,16].

The angular dependence of the upper critical magnetic field, $H_{c2}(\theta)$, where θ is the angle between the applied magnetic field and the crystal c axis, has been less studied. If the bands contributing to the superconductivity have different anisotropies, then $H_{c2}(\theta)$ may differ from the single-band 3D-anisotropic Ginzburg-Landau (3D-aGL) approach, that may be written as[17]

$$H_{c2}(\theta) = \left(\frac{\cos^2\theta}{H_{c2}^{\perp 2}} + \frac{\sin^2\theta}{H_{c2}^{\parallel 2}} \right)^{-1/2}, \tag{1}$$

where $H_{c2}^{\perp}$ and $H_{c2}^{\parallel}$ correspond to $\theta = 0°$ and 90° respectively. In some compounds from the 122 family $H_{c2}(\theta)$ is well described by Eq. (1), with a moderate anisotropy factor $\gamma \equiv H_{c2}^{\parallel}/H_{c2}^{\perp}$[18–21]. However, an anomalous behavior

[1]QMatterPhotonics Research Group, Departamento de Física de Partículas, Universidade de Santiago de Compostela, 15782 Santiago de Compostela, Spain. [2]Unidade de Magnetosusceptibilidade, RIAIDT, Universidade de Santiago de Compostela, 15782 Santiago de Compostela, Spain. [3]Instituto de Fisica, Universidade Federal do Rio de Janeiro, Rio de Janeiro, RJ 21941-972, Brazil. [4]Oak Ridge National Laboratory, Oak Ridge, TN 87831, USA. ✉email: j.mosqueira@usc.es

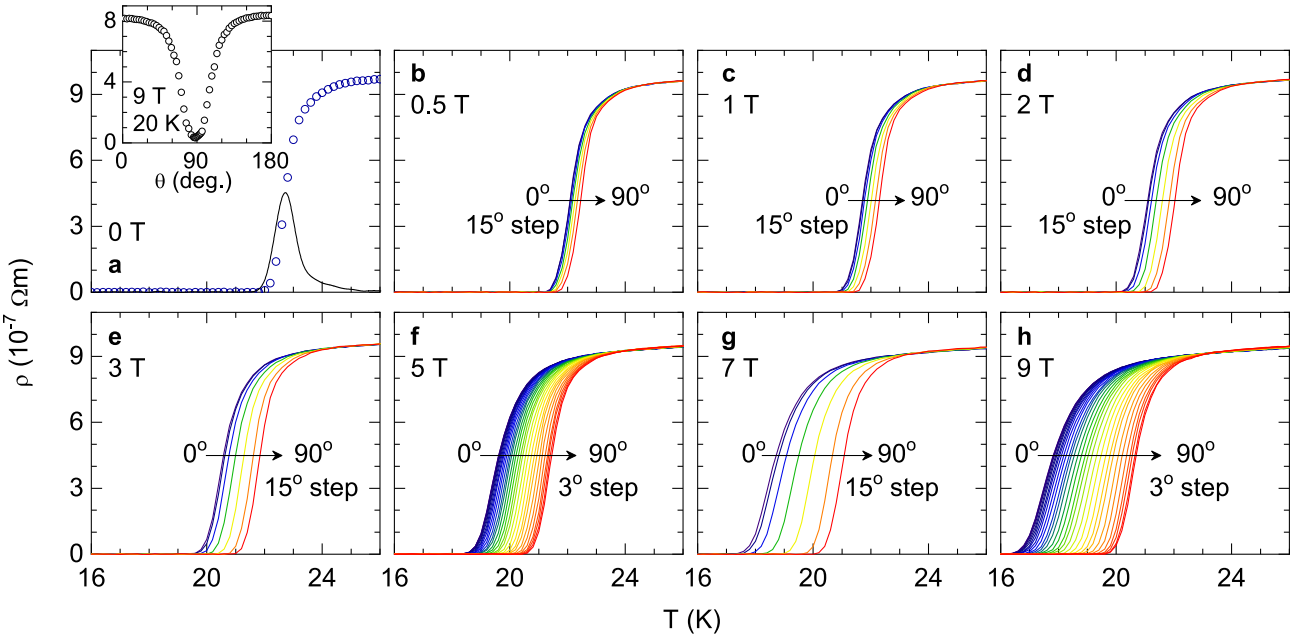

Figure 1. Temperature dependence of the in-plane resistivity around T_c in the presence of magnetic fields with different amplitudes (from 0 to 9 T, **a** to **h**), and different orientations with respect to the crystal *c* axis. $T_c = 22.7$ K was determined as the temperature at which $(d\rho/dT)_{H=0}$ is maximum (solid line in **a**). Inset in (**a**): $\rho(\theta)$ measurement performed before the measurements in (**a**–**h**) to determine the precise $\theta = 90°$ position.

has been reported in some of these compounds[22,23], qualitatively similar to the behavior observed in other two-band superconductors, such as MgB_2[24,25].

The reason for the discrepancies lies in the experimental difficulties to determine the upper critical field. The $H_{c2}(T)$ line is generally obtained from the T and H pairs at which the electrical resistivity falls to a given percentage of the normal-state resistivity[18–23]. Nonetheless, this procedure is strongly dependent on the particular criterion used (e.g., 20%, 50% or 80% of ρ_n), as different factors *round* the $\rho(T)$ curves near the superconducting transition temperature, $T_c(H)$. Firstly, due to the relatively high T_c and the small value of the coherence length (just a few nm), thermal fluctuation effects near $T_c(H)$ play an important role in these materials[26], and contribute to the rounding of the resistive transition[27–31]. These effects are also strongly dependent on the amplitude and orientation of the applied magnetic field[32]. A second factor is the effect of T_c inhomogeneities: These compounds are generally non-stoichiometric, and their T_c depends on the doping level. Given the small values of the coherence length, it is expected that even a random distribution of dopants would lead to nanoscale T_c variations[33], which results in a smoothing of the resistive transition, an effect particularly important in non-optimally-doped compounds[27]. Finally, the resistive transition is extended by vortex dynamics below $T_c(H)$, down to the irreversibility temperature, under which the vortices are pinned.

In this work, we present measurements of the in-plane resistivity versus temperature under magnetic fields with different amplitudes and orientations with respect to the crystal *c* axis, in an optimally-doped $Ba(Fe_{1-x}Co_x)_2As_2$ (OP-BaFeCoAs) single crystal. This compound is one of the most studied FeSC, and nowadays it is possible to grow large single crystals of both the highest stoichiometric and structural quality. In contrast with the aforementioned procedures to obtain the upper critical field, the $\rho(T)_{H,\theta}$ rounding will be studied in terms of a generalization of the Aslamazov-Larkin (AL) approach for the effect of superconducting fluctuations, which is applicable in the region of high reduced temperatures and magnetic fields[27]. The analysis will allow us to obtain a criterion-independent determination of the angular dependence of the upper critical field, $H_{c2}(\theta)$. The result will be analyzed in terms of existing models for multiband superconductors[15,16].

Results

Figure 1 shows the measured $\rho(T)_{H,\theta}$ near the superconducting transition temperature. The zero-field transition temperature $T_c = 22.7$ K was estimated from the maximum of the $d\rho/dT$ curve (solid line in Fig. 1a). The T_c uncertainty is ± 0.5 K, which is primarily caused by the resistivity rounding associated with superconducting fluctuations[27]. As it can be seen, T_c shifts to lower temperatures as the magnetic field is increased. This effect is more pronounced for $H \perp ab$ (i.e., $\theta = 0$) than for $H \parallel ab$ ($\theta = 90°$), due to the anisotropy of the corresponding upper critical fields, $H_{c2}^{\perp}$ and $H_{c2}^{\parallel}$, respectively. These data may be then used to estimate $H_{c2}(T,\theta)$. However, in the available range of magnetic fields, the T_c shift is close to the T_c uncertainty, mainly attributed to the aforementioned resistivity rounding. For this reason, the results are highly dependent on the criterion used to determine $T_c(H,\theta)$ (typically the temperature at which the resistivity falls to a given fraction of the extrapolated normal-state resistivity). In the next section, a criterion-independent determination of the angular dependence of H_{c2} will be presented through the analysis of the superconducting fluctuations, obtained from the rounding above $T_c(H,\theta)$.

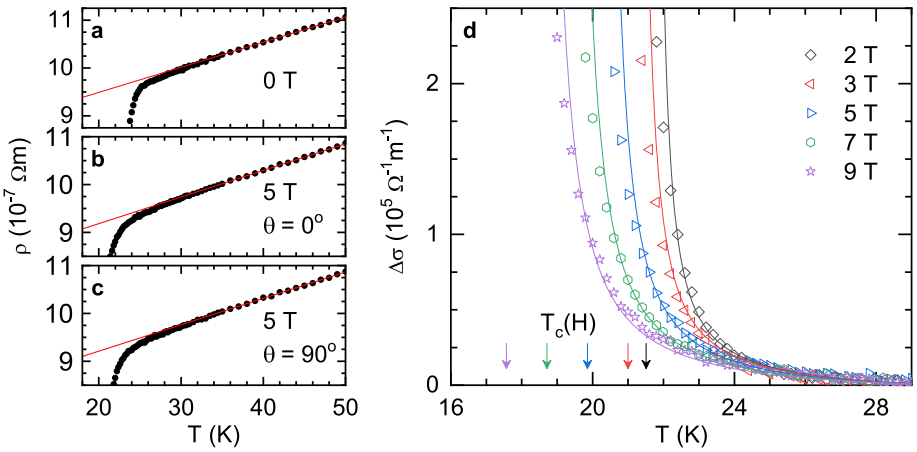

Figure 2. (**a**–**c**) Some examples (for different H amplitudes and orientations) of the in-plane resistivity temperature dependence well above T_c. The normal-state backgrounds (red lines) were determined by linear fits above 35 K ($\sim 1.5T_c$), where fluctuation effects are negligible. (**d**) Temperature dependence of the fluctuation conductivity under different magnetic fields, applied perpendicular to the crystal ab layers ($\theta = 0$). The lines are the best fit of Eq. (3) to the data between 2 and 9 T. The arrows indicate $T_c(H) = T_c(1 - H/H_{c2}^{\perp}(0))$ for the magnetic fields used in the experiments.

Determination of the normal state background. The conductivity induced by superconducting fluctuations (or paraconductivity) is given by

$$\Delta\sigma(T)_{H,\theta} = \frac{1}{\rho(T)_{H,\theta}} - \frac{1}{\rho_B(T)_{H,\theta}} \tag{2}$$

where $\rho_B(T)_{H,\theta}$ is the normal-state or background resistivity extrapolated to temperatures near T_c. This background resistivity was determined by a linear fit to the resistivity above 35 K (i.e., above $1.5T_c$) where fluctuation effects are expected to be negligible[27–31]. Some examples of this procedure for different field amplitudes and orientations are presented in Fig. 2a–c.

Analysis of $\Delta\sigma$ for $\theta = 0$ data. A first comparison with the experimental data was performed for the $\Delta\sigma$ data for $\theta = 0$ presented in Fig. 2d. As it can be seen, the rounding associated with fluctuation effects can be clearly observed a few degrees above T_c. The data were analyzed in terms of the 3D-anisotropic Ginzburg-Landau (GL) approach developed in Ref.[27], which is valid under finite magnetic field amplitudes. For $H \perp ab$, it may be written as

$$\Delta\sigma(\varepsilon, h) = \frac{e^2}{32\hbar\pi\xi_c(0)}\sqrt{\frac{2}{h}}\int_0^{\sqrt{\frac{c-\varepsilon}{2h}}} \mathrm{dx}\left[\psi^1\left(\frac{\varepsilon+\mathrm{h}}{2\mathrm{h}}+\mathrm{x}^2\right) - \psi^1\left(\frac{\mathrm{c}+\mathrm{h}}{2\mathrm{h}}+\mathrm{x}^2\right)\right], \tag{3}$$

where $\varepsilon \equiv \ln(T/T_c)$ is the reduced temperature, $h \equiv H/H_{c2}^{\perp}$ the reduced magnetic field, $H_{c2}^{\perp}$ the linear extrapolation to $T = 0$ K of the upper critical field for $H \perp ab$, e the electron charge, $\xi_c(0)$ the c axis coherence length amplitude, and c a cutoff constant of the order of magnitude of the unity, introduced to exclude the contribution of high-energy fluctuation modes[34]. It is clear to see that c corresponds to the reduced temperature at which fluctuation effects vanish. As it can be seen in Fig. 2a–c, the measured $\rho(T)$ deviates from $\rho_B(T)$ (beyond the experimental uncertainty) when $T < 30 - 31$ K, which corresponds to a reduced temperature around 0.3. Thus, in what follows we have set $c = 0.3$, a value that is close to the one found in other FeSC[27–31]. In the zero-field limit (for $h \ll \varepsilon$), and in the absence of cutoff ($c \to \infty$), Eq. (3) reduces to the well known Aslamazov-Larkin expression, $\Delta\sigma(\varepsilon) = e^2/32\hbar\xi_c(0)\varepsilon^{1/2}$.

The lines in Fig. 2d are the best fit of Eq. (3) to the set of data obtained with fields between 2 and 9 T, with only two free parameters: $\xi_c(0)$, which is directly related to the $\Delta\sigma$ amplitude, and $H_{c2}^{\perp}$, which is implicit in the equation through the reduced magnetic field h, and which is related to the temperature shift of $\Delta\sigma$ induced by the magnetic field. As it can be seen, the agreement is excellent, leading to $\xi_c(0) = 6.89 \pm 0.15$ Å and $H_{c2}^{\perp} = 42.5 \pm 0.5$ T. Experimental data up to 1 T were excluded from the fitting as a significant disagreement with the GL approach was found in previous works, while studying the fluctuation effects in other FeSC families. It has been hypothesized that this discrepancy may arise from a T_c distribution[27,28] or from phase fluctuations[35–37], which could be relevant near T_c and under low fields in these materials.

Analysis of $\Delta\sigma$ for arbitrary θ and angular dependence of H_{c2}. We will now analyze the experimental data obtained with different H orientations. To this purpose, the reduced magnetic field in Eq. (3) must be replaced by[32]

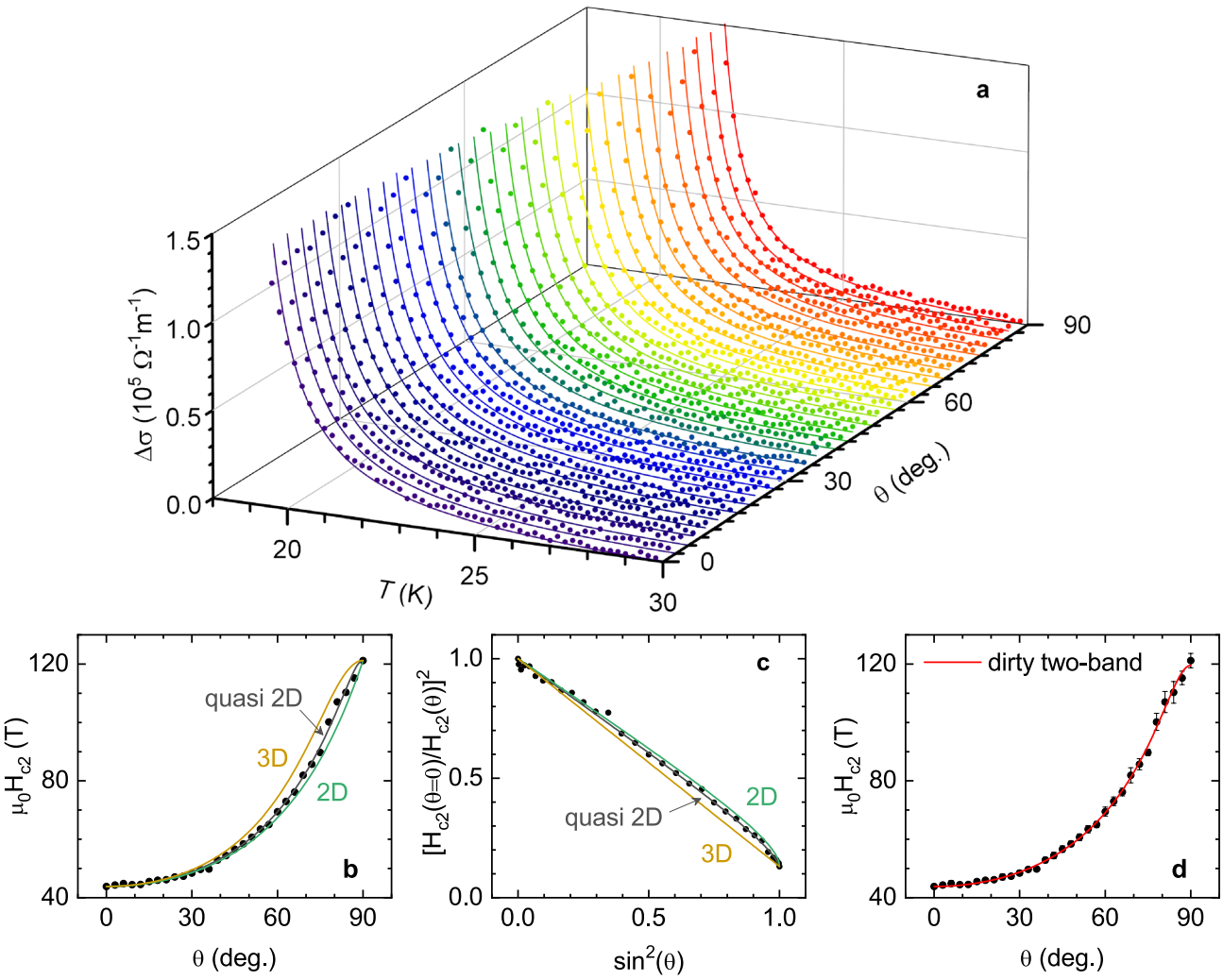

Figure 3. (**a**) Temperature dependence of the fluctuation conductivity obtained with a 9 T magnetic field, for different orientations relative to the crystal c axis (θ-steps of 3° between 0 and 90°). The lines are the best fits of Eq. (3), with the $\xi_c(0)$ value resulting from the analysis in Fig. 2**d**, and $H_{c2}(\theta)$ as the only free parameter. The resulting $H_{c2}(\theta)$ are the data points in (**b**, **c** and **d**) (the error bars are only shown in **d** for clarity). (**b**) $H_{c2}(\theta)$ data compared to the single-band 3D-anisotropic GL approach, (orange line, Eq. (1)), the 2D Tinkham's result (green line, Eq. (5)) and quasi-2D Mineev's result (black line, Eq. (6)). (**c**) Same plot as (**b**), in a linearized scale. (**d**) $H_{c2}(\theta)$ compared with Gurevich's approach for dirty 2-band superconductors (Eq. (7)).

$$h = \frac{H}{H_{c2}(\theta)}, \tag{4}$$

where $H_{c2}(\theta)$ is the upper critical field (linearly extrapolated to $T = 0$ K) for an arbitrary field orientation relative to the c axis. The $\Delta\sigma(T)$ data in Fig. 3a were obtained under a 9 T magnetic field applied with different orientations (θ runs from 0 to 90° in steps of 3°). The lines are fits of Eq. (3) to each θ dataset with the above $\xi_c(0)$ and c as fixed parameters, and $H_{c2}(\theta)$ as the only free parameter. As it can be seen, the fits are in excellent agreement with our data. The resulting angular dependence of the upper critical field is presented in Fig. 3b,c,d. From this figure, it follows that the upper critical fields extrapolated to $T = 0$ K are 43 T for $H \perp ab$ and 120 T for $H \parallel ab$. The corresponding slopes at T_c, -1.9 T/K for $H \perp ab$ and -5.3 T/K for $H \parallel ab$, are close to the ones found in the literature[38–43]. The orange line in this figure is the prediction of the single-band 3D anisotropic GL approach, Eq. (1), evaluated with the experimental $H_{c2}^{\perp}$ and $H_{c2}^{\parallel}$. A good agreement is found at low θ, but for large θ the behavior is qualitatively closer to the one found in 2D superconductors, approaching 90° with a finite slope. This can be clearly seen in the linearized representation shown in Fig. 3c. For comparison, Tinkham's result[44,45] for the upper critical field of 2D superconductors evaluated with the experimental $H_{c2}^{\perp}$ and $H_{c2}^{\parallel}$ has been included in Fig. 3b,c (green line)

$$\left|\frac{H_{c2}(\theta)\cos\theta}{H_{c2}^{\perp}}\right| + \left(\frac{H_{c2}(\theta)\sin\theta}{H_{c2}^{\parallel}}\right)^2 = 1. \tag{5}$$

As it can be seen, the experimental data fall between the 3D and 2D approaches. $H_{c2}(\theta)$ for layered quasi-2D superconductors was obtained in Ref.[46], and reads

$$\frac{H_{c2}^2(\theta)\sin^2\theta}{H_{c2}^{\parallel 2}}\left(1-\frac{H_{c2}^{\parallel}}{\gamma H_{c2}^{\perp}}\right)+\frac{H_{c2}(\theta)}{H_{c2}^{\perp}}\sqrt{\cos^2\theta+\frac{\sin^2\theta}{\gamma^2}}=1, \tag{6}$$

where $\gamma=(m_c^*/m_{ab}^*)^{1/2}$ is the anisotropy factor. This expression reduces to equations (1) and (5) in the appropriate limits, and fits the data in Fig. 3b in the entire θ-range with γ as free parameter (and by setting $H_{c2}^{\perp}$ and $H_{c2}^{\parallel}$ to the experimental values). However the resulting γ (that in this model is different from the ratio $H_{c2}^{\parallel}/H_{c2}^{\perp}$) is as high as 16.5, which is abnormally large for this compound, and inconsistent with the 3D nature of $\Delta\sigma$ in the whole temperature range above T_c. In comparison, a value of $\gamma\sim 10$ is found in optimally-doped $YBa_2Cu_3O_{7-\delta}$, and fluctuation effects already present a 3D-2D crossover at temperatures relatively close to T_c ($\varepsilon\sim 10^{-1}$)[17]. This indicates that the excellent fit of Eq. (6) is spurious, and that the anomalous angular dependence of $H_{c2}(\theta)$ cannot be attributed to a quasi-2D behavior.

Another possibility is that the anomalous $H_{c2}(\theta)$ behavior arises from the multiband nature of these materials. The presence of two effective superconducting gaps in $Ba(Fe_{1-x}Co_x)_2As_2$ was revealed by angle-resolved photoemission spectroscopy (ARPES)[47], and point-contact Andreev reflection[48]. Theoretical models for two-band superconductors also accounted for the anomalous temperature dependence of the magnetic penetration depth[10,49–55], and of the specific heat[10,11] in OP-BaFeCoAs. A recent review on the relevance of multiband effects in Fe-based and other superconductors may also be seen in Ref.[56]. However, it is worth noting that, in some cases, multiple superconducting bands and anisotropy affect some observables similarly (see e.g., Ref.[57] on the anomalous T-dependence of the superfluid density of $OsBe_2$). Nonetheless, our previous analysis clearly shows that the $H_{c2}(\theta)$ dependency cannot be explained with a reasonable anisotropy factor.

The angular dependence of the upper critical field in two-band superconductors was calculated by Gurevich in both the dirty[15] and clean limits[13,16]. A criterion for a superconductor to be in the dirty limit may be expressed as $\hbar/\pi\Delta(0)\gg\tau$, where $\Delta(0)$ is one-half the superconducting energy gap at $T=0$ K, and τ the quasiparticles relaxation time. In OP-BaFeCoAs the small and large gaps are, respectively, $\sim 3k_BT_c$ and $\sim 6k_BT_c$ (see e.g., Refs.[11,47–49,52–54]), which leads to $\hbar/\pi\Delta(0)\sim(7-3.5)\times 10^{-14}$ s. In turn, near T_c it is found that $\tau\sim(1-2)\times 10^{-14}$ s[58,59]. Thus, OP-BaFeCoAs may be closer to the dirty limit, for which $H_{c2}(\theta)$ may be expressed as[15]

$$H_{c2}(\theta)\propto\frac{T-T_c}{a_1D_1(\theta)+a_2D_2(\theta)}, \tag{7}$$

with $a_{1,2}=1\pm\lambda_-/\lambda_0$, where $\lambda_-=\lambda_{11}-\lambda_{22}$, $\lambda_0=(\lambda_-^2+4\lambda_{12}\lambda_{21})^{1/2}$, and $\lambda_{\alpha\beta}$ are the superconducing intra- ($\alpha=\beta$) and inter- ($\alpha\neq\beta$) band couplings. The angular dependency is contained in

$$D_m(\theta)=\sqrt{D_m^{a^2}\cos^2\theta+D_m^aD_m^c\sin^2\theta}, \tag{8}$$

being $D_m^{a,c}$ the electron diffusivities of band m in the a and c directions. Normalizing Eq. (7) by $H_{c_2}(\theta=0)$, we obtain

$$\frac{H_{c2}(\theta)}{H_{c2}(0)}=\frac{a_1D_1^a+a_2D_2^a}{a_1D_1(\theta)+a_2D_2(\theta)}. \tag{9}$$

Defining $\delta\equiv a_2D_2^a/a_1D_1^a$ (that represents the relative contribution of the second band), and $\gamma_m=\sqrt{D_m^a/D_m^c}$, the anisotropy of each band, it follows that

$$\frac{H_{c_2}(\theta)}{H_{c_2}(0)}=\frac{1+\delta}{\sqrt{\cos^2\theta+\gamma_1^{-2}\sin^2\theta}+\delta\sqrt{\cos^2\theta+\gamma_2^{-2}\sin^2\theta}}. \tag{10}$$

The line in Fig. 3d is the best fit of Eq. (10) to the $H_{c2}(\theta)$ data resulting from the analysis of $\Delta\sigma$. As it can be seen, the agreement is excellent in the entire θ range, and leads to $\delta=0.61\pm0.21$, $\gamma_1=8.7\pm2.2$, $\gamma_2=1.28\pm0.16$. As OP-BaFeCoAs is not strictly in the dirty limit these values may be just approximated, but the result suggests that both bands contribute similarly, and that the observed anisotropy comes essentially from one of the bands.

Comparison with the usual procedure to obtain the upper critical field. Figure 4a–c shows $H_{c2}(T)_\theta$, as obtained from the magnetic field and temperature pairs at which the resistivity $\rho(T)_{H,\theta}$ falls to a given percentage of the background resistivity, which is the most often used procedure in the literature to determine the upper critical field. As it can be seen, the obtained $H_{c2}(T)_\theta$ is linear with T, except very close to T_c (within the resistive transition width). The linear extrapolation of H_{c2} to $T=0$ K is presented in Fig. 4d as a function of θ. As expected in view of the important fluctuation effects around T_c, the H_{c2} amplitude is highly dependent on the chosen criterion. Furthermore, the $H_{c2}(\theta)$ profile is different from the one resulting from the $\Delta\sigma$ analysis (solid data points), with a less pronounced maximum near $\theta=90°$. However, as shown in Fig. 4e, the calculated $H_{c2}(\theta)$ resulting from a criterion neither follows the behavior predicted by the 3D anisotropic GL approach, which is consistent with previous works[22,23].

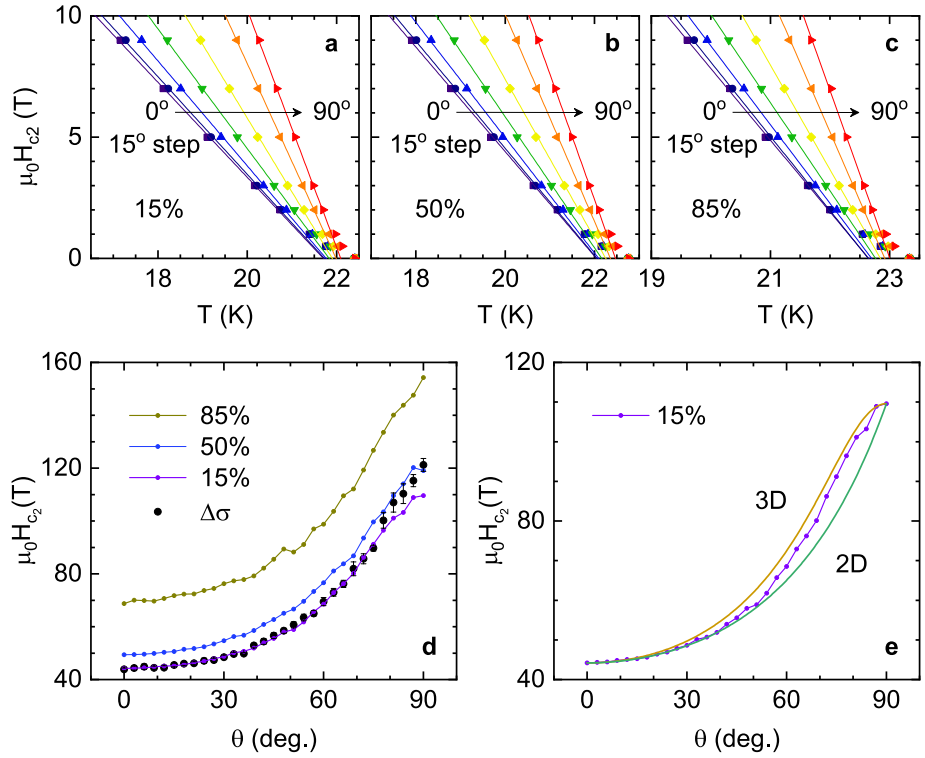

Figure 4. (**a**–**c**) $H_{c2}(T)_\theta$ calculated as the magnetic field and temperature pairs at which the resistivity falls to a given percentage of the background resistivity at T_c. The behavior is linear up to very close to T_c (within the resistive transition width), where a T_c distribution may strongly affect the $\rho(T)_{H,\theta}$ behavior. The extrapolation to 0 K is presented in (**d**), where it is shown that no criteria match the result from the $\Delta\sigma$ analysis (black circles), which shows a more pronounced maximum close to 90°. In (**e**), it is shown that the H_{c2} resulting from a criteria neither follows the 3D-aGL angular dependence.

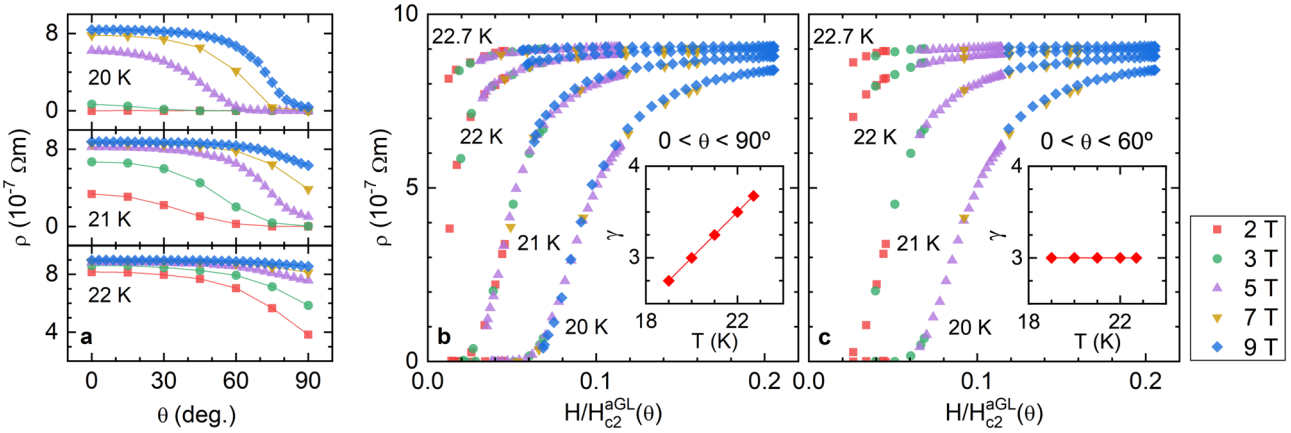

Figure 5. Analysis of the 3D-aGL scaling of the resistivity for different temperatures near T_c. (**a**) Some examples of the raw unscaled data. (**b**) Scaling obtained by using a temperature dependent anisotropy factor (shown in the inset). (**c**) Scaling of the data with $\theta < 60°$ (for which H_{c2} still follows the 3D-aGL approach). In the latter, an excellent scaling is obtained with a temperature independent γ.

3D-anisotropic GL scaling of the resistivity around T_c. Previous works in different FeSC families showed that the $\rho(T)_{H,\theta}$ data scale when represented against $H(\cos^2\theta + \sin^2\theta/\gamma^2)^{1/2}$, according to the 3D-aGL approach[60–64]. This scaling was used to determine the anisotropy factor, that in most cases was found to be temperature-dependent[60–63]. As it can be seen in Fig. 5b such scaling also works with our data (examples of unscaled data for 20-22 K are presented in Fig. 5a). The resulting anisotropy factor (inset in Fig. 5b) presents a significant temperature dependence, increasing linearly from 2.75 at 19 K to 3.75 near T_c. Nonetheless, this γ-dependence must be affected to some extent by the anomalous $H_{c2}(\theta)$ observed above. To test this hypothesis, we repeated the scaling only using data with $\theta < 60°$, for which the $H_{c2}(\theta)$ is still close to the *single-band* 3D-aGL predic-

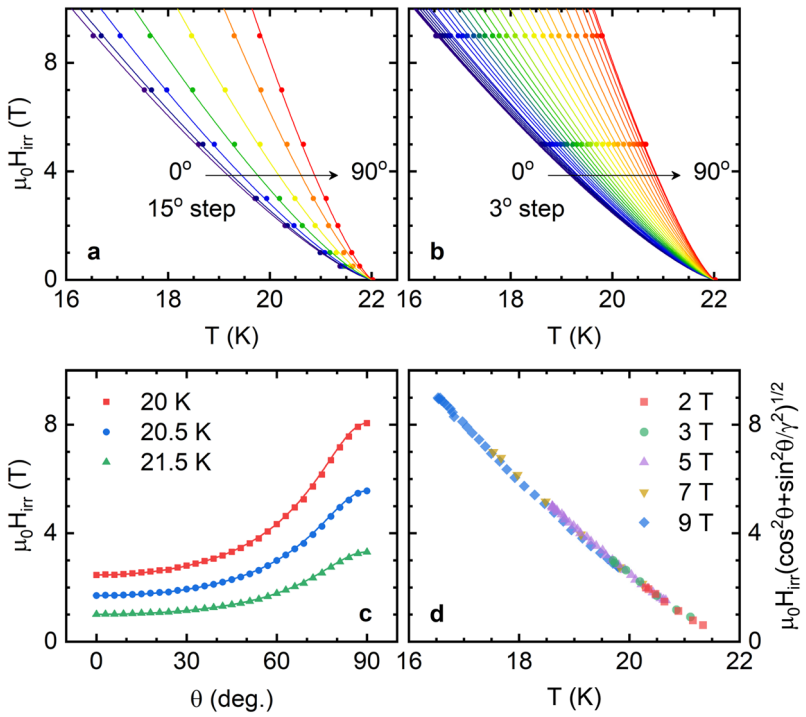

Figure 6. (**a**) Temperature dependence of the irreversibility field for different field orientations, obtained from a 1% of $\rho_B(T_c)$ criterion. The lines are a fit of a power law $H_{irr} = A(\theta)(T - T_c)^n$ to the entire set of data, that leads to $n \approx 1.3$. (**b**) $H_{irr}(T)_\theta$ in steps of 3°, obtained from the detailed 5 T and 9 T data in Fig. 1f, h. The lines are fits to the above power law with n fixed to 1.3, that allowed us to obtain the $H_{irr}(\theta)$ presented in (**c**). In this case the 3D-aGL approach (solid line) accounts for the angular dependence of H_{irr} in the entire θ range. (**d**) 3D-aGL scaling of the irreversibility field, obtained with $\gamma = 3.27$.

tion. As it can be seen in Fig. 5c, with this criterion, a good scaling is achieved with a temperature-independent anisotropy factor $\gamma = 3$ (a similar agreement is obtained with a γ value between 2.7 and 3.3). A T-independent γ was also found in Ref.[64] in $Ba_{1-x}Na_xFe_2As_2$ ($x = 0.35 - 0.4$), after excluding θ data close to 90°. The failure of the scaling at high θ in the aforementioned paper was attributed to a transition to a 2D behavior. Nevertheless, in the present case such a possibility is ruled out by the excellent agreement of the 3D approach for $\Delta\sigma$ with the experimental data up to $\theta = 90°$.

Analysis of the irreversibility field. For completeness, we present the temperature dependence of the irreversibility field, H_{irr}, for different θ values, as shown in Fig. 6a. H_{irr} was determined by using a 1% criterion on $\rho_B(T_c)$. The solid lines were obtained as the best fit to the power law $H_{irr} = A(\theta)(T_c - T)^n$ to all $H_{irr}(T)_\theta$ curves by leaving A as a free parameter for each θ and the same n for all curves. The fit quality is excellent, and leads to $n = 1.30 \pm 0.14$, close to the value found in other iron-based superconductors[65,66], and in high-T_c cuprates[67,68].

The 5 T and 9 T series, for which H_{irr} was obtained in θ-steps of 3°, were analyzed to obtain the angular dependence of the irreversibility field, as shown in Fig. 6b. The solid lines in this figure are fits to the previously mentioned power law with $n = 1.30$ and A as the only free parameter for each θ-series. From these curves $H_{irr}(\theta)$ was obtained for different temperatures (see Fig. 6c). Contrary to the results obtained for the upper critical field, we found that the irreversibility field follows the 3D-aGL angular dependence closely (Eq. (1), solid lines). This result is confirmed by the excellent 3D-aGL scaling presented in Fig. 6d, that was obtained with $\gamma = H_{irr}^{\parallel}/H_{irr}^{\perp} = 3.27$ (consistent with the value obtained in the previous section). We speculate that this discrepancy may arise from the vortex pinning by defects not being appreciably affected by the multiband electronic structure.

Conclusions

The electrical resistivity was measured in a high-quality OP-BaFeCoAs crystal, under magnetic fields with different amplitudes and orientations relative to the crystal c axis. The rounding observed just above $T_c(H)$ was interpreted in terms of Cooper pairs created by thermal fluctuations. The comparison with a generalization to finite fields of the AL approach for fluctuation effects, allowed a criterion-independent determination of $H_{c2}(\theta)$ to be made. The result differs significantly with the prediction of the single-band 3D-anisotropic Ginzburg-Landau approach, particularly for magnetic fields close to the crystal *ab* layers. The behavior is similar to the one of quasi-2D superconductors, but this possibility is inconsistent with the 3D nature of the superconducting fluctuations above $T_c(H)$. $H_{c2}(\theta)$ was then successfully compared with a theoretical approach for dirty two-band superconductors. Although OP-BaFeCoAs is not strictly in the dirty limit, the result suggests that both bands

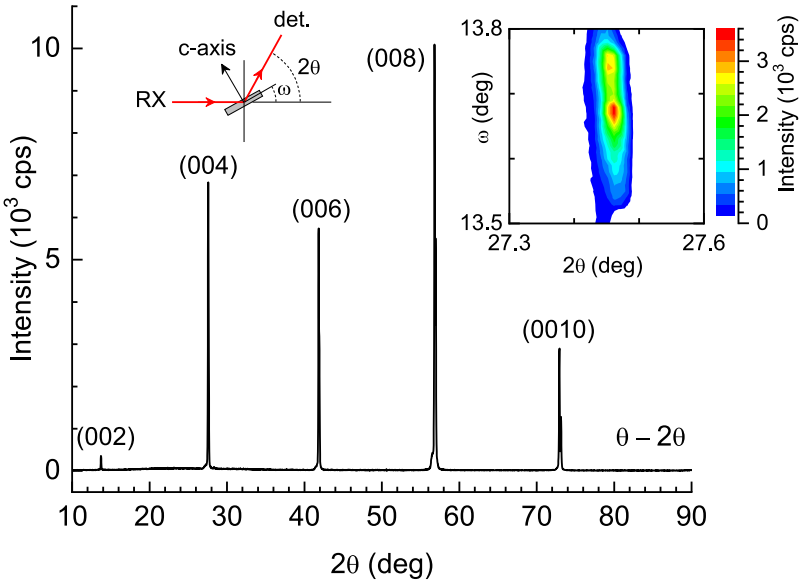

Figure 7. X-ray diffraction pattern obtained with the geometry indicated in the diagram. Only the (00*l*) reflections are observed. Inset: $\omega - 2\theta$ intensity map for the (004) peak, showing that the dispersion in the orientation of the crystal *c* axis is about 0.2°.

contribute with roughly the same weight, and that the observed anisotropy comes essentially from a highly anisotropic band ($\gamma_1 = 8.7 \pm 2.2$), while the other band is almost isotropic ($\gamma_2 = 1.28 \pm 0.16$). This result contrasts with alternative explanations for a similar anomalous $H_{c2}(\theta)$ behavior observed in these materials[20–23].

We have also found that the resistivity scales with $H(\cos^2\theta + \sin^2\theta/\gamma^2)^{1/2}$, as predicted by the 3D-aGL approach, if the data are restricted to $\theta < 60°$, where $H_{c2}(\theta)$ is reasonably well described by the 3D-aGL expression (Eq. (1)). This leads to a temperature-independent *effective* γ, in striking contrast with previous works reporting a strongly temperature-dependent γ near T_c[60–63]. Finally, in contrast with the upper critical field, the irreversibility field (determined from a 1% criterion on the normal-state resistivity) presents an angular dependence fully consistent with the one expected for 3D anisotropic superconductors, suggesting that the multiband electronic structure does not noticeably affect the vortex pinning. Nevertheless, it is possible that the symmetry of the vortex lattice in these materials could be affected by the presence of several bands, as recently observed in MgB_2[69].

It would be interesting to extend the present study to other FeSC families (e.g., 112[70], 10-3-8 and 10-4-8[71–73], for which a possible quasi-2D behavior[29] may also affect the $H_{c2}(\theta)$ angular dependence), and to probe signatures of crossband pairing, that could be present in these materials, as it has been recently proposed[74].

Methods

The $Ba(Fe_{1-x}Co_x)_2As_2$ ($x = 0.065$) crystal was grown following the procedure described in previous works[75,76]. It is a 2.902 mg plate with a 3.1 mm^2 surface parallel to the crystal *ab* layers, and a thickness of 144 μm along the crystal *c* axis (as determined from the density calculated from the lattice parameters).

The homogeneity of the crystal structure was tested by *x*-ray diffraction. As it can be seen in Fig. 7, the $\theta - 2\theta$ pattern (performed with a Rigaku Miniflex II diffractometer with a Cu target and a graphite monochromator) presents only (00*l*) reflections, indicating the excellent structural quality of the crystal. The resulting *c* axis lattice parameter (that is the same as the FeAs layers interdistance, *s*) is 12.979(2) Å, in agreement with data in the literature for crystals with a similar composition[43,76]. The inset in Fig. 7 represents the $\omega - 2\theta$ intensity map for the (004) peak, performed with a Panalytical-Empyrean diffractometer. As it can be seen, the dispersion in ω is $\sim 0.2°$, which indicates the excellent alignment of the crystal *c* axis.

The *ab* layers dc resistivity ρ was measured in the presence of magnetic fields up to 9 T with different orientations θ relative to the crystal *c* axis. To obtain these measurements, a Quantum Design's Physical Property Measurement System (PPMS) equipped with a rotating sample holder with an angular resolution of about 0.01°, was used. The electrical contacts (in-line configuration) were made with four gold wires (50 μm diameter) attached to the crystal with silver paste. The excitation current was 1 mA. To avoid the mechanical backlash, the target angles were always approached from an angle smaller by a few degrees. Prior to the measurements, the precise $\theta = 90°$ position was identified by a $\rho(\theta)$ calibration measurement at 20 K under a 9 T magnetic field (see the inset in Fig. 1). The actual $\theta = 90°$ position was found to be $\sim 2°$ away from the nominal value, probably due to the General Electric varnish used to attach the sample to the holder.

Received: 12 March 2021; Accepted: 13 May 2021
Published online: 01 June 2021

References

1. Kamihara, Y., Watanabe, T., Hirano, M. & Hosono, H. Iron-based layered superconductor La[O_{1-x} F_x]FeAs ($x = 0.05 - 0.12$) with $T_c = 26$ K. *J. Am. Chem. Soc.* **130**, 3296–3297 (2008).
2. Hosono, H., Yamamoto, A., Hiramatsu, H. & Ma, Y. Recent advances in iron-based superconductors toward applications. *Mater. Today* **21**, 278–302 (2018).
3. Pyon, S. *et al.* Enhancement of critical current density in (Ba, Na)Fe_2 As_2 round wires using high-pressure sintering. *Supercond. Sci. Technol.* **33**, 065001 (2020).
4. Paglione, J. & Greene, R. L. High-temperature superconductivity in iron-based materials. *Nat. Phys.* **6**, 645–658 (2010).
5. Hirschfeld, P. J., Korshunov, M. M. & Mazin, I. I. Gap symmetry and structure of Fe-based superconductors. *Rep. Prog. Phys.* **74**, 124508 (2011).
6. Fa, W. & Lee, D.-H. The electron-pairing mechanism of iron-based superconductors. *Science* **332**, 200–204 (2011).
7. Stewart, G. R. Superconductivity in iron compounds. *Rev. Mod. Phys.* **83**, 1589–1652 (2011).
8. Chen, X.Dai, P., Feng, D., Xiang, T. & Zhang, F.-C. Iron-based high transition temperature superconductors. *Natl. Sci. Rev.* **1**, 371–395 (2014).
9. Prozorov, R. & Kogan, V. G. London penetration depth in iron-based superconductors. *Rep. Prog. Phys.* **74**, 124505 (2011).
10. Maksimov, E. G. *et al.* Two-band Bardeen-Cooper-Schrieffer superconducting state of the iron pnictide compound, Ba($Fe_{0.9}$ $Co_{0.1}$ $)_2$ As_2. *Phys. Rev. B* **83**, 140502 (2011).
11. Hardy, F. *et al.* Calorimetric evidence of multiband superconductivity in Ba($Fe_{0.925}$ $Co_{0.075})_2$ As_2 single crystals.. *Phys. Rev. B* **81**, 060501(R) (2010).
12. Hunte, F. *et al.* Two-band superconductivity in $LaFeAsO_{0.89}$ $F_{0.11}$ at very high magnetic fields. *Nature* **453**, 903–905 (2008).
13. Gurevich, A. Iron-based superconductors at high magnetic fields. *Rep. Prog. Phys.* **74**, 124501 (2011).
14. Xingu, X. *et al.* Two-band and pauli-limiting effects on the upper critical field of 112-type iron pnictide superconductors. *Sci. Rep.* **7**, 45943 (2017).
15. Gurevich, A. Enhancement of the upper critical field by nonmagnetic impurities in dirty two-gap superconductors. *Phys. Rev. B* **67**, 184515 (2003).
16. Gurevich, A. Upper critical field and the Fulde–Ferrel–Larkin–Ovchinnikov transition in multiband superconductors. *Phys. Rev. B* **82**, 184504 (2010).
17. Tinkham, M. *Introduction to Superconductivity* (McGraw-Hill, New York, 1996).
18. Terashima, T. *et al.* Resistivity and upper critical field in KFe_2 As_2 single crystals. *J. Phys. Soc. Jpn.* **78**, 063702 (2009).
19. Yuan, H. Q. *et al.* Nearly isotropic superconductivity in (Ba, K)Fe_2 As_2. *Nature* **457**, 565–568 (2009).
20. Su, T. S., Yin, Y. W., Teng, M. L., Zhang, M. J. & Li, X. G. Angular dependence of vortex dynamics in $BaFe_{1.9}$ $Ni_{0.1}$ As_2 single crystal. *Mater. Res. Express* **1**, 016003 (2014).
21. Hao, F. X. *et al.* Angle-resolved vortex glass transition and pinning properties in $BaFe_{1.8}$ $Co_{0.2}$ As_2 single crystals. *J. Appl. Phys.* **117**, 173901 (2015).
22. Murphy, J. *et al.* Angular-dependent upper critical field of overdoped Ba(Fe_{1-x} $Ni_x)_2$ As_2. *Phys. Rev. B* **87**, 094505 (2013).
23. Hänisch, J. *et al.* High field superconducting properties of Ba(Fe_{1-x} $Co_x)_2$ As_2 thin films. *Sci. Rep.* **5**, 17363 (2015).
24. Shi, Z. X. *et al.* Out-of-plane and in-plane anisotropy of upper critical field in MgB_2. *Phys. Rev. B* **68**, 104513 (2003).
25. Kim, H.-J. *et al.* Comparison of temperature and angular dependence of the upper critical field in Mg_{1-x} Al_x B_2 single crystals in dirty-limit two-gap theory. *Phys. Rev. B* **73**, 064520 (2006).
26. Mosqueira, J. *et al.* Observation of anisotropic diamagnetism above the superconducting transition in iron pnictide Ba_{1-x} K_x Fe_2 As_2 single crystals due to thermodynamic fluctuations. *Phys. Rev. B* **83**, 094519 (2011).
27. Rey, R. I. *et al.* Measurements of the fluctuation-induced in-plane magnetoconductivity at high reduced temperatures and magnetic fields in the iron arsenide $BaFe_{2-x}$ Ni_x As_2. *Supercond. Sci. Technol.* **26**, 055004 (2013).
28. Ramos-Álvarez, A. *et al.* Superconducting fluctuations in isovalently-substituted $BaFe_2(As_{1-x}$ $P_x)_2$: Possible observation of multi-band effects. *Phys. Rev. B* **92**, 094508 (2015).
29. Sóñora, D. *et al.* Quasi-two-dimensional behavior of 112-type iron-based superconductors. *Phys. Rev. B* **96**, 014516 (2017).
30. Ahmad, D. *et al.* Effect of proton irradiation on the fluctuation-induced magnetoconductivity of $FeSe_{1-x}$ Te_x thin films. *New J. Phys.* **19**, 093004 (2017).
31. Ahmad, D. *et al.* Anisotropy dependence of the fluctuation spectroscopy in the critical and gaussian regimes in superconducting $NaFe_{1-x}$ Co_xAs single crystals. *Sci. Rep.* **8**, 8556 (2018).
32. Rey, R. I. *et al.* Measurements of the superconducting fluctuations in optimally doped $BaFe_{2-x}$ Ni_x As_2 under high magnetic fields: probing the 3D-anisotropic Ginzburg-Landau approach. *Supercond. Sci. Technol.* **27**, 075001 (2014).
33. See, e.g., Mosqueira, J., Cabo, L. & Vidal, F. Structural and T_c inhomogeneities inherent to doping in La_{2-x} Sr_x CuO_4 superconductors and their effects on the precursor diamagnetism. *Phys. Rev. B* **80**, 214527 (2009).
34. Vidal, F. *et al.* On the consequences of the uncertainty principle on the superconducting fluctuations well inside the normal state. *Europhys. Lett.* **59**, 754–760 (2002).
35. Bernardi, E. *et al.* Superconducting diamagnetic fluctuations in Sm-based underdoped cuprates studied via SQUID magnetometry. *Phys. Rev. B* **81**, 064502 (2010).
36. Prando, G. *et al.* Superconducting phase fluctuations in $SmFeAsO_{0.8}$ $F_{0.2}$ from diamagnetism at a low magnetic field above T_c. *Phys. Rev. B* **84**, 064507 (2011).
37. Bossoni, L., Romanò, L., Canfield, P. C. & Lascialfari, A. Non-conventional superconducting fluctuations in Ba(Fe_{1-x} $Rh_x)_2$ As_2 iron-based superconductors. *J. Phys.: Condens. Matter* **26**, 405703 (2014).
38. Sun, D. L., Liu, Y. & Lin, C. T. Comparative study of upper critical field H_{c2} and second magnetization peak H_{sp} in hole- and electron-doped $BaFe_2$ As_2 superconductor. *Phys. Rev. B* **80**, 144515 (2009).
39. Tanatar, M. A. Anisotropy of the iron pnictide superconductor Ba(Fe_{1-x} $Co_x)_2$ As_2 ($x = 0.074, T_c = 23$ K). *Phys. Rev. B* **79**, 094507 (2009).
40. Yamamoto, A. *et al.* Small anisotropy, weak thermal fluctuations, and high field superconductivity in Co-doped iron pnictide Ba(Fe_{1-x} $Co_x)_2$ As_2. *Appl. Phys. Lett.* **94**, 062511 (2009).
41. Soo, H. K. *et al.* Fluctuation conductivity of single-crystalline $BaFe_{1.8}$ $Co_{0.2}$ As_2 in the critical region. *J. Appl. Phys.* **108**, 063916 (2010).
42. Vinod, K., Satya, A. T., Shilpam, S., Sundar, C. S. & Bharathi, A. Upper critical field anisotropy in $BaFe_{2-x}$ Co_x As_2 single crystals synthesized without flux. *Phys. Rev. B* **84**, 012502 (2011).
43. Ni, N. *et al.* Effects of Co substitution on thermodynamic and transport properties and anisotropic H_{c2} in Ba(Fe_{1-x} $Co_x)_2$ As_2. *Phys. Rev. B* **78**, 214515 (2008).
44. Tinkham, M. Effect of fluxoid quantization on transitions of superconducting films. *Phys. Rev.* **129**, 241–2422 (1963).
45. Harper, F. E. & Tinkham, M. The mixed state in superconducting thin films. *Phys. Rev.* **172**, 441–450 (1968).
46. Mineev, V. P. General expression for the angular dependence of the critical field in layered superconductors. *Phys. Rev. B* **65**, 012508 (2001).
47. Terashima, K. *et al.* Fermi surface nesting induced strong pairing in iron-based superconductors. *Proc. Natl. Acad. Sci. U. S. A.* **106**, 7330–7333 (2009).

48. Tortello, M. *et al.* Multigap superconductivity and strong electron-boson coupling in fe-based superconductors: a point-contact Andreev-reflection study of $Ba(Fe_{1-x}\ Co_x)_2\ As_2$ single crystals. *Phys. Rev. Lett.* **105**, 237002 (2010).
49. Williams, T. J. *et al.* Muon spin rotation measurement of the magnetic field penetration depth in $Ba(Fe_{0.926}\ Co_{0.074})_2\ As_2$: evidence for multiple superconducting gaps. *Phys. Rev. B* **80**, 094501 (2009).
50. Ki-Young, C. *et al.* Two S-wave gap symmetry for single crystals of the superconductor $BaFe_{1.8}\ Co_{0.2}\ As_2$. *Physica C* **470**, S506–S507 (2010).
51. Gordon, R. T. *et al.* Doping evolution of the absolute value of the London penetration depth and superfluid density in single crystals of $Ba(Fe_{1-x}\ Co_x)_2\ As_2$. *Phys. Rev. B* **82**, 054507 (2010).
52. Fischer, *et al.* Highly anisotropic energy gap in superconducting $Ba(Fe_{0.9}\ Co_{0.1})_2\ As_2$ from optical conductivity measurements. *Phys. Rev. B* **82**, 224507 (2010).
53. Luan, L. *et al.* Local measurement of the penetration depth in the pnictide superconductor $Ba(Fe_{0.95}\ Co_{0.05})_2\ As_2$. *Phys. Rev. B* **81**, 100501 (2010).
54. Luan, L. *et al.* Local measurement of the superfluid density in the pnictide superconductor $Ba(Fe_{1-x}\ Co_x)_2\ As_2$ across the superconducting dome. *Phys. Rev. Lett.* **106**, 067001 (2011).
55. Yong, Jie *et al.* Superfluid density measurements of $Ba(Fe_{1-x}\ Co_x)_2\ As_2$ films near optimal doping. *Phys. Rev. B* **83**, 104510 (2011).
56. Milosević, M. V. & Perali, A. Emergent phenomena in multicomponent superconductivity: an introduction to the focus issue. *Supercond. Sci. Technol.* **28**, 060201 (2015).
57. Bekaert, J. *et al.* Anisotropic type-I superconductivity and anomalous superfluid density in OsB2. *Phys. Rev. B* **94**, 144506 (2016).
58. Cherpak, N. T., Barannik, A. A., Prozorov, R., Tanatar, M. & Velichko, A. V. On the determination of the quasiparticle scattering rate in unconventional superconductors by microwave surface impedance. *Low Temp. Phys.* **39**, 1110–1112 (2013).
59. Barannik, A. *et al.* Millimeter-wave surface impedance of optimally-doped $Ba(Fe_{1-x}\ Co_x)_2\ As_2$ single crystals. *Phys. Rev. B* **87**, 014506 (2013).
60. Wang, Z.-S., Luo, H.-Q., Ren, C. & Wen, H.-H. Upper critical field, anisotropy, and superconducting properties of $Ba_{1-x}\ K_x\ Fe_2\ As_2$ single crystals. *Phys. Rev. B* **78**, 140501R (2008).
61. Yi, Xiaolei *et al.* Vortex phase transition and anisotropy behavior of optimized $(Li_{1-x}\ Fe_xOH)FeSe$ single crystals. *Supercond. Sci. Technol.* **29**, 105015 (2016).
62. Yuan, F. F. *et al.* Anisotropy of iron-platinum-arsenide $Ca_{10}(Pt_n\ As_8)(Fe_{2-x}\ Pt_x\ As_2)_5$ single crystals. *Appl. Phys. Lett.* **107**, 012602 (2015).
63. Ying, J. *et al.* Angular dependence of resistivity in the superconducting state of $NdFeAsO_{0.82}\ F_{0.18}$ single crystals. *Supercond. Sci. Technol.* **21**, 105018 (2008).
64. Kalenyuk, A. A. *et al.* Unusual two-dimensional behavior of iron-based superconductors with low anisotropy. *Phys. Rev. B* **96**, 134512 (2017).
65. Bendele, M. *et al.* Anisotropic superconducting properties of single-crystalline $FeSe_{0.5}\ Te_{0.5}$. *Phys. Rev. B* **81**, 224520 (2010).
66. Prando, G. *et al.* Vortex dynamics and irreversibility line in optimally doped $SmFeAsO_{0.8}\ F_{0.2}$ from AC susceptibility and magnetization measurements. *Phys. Rev. B* **83**, 174514 (2011).
67. Malozemoff, A. P., Worthington, T. K., Yeshurun, Y., Holtzberg, F. & Kes, P. H. Frequency dependence of the AC susceptibility in a Y–Ba–Cu–O crystal: a reinterpretation of H_{c2}. *Phys. Rev. B* **38**, 7203-7206(R) (1988).
68. Yeshurun, Y. & Malozemoff, A. P. Giant flux creep and irreversibility in an Y–Ba–Cu–O crystal: an alternative to the superconducting-glass model. *Phys. Rev. Lett.* **60**, 2202–2205 (1988).
69. Curran, P. J. *et al.* Spontaneous symmetry breaking in vortex systems with two repulsive lengthscales. *Sci. Rep.* **5**, 15569 (2015).
70. Katayama, N. *et al.* Superconductivity in $Ca_{1-x}\ La_x\ FeAs_2$: a novel 112-type iron pnictide with arsenic zigzag bonds. *J. Phys. Soc. Jpn.* **82**, 123702 (2013).
71. Kakiya, S. *et al.* Superconductivity at 38K in iron-based compound with platinum-arsenide layers $Ca_{10}(Pt_4\ As_8)(Fe_{2-x}\ Pt_x\ As_2)_5$. *J. Phys. Soc. Jpn.* **80**, 093704 (2011).
72. Löhnert, C. *et al.* Superconductivity up to 35 K in the iron platinum arsenides $(CaFe_{1-x}\ Pt_xAs)_{10}\ Pt_{4-y}\ As_8$ with layered structures. *Angew. Chem. Int. Ed.* **50**, 9195–9199 (2011).
73. Ni, N., Allred, J. M., Chan, B. C. & Cava, R. J. High T_c electron doped $Ca_{10}(Pt_3\ As_8)(Fe_2\ As_2)_5$ and $Ca_{10}(Pt_4\ As_8)(Fe_2\ As_2)_5$ superconductors with skutterudite intermediary layers. *Proc. Natl. Acad. Sci. U. S. A.* **108**, E1019–E1026 (2011).
74. Vargas-Paredes, A. A., Shanenko, A. A., Vagov, A., Milosević, M. V. & Perali, A. Crossband versus intraband pairing in superconductors: Signatures and consequences of the interplay. *Phys. Rev. B* **101**, 094516 (2020).
75. Sefat, A. S. *et al.* Superconductivity at 22 K in Co-doped $BaFe_2\ As_2$ls. *Phys. Rev. Lett.* **101**, 117004 (2008).
76. Sefat, A. S. *et al.*$BaT_2\ As_2$ single crystals (T=Fe Co, Ni) and superconductivity upon Co-doping. *Physica C* **469**, 350–354 (2009).

Acknowledgements

This work was supported by the Agencia Estatal de Investigación (AEI) and Fondo Europeo de Desarrollo Regional (FEDER) through projects FIS2016-79109-P and PID2019-104296GB-I00, and by Xunta de Galicia (grant GRC no. ED431C 2018/11). The work at Oak Ridge National Laboratory was funded by U.S. Department of Energy, Materials Sciences and Engineering Division, Basic energy Sciences. SSS acknowledges support from CNPq. I.F. Llovo acknowledges financial support from Xunta de Galicia through grant ED481A-2020/149. Authors would like to thank the use of RIAIDT-USC analytical facilities.

Author contributions

J.M. conceived the experiments, A.S.S. fabricated the sample, J.M. and J.P. conducted the experiments, I.F.L., C.C., and J.M. analyzed the results, D.S., A.P., and S.S. also helped in data analysis, J.M. and I.F.L. wrote the manuscript. All authors reviewed the manuscript.

Competing interests

The authors declare no competing interests.

Additional information

Correspondence and requests for materials should be addressed to J.M.

Vortex dynamics and second magnetization peak in the iron-pnictide superconductor $Ca_{0.82}La_{0.18}Fe_{0.96}Ni_{0.04}As_2$

I F Llovo[1], D Sóñora[1], J Mosqueira[1], S Salem-Sugui Jr[2,†], Shyam Sundar[2,§], A D Alvarenga[3], T Xie[4], C Liu[4], S -L Li[4,5] and H -Q Luo[4,5]

[1]QMatterPhotonics Research Group, Departamento de Física de Partículas, Universidade de Santiago de Compostela, Santiago de Compostela E-15782, Spain
[2]Instituto de Fisica, Universidade Federal do Rio de Janeiro, 21941-972 Rio de Janeiro, RJ, Brazil
[3]Instituto Nacional de Metrologia Qualidade e Tecnologia, 25250-020 Duque de Caxias, RJ, Brazil
[4]Beijing National Laboratory for Condensed Matter Physics, Institute of Physics, Chinese Academy of Sciences, Beijing 100190, P. R. China
[5]Songshan Lake Materials Laboratory, Dongguan, Guangdong 523808, P. R. China

E-mail: [†]said@if.ufrj.br

E-mail: [§]shyam.phy@gmail.com

June 2021

Abstract. We report the studies of detailed magnetic relaxation and isothermal magnetization measurements in the vortex state of the 112-type iron-pnictide $Ca_{0.82}La_{0.18}Fe_{0.96}Ni_{0.04}As_2$ superconductor with $T_c \sim 22$ K. In the isothermal $M(H)$, a well defined second magnetization peak (SMP) feature is observed in the entire temperature range below T_c for measurements with $H \parallel c$-axis. However, for $H \parallel ab$-planes, the SMP feature is suppressed at low temperatures, which might be due to 2D Josephson vortices forming at low temperatures and high magnetic fields in such an anisotropic system. A rigorous analysis considering the magnetic relaxation data for $H \parallel c$-axis suggests an elastic to plastic pinning crossover across H_p, which also seems accompanied with a possible phase transition in vortex lattice near H_p. Moreover, point disorder and surface defects are likely to be the dominant sources of pinning, which contribute to the δl-type of pinning in the sample. A high J_c, in access of 10^5 A/cm^2 observed could potentially make this material technologically important.

1. Introduction

Vortex physics in iron-pnictide superconductors is of a great importance for many future technological advancements [1] as well as for the understanding of various exciting phases of vortex matter [2]. Among the various interesting phenomenon observed in the vortex state of type-II superconductors, the second magnetization peak (SMP) phenomenon in the isothermal magnetization curves is one of them. Such phenomenon is ubiquitous in various low-T_c conventional [3, 4] as well as in high-T_c unconventional superconductors [5, 6] and even in superconductors exhibiting multiple superconducting gaps, such as MgB_2 [4]. Also, the SMP has been investigated in nearly all families of iron-pnictide superconductors for magnetic field directions parallel and perpendicular to the crystal ab-plane [7] (and references therein), its occurrence has not been observed in some pnictide crystals even with $H \parallel c$-axis, as for instance in overdoped Ba-KFe_2As_2 [8], in (Li-Fe)OHFeSe [9], in La-doped $CaFe_2As_2$ [10] and in $La_{0.34}Na_{0.66}Fe_2As_2$ [11]. The importance of the SMP appearing on isothermal magnetization curves relies on its direct association with the peak effect appearing in the magnetic field dependence of critical current density, $J_c(H)$ [12], which is of technological importance.

Despite it being observed in many superconductors, the mechanism responsible for the SMP is not totally understood and it appears to be material dependent [13]. For this reason the SMP has been studied in many different systems, usually by means of the vortex dynamics. Since the discovery of iron-pnictide superconductors [14] the SMP has been observed in many of these systems and explained in terms of a pinning-crossover as observed for Ba(Fe-Co)$_2$As$_2$, (Ba-K)Fe_2As_2, Ba(Fe-Ni)$_2$As$_2$, Ca(Fe-Co)As and (Ca-La)(Fe-Co)As_2 [15, 16, 17, 18, 19, 20, 21, 22], in terms of a phase transition in the vortex lattice as observed for Ba(Fe-Co)$_2$As$_2$,LiFeAs, and $BaFe_2$(As-P)$_2$ [23, 24, 25, 26], and also in terms of an order-disorder transition in some compounds [27, 28, 29]. It is to note that all the systems mentioned above share a similar layered crystal structure which consists of a spacer layer in-between of FeAs superconducting layers. However, the crystal structure in the 112 family has an additional spacer layer which leads to the enhanced spacing between FeAs superconducting layers [30]. This contributes to the anisotropic superconducting properties in 112 family [31, 32, 33]. Since, the observed SMP in moderate anisotropic 1111-system is found to be due to the 3D order to 2D disorder phase transition [34, 35], it is interesting to find if a sample of 112-system with similar anisotropy as 1111-system, has the same origin of SMP.

Here, we investigate the SMP and pinning behavior in a single crystal of the 112 type pnictide $Ca_{0.82}La_{0.18}Fe_{0.96}Ni_{0.04}As_2$ superconductor with superconducting temperature transition $T_c \sim 22$ K [36] and moderate anisotropy [33]. A well pronounced SMP is observed in all isothermal $M(H)$ curves obtained with $H \parallel c$-axis even for temperatures very close to T_c ($T = 20$ K), and also for $H \parallel ab$-planes but only for temperatures above 14 K. As the SMP has been observed for $H \parallel c$-axis and $H \parallel ab$-planes in most of the pnictide superconductors [37, 38, 39], its absence for $H \parallel ab$-planes at lower temperatures (below 7.5 K) might be related to the anisotropic nature of the sample

[33] that might leads to the possible emergence of two dimensional Josephson vortices at low temperatures and high magnetic fields [6, 40].

In order to study the possible origin of the SMP observed for H||c-axis in our sample, extensive magnetic relaxation measurements were performed. For $H \parallel ab$-planes, magnetic relaxation data were within the noise level of the measurements, which prevented us from studying the vortex dynamics for this direction. The behaviour of the relaxation rate, R=dln$M$/dln(time), with field and temperature, as well as the dependence of the activation energy, U_0 = -T/R [41] with the critical current [42] and of $U(M)$ with $M - M_{eq}$ [43, 44, 45], allowed us to study the vortex dynamics in the magnetic phase diagram of the system, and also to address the underlying mechanism for SMP. A crossover from collective (elastic) to plastic pinning has been observed across SMP, which is also accompanied with a possible phase transition in vortex lattice near H_p. Moreover, point disorder and surface defects seem to be the possible sources of vortex pinning in the sample. Self-field critical current density for $H \parallel c$-axis achieves J_c= 7×10^5 A/cm^2 at T = 2 K.

2. Experimental Details

The $Ca_{0.82}La_{0.18}Fe_{0.96}Ni_{0.04}As_2$ single crystal used in this work was grown by a self-flux method as used in many other iron-based superconductors. A small crystal of mass, 0.306 mg with a roughly triangular platelet shape of surface area S = 0.65 mm^2 and thickness t = 83.4 μm (as determined from the density = 5.64 g/cm^3, calculated from the lattice parameters) was used in this study. A thorough description of the growth procedure can be seen in Ref.[36]. Details of the characterization by energy-dispersive x-ray spectroscopy (EDX) and x-ray diffraction can be seen in Ref.[33] (crystal 11 of that reference). Let us just mention that it presents an excellent stoichiometric quality, with $x = 0.176(3)$ and $y = 0.045(3)$, and its diffraction pattern shows no spurious diffraction peaks, the c-axis lattice parameter being 10.348(1) Å.

The magnetization M measurements were performed with a magnetic-properties measurement system (Quantum Design, model MPMS-XL) with magnetic fields up to 7 T applied both parallel and perpendicular to the crystal's ab layers. For this purpose, a quartz tube was used as sample holder, to which the crystal was glued with GE varnish. In the case of $H \parallel c$, the crystal was glued to a ∼0.3 mm-wide slit, perpendicular to the quartz tube axis. Two plastic rods at the sample holder ends ensured an alignment of about 0.1°. $M(H)$ hysteresis curves were measured for both $H \parallel ab$ and $H \parallel c$, by using the MPMS's *hysteresis* magnetic field charging mode. $M(t)$ relaxation curves were measured for $H \parallel c$ only (for $H \parallel ab$ the M variation was of the order of the noise level).

3. Results and Discussion

Figure 1 shows selected isothermal magnetization, $M(H)$, curves as obtained for $H \parallel c$-axis (a) and $H \parallel ab$- planes (b). All M(H) curves shown in Fig. 1 are symmetric with respect to the magnetic field axis which reflects the dominant bulk pinning of the samples. The main information that can be extracted from these figures is that a pronounced second magnetization peak is observed for all $M(H)$ curves obtained with $H \parallel c$-axis. However, for $H \parallel ab$-planes the SMP is only observed in the temperature region above 7.5 K. As shown in Fig. 1b, the $M(H)$ curves below 14 K would show a SMP developing at increasingly higher fields at low temperatures, although below 7.5 K both branches of the $M(H)$ curves decreases monotonically. The disappearance of the SMP for $H \parallel ab$-planes below 7.5 K is possibly related to the moderate anisotropy of the studied system, which may cause it to enter in a two dimensional regime for higher fields [33]. We conjecture that the possible emergence of the Josephson vortices within the 2D regime would prevent the SMP to develop at low temperatures (below 7.5 K) due to the weaker pinning of the Josephson vortices than Abrikosov vortices [6, 46]. The curves of Fig. 1 (a) allow to extract the characteristic fields H_{on}, H_p and H_{irr} which are respectively the onset field of the SMP, the peak field, and the irreversible field. H_{irr} was selected as the magnetic field at which the hysteresis amplitude becomes of the order of magnitude of the experimental noise. An example of H_{irr} obtained by this criterion is shown in the inset of Fig. 1 (a). We observe that the SMP develops even for temperatures very close to T_c for $H \parallel c$-axis direction. It is worth mentioning that the onset field H_{on} and peak field, H_p associated to the SMP for $H \parallel c$-axis are well defined in all isothermal $M(H)$ curves even at $T = 2$ K.

In order to study the possible origin of the second magnetization peak in the sample, magnetic relaxation measurements were performed as a function of field for selected isothermal $M(H)$ curves, and as a function of temperature for selected applied magnetic fields. The study was only conducted for $H \parallel c$, as values of the magnetic moment during relaxation were within the noise level observed for $H \parallel ab$- planes measurements. Magnetic relaxation curves were obtained for span times of about 80 minutes, and plots of ln$M$ vs ln(time) produced the usual linear curves from which the values of the relaxation rate R=dln$M$/dln(time) were extracted. Figure 2 shows plots of $M(H)$ curves obtained at T=10 K and 12 K, along with the respective relaxation rate curves obtained over each $M(H)$ curve from fields going from below H_{on} up to above H_p. A change in the curvature of R vs. H can be observed for fields in the vicinity of H_p, the peak field, which might suggests a change in the pinning behaviour occurring near H_p. Moreover, a change in the curvature of each R vs. H near H_{on} is associated to crossover of the single vortex pinning to collective vortex pinning [16]. Similar peaks in the R vs. H curves, appearing between H_{on} and H_p have also been observed previously in other iron-pnictide superconductors [16, 18] which have been attributed to a precursor phenomenon that leads to a SMP at higher fields [47].

To check for the change in curvature observed in the curves of Fig. 2(a,b) for H

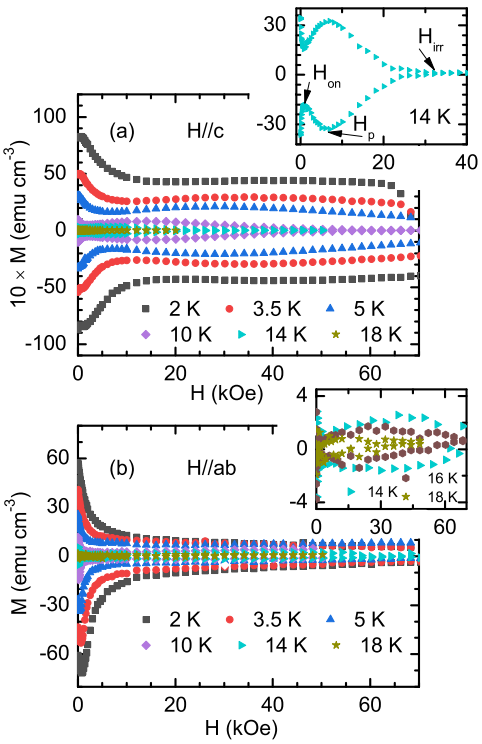

Figure 1. (a) Isothermal magnetic field dependence of the magnetization, $M(H)$, at selected temperatures well below T_c for $H \parallel c$. In inset, the characteristic fields H_{on}, H_p and H_{irr} are well defined for $M(H)$ measured at $T = 14$ K. (b) Isothermal $M(H)$ at selected temperatures for $H \parallel ab$. Inset shows the clear signature of SMP in isothermal $M(H)$ measured at 14 K, 16 K and 18 K.

near H_p, magnetic relaxation measurements as a function of temperature for H=10, 15, and 20 kOe were performed. Figure 2(c) shows the resulting R vs T curves where a clear change in the behaviour of R is observed near T_{cr} (marked with an arrow). Later in the paper, it will be shown in the H-T phase diagram that the T_{cr} obtained for each field is well matched with H_p vs. T.

As the R vs. T, and R vs. H plots suggest a possible pinning crossover near H_p, it would be interesting to see the behaviour of the activation pinning energy, $-T/R$ against $1/J_c$, where J_c is the critical current density. Figure 3 (a) shows selected curves of the magnetic field dependence of the critical current density, $J_c(H)$ for $H \| c$-axis as calculated using the Bean's critical-state model [48]. An expression for a triangular platelet with magnetic field parallel to c-axis was used to estimate the J_c in the sample [49], $J_c(T,H) = \frac{15\Delta M(T,H)}{\sqrt{s^{-1}(s-a)(s-b)(s-c)}}$, where $a \approx 1.25$ mm, $b \approx 1.10$ mm, and $c \approx 1.37$ mm are the sides of the triangle, $s = (a+b+c)/2$ is its semiperimeter, and $\Delta M(T,H)$ is the magnetization hysteresis. A peak, associated to the SMP in $M(H)$, is clearly visible for each $J_c(H)$ curve shown in Fig. 3 (a).

According to the collective pinning theory [42] the activation energy $U \sim (1/J_c)^{\mu}$, where μ is a critical exponent. From this critical exponent, information about how the

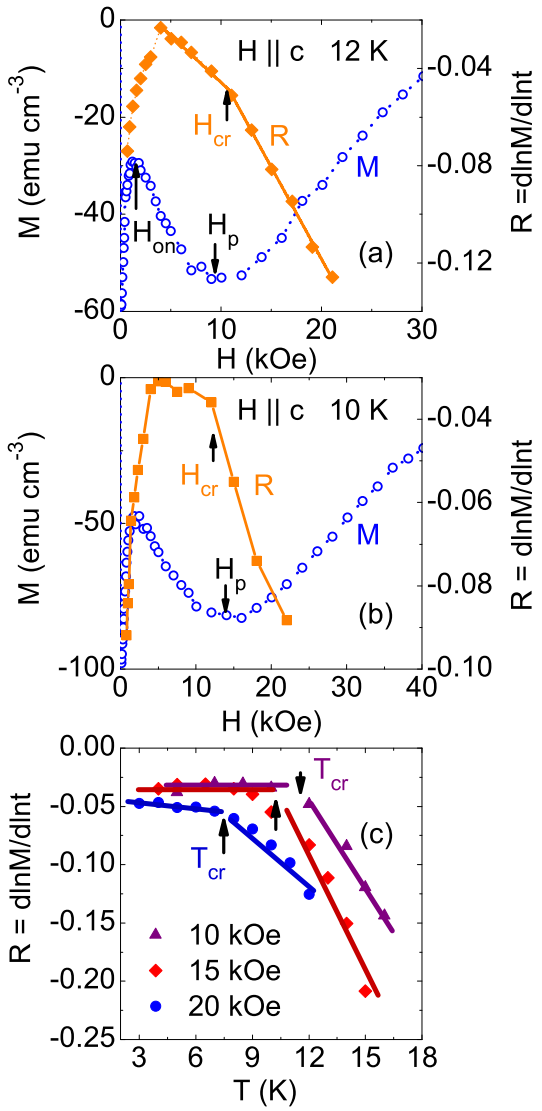

Figure 2. (a,b) Isothermal magnetic field dependence of the magnetization, $M(H)$, measured at $T = 12$ K and 10 K, in the increasing magnetic field branch and the obtained relaxation rates, R, at fixed magnetic fields between H_{on} and H_p for respective $M(H)$. H_{cr} indicates the change in slope in $R(H)$ which matches well with H_p. (c) Relaxation rate as a function of temperature,$R(T)$, for $H = 10$ kOe, 15 kOe and 20 kOe. Arrows indicate, T_{cr}, the temperature where slop changes in each $R(T)$.

vortices are collectively pinned can be obtained. For instance, μ=1/7 corresponds to single vortex, μ=3/2 to small bundles of vortices and μ=7/9 to large bundles. Figure 3 (b) shows two distinct behaviours occurring for all isofield curves where for lower values of the inverse critical current density, which corresponds to the region below H_p, the exponent $\mu = 1.07$ and 0.98 for $H = 10$ kOe and 15 kOe respectively and $\mu = 0.63$ for $H = 20$ kOe. Such values of μ are in agreement with a vortex lattice collectively pinned as small bundles and large bundles. The region corresponding to larger values of the inverse critical current density, which corresponds to the region above H_p, possesses a

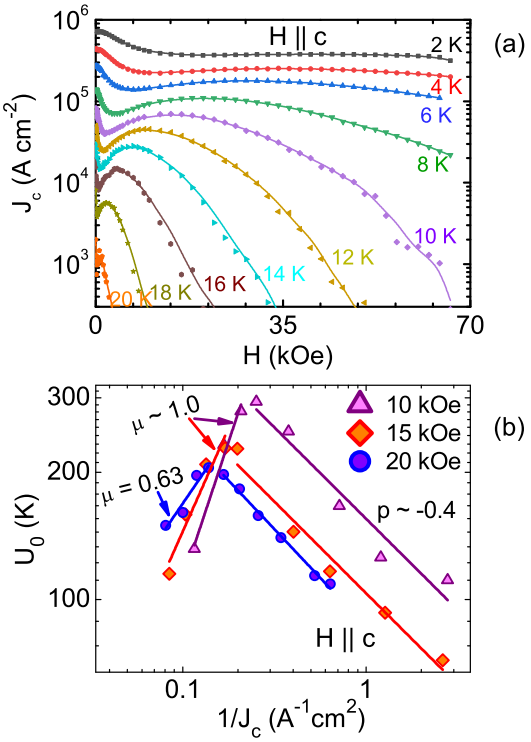

Figure 3. (a) Critical current density as a function of magnetic field, $J_c(H)$ obtained using Bean's critical state model [48] for $H \| c$. Solid lines are guide to eyes. (b) Activation energy, U_0 = T/R, as a function of inverse critical current density, $1/J_c$, for H = 10 kOe, 15 kOe, and 20 kOe. The exponents μ and p found for each curve indicates an elastic pinning to plastic pinning crossover across SMP.

negative exponent which can not be explained in terms of the collective pinning theory. Such a region with a negative exponent [17, 21] has been associated to plasticity of the vortex lattice, where the characteristic exponent is p=-0.5. As it can be observed in Fig. 3 (b) the exponent p obtained for the three fields data is $p\sim$-0.4 (p=-0.4 for H=10, p=-0.37 for 15 kOe and p=-0.46 for H=20 kOe) which agrees with the plastic exponent p=-0.5. Figure 4 suggests that the mechanism responsible for the second magnetization peak appearing in $M(H)$ curves in our sample is a crossover from collective to plastic pinning occurring as the SMP develops. It should be mentioned that such behavior, separating a low J_c region from a higher J_c region in U_0 vs. $1/J_c$ isofield curves has also been observed previously in systems which do not exhibit the second magnetization peak [11]. To further study this change in behavior, a more rigorous analysis of the activation energy was performed, as first presented in Ref.[45].

The characteristic fields, H_{on}, H_p and H_{irr} obtained from the isothermal $M(H)$ curves for $H \| c$-axis are plotted as a function of temperature in the H-T phase diagram, shown in Fig. 4. Contrary to the H_{on} line, the temperature dependence of H_p and H_{irr} follow $\sim (1-(T/T_c))^n$ behavior, where, n = 2, 1.3 are obtained for H_p and H_{irr} lines respectively. A similar temperature dependence of the irreversibility line was also observed in Ref. [50]. It is interesting to note that at low T, the H_{on} and H_p follow

relatively opposite curvatures with temperatures, which may lead to the merging of H_p and H_{on} lines at temperatures below 2 K. A merging of the H_{on} line with the H_p line at high fields would imply the disappearance of the SMP, which in the present case of a highly anisotropic system could be associated to a possible field-induced crossover to a two dimensional vortex system. It should be mentioned that the vortex physics associated to the H_{on} and H_p are different in nature, where, H_{on} is reported to be associated to a crossover from single vortex-pinning to a collective vortex-pinning regime [17, 19, 45]. This supports a change in pinning strength from weak to strong across H_{on} as reported in ref. [51]. On the other hand, different mechanisms have been reported to be responsible for the SMP at H_p in different systems, as discussed in the introduction. The origin of the SMP in present sample is discussed in the later part of the paper. We also plot in the phase diagram the corresponding H_{cr} and T_{cr} values of the kinks observed in R vs. H and R vs. T plots respectively. It is interesting to note that the H_{cr} and T_{cr} points in the $H-T$ phase diagram lie almost perfectly on the H_p line. This fact, despite evidencing a change in the pinning mechanism, as discussed above, may also be related to a possible vortex lattice phase transition taking place as the second magnetization peak develops [5, 52], which deserves further investigation. Moreover, a contour plot of J_c obtained at various temperatures below T_c in the magnetic field range 0-7 T is also shown in Fig. 4, to track the H_{on}, H_p and H_{irr} with the changes in $J_c(H,T)$.

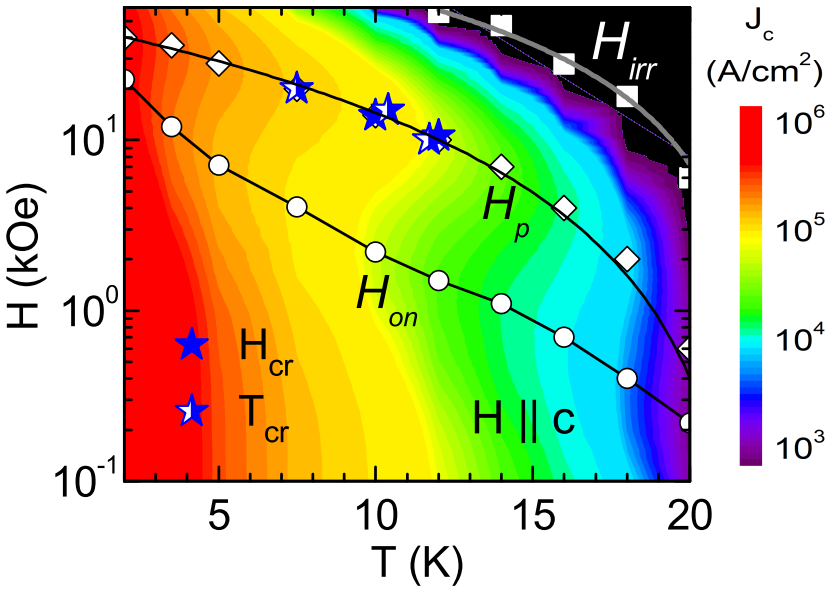

Figure 4. An H-T phase diagram representing the characteristic fields, H_{on}, H_p and H_{irr}. Solid lines in H_{irr} and H_p are fit to the data as explained in the text. H_{cr} and T_{cr} are field and temperature marked in Fig. 2. Solid line in H_{on} is guide to the eyes. The critical current density as a function of magnetic field at different temperatures is plotted in a contour plot.

The activation energy, $U(M)$, was obtained following an approach developed by

Maley et al. [43, 44] assuming that the isofield $U(M)$ curves measured at different temperatures should be a smooth function of $M - M_{eq}$, where M_{eq} is the equilibrium magnetization. It should be mentioned that for our system $M - M_{eq} \approx M$. In this approach, $U(M)$=-Tln(dM/dt)+CT, where C is an intrinsic constant. $U(M)$ is then calculated from the isofield relaxation curves obtained for several temperatures and plotted as a function of M. The appropriate constant C for the system defines the smooth curve. But as pointed out in Ref.[44], for most systems the smooth curve is only obtained by dividing $U(M)$ by a scaling function $g(T/T_c)$ which carries the behavior of the coherence length $\xi(T)$. Figure 5 shows a plot of $U/(1\text{-}T/T_c)^{3/2}$ vs. M for H = 10 kOe exhibiting a smooth behavior with M, which was obtained for $C = 15$. Similar curves with the same constant C were obtained for $H = 15$ and 20 kOe (not shown here for brevity). With the value of $C = 15$ we can calculate $U(M)$ from the isofield magnetic relaxations obtained on the isothermic $M(H)$ curves for fields below and above the H_p. Figure 6 (a) shows the $U(M)$ curves obtained for isothermal $M(H)$ at 12 K where a clear change in the behavior of $U(M)$ is observed as H_p is crossed. To check for a possible pinning crossover across H_p, we exploited an expression from the collective pinning theory, $U(B, J) = B^{\nu} J^{-\epsilon} \approx H^{\nu} M^{-\epsilon}$, where, ν and ϵ are exponents for specific pinning. Figure 6 (b) shows plots of selected $U(M)$ curves of Fig. 6 (a) after being scaled by H^{ν}, as in Ref. [45]. For H below and above H_p, the scaling was obtained for $\nu = 0.5$ and -0.5 respectively. A positive value of exponent ν supports the collective pinning for $H < H_p$ [42, 45], whereas a negative ν exponent for fields above H_p supports plastic pinning. Although, the expected values of ν are 1 and -0.5 for collective and plastic pinning respectively, exponent ν smaller than 1, associated to collective pinning, have also been observed in other systems [6, 17, 18]. The inset of Fig. 6 (b) shows the corresponding $M(H)$ at 12 K evidencing H_p. The plots of Fig. 6 (b) clearly demonstrate that the mechanism explaining the second magnetization peak in our sample is a crossover from collective to plastic pinning occurring as the peak field H_p is crossed. As discussed in the last paragraph, there is also a possibility of vortex lattice phase transition below H_p. Such change in vortex lattice near H_p may creates an energetically favorable scenario for the plastic pinning at fields above H_p. Similar behavior has also been observed in the case of Co-doped 122 iron pnictide superconductor, where a a vortex lattice phase transition below H_p accompany the collective to plastic creep crossover across H_p [16, 23, 53]. Moreover, Kopeliansky *et al* [23] also stated that such a crossover (collective-plastic) in vortex dynamics may accompany a thermodynamic phase transition in vortex lattice, as seen previously in case of YBCO [45, 54]. However, any direct observation of vortex lattice phase transition below H_p and its correlation with SMP is yet to be confirmed in iron pnictide superconductors.

Figure 7(a) shows a plot of the so called remanent critical current density normalized by its value extrapolated to T=0, $J_c(T)/J_c(0)$ against temperature for $H \parallel c$-axis. The remanent critical current corresponds to the critical current at zero field extracted from the Bean's model, where ΔM is obtained by subtracting the magnetization for H=0 belonging to the decreasing field branch from the magnetization curve for H=0 belonging

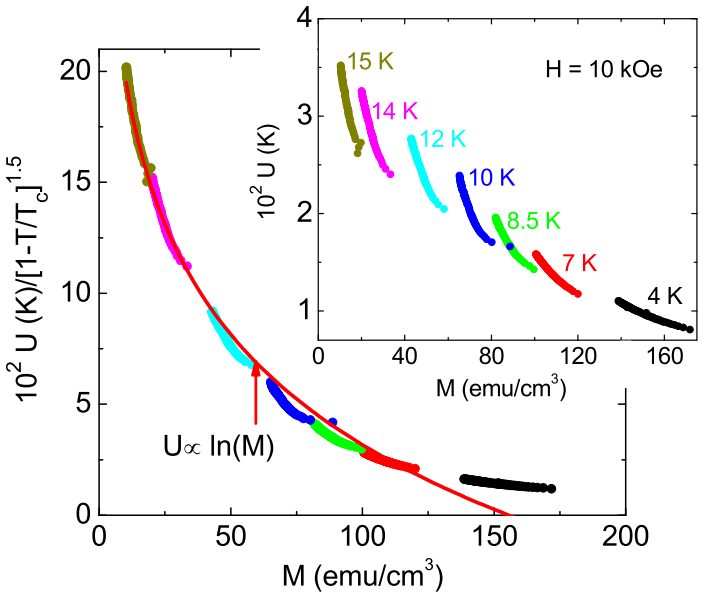

Figure 5. $U/g(T/T_c)$ vs. M scaled plot obtained for H = 10 kOe using Maley's criterion explained in the text. Solid line shows the ln(M) dependence of scaled curve. Inset shows the $U(M)$ without scaling using $g(T/Tc)$ function.

to the increasing field branch after cycling the correspondent isotherm $M(H)$ in negative magnetic fields. For comparison, Fig. 7(a) also shows the values obtained from a model developed in Ref.[55] which considers two possible pinning of the type δl, for which $J_c(T)/J_c(0) \sim (1\text{-}t^2)^{5/2}(1+t^2)^{-1/2}$, and δT_c, for which $J_c(T)/J_c(0) \sim (1\text{-}t^2)^{7/6}(1+t^2)^{5/6}$, where $t = T/T_c$. As observed in other pnictides [17] and references therein, the dominant pinning in our sample follows neither of the above two behaviors considered in Ref.[55]. However, such behavior of $J_c(T)$ may be explained considering the weak and strong pinning at low and high magnetic fields respectively, as shown in case of $FeSe_{0.5}Te_{0.5}$ superconductor [56].

Figure 7(b) shows a plot of the normalized pinning force density, $F_p(H)/F_{pmax}$, as a function of the reduced field h=H/H_{irr}, for several temperatures. The pinning force density is obtained using expression, F_p=$H\times J_c$. The scaling of the different isothermal $F_p(H)/F_{pmax}$ curves with h=H/H_{irr} is a powerful tool [57, 58] commonly used in new materials to identify the dominant pinning acting within certain temperature regions [59]. The importance of this plot also relies on the identification of the magnetic field region, h_{max}, where the pinning force presents its maximum, which might be important for application purposes [57, 58]. As shown in Fig.7 (b), all curves collapse in one, with a very clear maximum appearing for H/H_{irr}=0.27. The solid curve in this figure is a best fit to the well known Dew-Hughes expression, $F_p(H)/F_{pmax} \sim h^p(1\text{-}h)^q$, where values of p and q are associated to the characteristic types of pinning explained in the model [57]. The best fit shown in Fig. 7(b) was obtained with p=2 and q = 5.5 where h_{max}= $p/(p+q) \sim 0.27$, which is consistent with the h_{max} observed from data. It is important to mention that in Dew-Hughes model [57, 58], δl pinning due to point disorder expects,

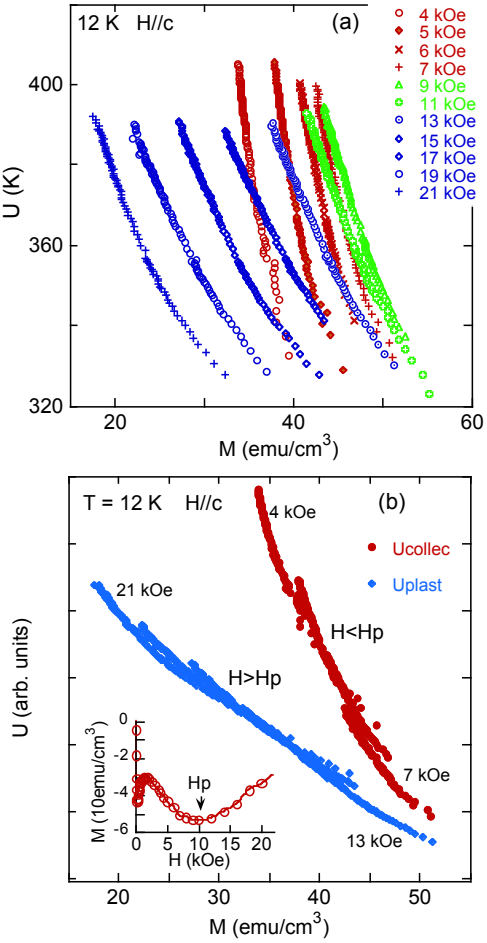

Figure 6. (a) Activation energy, U, vs. magnetization, M, for different magnetic fields above and below the H_p at $T = 12$ K. (b) Scaled U curves using collective pinning theory show elastic pining for $H < H_p$ and plastic pinning for $H > H_p$. Inset shows the initial branch of $M(H)$ measured at $T = 12$ K for $H \parallel c$-axis.

$p = 1$ and $q = 2$, with $h_{max} = 0.33$. Therefore, in our case, $h_{max} = 0.27$ indicates the pinning due to point disorder. However, higher values of p and q and slightly lower h_{max} than what is ideally expected for Dew-Hughes model, suggests additional pinning at play, likely due to the surface defects. Similar results have been observed in other iron pnictide superconductors as reported in Refs. [18, 60, 61, 62]. Moreover, according to Dew-Hughes model [57], $h_{max} < 0.5$ indicates a δl pinning, while $h_{max} > 0.5$ suggests δT_c pinning, therefore, $h_{max} = 0.27$ in present case is suggestive of δl pinning. In addition, more than one pinning centers at play may lead to the deviation from the δl pinning model, as observed in Fig. 7(a).

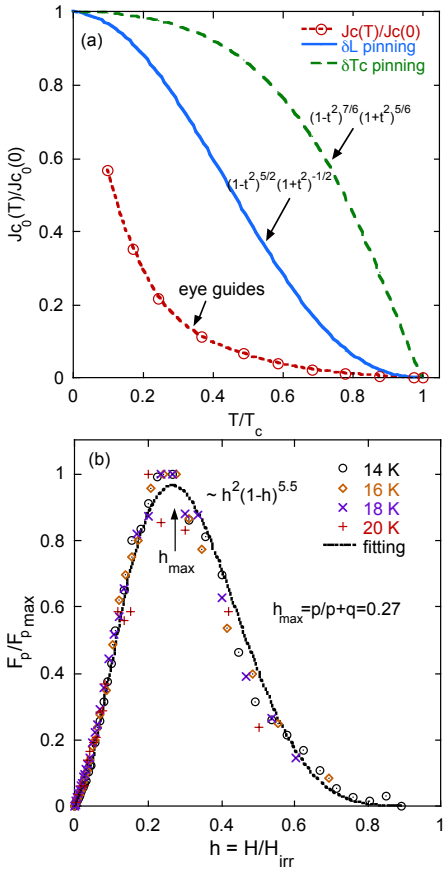

Figure 7. (a) Normalized critical current density, $J_c(T)/J_c(0)$ as a function of reduced temperature, $t = T/T_c$ from experimental data. Solid lines represents the δl and δT_c pinning using models in Ref. [55]. (b) Normalized pinning force density, $F_p(H)/F_{pmax}$, as a function of the reduced field, $h = H/H_{irr}$ for different temperatures. The solid line is the fitting of scaled curves using the expression, $F_p(H)/F_{pmax} \sim h^p(1\text{-}h)^q$, where, p and q are fitting parameters [57]. Details of the fit are given in the main text.

4. Conclusions

In conclusion, we investigated the second magnetization peak (SMP) and the associated pinning properties in a single crystal of the iron-pnictide $Ca_{0.82}La_{0.18}Fe_{0.96}Ni_{0.04}As_2$ superconductor. In isothermal $M(H)$ measurements for $H \parallel c$-axis, the SMP was observed for the entire temperature range below T_c. However, the SMP was observed only for temperatures close to T_c for $H \parallel ab$-planes. A detailed investigation based on Maley's analysis and collective pinning theory suggests that the SMP in the sample may be explained in terms of an elastic pinning to plastic pinning crossover across H_p, which also seems accompanied with a possible vortex lattice phase transition. However, any direct observation of such phase transition in vortex lattice near H_p and its correlation with SMP is yet to be confirmed. For $H \parallel ab$-planes, the suppression of the SMP at low temperature may be related to the sample anisotropy, which in turn leads to the 2D Josephson vortices at low temperature and high magnetic fields. Based on the

Dew-Hughes model, pinning analysis for $H \parallel c$ suggests that point disorder in addition with surface defects are the possible sources of vortex pinning, which are in favor of a δl-type pinning in the sample. Moreover, the critical current density has been found to be higher than 10^5 A/cm^2 for temperatures below 8 K in the entire magnetic field range of the measurements. This property makes this compound technologically relevant for use in high magnetic field generation.

Acknowledgements

IFL, DS, and JM acknowledge support by the Spanish Agencia Estatal de Investigación (AEI) and Fondo Europeo de Desarrollo Regional (FEDER) through project PID2019-104296GB-I00, and by Xunta de Galicia (grant GRC no. ED431C 2018/11). IFL acknowledges financial support from Xunta de Galicia through grant ED481A-2020/149. Authors would like to thank the use of RIAIDT-USC analytical facilities. SSS and ADA acknowledges support from CNPq. This work at IOP, CAS is supported by the National Key Research and Development Program of China (Grants No. 2018YFA0704200, No. 2017YFA0303100, and No. 2017YFA0302900), the National Natural Science Foundation of China (Grants No. 11822411, No. 11961160699, and No. 11874401), the Strategic Priority Research Program (B) of the Chinese Academy of Sciences (CAS) (Grants No. XDB25000000 and No. XDB07020300) and K. C. Wong Education Foundation (GJTD-2020-01). HL is grateful for the support from the Youth Innovation Promotion Association of CAS (Grant No. Y202001).

References

[1] Hosono H, Yamamoto A, Hiramatsu H and Ma Y 2018 *Materials Today* **21** 278
[2] Kwok W K, Welp U, Glatz A, Koshelev A E, Kihlstrom K J and Crabtree G W 2016 *Rep. Prog. Phys.* **79** 116501
[3] Lortz R, Musolino N, Wang Y, Junod A and Toyota N 2007 *Phys. Rev. B* **75** 094503
[4] Stamopoulos D, Speliotis A and and D N 2004 *Supercond. Sci.Technol.* **17** 1261
[5] Rosenstein B, Shapiro B Y, Shapiro I, Bruckental Y, Shaulov A and Yeshurun Y 2005 *Phys. Rev. B* **72** 144512
[6] Salem-Sugui S Jr S, Lopes P V, Kern M P, Sundar S, Liu S, Li S and Ghivelder H L L 2020 *Phys. Rev. B* **102** 064509
[7] Cheng W, Lin H, Shen B and Wen H H 2019 *Science Bulletin* **64** 81
[8] Song D, Ishida S, Iyo A, Nakajima M, ichi Shimoyama J, Eisterer M and Eisaki H 2016 *Sci. Rep.* **6** 26671
[9] Wang C, Yi X, Sun X, Tang Q, Qiu Y, Luo Y, and Yu B 2017 *Supercond. Sci. Technol.* **30** 085004
[10] Jung S G, Shin S, Jang H, Mikheenko P, Johansen T H and Park T 2017 *Supercond. Sci. Technol.* **30** 085009
[11] Sundar S, Salem-Sugui Jr S, Alvarenga A D, Doria M M, Gu Y, Li S, , Luo H and Ghivelder L 2019 *J. Appl. Phys.* **125** 123902
[12] Rosenstein B and Li D 2010 *Rev. Mod. Phys.* **82** 109
[13] Wang C, He T, Han Q, Fan C, Tang Q, Chen D, Lei Q, Sun S, Li Y and Yu B 2021 *Supercond. Sci. Technol.* **34** 055001
[14] Kamihara Y, Watanabe T, Hirano M and Hosono H 2008 *J. Am. Chem. Soc.* **130** 3296

[15] Shen B, Cheng P, Wang Z, Fang L, Ren C, Shan L and Wen H H 2010 *Phys. Rev. B* **81** 014503
[16] Sundar S, Mosqueira J, Alvarenga A D, Sóñora D, Sefat A S and Jr S S S 2017 *Supercond. Sci. Technol.* **30** 125007
[17] Sundar S, Jr S S S, Amorim H S, Wen H H, Yates K A, Cohen L F and Ghivelder L 2017 *Phys. Rev. B* **95** 134509
[18] Sundar S, Salem-Sugui S Jr S, Lovell E, Vanstone A, Cohen L F, Gong D, Lu R Z X, Luo H and Ghivelder L 2019 *ACS Appl. Electron. Mater.* **1** 179
[19] Salem-Sugui Jr S, Ghivelder L, Alvarenga A D, Cohen L F, Yates K A, Morrison K, Jr J L P, Luo H, Wang Z and Wen H H 2010 *Phys. Rev. B* **82** 054513
[20] Ahmad D, Choi W J, Seo Y I, Jung S G, Kim Y C, Jr S S S, Park T, and Kwon Y S 2017 *Supercond. Sci. Technol.* **30** 105006
[21] Zhou W, Xing X, Wu W, Zhao H and Shi Z 2016 *Sci. Rep.* **6** 22278
[22] Galluzzi A, Buchkov K, Nazarova E, Tomov V, Grimaldi G, Leo A, Pace S and Polichetti M 2019 *Nanotechnology* **30** 254001
[23] Kopeliansky R, Shaulov A, Shapiro B Y, Yeshurun Y, Rosenstein B, Tu J J, Li L J, Cao G H and Xu Z A 2010 *Phys. Rev. B* **81** 092504
[24] Pramanik A K, Harnagea L, Nacke C, Wolter A U B, Wurmehl S, Kataev V and Büchner B 2011 *Phys. Rev. B* **83** 094502
[25] Salem-Sugui Jr S, Mosqueira J, Alvarenga A D, Sóñora D, Herculano E P, Hu D, Chen G and Luo H 2015 *Supercond. Sci. Technol.* **28** 055017
[26] Miu L, Ionescu A M, Miu D, Burdusel M, Badica P, Batalu D and Crisan A 2020 *Sci. Rep.* **10** 17274
[27] Zehetmayer M 2015 *Sci. Rep.* **5** 9244
[28] Miu D, Noji T, Adachi T, Koike Y and Miu L 2012 *Supercond. Sci. Technol.* **25** 115009
[29] Ionescu A M, Miu D, Crisan A and Miu L 2018 *J Supercond Nov Magn* **31** 2329
[30] Yakita H, Ogino H, Okada T, Yamamoto A, Kishio K, Tohei T, Ikuhara Y, Gotoh Y, Fujihisa H, Kataoka K, Eisaki H and ichi Shimoyama J 2014 *J. Am. Chem. Soc.* **136** 846
[31] Zhou W, Zhuang J, Yuan F, Li X, Xing X, Sun Y and Shi Z 2014 *Applied Physics Express* **7** 063102
[32] Xing X, Zhou W, Zhou N, Yuan F, Pan Y, Zhao H, Xu X and Shi Z 2016 *Supercond. Sci. Technol.* **29** 055005
[33] Sóñora D, Carballeira C, Ponte J J, Xie T, Luo H, Li S and Mosqueira J 2017 *Phys. Rev. B* **96** 014516
[34] Weyeneth S, Puzniak R, Mosele U, Zhigadlo N, Katrych S, Bukowski Z, Karpinski J, Kohout S, Roos J and Keller H 2009 *J Supercond Nov Magn* **22** 325
[35] Prozorov R, Tillman M E, Mun E D and Canfield P C 2009 *New Journal of Physics* **11** 035004
[36] Xie T, Gong D, Zhang W, Gu Y, Huesges Z, Chen D, Liu Y, Hao L, Meng S, Lu Z, Li S and Luo H 2017 *Supercond. Sci. Technol.* **30** 095002
[37] Salem-Sugui Jr S, Ghivelder L, Alvarenga A D, Cohen L F, Luo H and Lu X 2011 *Phys. Rev. B* **84** 052510
[38] Salem-Sugui Jr S, Ghivelder L, Alvarenga A D, Cohen L F, Luo H and Lu X 2013 *Supercond. Sci. Technol.* **26** 025006
[39] Sharma S, Vinod K, Sundar C S and Bharathi A 2013 *Supercond. Sci. Technol.* **26** 015009
[40] Moll P J W, Balicas L, Geshkenbein V, Blatter G, Karpinski J, Zhigadlo N D and Batlogg B 2012 *Nature Materials* **12** 134
[41] Beasley M R, Labusch R and Webb W W 1969 *Phys. Rev.* **181** 682 references therein
[42] Feigel'man M V, Geshkenbein V B, Larkin A I and Vinokur V M 1989 *Phys. Rev. Lett.* **63** 2303
[43] Maley M P, Willis J O, Lessure H, and McHenry M E 1990 *Phys. Rev. B* **42** 2639(R)
[44] McHenry M E, Simizu S, Lessure H, Maley M P, Coulter J Y, Tanaka I and Kojima H 1991 *Phys. Rev. B* **44** 7614
[45] Abulafia Y, Shaulov A, Wolfus Y, Prozorov R, Burlachkov L, Yeshurun Y, Majer D, Zeldov E,

Wühl H, Geshkenbein V B and Vinokur V M 1996 *Phys. Rev. Lett.* **77** 1596
[46] Fehrenbacher R, Geshkenbein V B and Blatter G 1992 *Phys. Rev. B* **45** 5450
[47] Polichetti M, Galluzzi A, Buchkov K, Tomov V, Nazarova E, Leo A, Grimaldi G and Pace S 2021 *Sci. Rep.* **11** 7247
[48] Bean C P 1962 *Phys. Rev. Lett.* **8** 250
[49] Poole C, Farach H, Creswick R and R P 2007 *Superconductivity* (Academic Press)
[50] Yeshurun Y and Malozemoff A P 1988 *Phys. Rev. Lett.* **60** 2202
[51] Galluzzi A, Buchkov K, Tomov V, Nazarova E, Leo A, Grimaldi G, Nigro A, Pace S and Polichetti M 2018 *Supercond. Sci. Technol.* **31** 015014
[52] Rosenstein B and Zhuravlev V 2007 *Phys. Rev. B* **76** 014507
[53] Prozorov R, Ni N, Tanatar M A, Kogan V G, Gordon R T, Martin C, Blomberg E C, Prommapan P, Yan J Q, Bud'ko S L and Canfield P C 2008 *Phys. Rev. B* **78** 224506
[54] Deligiannis K, de Groot P A J, Oussena M, Pinfold S, Langan R, Gagnon R and Taillefer L 1997 *Phys. Rev. Lett.* **79** 2121
[55] Griessen R, Wen H H, van Dalen A J J, Dam B, Rector J and Schnack H G 1994 *Phys. Rev. Lett.* **72** 1910
[56] Galluzzi A, Buchkov K, Tomov V, Nazarova E, Leo A, Grimaldi G, Nigro A, Pace S and Polichetti M 2019 *J. Phys.: Conf. Ser.* **1226** 012012
[57] D Dew-Hughes 1974 *Philosophical Magazine* **30** 293
[58] Koblischka M R and Muralidhar M 2016 *International Journal of Modern Physics B* **30** 1630017
[59] Zhang Q, Zhang X, Yao C, Huang H, Wang D, Dong C, Ma Y, Ogino H and Awaji S 2017 *Superc. Sci. Techno.* **30** 065004
[60] Shahbazi M, Wang X L, Dou S X, Fang H and Lin C T 2013 *J. Appl. Phys.* **113** 17E115
[61] Shahbazi M, Wang X L, Choi K Y and Dou S X 2013 *Applied Physics Letters* **103** 032605
[62] Gennep D V, Hassan A, Luo H and Abdel-Hafiez M 2020 *Phys. Rev. B* **101** 235163

Enhancement of the critical current by surface irregularities in Fe-based superconductors

I. F. Llovo,[1] J. Mosqueira,[1,*] Ding Hu,[2] Huiqian Luo,[3] and Shiliang Li[3]

[1] *QMatterPhotonics Research Group, Departamento de Física de Partículas, Universidade de Santiago de Compostela, E-15782 Santiago de Compostela, Spain*
[2] *School of Physics, Hangzhou Normal University, Hangzhou 311121, China*
[3] *Beijing National Laboratory for Condensed Matter Physics, Institute of Physics, Chinese Academy of Sciences, Beijing 100190, PR China*

(Dated: November 28, 2023)

The maximum non-dissipative current (or critical current, I_c) that a superconductor can carry is one of the most important factors towards its implementation in many practical applications. I_c is limited by the movement of quantized vortices due to the force acting on them when an electrical current flows through the material. The introduction of bulk pinning centers for the vortices is the main procedure to enhance I_c. However, it has been shown that in clean low-T_c superconductors, surface pinning of vortices may be even more important than bulk pinning. Up to date, no study of the possible effect of surface pinning has been performed in Fe-based superconductors. Here, we show that surface irregularities introduced in high-quality single crystals of a Fe-based superconductor significantly enhance their critical current. The effect is consistent with a theoretical estimate of the maximum non-dissipative surface current that a rough surface can sustain.

I. INTRODUCTION

Since the 2008 discovery of superconductivity at high critical temperature in iron-based superconductors (FeSC),[1] intensive research on these materials has been taking place. On the one hand, these materials have a fundamental interest, as they share multiple similarities with high-T_c cuprates, such as elevated transition temperatures and the emergence of superconductivity with the introduction of dopants which destroy the antiferromagnetic order of the parent system,[2–4] suggesting their Wang11 mechanism may be similar.[5] They also present a multiband electronic structure,[2–4] which leads to unconventional behavior of observables such as the magnetic penetration depth,[6] the Seebeck coefficient[7], the specific heat,[8,9] or the upper critical field.[10–13] On the other hand, these materials present some properties that make them interesting from the point of view of applications, such as high critical and irreversibility magnetic fields,[14–18] a relatively low anisotropy (particularly the 122 family), and large grain boundary critical angles (as high as 9°).[19] These characteristics are crucial for the potential mass manufacture and application of polycrystalline wires and tapes,[20,21] and for the development of superconducting devices such as bulk magnets[22] or thin-film nanocircuits including integrated Josephson junctions and SQUIDs.[23]

For the aforementioned reasons, much attention has been put on enhancing the critical current density J_c in these materials. Multiple techniques have been shown to serve this purpose, such as proton, neutron and heavy ion irradiation to produce point-like[24–26] or columnar[24,25,27,28] defects, self-assembled oxygen-rich impurities addition,[29] and the artificial generation of compositionally modulated superlattices, e.g. $BaFe_2As_2/Ba(Fe_{1-x}Co_x)_2As_2$.[30]

In addition to bulk pinning, surface irregularities have also been shown to be effective at enhancing the critical current in conventional low-T_c superconductors.[31] Among the procedures used to create surface defects in these materials are sandblasting,[31] mechanical abrasion,[32] buffered chemical or electrolytic polishing,[33] and low temperature bakeout.[34] More recent work in metallic niobium sheets has shown that laser-induced periodic structuration can make the irreversibility field H_{irr} to increase[35] or decrease when using a femtosecond-pulsed laser.[36] Nevertheless, no similar studies have been conducted on FeSC so far.

In this work, the effect of surface irregularities on the critical current of FeSC single crystals is studied. For this, we have chosen the 122 family, the most studied among the FeSC in applied research due to its lower anisotropy and higher J_c.[23] In particular, optimally-doped $BaFe_2(As_{1-x}P_x)_2$ (Ba122:P) was used, for which crystals of considerable dimensions and high stoichiometric quality can be grown.[37–39] The results will be compared with a theoretical estimate for the critical current density that a rough surface can sustain, based on Mathieu-Simon continuum theory for the mixed state.[31,40]

II. EXPERIMENTAL DETAILS

A. Crystals growth and characterization

$BaFe_2(As_{1-x}P_x)_2$ ($x = 0.35$) single crystals were grown using the Ba_2As_3/Ba_2P_3 self-flux method described in Ref. 37. They are platelike, with typical surfaces of several mm^2 and thicknesses up to ∼0.1 mm (see Table I). A thorough characterization of crystals from the same batch was presented in Ref. 39, where energy

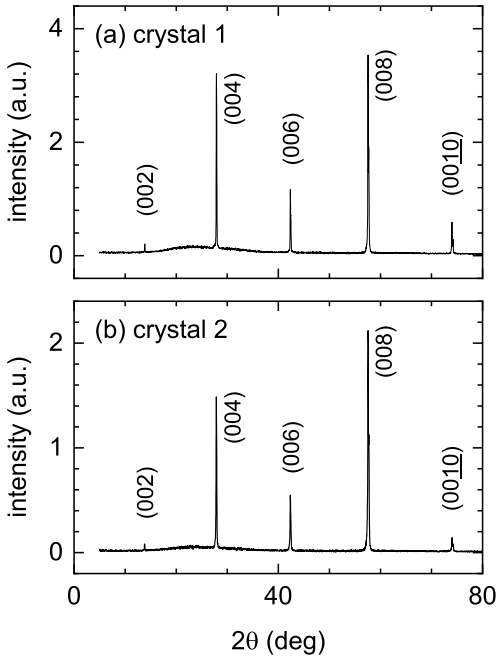

FIG. 1. X-ray diffraction patterns of the studied single crystals, obtained by using the geometry to observe the reflections by the *ab* layers. Only (00ℓ) diffraction peaks can be observed, evidencing excellent structural quality of the crystals.

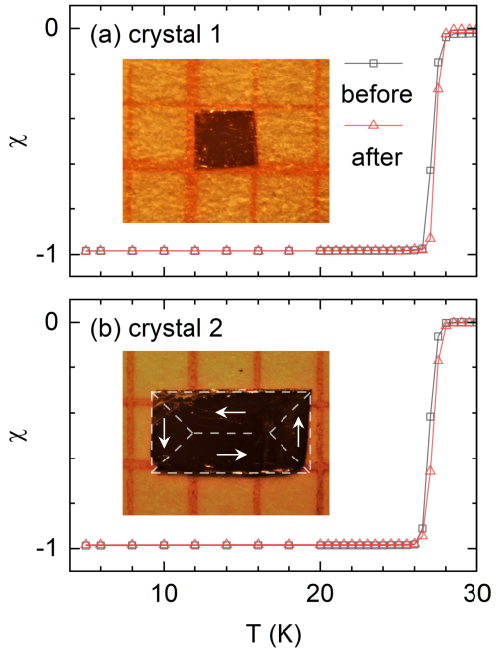

FIG. 2. Magnetic susceptibility vs temperature for the $BaFe_2(As_{1-x}P_x)_2$ crystals studied. They have T_c values about 27 K and transition widths under 1 K, evidencing an excellent stoichiometric purity. Photographs of the samples are included in the insets. The arrows on crystal 2 indicate the critical-state electrical current distribution used to evaluate Eq. (3).

dispersive x-ray (EDX) analysis showed an excellent compositional homogeneity, the average stoichiometry varying less than 0.4% between different crystals and different studied areas. The crystallographic structure of the samples used in this work was studied by x-ray diffraction (XRD), using a Rigaku MiniFlex II diffractometer with a Cu target and a graphite Cu Kα monocromator. The reflections by the crystal *ab* planes (parallel to the FeAs layers) are presented in Fig. 1. The absence of reflections other than the (00ℓ) indicates the excellent structural quality of the crystals. The resulting *c*-axis lattice parameter is about 12.80 Å (see Table I), in agreement with data in the literature for crystals with a similar As-P proportion.[41–43].

B. Surface etching process

The crystals were subjected to an abrasive sandblasting to create micrometric irregularities on their surfaces. A commercial sandblasting machine (Damglass E. Fexas, model DAM-1) was used with silica sand of diameter $\sim 50-100$ µm. The samples were kept centered in the ejection cone, with the nozzle-to-sample distance set to 8.5 cm. A 5 second burst at 1 bar nozzle pressure was used to etch one of the *ab* surfaces of crystals 1 and 2. The reverse side of crystal 2 was also subjected to an identical etching process. After the sandblasting, the samples were carefully cleaned from sand residue. Atomic force microscopy (AFM) micrographs of the surface of the samples before and after the sandblasting process are shown in Fig. 3. As it can be seen, the sandblasting process creates defects typically ~ 5 µm wide and ~ 1 µm deep, covering most of the surface of the crystals.

C. Magnetization measurements and results

The magnetization measurements were performed with a commercial SQUID magnetometer (MPMS-XL, Quantum Design) with the magnetic field applied perpendicular to *ab* layers of the crystals. For this purpose, a quartz tube was used as sample holder. The crystals were placed in a slit perpendicular to the tube axis, and glued with a small amount of GE varnish. Two plastic rods at the tube ends ensured an alignment of the *c* axis of the crystals with the applied magnetic field of about 0.1°.

The temperature dependence of the magnetic susceptibility χ, measured after zero-field-cooling (ZFC) with a low field (~ 0.3 mT) perpendicular to *ab* layers, is presented in Fig. 2. These data are corrected for demagnetizing effects by using the demagnetizing factors D calculated from the dimensions of the crystals (see Table I). As shown, χ is close to the ideal value of -1 at low temperatures, and the diamagnetic transition is very sharp (less than ~ 1 K wide), which confirms the excellent sto-

crystal	T_c (K)	c (Å)	size ($L_a \times L_b \times L_c$) ($mm^3$)	D_c	mass (mg)	sides etched
1	27.2	12.802(3)	$0.94 \times 0.94 \times 0.042$	0.933	0.230	1
2	26.9	12.795(3)	$2.48 \times 1.28 \times 0.070$	0.937	1.386	2

TABLE I. Some characteristics of the crystals studied. The critical temperature T_c was obtained from low-field magnetic susceptibility measurements (Fig. 2). The c-axis lattice parameter c was obtained from x-ray diffraction (Fig. 1). Both T_c and c agree with data in the literature for $BaFe_2(As_{1-x}P_x)_2$ with the same P content. The demagnetizing factor for $H \parallel c$, D_c, was estimated from the dimensions of the samples.

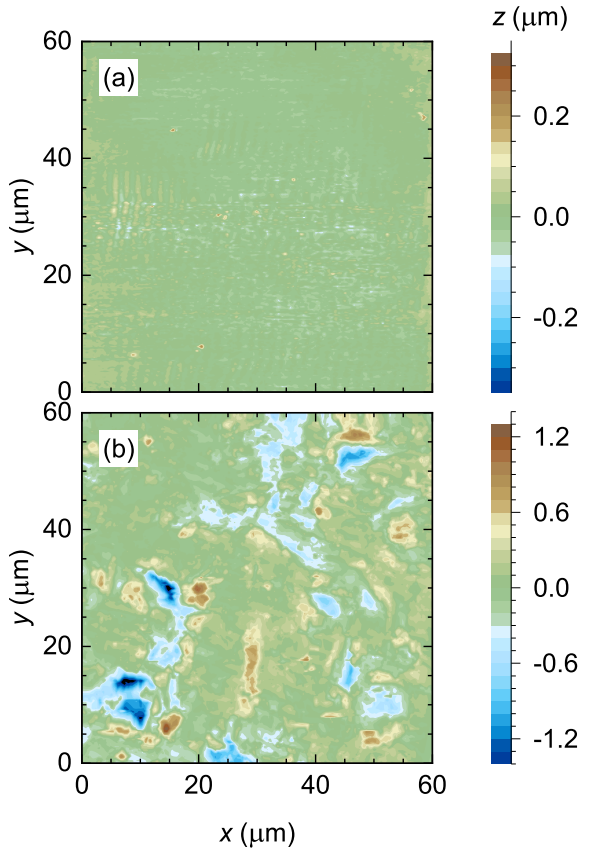

FIG. 3. Example of AFM micrographs of the crystal surfaces (a) before and (b) after the abrasive blasting process. While in (a) the irregularities are limited to ± 0.1 μm, in (b) they extend up to ± 1.4 μm (note the difference in the scale).

ichiometric quality of the crystals. The superconducting transition temperature, estimated from the diamagnetic transition midpoint, is $T_c \approx 27$ K (see Table I) typical of optimally-doped $BaFe_2(As_{1-x}P_x)_2$.[44]

To estimate the *ab*-layers critical current density of the crystals before and after sandblasting, magnetic moment vs. magnetic field $m(H)$ hysteresis cycles were measured with $H \perp ab$ at different temperatures below T_c. These measurements were performed by first zero-field cooling (ZFC) to the target temperature. The magnetic field was set by using the so-called *hysteresis* charging mode (with the power supply continuously turned on), and data were acquired by using MPMS's *reciprocating sample option* (RSO), averaging 10 measuring cycles at 1 Hz. Fig. 4 shows the $m(H)$ hysteresis loops obtained for both crystals before (dashed lines) and after (solid lines) sandblasting. As it can be seen, this surface treatment appreciably increases the hysteresis amplitude in all the studied temperatures and magnetic fields. It is worth noting that this compound presents a *second magnetization peak* (SMP) which can be clearly observed for temperatures above 15 K, consistently with previous measurements.[15,45,46]

To observe the effect of sandblasting at low fields and close to T_c more clearly, a detailed log-log representation of the upper-right branch of the hysteresis cycles for both samples is presented in Fig 5. In order to compare both crystals with each other and with other samples in the literature, m is normalized by the volume of the crystals, and the normal-state paramagnetic signal was subtracted. As it can be seen, the surface treatment produced an increase of the hysteresis amplitude, and this increase extends to the low-H region and is relatively more significant at temperatures closer to T_c. Also, the irreversibility magnetic field H_{irr} (above which the hysteresis vanishes), was increased after the sandblasting process. In the following Section, these effects will be interpreted in terms of an extra non-dissipative surface current made possible by the surface irregularities.

III. DATA ANALYSIS

A. Critical current enhancement

The *ab*-layers critical current density J_c before the sandblasting process can be obtained from the $m(H)$ hysteresis loops measured with $H \perp ab$ by using Bean's critical-state model[47,48]. For a crystal of dimensions L_a, L_b and L_c (where $L_a > L_b > L_c$) it leads to[49]

$$J_c = \frac{2m_h/V}{L_b\,(1 - L_b/3L_a)}, \qquad (1)$$

where $V = L_a L_b L_c$ and m_h is the amplitude of the $m(H)$ hysteresis loop. The temperature dependence of the resulting J_c at different applied magnetic fields is presented in Figs. 6(a, b) for both crystals. As shown, J_c presents

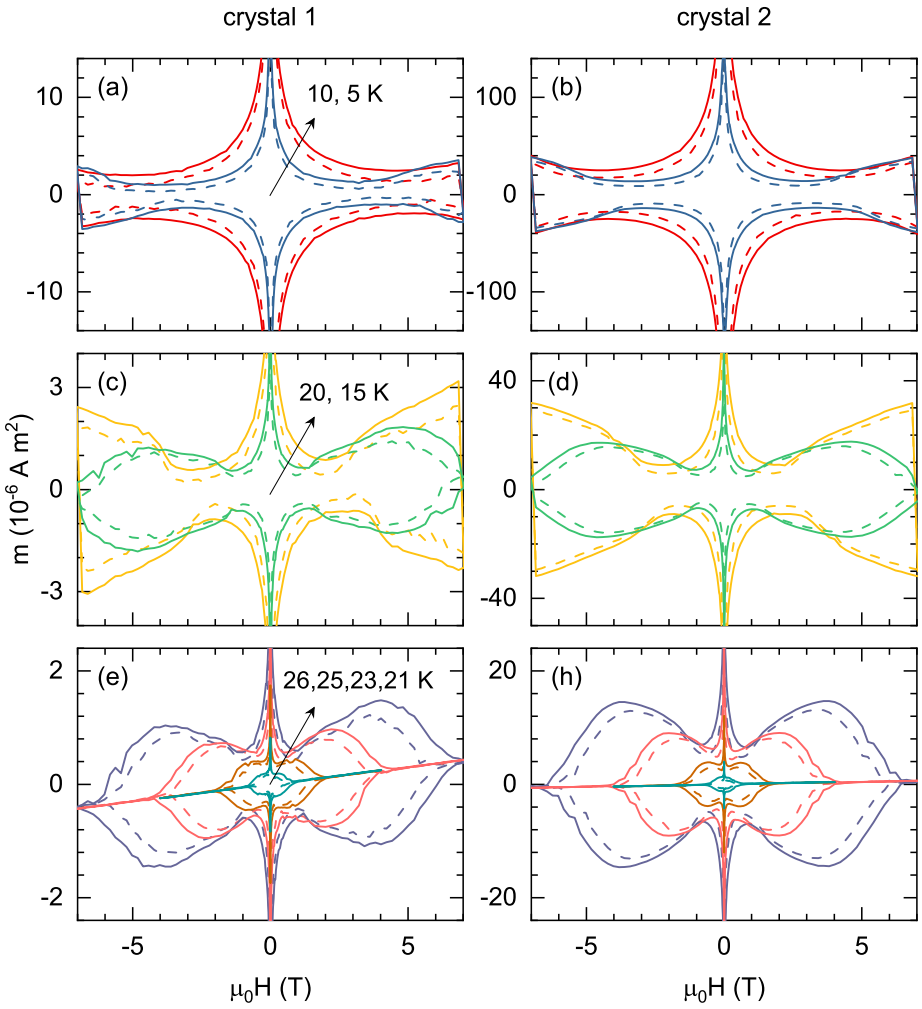

FIG. 4. Isothermal $m(H)$ hysteresis curves for the two single crystals, before (dashed lines) and after (solid lines) sandblasting. Crystal 1 was sandblasted only from one side, while crystal 2 was sandblasted from both sides. As it can be seen, the hysteresis amplitude increased after the sandblasting process for both samples.

a similar amplitude, temperature and magnetic field dependences in both crystals.

The increase in the hysteresis amplitude after sandblasting (hereafter denoted as Δm_h) can be understood in terms of non-dissipative surface currents enabled by the surface irregularities. The mechanism for the existence of such currents has been explained in detail in previous works (see, e.g., Ref. 31 and references therein). Let us just mention that the surface roughness gives rise to many ways for the vortices to terminate at the sample surface while satisfying the boundary condition. This enables a collective bending of the vortices in a depth of the order of the London penetration length, which sustains an extra non-dissipative current loop. The magnetic moment m_s due to these surface currents is given by

$$m_s = \frac{1}{2}\int_{surface} (\vec{r}\times\vec{K})\, d\vec{S}, \qquad (2)$$

where $\vec{K}$ is the surface current density. In the critical state $\vec{K}$ corresponds to the critical surface current density $\vec{K}_c$, and the associated increase in the hysteresis loop amplitude is

$$\Delta m_h = \left|\int_{surface} (\vec{r}\times\vec{K}_c)\, d\vec{S}\right|. \qquad (3)$$

To evaluate Eq. (3), the spatial dependence of $\vec{K}_c$ can be approximated by a Bean-like distribution, similar to the one expected for the underlying bulk current density (see diagram inset in Fig. 2(b)). For a crystal of dimensions L_a, L_b and L_c (where $L_a > L_b > L_c$) this leads to

$$\Delta m_h = \frac{K_c L_b^3}{2}\left(\frac{L_a}{L_b} - \frac{1}{3}\right) \qquad (4)$$

for each sandblasted surface.

The surface critical current resulting from Eq. (4) and the Δm_h data in Fig. 4, are shown in Figs. 6 (c, d). As it

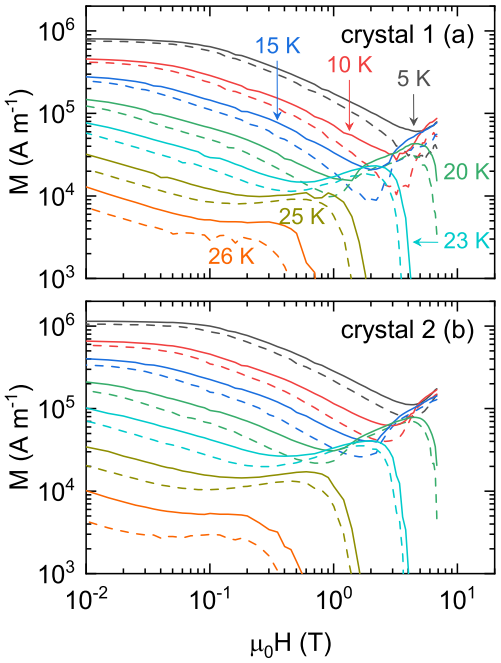

FIG. 5. Detail of isothermal $M(H)$ cycles for $M, H > 0$, before (dashed lines) and after sandblasting (solid lines). The magnetization hysteresis increases at all applied magnetic fields, and is comparatively higher at temperatures closer to T_c. The irreversibility field H_{irr} was also increased, suggesting stronger pinning is taking place (see main text for details).

can be seen, K_c decreases monotonically with T and H, but the T dependence is qualitatively different from the one of J_c: while K_c is roughly linear in all the studied temperature range, J_c grows faster at low temperatures. Moreover, J_c presents a broad maximum related to the second magnetization peak (SMP), which is absent in K_c at the same temperature (this can be better seen in the detail near T_c presented in Figs. 6(e, f). In turn, $K_c(T)$ presents a sharp peak just before vanishing, similar to the *peak effect* observed in the critical current of some low-T_c compounds[50,51] and high-T_c cuprates,[52] which has been attributed to the different T-dependence of pinning and elastic forces near $H_{c2}(T)$.[53] The different behavior of J_c and K_c confirms that the m_h increase after sandblasting is not due to enhanced bulk pinning but to a true surface effect.

B. Comparison with theoretical approaches

We will now discuss if the observed K_c behavior and amplitude is consistent with an estimate based on Mathieu-Simon continuum theory of the mixed state for the non-dissipative current enabled by a rough surface. Let's assume that the external magnetic field B is applied along the z axis (parallel to the crystal c axis), and the electrical current flows in the y direction. At a point in which the surface normal makes an angle α with the z axis, the vortices are bent in the xz plane so that the associated flux density ω makes an angle θ with z, given by $\tan\theta = \gamma^2 \tan\alpha$ (γ is the superconducting anisotropy factor). The flux density at the surface is $\omega = B/\cos\theta$. According to Mathieu-Simon theory, the non dissipative local surface current density K is given by[31]

$$K = |M_x(\omega, \theta)|, \tag{5}$$

where $M_x(\omega, \theta)$ is the x component of the reversible magnetization of an anisotropic superconductor under a flux density ω at an angle θ relative to the crystal c axis. Using the result from Ref. 54 for the reversible magnetization vector of anisotropic superconductors in intermediate magnetic fields (far from both the upper and lower critical magnetic fields), we find that

$$K = \frac{\phi_0}{8\pi\mu_0\lambda_{ab}^2} \ln\left(\frac{\eta/b}{\sqrt{1+\gamma^2\tan^2\alpha}}\right) \frac{\tan\alpha}{\sqrt{1+\gamma^2\tan^2\alpha}}. \tag{6}$$

Here, λ_{ab} is the magnetic penetration depth for currents along the ab layers, $b \equiv B/B_{c2}^{\perp}$, where $B_{c2}^{\perp}$ is the upper critical field perpendicular to the ab layers, ϕ_0 is the magnetic flux quantum, μ_0 is vacuum's magnetic permeability, and η is a constant of order unity. For a given b, K has a maximum for some angle α_0. This can be seen in Fig. 7(a), where Eq. (6) is plotted against α for different b values, using parameters for optimally-doped $BaFe_2(As_{1-x}P_x)_2$ (see below). If the surface is sufficiently rugous, the vortices have many possible angles to terminate at the surface, and the critical surface current K_c will correspond to Eq. (6) evaluated with α_0. The condition $dK/d\alpha|_{\alpha_0} = 0$ leads to

$$\gamma^2 \tan^2\alpha_0 = \frac{1}{2} W\left(\frac{2e^2\eta^2}{b^2}\right) - 1, \tag{7}$$

where $W(x)$ is Lambert's function (the inverse of xe^x), and e is Euler's constant. Substituting α_0 into Eq. (6) and simplifying, we finally obtain

$$K_c = \frac{\phi_0}{16\pi\mu_0\gamma\lambda_{\perp}^2} W\left(\frac{2e^2\eta^2}{b^2}\right)\left[1 - \frac{2}{W\left(\frac{2e^2\eta^2}{b^2}\right)}\right]^{3/2}. \tag{8}$$

A similar calculation was obtained in Ref. 31 using Abrikosov's result for M_x close to the upper critical magnetic field, although this result is not applicable in the present case as the irreversibility field $H_{irr}(T) \sim 0.5H_{c2}(T)$ (see Fig. 8), impeding the study of K_c for fields close to H_{c2}.

Fig. 7(b) shows the theoretical $K_c(T)$ for the same B values as in Fig. 6, evaluated by assuming a Ginzburg-Landau temperature dependence for the upper critical field $H_{c2}^{\perp}(T) = H_{c2}^{\perp\prime}(T - T_c)$ and the magnetic penetration depth $\lambda_{ab}(T) = \lambda_{ab}(0)/\sqrt{1 - T/T_c}$. The $\lambda_{ab}(0)$, $H_{c2}^{\perp\prime}$ and γ values used were obtained from from the data

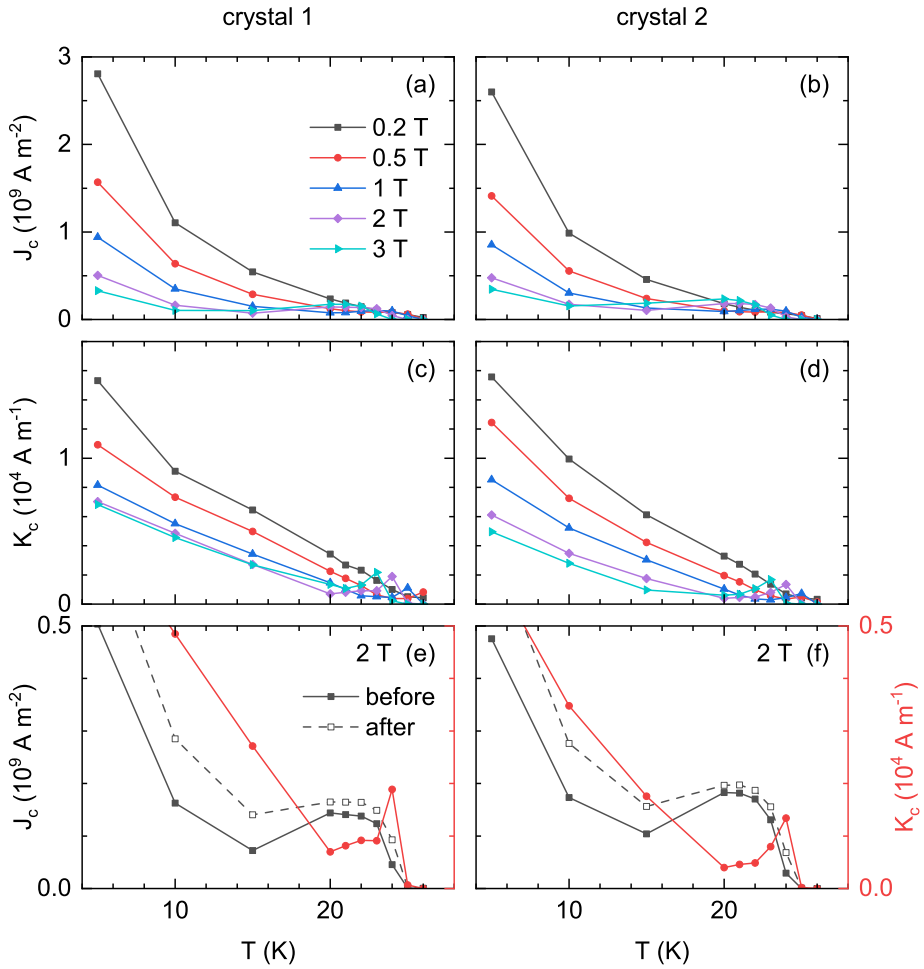

FIG. 6. (a, b) critical current density J_c obtained by applying Bean's critical state model before sandblasting; (c, d) critical current surface density K_c obtained assuming that all additional pinning occurs at the surface of the sample (Eq. (4)). As it can be seen, the $K_c(T)$ curves follow a different trend than $J_c(T)$. This can be better observed in (e, f), where the detail of $J_c(T)$ (black squares) and $K_c(T)$ (red circles) close to T_c is shown, for an applied magnetic field of 2 T.

in Ref. 44 for the optimally-doped $BaFe_2(As_{1-x}P_x)_2$. Finally, the parameter η was approximated to 1. As it can be seen, Fig. 7(b) resembles the experimental results for K_c summarized in Figs. 6(c, d), in both the temperature and magnetic field dependences (except for the peak effect observed just before vanishing). The difference in the amplitude (a factor of about two), could be probably attributed to the uncertainties in the superconducting parameters and in the geometry of the samples.

C. $H-T$ phase diagram and irreversibility field increase

In addition to the critical current enhancement, an increase of the irreversibility field H_{irr} was also observed after sandblasting, as shown in the $H-T$ phase diagrams presented in Fig. 8. In these figures, the $H_{irr}(T)$ values were estimated from the $m(H)$ cycles presented in Figs. 4(e, h), as the magnetic field at which $dm/dH = 0$ (roughly above which the normal-state paramagnetic contribution becomes dominant). As it can be seen, the sandblasting essentially shifts the $H_{irr}(T)$ line ~ 0.5 K to higher temperatures. Eq. (8) predicts that K_c should vanish at the $H_{c2}(T)$ line. However, this equation does not consider the effect of thermal fluctuations on the vortices, which play a non negligible role in these materials.[39,55–58] For completeness, the phase diagrams of Fig. 8 also include the onset and the maximum of the second magnetization peak (H_{on} and H_p, respectively), and the upper critical field line estimated from the data in Ref. 44.

IV. CONCLUSIONS

The increase in vortex pinning induced by the addition of surface rugosity through abrasive sandblasting

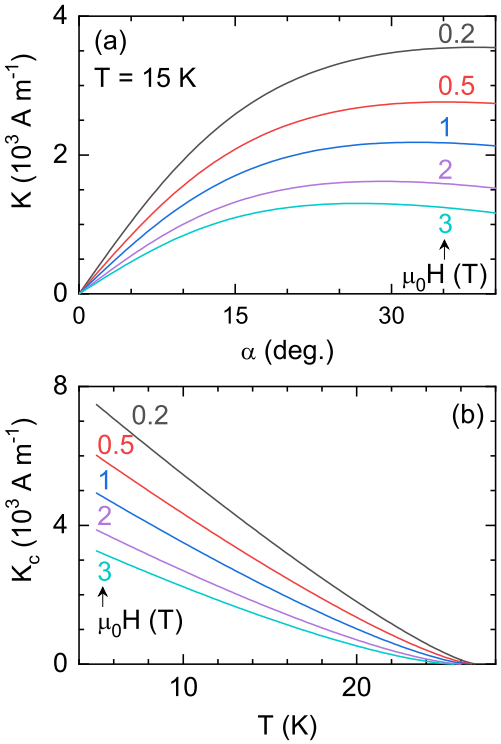

FIG. 7. (a) Theoretical non-dissipative surface current density against α (the angle between the surface normal and the crystal c axis) for different applied magnetic fields. These curves were obtained from Eq. 6 with the superconducting parameters for optimally-doped $BaFe_2(As_{1-x}P_x)_2$ from Ref. 44. As it can be seen, there is an angle α_0 for each field for which K is maximum. In a sufficiently rough surface, the critical current density corresponds to $K(\alpha_0)$, Eq. 8, which is plotted against T in (b). Note the good agreement with the experimental $K_c(T)$ shown in Figs. 6 (c, d).

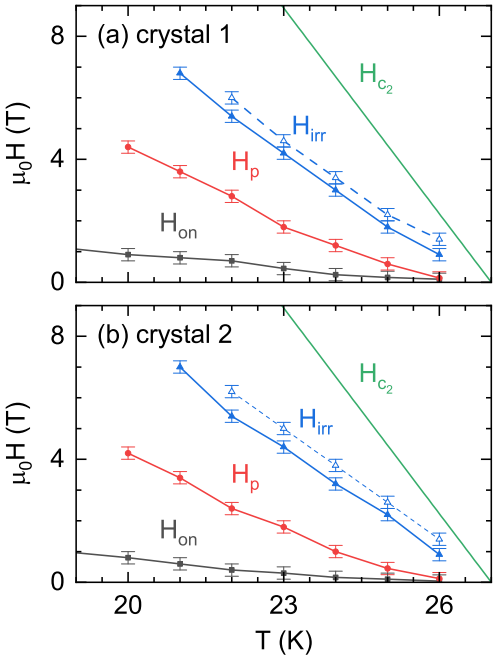

FIG. 8. $H-T$ vortex phase diagrams for (a) crystal 1 and (b) crystal 2. H_{on} and H_p are, respectively, the onset and the maximum of the SMP before sandblasting. H_{irr} is the irreversibility field before (solid line) and after (dashed line) sandblasting. H_{c2} is the upper critical field obtained from the data in Ref. 44.

was studied in high-quality single crystals of optimally-doped $BaFe_2(As_{1-x}P_x)_2$. The effect on the critical current was investigated by measuring isothermal $m(H)$ hysteresis cycles with H perpendicular to the etched surfaces (i.e., the ab layers of the crystals), before and after the sandblasting process. A significant increase in the amplitude of the hysteresis loops was observed for both samples and at all temperatures. From this increase, the non-dissipative surface current density K_c that the rough surface can sustain was estimated. K_c presents a temperature dependence qualitatively different from that of J_c, estimated from $m(H)$ cycles measured before sandblasting by using Bean's critical state model. However, K_c is in good agreement, in both the T and H dependence, with a theoretical estimate for intermediate fields based on Mathieu-Simon continuum theory for the mixed state. In addition, a slight increase of the irreversibility field $H_{irr}(T)$ was also observed after sandblasting. These findings suggest that surface treatments could be useful to complement the procedures to create bulk pinning, to further enhance the critical current of FeSC wires or tapes for electrical transport applications. Finally, our measurements revealed a sharp increase in $K_c(T)$ just before vanishing (the so called *peak effect*), which is not present in $J_c(T)$, suggesting that surface roughness is among the causes that promote its appearance.

ACKNOWLEDGMENTS

This work was supported by the Agencia Estatal de Investigación (AEI) through project PID2019-104296GB-I00. I.F. Llovo acknowledges financial support from Xunta de Galicia through grant ED481A-2020/149. H. Q. Luo is supported by the National Key Research and Development Program of China (Grant No. 2018YFA0704200), the Strategic Priority Research Program (B) of the CAS (Grants Nos. XDB25000000), and the Youth Innovation Promotion Association of CAS (Grant No. Y202001). The research at HangZhou Normal University is supported by the Open Project of Guangdong Provincial Key Laboratory of Magnetoelectric Physics and Devices (Grant No. 2022B1212010008), Startup Project of HangZhou Normal University (Grant No. 2020QDL026) and Natural Science Foundation of Zhejiang Province (Grant No. LY22A040009). Authors would like to thank the use of RIAIDT-USC analytical facilities.

* j.mosqueira@usc.es

[1] Y. Kamihara, T. Watanabe, M. Hirano, and H. Hosono, "Iron-based layered superconductor La[$O_{1-x}F_x$]FeAs ($x = 0.05 - 0.12$) with $t_c = 26$ K," J. Am. Chem. Soc. **130**, 3296–3297 (2008), pMID: 18293989, https://doi.org/10.1021/ja800073m.

[2] David C. Johnston, "The puzzle of high temperature superconductivity in layered iron pnictides and chalcogenides," Adv. Phys. **59**, 803–1061 (2010), https://doi.org/10.1080/00018732.2010.513480.

[3] G. R. Stewart, "Superconductivity in iron compounds," Rev. Mod. Phys. **83**, 1589–1652 (2011).

[4] Kenji Ishida, Yusuke Nakai, and Hideo Hosono, "To what extent iron-pnictide new superconductors have been clarified: A progress report," J. Phys. Soc. Jpn. **78**, 062001 (2009), https://doi.org/10.1143/JPSJ.78.062001.

[5] Fa Wang and Dung-Hai Lee, "The electron-pairing mechanism of iron-based superconductors," Science **332**, 200–204 (2011), https://www.science.org/doi/pdf/10.1126/science.1200182.

[6] R I Rey, A Ramos-Álvarez, J Mosqueira, S Salem-Sugui Jr., A D Alvarenga, H-Q Luo, X-Y Lu, R Zhang, and F Vidal, "Direct measurement of the temperature dependence of the magnetic penetration depth in $Ba(Fe_{1-x}Ni_x)_2As_2$ superconductors," Supercond. Sci. Technol. **27**, 055015 (2014).

[7] Ilaria Pallecchi, Federico Caglieris, and Marina Putti, "Thermoelectric properties of iron-based superconductors and parent compounds," Supercond. Sci. Technol. **29**, 073002 (2016).

[8] E. G. Maksimov, A. E. Karakozov, B. P. Gorshunov, A. S. Prokhorov, A. A. Voronkov, E. S. Zhukova, V. S. Nozdrin, S. S. Zhukov, D. Wu, M. Dressel, S. Haindl, K. Iida, and B. Holzapfel, "Two-band Bardeen-Cooper-Schrieffer superconducting state of the iron pnictide compound $Ba(Fe_{0.9}Co_{0.1})_2As_2$," Phys. Rev. B **83**, 140502 (2011).

[9] F. Hardy, T. Wolf, R. A. Fisher, R. Eder, P. Schweiss, P. Adelmann, H. v. Löhneysen, and C. Meingast, "Calorimetric evidence of multiband superconductivity in $Ba(Fe_{0.925}Co_{0.075})_2As_2$ single crystals," Phys. Rev. B **81**, 060501 (2010).

[10] F. Hunte, J. Jaroszynski, A. Gurevich, D. C. Larbalestier, R. Jin, A. S. Sefat, M. A. McGuire, B. C. Sales, D. K. Christen, and D. Mandrus, "Two-band superconductivity in $LaFeAsO_{0.89}F_{0.11}$ at very high magnetic fields," Nature **453**, 903–905 (2008).

[11] A. Gurevich, "Iron-based superconductors at high magnetic fields," Rep. Prog. Phys. **74**, 124501 (2011).

[12] Xiangzhuo Xing, Wei Zhou, Jinhua Wang, Zengwei Zhu, Yufeng Zhang, Nan Zhou, Bin Qian, Xiaofeng Xu, and Zhixiang Shi, "Two-band and Pauli-limiting effects on the upper critical field of 112-type iron pnictide superconductors," Sci. Rep. **7**, 45943 (2017).

[13] I. F. Llovo, C. Carballeira, D. Sóñora, A. Pereiro, J. J. Ponte, S. Salem-Sugui, A. S. Sefat, and J. Mosqueira, "Multiband effects on the upper critical field angular dependence of 122-family iron pnictide superconductors," Sci. Rep. **11**, 11526 (2021).

[14] Masashi Miura, Boris Maiorov, Takeharu Kato, Takashi Shimode, Keisuke Wada, Seiji Adachi, and Keiichi Tanabe, "Strongly enhanced flux pinning in one-step deposition of $BaFe_2(As_{0.66}P_{0.33})_2$ superconductor films with uniformly dispersed $BaZrO_3$ nanoparticles," Nat. Commun. **4**, 2499 (2013).

[15] Shigeyuki Ishida, Dongjoon Song, Hiraku Ogino, Akira Iyo, Hiroshi Eisaki, Masamichi Nakajima, Jun-ichi Shimoyama, and Michael Eisterer, "Doping-dependent critical current properties in K, Co, and P-doped $BaFe_2As_2$ single crystals," Phys. Rev. B **95**, 014517 (2017).

[16] Shyam Mohan, Toshihiro Taen, Hidenori Yagyuda, Yasuyuki Nakajima, Tsuyoshi Tamegai, Takayoshi Katase, Hidenori Hiramatsu, and Hideo Hosono, "Transport and magnetic properties of Co-doped $BaFe_2As_2$ epitaxial thin films grown on MgO substrate," Supercond. Sci. Technol. **23**, 105016 (2010).

[17] Masahito Sakoda, Kazumasa Iida, and Michio Naito, "Recent progress in thin-film growth of Fe-based superconductors: superior superconductivity achieved by thin films," Supercond. Sci. Technol. **31**, 093001 (2018).

[18] E F Talantsev, "Evaluation of a practical level of critical current densities in pnictides and recently discovered superconductors," Supercond. Sci. Technol. **32**, 084007 (2019).

[19] Takayoshi Katase, Yoshihiro Ishimaru, Akira Tsukamoto, Hidenori Hiramatsu, Toshio Kamiya, Keiichi Tanabe, and Hideo Hosono, "Advantageous grain boundaries in iron pnictide superconductors," Nat. Commun. **2**, 409 (2011).

[20] Chao Yao and Yanwei Ma, "Recent breakthrough development in iron-based superconducting wires for practical applications," Supercond. Sci. Technol. **32**, 023002 (2019).

[21] Sunseng Pyon, Daisuke Miyawaki, Tsuyoshi Tamegai, Satoshi Awaji, Hijiri Kito, Shigeyuki Ishida, and Yoshiyuki Yoshida, "Enhancement of critical current density in $(Ba,Na)Fe_2As_2$ round wires using high-pressure sintering," Supercond. Sci. and Technol. **33**, 065001 (2020).

[22] J D Weiss, A Yamamoto, A A Polyanskii, R B Richardson, D C Larbalestier, and E E Hellstrom, "Demonstration of an iron-pnictide bulk superconducting magnet capable of trapping over 1 T," Supercond. Sci. Technol. **28**, 112001 (2015).

[23] Hideo Hosono, Akiyasu Yamamoto, Hidenori Hiramatsu, and Yanwei Ma, "Recent advances in iron-based superconductors toward applications," Materials Today **21**, 278–302 (2018).

[24] M Eisterer, "Radiation effects on iron-based superconductors," Supercond. Sci. Technol. **31**, 013001 (2017).

[25] B. Maiorov, T. Katase, I. O. Usov, M. Weigand, L. Civale, H. Hiramatsu, and H. Hosono, "Competition and cooperation of pinning by extrinsic point-like defects and intrinsic strong columnar defects in $BaFe_2As_2$ thin films," Phys. Rev. B **86**, 094513 (2012).

[26] Toshihiro Taen, Yasuyuki Nakajima, Tsuyoshi Tamegai, and Hisashi Kitamura, "Enhancement of critical current density and vortex activation energy in proton-irradiated Co-doped $BaFe_2As_2$," Phys. Rev. B **86**, 094527 (2012).

[27] Y. Nakajima, Y. Tsuchiya, T. Taen, H. Yagyuda, T. Tamegai, S. Okayasu, M. Sasase, H. Kitamura, and T. Murakami, "Critical current densities and flux creep rate in Co-doped $BaFe_2As_2$ with columnar defects introduced by heavy-ion irradiation," Phys. C: Supercond. Appl. **470**, 1103–1105 (2010), proceedings of the 22nd In-

ternational Symposium on Superconductivity (ISS 2009).
[28] Edmund Soji Otabe, Kazuaki Myose, Kohji Murakami, Masaru Kiuchi, Teruo Matsushita, Jun Ge, Baorong Ni, Yasuyuki Nakajima, and Tsuyoshi Tamegai, "Condensation energy density properties of Ba-122 pnictide superconductor with columnar defects introduced by heavy-ion irradiation," Phys. Procedia **36**, 693–697 (2012), sUPERCONDUCTIVITY CENTENNIAL Conference 2011.
[29] C. Tarantini, S. Lee, F. Kametani, J. Jiang, J. D. Weiss, J. Jaroszynski, C. M. Folkman, E. E. Hellstrom, C. B. Eom, and D. C. Larbalestier, "Artificial and self-assembled vortex-pinning centers in superconducting $Ba(Fe_{1-x}Co_x)_2As_2$ thin films as a route to obtaining very high critical-current densities," Phys. Rev. B **86**, 214504 (2012).
[30] S. Lee, C. Tarantini, P. Gao, J. Jiang, J. D. Weiss, F. Kametani, C. M. Folkman, Y. Zhang, X. Q. Pan, E. E. Hellstrom, D. C. Larbalestier, and C. B. Eom, "Artificially engineered superlattices of pnictide superconductors," Nat. Mater. **12**, 392–396 (2013).
[31] G. Lazard, P. Mathieu, B. Plaçais, J. Mosqueira, Y. Simon, C. Guilpin, and G. Vacquier, "Critical currents in the anisotropic superconductor $2H-NbSe_2$: evidence for an upper bound of the surface critical-current density," Phys. Rev. B **65**, 064518 (2002).
[32] Muhamad Aburas, Alain Pautrat, and Natalia Bellido, "Change of surface critical current in the surface superconductivity and mixed states of superconducting niobium," Supercond. Sci. Technol. **30**, 015009 (2016).
[33] S. Casalbuoni, E.A. Knabbe, J. Kötzler, L. Lilje, L. von Sawilski, P. Schmüser, and B. Steffen, "Surface superconductivity in niobium for superconducting RF cavities," Nucl. Instrum. Methods Phys. Res. **538**, 45–64 (2005).
[34] Z-H Sung, A Dzyuba, P J Lee, D C Larbalestier, and L D Cooley, "Evidence of incomplete annealing at 800 °C and the effects of 120 °C baking on the crystal orientation and the surface superconducting properties of cold-worked and chemically polished Nb," Supercond. Sci. Technol. **28**, 075003 (2015).
[35] A. Cubero, E. Martínez, L.A. Angurel, G.F. de la Fuente, R. Navarro, H. Legall, J. Krüger, and J. Bonse, "Effects of laser-induced periodic surface structures on the superconducting properties of niobium," Appl. Surf. Sci. **508**, 145140 (2020).
[36] A. Cubero, E. Martínez, L.A. Angurel, G.F. de la Fuente, R. Navarro, H. Legall, J. Krüger, and J. Bonse, "Surface superconductivity changes of niobium sheets by femtosecond laser-induced periodic nanostructures," Nanomaterials **10**, 2525 (2020).
[37] Masamichi Nakajima, Shin-ichi Uchida, Kunihiro Kihou, Chul-Ho Lee, Akira Iyo, and Hiroshi Eisaki, "Growth of BaFe2$(As_{1-x}P_x)_2$ single crystals ($0 \leq x \leq 1$) by Ba_2As_3/Ba_2P_3-flux method," J. Phys. Soc. Jpn. **81**, 104710 (2012), https://doi.org/10.1143/JPSJ.81.104710.
[38] Ding Hu, Xingye Lu, Wenliang Zhang, Huiqian Luo, Shiliang Li, Peipei Wang, Genfu Chen, Fei Han, Shree R. Banjara, A. Sapkota, A. Kreyssig, A. I. Goldman, Z. Yamani, Christof Niedermayer, Markos Skoulatos, Robert Georgii, T. Keller, Pengshuai Wang, Weiqiang Yu, and Pengcheng Dai, "Structural and magnetic phase transitions near optimal superconductivity in $BaFe_2(As_{1-x}P_x)_2$," Phys. Rev. Lett. **114**, 157002 (2015).
[39] A. Ramos-Álvarez, J. Mosqueira, F. Vidal, Ding Hu, Genfu Chen, Huiqian Luo, and Shiliang Li, "Superconducting fluctuations in isovalently substituted $BaFe_2(As_{1-x}P_x)_2$: Possible observation of multiband effects," Phys. Rev. B **92**, 094508 (2015).
[40] P. Mathieu and Y. Simon, "Phenomenological theory of vortex motion in type-II superconductors," Europhys. Lett. **5**, 67 (1988).
[41] Shuai Jiang, Hui Xing, Guofang Xuan, Cao Wang, Zhi Ren, Chunmu Feng, Jianhui Dai, Zhu'an Xu, and Guanghan Cao, "Superconductivity up to 30 k in the vicinity of the quantum critical point in $BaFe_2(As_{1-x}P_x)_2$," J. Phys. Condens. Matt. **21**, 382203 (2009).
[42] Swee K. Goh, Y. Nakai, K. Ishida, L. E. Klintberg, Y. Ihara, S. Kasahara, T. Shibauchi, Y. Matsuda, and T. Terashima, "Anisotropic superconducting properties of optimally doped $BaFe_2(As_{0.65}P_{0.35})_2$ under pressure," Phys. Rev. B **82**, 094502 (2010).
[43] M. Ishikado, K. Kodama, R. Kajimoto, M. Nakamura, Y. Inamura, S. Wakimoto, A. Iyo, H. Eisaki, M. Arai, and S. Shamoto, "Inelastic neutron scattering on iron-based superconductor $BaFe_2(As,P)_2$," Physica C Supercond. **471**, 643–646 (2011), the 23rd International Symposium on Superconductivity.
[44] C. Chaparro, L. Fang, H. Claus, A. Rydh, G. W. Crabtree, V. Stanev, W. K. Kwok, and U. Welp, "Doping dependence of the specific heat of single-crystal $BaFe_2(As_{1-x}P_x)_2$," Phys. Rev. B **85**, 184525 (2012).
[45] S Salem-Sugui Jr, J Mosqueira, A D Alvarenga, D Sóñora, E P Herculano, Ding Hu, Genfu Chen, and Huiqian Luo, "Observation of an anomalous peak in isofield M(T) curves in $BaFe_2(As_{0.68}P_{0.32})_2$ suggesting a phase transition in the irreversible regime," Superconductor Science and Technology **28**, 055017 (2015).
[46] S Salem-Sugui, J Mosqueira, A D Alvarenga, D Sóñora, A Crisan, A M Ionescu, S Sundar, D Hu, S-L Li, and H-Q Luo, "Vortex–glass state in the isovalent optimally doped pnictide superconductor $BaFe_2(As_{0.68}P_{0.32})_2$," Supercond. Sci. Technol. **30**, 055003 (2017).
[47] C. P. Bean, "Magnetization of hard superconductors," Phys. Rev. Lett. **8**, 250–253 (1962).
[48] CHARLES P. BEAN, "Magnetization of high-field superconductors," Rev. Mod. Phys. **36**, 31–39 (1964).
[49] C. P. Poole Jr., H. A. Farach, R. J. Creswick, and R. Prozorov, Superconductivity, 2nd Edition (Academic Press, London, 2007).
[50] S. Bhattacharya and M. J. Higgins, "Peak effect and anomalous flow behavior of a flux-line lattice," Phys. Rev. B **49**, 10005–10008 (1994).
[51] Z. L. Xiao, E. Y. Andrei, P. Shuk, and M. Greenblatt, "Equilibration and dynamic phase transitions of a driven vortex lattice," Phys. Rev. Lett. **85**, 3265–3268 (2000).
[52] W. K. Kwok, J. A. Fendrich, C. J. van der Beek, and G. W. Crabtree, "Peak effect as a precursor to vortex lattice melting in single crystal $YBa_2Cu_3O_{7-\delta}$," Phys. Rev. Lett. **73**, 2614–2617 (1994).
[53] X. B. Xu, H. Fangohr, X. N. Xu, M. Gu, Z. H. Wang, S. M. Ji, S. Y. Ding, D. Q. Shi, and S. X. Dou, "Peak effect in the critical current of type II superconductors with strong magnetic vortex pinning," Phys. Rev. Lett. **101**, 147002 (2008).
[54] V. G. Kogan, M. M. Fang, and Sreeparna Mitra, "Reversible magnetization of high-T_c materials in intermediate fields," Phys. Rev. B **38**, 11958–11961 (1988).

[55] S. Salem-Sugui, L. Ghivelder, A. D. Alvarenga, J. L. Pimentel, Huiqian Luo, Zhaosheng Wang, and Hai-Hu Wen, "Superconducting fluctuations in the reversible magnetization of the iron-pnictide $Ba_{1-x}K_xFe_2As_2$," Phys. Rev. B **80**, 014518 (2009).

[56] J. Mosqueira, J. D. Dancausa, F. Vidal, S. Salem-Sugui, A. D. Alvarenga, H.-Q. Luo, Z.-S. Wang, and H.-H. Wen, "Observation of anisotropic diamagnetism above the superconducting transition in iron pnictide $Ba_{1-x}K_xFe_2As_2$ single crystals due to thermodynamic fluctuations," Phys. Rev. B **83**, 094519 (2011).

[57] R I Rey, C Carballeira, J Mosqueira, S Salem-Sugui Jr, A D Alvarenga, H-Q Luo, X-Y Lu, Y-C Chen, and F Vidal, "Measurements of the fluctuation-induced in-plane magnetoconductivity at high reduced temperatures and magnetic fields in the iron arsenide $BaFe_{2-x}Ni_xAs_2$," Supercond. Sci. Technol. **26**, 055004 (2013).

[58] R I Rey, A Ramos-Álvarez, C Carballeira, J Mosqueira, F Vidal, S Salem-Sugui, A D Alvarenga, Rui Zhang, and Huiqian Luo, "Measurements of the superconducting fluctuations in optimally doped $BaFe_{2-x}Ni_xAs_2$ under high magnetic fields: probing the 3D-anisotropic Ginzburg–Landau approach," Supercond. Sci. Technol. **27**, 075001 (2014).

Chapter 3

Fluctuations vs percolation in cuprate superconductors

The following articles are part of this chapter:

- I. F. Llovo, J. Mosqueira, C. Carballeira and F. Vidal. Precursor superconducting effects in the optimally doped $YBa_2Cu_3O_{7-\delta}$ superconductor: the confrontation between superconducting fluctuations and percolative effects revisited. *SN Appl. Sci.*, **4**, 110 (2022) dx.doi.org/10.1007/s42452-022-04995-0.
- I. F. Llovo, J. Mosqueira and F. Vidal. On the dilemma between percolation processes and fluctuating pairs as the origin of the enhanced conductivity above the superconducting transition in cuprates. *Supercond. Sci. Technol.*, **36**, 125004 (2023) dx.doi.org/10.1088/1361-6668/acff8a.

The rounding of the superconducting transition above T_c has been a prolific source of scientific literature. So, with the advent of cuprate superconductors, the debate between emergent percolative processes and superconducting fluctuations was extended to these materials. Bednorz and Müller discussed in their 1986 seminal work that the resistivity decrease observed above but near T_c in Ba-La-Cu-O *results partially from the percolative nature, but possibly also from 2D superconducting fluctuations of double perovskite layers of one of the phases present.* [25] However, in an early study using effective medium theory (EMT) calculations on the dc in-plane resistivity of optimally doped $YBa_2Cu_3O_{7-\delta}$ (YBCO) by Maza and Vidal, [85–87] the possible presence of emergent percolative processes was shown to play a negligible role in the measured paraconductivity, and instead they attributed the rounding in the so-called mean field region to the thermodynamically necessary thermal fluctuations, which for laminar materials (such as cuprate superconductors) had been calculated by Lawrence and Doniach (LD) in the Gaussian-Ginzburg-Landau (GGL) scenario. [169, 170] Since these early results, multiple authors have discussed if emergent percolative processes, caused by intrinsic inhomogeneities, could be the only source of rounding in cuprate superconductors, [71–73] while other authors have studied scenarios in which both fluctuations and percolation may be present. [171–173] Nevertheless, multiple studies have found that, in certain scenarios, thermal fluctuations alone can produce sufficient increased conductivity to explain the data. [75–84]

In the two articles that are part of this Chapter, we show that the observed $\rho_{ab}(T)$ rounding around T_c in optimally doped cuprates can can be accounted for by the thermodynamically necessary superconducting fluctuations up to the very temperature onset of the paraconductivity T_{onset}, where the conductivity begins to increase from the normal state contribution. To explain these data, we have used an extension of the LD model which includes a total energy cutoff in the fluctuation modes, to adequately consider the contribution of short wavelength fluctuating modes. [174–178] Specifically, in the first article of this Chapter, *Precursor superconducting effects in the optimally doped $YBa_2Cu_3O_{7-\delta}$ superconductor: the confrontation between superconducting fluctuations and percolative effects revisited*, we focused our analysis on a prototypical cuprate, an optimally doped YBCO film. This material shows high interlayer coupling and is well described by the LD model. In the second article, *On the dilemma between percolation processes and fluctuating pairs as the origin of the enhanced conductivity above the superconducting transition in cuprates*, we instead focus on high quality crystals and films of the more anisotropic (hence, less coupled) $La_{2-x}Sr_xCuO_4$, $Bi_2Sr_2CaCu_2O_{8+\delta}$ and $Tl_2Ba_2Ca_2Cu_3O_{10}$. Our analyses show the poor adequacy of percolative effects to describe the paraconductivity in optimally doped cuprates, and that even though these effects may exist in more inhomogeneous samples, they are nevertheless small compared to the rounding caused by superconducting fluctuations. To reinforce this point, in the second article we added data from a recent proposal which supported a percolative-only scenario as the source of paraconductivity in underdoped cuprates to our analysis. [74] We have shown that these data can be successfully explained with the same fluctuation

models which explain optimally doped compounds, when the total energy cutoff is included. Additionally, we have also shown that the alleged *universal* behavior reported by these authors does not hold true when other samples are included to the comparison with their percolative model.

Our analyses demonstrate that with the addition of a total energy cutoff to the GGL fluctuation models, their predictability is extended up to temperatures close to T_{onset}, and that the interlayer coupling between *ab* layers determines the amplitude of the fluctuations through the effective interlayer distance d_{eff}, defined as the crystal c-axis periodicity length divided by the number of CuO_2 layers which are part of that length. [80, 170, 176, 179–187]

Research Article

Precursor superconducting effects in the optimally doped $YBa_2Cu_3O_{7-\delta}$ superconductor: the confrontation between superconducting fluctuations and percolative effects revisited

I. F. Llovo[1,2] · J. Mosqueira[1,2] · C. Carballeira[1] · F. Vidal[1]

Received: 22 December 2021 / Accepted: 25 February 2022
Published online: 22 March 2022

Abstract
The confrontation between the superconducting fluctuations and percolation effects as the origin of the in-plane paraconductivity in cuprate superconductors was earlier addressed at a quantitative level in the case of the optimally doped $YBa_2Cu_3O_{7-\delta}$ (YBCO) compound. Using in-plane resistivity data from a high-quality YBCO thin film, we will extend these analyses to high reduced temperatures, in the case of the Gaussian-Ginzburg–Landau (GGL) approach for the conventional superconducting fluctuations, by considering the total energy cutoff. These data will also be analysed in terms of the mean field-approach of the effective-medium theory, to probe if emergent percolative effects may account for the resistivity rounding above T_c. Our analyses confirm earlier conclusions: the measured paraconductivity cannot be explained in terms of emergent percolation processes, but it may be accounted for in terms of the GGL approach. These results also call into question alternative scenarios, including a recent proposal derived from emergent percolative effects.

Keywords Superconductivity · Cuprates · Fluctuation · Percolation

1 Introduction

The dilemma between percolation processes and superconducting fluctuations to account for the electrical resistivity rounding observed above but near the critical temperature T_c in cuprate superconductors was already posed by Bednorz and Müller in their seminal work [1]. This dilemma was addressed at a quantitative level in Ref. [2] by studying the dc in-plane resistivity $\rho_{ab}(T)$ of the prototypical optimally doped $YBa_2Cu_3O_{7-\delta}$ (YBCO) superconductor. By using the simplest version of the mean field-approach of the effective-medium theory (EMT) [3], the possible presence of emergent percolative processes was shown to play a negligible role in the measured paraconductivity. In contrast, the rounding could be explained in the so-called mean field region by considering the unavoidable presence of the superconducting fluctuations [2], using the Lawrence–Doniach (LD) approach for layered superconductors of the Gaussian-Ginzburg–Landau (GGL) scenario [4].

Despite the earlier confrontation commented above (see also Refs. [5–7]), the dilemma between superconducting fluctuations and emergent percolation mechanisms to explain the measured paraconductivity in cuprate superconductors is still far from being closed [8–18]. In this paper, previous measurements obtained in high-quality YBCO thin films will be analysed, by comparing the paraconductivity data with conventional superconducting fluctuation models, extended to higher reduced temperatures $\varepsilon = \log\left(T/T_c\right)$ with the inclusion of a total energy cutoff

✉ I. F. Llovo, iagof.llovo@usc.es | [1]QMatterPhotonics, Departamento de Física de Partículas, Universidade de Santiago de Compostela, 15782 Santiago de Compostela, Spain. [2]iMATUS, Universidade de Santiago de Compostela, 15706 Santiago de Compostela, Spain.

in the energy spectrum to account for the high-energy fluctuating modes [19, 20]. Complementarily, in order to probe if emergent percolative effects may account for the resistivity rounding above T_c, the data will be analysed in terms of the EMT approach used in Ref. [2], extended now up to the resistivity rounding onset ($T_{onset} \approx 150$ K), determined as the temperature above which ρ(T) follows the normal-state linear behaviour within the noise level.

Our findings evidence that the GGL approach can account for the sudden decrease that paraconductivity experiences at high ε (for $\varepsilon \gtrsim 0.1$). However, the EMT approach fails to qualitatively explain our data when percolation is considered as the sole cause of paraconductivity. Our results are in stark contrast with recent proposals that postulate emergent percolation as the sole cause of rounding above T_c in underdoped compounds [14].

2 2. Theoretical background

2.1 Conventional superconducting fluctuations: Lawrence–Doniach model with a total energy cutoff

Fluctuation effects in superconductors induce the creation of evanescent Cooper pairs above the superconducting transition temperature, which have a measurable effect in different observables. For instance, a progressive decrease of the resistivity is manifested as the temperature approaches T_c from above. In low-T_c superconductors, such a decrease is negligible. In contrast, the small amplitude of the superconducting coherence length in cuprate superconductors (about 1 nm) enhances fluctuation effects, and the change in the resistivity just above T_c is notable (~ 20% the normal-state resistivity 1 K above T_c). The fluctuation-induced electrical conductivity, defined as $\Delta\sigma \equiv \sigma - \sigma_B$ where σ_B is the background (normal-state) contribution, can be calculated in the framework of the Lawrence–Doniach model of Josephson coupled superconducting layers. Previous calculations in the framework of the GGL approach for conventional superconducting fluctuations have shown that a so-called total-energy cutoff is required to explain the high reduced temperature paraconductivity data when the high energy modes are considered [19, 20]. For layered materials with strong inter-layer coupling, for which the Lawrence–Doniach (LD) approximation is applicable, the paraconductivity is given by [19],

$$\Delta\sigma^{LD} = \frac{e^2}{16\hbar d_{eff}}\left[\frac{1}{\varepsilon}\left(1+\frac{B_{LD}}{\varepsilon}\right)^{-\frac{1}{2}} - \frac{1}{\varepsilon^c}\left(1+\frac{B_{LD}}{\varepsilon^c}\right)^{-\frac{1}{2}}\right], \quad (1)$$

where d_{eff} is the *effective* interlayer distance, calculated as the layer periodicity length d divided by the number of layers per periodicity length; $B_{LD} = \left[2\xi_c(0)/d\right]^2$ is the Lawrence–Doniach dimensionality parameter, where $\xi_c(0)$ is the coherence length at $T = 0$ K; and ε^c is the total-energy cutoff parameter, which represents the reduced temperature at which the fluctuations vanish (i.e., the fully normal behaviour is recovered). When $\varepsilon^c \to \infty$, the well-known Lawrence–Doniach result is obtained [4].

2.2 Effective-medium approach for the percolative scenario

As it is well known, the presence of T_c inhomogeneities can significantly alter the properties of cuprate superconductors [21, 22]. The effect of a continuous T_c distribution on the resistivity can be studied through the approach proposed in Ref. [2], which is based on Bruggeman's effective medium theory [3]. This approach assumes that the sample consists of domains (of larger dimensions than the superconducting coherence length amplitude) with T_c values following a Gaussian distribution $G(T_c)$, characterized by its average critical temperature $\overline{T_c}$, and its full width at half-maximum (FWHM) ΔT_c. The electrical conductivity of each domain is assumed to be $\sigma(T, T_c) \to \infty$ if $T < T_c$, and $\sigma = \sigma_B$ when $T > T_c$, where σ_B is the background conductivity, obtained by linear extrapolation from the strange metal region of the normal state. The *effective electrical conductivity* σ^e can be then obtained by numerically solving

$$\int_0^\infty \frac{\sigma(T,T_c) - \sigma^e(T)}{\sigma(T,T_c) + 2\sigma^e(T)} G(T_c)\mathrm{d}T_c = 0. \quad (2)$$

3 Analysis

As commented in the introduction, the resistivity data obtained on an optimally doped $YBa_2Cu_3O_{7-\delta}$ (YBCO) thin film, previously reported in Ref. [19], will be analysed. These data are shown in Fig. 1. Details of the thin film growth, characterization, and measuring process are summarized in Ref. [19]. Let us just mention that T_c is 91.1 K, and the transition width is as small as 0.6 K. The normal-state in-plane resistivity ratio $\rho(300\text{K})/\rho(100\text{K})$ is about 3.1, and the extrapolation to $T = 0$ K leads to a small residual value. These results are consistent with previous measurements in high-quality optimally doped YBCO obtained by other groups [23–34].

The resistivity rounding above but near T_c can be clearly observed in Fig. 1. The associated excess electrical

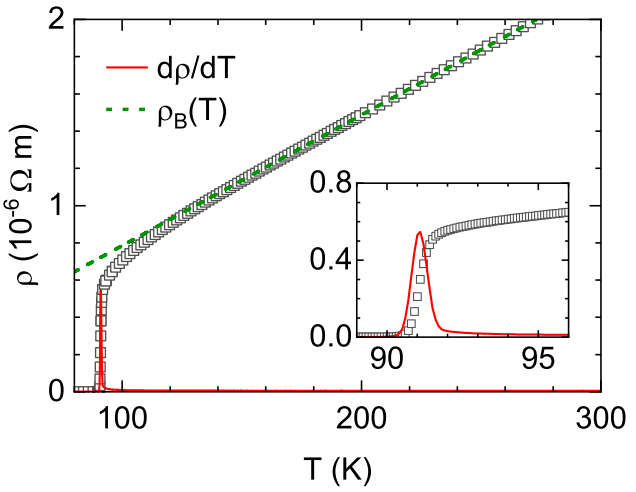

Fig. 1 In-plane resistivity data $\rho_{ab}(T)$ (black squares) used for the analyses in this work, corresponding to measurements of Ref. [19] in a high quality, optimally doped YBCO thin film. The normal state background resistivity $\rho_B(T)$ (dashed green line) was estimated by using a linear fit of the data between 200 and 250 K (2.2–2.7 T_c), well into the strange metal regime of the normal state (i.e., above $T_{onset} \approx 1.7T_c$). A sharp superconducting transition occurs at $T = 91.1$K, with FWHM $\Delta T_c = 0.6$ K, as evidenced by the derivative of data (solid red line), also shown in the inset. See Ref. [19] for more details

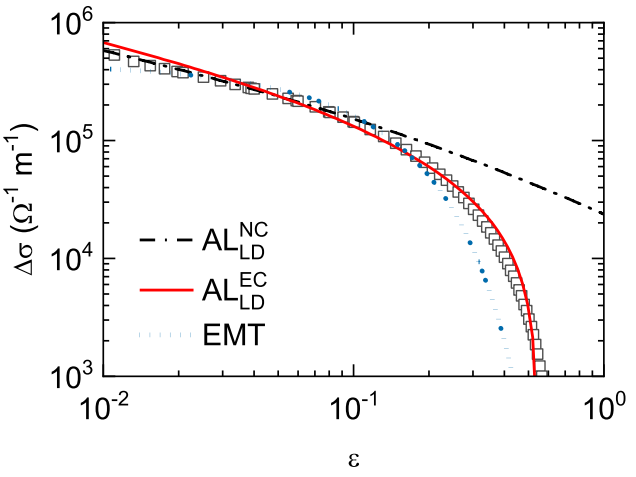

Fig. 2 Excess conductivity data (black squares) compared with LD and EMT approaches: In the case of the LD approach, B_{LD} is the only free parameter. The solid red line was obtained by imposing $\varepsilon^c = 0.55$ in Eq. (2), as predicted in Ref. [20], and leads to $B_{LD} = 0.15$, whereas the dot-dashed black line was obtained without a cutoff (imposing $\varepsilon^c \to \infty$ in Eq. (2)) and leads to $B_{LD} = 0.19$. The best fit to the EMT approach, with both $\overline{T_c}$ and ΔT_c as free parameters, is shown as a dotted blue line. While the LD approach with total energy cutoff for the superconducting fluctuation scenario successfully explains the measurements, the EMT approach for the percolative scenario cannot even qualitatively account for our data, mainly in the high reduced temperature region

conductivity, defined as $\Delta\sigma = \sigma - \sigma_B$, is plotted in Fig. 2 against the reduced temperature $\varepsilon = \log\left(T/T_c\right)$ in a convenient log–log scale. The dotted blue line is the best fit of Eq. (2) to the data, in the accessible ε range (0.01–0.6), with $\overline{T_c}$ and ΔT_c as free parameters. This leads to $\overline{T_c} = 55.4 \pm 0.8K$ and $\Delta T_c = 57.7 \pm 1.1K$. This fit does not reproduce the observed ε-dependence of $\Delta\sigma$, particularly in the high ε range ($\varepsilon \gtrsim 0.1$). Moreover, the resulting T_c distribution is anomalously wide and inconsistent with the experimental data. This can be better observed in Fig. 3, where the temperatures at which the percolation fraction would be attained (between $p_c \sim 0.15$ and 0.30 [14, 35]) are substantially below the temperature at which $\rho = 0$ is observed. A similar analysis was performed with 2D EMT [3], to explore if the anisotropic nature of these materials could have an influence in the distribution $G\left(\overline{T_c}, \Delta T_c\right)$ and in the percolation thresholds. However, the differences are absorbed by the free parameters, obtaining equally bad fits to our data. The corresponding T_c distribution obtained from the best fit to 2D EMT is also anomalously wide: $\overline{T_c} = 63.5 \pm 0.6$K and $\Delta T_c = 54.2 \pm 1.0$K.

Additionally, a comparison with the Lawrence–Doniach model, summarized in 2.1, is also included in Fig. 2 (solid red line). The description of this analysis was already presented in Ref. [19]. Let us just mention that the agreement with the experimental data is excellent in the accessible ε range, leaving the transverse coherence length amplitude $\xi_c(0)$ as the only free parameter, which results to be about 0.1 nm, as expected for optimally doped YBCO. Other parameters in Eq. (2), as T_c or the cutoff constant ε^c, were obtained from the resistive transition midpoint and from the temperature onset of the resistivity rounding, respectively. Finally, it is worth noting that the conventional LD model without a cutoff (dot-dashed black line), fails to describe the data at high reduced temperatures, where the contribution of high-energy fluctuation modes is relevant.

4 Conclusion

In this work, the earlier analyses of the possible contributions of emergent percolative effects to the rounding above T_c in optimally doped YBCO [2] have been extended to the high reduced temperature region. Our analysis was performed by comparing data from a high-quality thin film sample to both a percolative model using effective-medium theory (EMT), and the Gaussian-Ginzburg–Landau (GGL) approach for layered superconductors, with the inclusion of a total energy cutoff [19, 20]. We found that extreme T_c distributions are required to try to explain the data in the EMT scenario, as it was previously reported for underdoped compounds

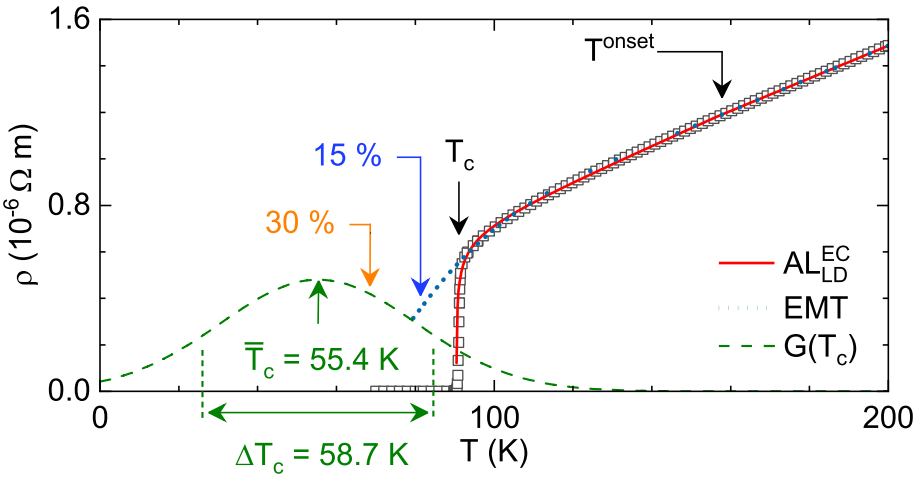

Fig. 3 Best fits of LD with total energy cutoff (solid red line) and EMT (dotted blue line) approaches to the in-plane resistivity $\rho_{ab}(T)$ data. The EMT scenario fails to faithfully represent the transition both close and far from T_c (see also Fig. 2). The curve representing the distribution $G(T_c)$ resulting from the best fit is shown for comparison ($\overline{T_c} = 55.4$K, $\Delta T_c = 57.7$K, dashed green line). As it can be seen, the T_c distributions that are required to try to explain the data are extremely wide, as previously reported for underdoped compounds [14]. However, the percolation fractions $p_c = 0.15$ and $p_c = 0.3$ [14, 35] that have been proposed for such percolative effects do not appear anywhere near T_c for optimally doped samples. Moreover, the existence of regions with T_c as high as 120K and all the way down to absolute zero, predicted for YBCO by this model, is not corroborated by previous magnetic transition measurements [19]

[14]. However, the optimally doped sample used in this paper has excellent stoichiometric homogeneity. Additionally, the percolation fraction predicted by EMT for this compound is substantially lower that the expected value $p_c \approx 0.15 - 0.3$ [14, 35]. More worryingly, the existence of regions with T_c as high as 120K and as low as absolute zero, which the EMT model requires, have not been observed in previous magnetic transition measurements. Therefore, the excess conductivity observed for optimally doped YBCO cannot be explained by effects of emergent percolation alone. Nevertheless, this result does not exclude that T_c distributions may play a role in the paraconductivity of heavily underdoped compounds, as stoichiometric homogeneity cannot be ensured for these compounds, and wider transitions are generally observed. On the other hand, the GGL phenomenological approach offers a much better fit of the data, when a total-energy cutoff is introduced to account for the high-energy fluctuating modes. This approach successfully accounts for the sudden decrease of paraconductivity at high ε. Our results provide quantitative confirmation of the earlier conclusions of Ref. [2], which are now extended to high reduced temperatures: conventional fluctuations alone can quantitatively account for the optimally doped YBCO paraconductivity data both close and far from T_c, and that the emergence of percolation must be a second order effect in the resistive rounding above T_c of samples of such stoichiometric quality.

Acknowledgements This work was supported by the Agencia Estatal de Investigación (AEI) and Fondo Europeo de Desarrollo Regional (FEDER) through project PID2019-104296GB-I00, and by Xunta de Galicia (grant GRC no. ED431C 2018/11). I.F. Llovo acknowledges financial support from Xunta de Galicia through grant ED481A-2020/149.

Author contributions FV and JM conceptualised the study. IFL and JM performed the data analyses. CC writing the manuscript. All authors read and approved the final manuscript.

Data availability Data will be made available on reasonable request.

Declarations

Conflict of interest On behalf of all authors, the corresponding author states that there is no conflict of interest.

Appendix: numerical methods The effective medium theory model was calculated with the self-consistent approach used in Ref. 2. In order to solve Eq. (2) for each temperature T, the integral was split in two terms,

$$\int_0^T G\left(\overline{T_c}, \Delta T_c\right) dT_c + \int_T^{\overline{T_c}+4\Delta T_c} \frac{\sigma\left(T, T_c\right) - \sigma^e(T)}{\sigma\left(T, T_c\right) + 2\sigma^e(T)} G\left(\overline{T_c}, \Delta T_c\right) dT_c = 0, \tag{3}$$

to avoid numerical divergences when $\sigma\left(T, T_c\right) \to \infty$. All the calculations were performed using Python *scipy* library. The integrals were solved by numerical quadrature integration. Equation (3) was numerically solved to obtain the values of σ^e for any given $\overline{T_c}$ and ΔT_c pair. The resulting curves were then minimized against the free parameters $\overline{T_c}$ and ΔT_c, to obtain the gaussian distribution $G\left(\overline{T_c}, \Delta T_c\right)$ with mean value $\overline{T_c}$ and full width at half maximum ΔT_c which best explains the data. The results of Eq. (3) were fit to the paraconductivity data obtained with the procedure described in Sect. 3.

References

1. Bednorz JG, Müller KA (1986) Possible high T_c superconductivity in the Ba–La–Cu–O system. Z Phys B 64:189. https://doi.org/10.1007/BF01303701
2. Maza J, Vidal F (1991) Critical-temperature inhomogeneities and resistivity rounding in copper oxide superconductors. Phys Rev B 43:10560. https://doi.org/10.1103/PhysRevB.43.10560
3. Landauer R (1978) Electrical conductivity in inhomogeneous media. In: Garland JC, Tanner DB (eds) Proceedings of the first conference on electrical transport and optical properties in inhomogeneous media. AIP conference proceedings Nº 40. AIP, New York, p 2. https://doi.org/10.1063/1.31150
4. Vidal F, Ramallo MV (1998) Multilayering effects on the thermal fluctuations of Cooper pairs around the superconducting transition in cuprates. In: Bok J et al (eds) The Gap symmetry and fluctuations in high-Tc superconductors NATO-ASI series. Plenum, New York, p 443. https://doi.org/10.1007/b114887
5. Lang W (1994) Influence of a distribution of critical temperatures on the paraconductivity and the fluctuation magnetoconductivity in high-temperature superconductors. Physica C 226:267. https://doi.org/10.1016/0921-4534(94)90205-4
6. Casaca A, Bonfait G, Leskens M, Muller G, Lander K, Edwears JA (1997) Model for the broadening of the resistive transition in YBa2Cu3O7-d thin films. Supercond Sci Technol 10:75. https://doi.org/10.1088/0953-2048/10/2/001
7. Ghosh AG, Bandyopadhyay SK, Basu AN (1999) Generalization of fluctuation induced conductivity in polycrystalline $Y_{1-x}Ca_xBa_2Cu_3O_y$ and $B1_2Sr_2Ca_1Cu_2O_{8+d}$ superconductors. J Appl Phys 86:3247. https://doi.org/10.1063/1.371197
8. Larkin AI, Varlamov AA (2005) Theory of fluctuations in superconductors. Clarendon, Oxford. https://doi.org/10.1093/acprof:oso/9780198528159.001.0001
9. Serbyn MN, Skvortsov MA, Varlamov AA, Galitski V (2009) Giant nernst effect due to fluctuating cooper pairs in superconductors. Phys Rev Lett 102:067001. https://doi.org/10.1103/PhysRevLett.102.067001
10. Alloul H, Rullier-Albenque F, Vignolle B, Colson D, Forget A (2010) Superconducting fluctuations, pseudogap and phase diagram in cuprate. Europhys Lett 91:37005. https://doi.org/10.1209/0295-5075/91/37005
11. Rullier-Albenque F, Alloul H, Rikken G (2011) High-field studies of superconducting fluctuations in high-T_c cuprates: evidence for a small gap distinct from the large pseudogap. Phys Rev B 84:014522. https://doi.org/10.1103/PhysRevB.84.014522(seealsoRef.14)
12. Ramallo MV, Carballeira C, Rey RI, Mosqueira J, Vidal F (2011) Comment on "High-field studies of superconducting fluctuations in high-T_c cuprates: evidence for a small gap distinct from the large pseudogap." Phys Rev B 85:106501. https://doi.org/10.1103/PhysRevB.85.106501
13. Grbić MS, Požek M, Paar D, Hinkov V, Raichle M, Haug D, Keimer B, Barišić N, Dulčić A (2011) Temperature range of superconducting fluctuations above T_c in $YBa_2Cu_3O_{7-\delta}$ single crystals. Phys Rev B 83:144508. https://doi.org/10.1103/PhysRevB.83.144508
14. Pelc D, Vuckovic M, Grbic MS, Pzek M, Yu G, Sasegawa T, Greven M, Barisic N (2018) Emergence of superconductivity in cuprates via a universal percolation process. Nat Commun 9:4327. https://doi.org/10.1038/s41467-018-06707-y
15. Caprara S (2019) The ancient romans' route to charge density waves in cuprates. Condens Matter 4(2):60. https://doi.org/10.3390/condmat4020060
16. Sóñora D, Mosqueira J, Vidal F (2020) Comment on "temperature range of superconducting fluctuations above T_c in $YBa_2Cu_3O_{7-\delta}$ single crystals." Phys Rev B 102:176501. https://doi.org/10.1103/PhysRevB.102.176501
17. Wahlberg E et al (2021) Restored strange metal phase through suppression of charge density waves in underdoped $YBa_2Cu_3O_{7-\delta}$. Science 373:6562. https://doi.org/10.1126/science.abc8372
18. Borna AS, Islam RS, Naqib SH (2021) Hole content dependent fluctuation diamagnetism in $YBa_2Cu_3O_{7-d}$: possible role of the pseudogap. J Supercond Nov Magn. https://doi.org/10.1007/s10948-021-06035-1
19. Rey RI, Carballeira C, Doval JM, Mosqueira J, Ramallo MV, Ramos-Álvarez A, Sóñora D, Veira JA, Verde JC, Vidal F (2019) The conductivity and the magnetization around T_c in optimally-doped $YBa_2Cu_3O_{7-\delta}$ revisited: quantitative analysis in terms of fluctuating superconducting pairs. Supercond Sci Technol 32:045009. https://doi.org/10.1088/1361-6668/aafe93
20. Vidal F, Carballeira C, Curras SR, Mosqueira J, Ramallo MV, Veira JA, Viña J (2002) On the consequences of the uncertainty principle on the superconducting fluctuations well inside the normal state. Europhys Lett 59:754. https://doi.org/10.1209/epl/i2002-00190-3
21. Barba-Ortega J, Joya MR, Sardella E (2019) Resistive state of a thin superconducting strip with an engineered central defect. Eur Phys J B 92:143. https://doi.org/10.1140/epjb/e2019-100082-y
22. Vidal F, Veira JA, Maza J, Mosqueira J, Carballeira C (2001) On the interplay between Tc-inhomogeneities at long length scales and thermal fluctuations around the average superconducting transition in cuprates. In: Drechsler SL, Mishonov T (eds) High-Tc superconductors and related materials. NATO science series (series 3. high technology), vol 86. Springer, Dordrecht
23. Freitas PP, Tsuei CC, Plaskett TS (1987) Thermodynamic fluctuations in the superconductor Y1Ba2Cu3O9-δ: evidence for three-dimensional superconductivity. Phys Rev B 36:833(R). https://doi.org/10.1103/PhysRevB.36.833
24. Oh B, Char K, Kent AD, Naito M, Beasley MR, Geballe TH, Hammond RH, Kapitulnik A, Graybeal JM (1988) Upper critical field, fluctuation conductivity, and dimensionality of YBa2Cu3O7-x. Phys Rev B 37:7861. https://doi.org/10.1103/PhysRevB.37.7861
25. Friedmann TA, Rice JP, Giapintzakis J, Ginsberg DM (1989) In-plane paraconductivity in a single crystal of superconducting YBa2Cu3O7-x. Phys Rev B 39:4258. https://doi.org/10.1103/PhysRevB.39.4258

26. Vidal F, Torron C, Veira JA, Miguelez F, Maza J (1991) Electrical resistivity and magnetic susceptibility roundings above the superconducting transition in Y1Ba2Cu3O7- delta. J Phys Condens Matter 3:5219. https://doi.org/10.1088/0953-8984/3/27/01
27. Pomar A, Díaz A, Ramallo MV, Torrón C, Veira JA, Vidal F (1993) Measurements of the paraconductivity in the a-direction of untwinned Y1Ba2Cu3O7−δ single crystals. Physica C 218(1–2):257. https://doi.org/10.1016/0921-4534(93)90291-W
28. Gauzzi A, Pavuna D (1995) Evidence for nonuniversal behavior of paraconductivity caused by predominant short-wavelength Gaussian fluctuations in YBa2Cu3O6.9. Phys Rev B 51:15420. https://doi.org/10.1103/PhysRevB.51.15420
29. Holm W, Eltsev Yu, Rapp Ö (1995) Paraconductivity along the a and b axes in YBa2Cu3O7-δ. Phys Rev B 51:11992. https://doi.org/10.1103/PhysRevB.51.11992
30. Ramallo MV, Pomar A, Vidal F (1996) In-plane paraconductivity and fluctuation-induced magnetoconductivity in biperiodic layered superconductors: application to YBa2Cu3O7-δ. Phys Rev B 54:4341. https://doi.org/10.1103/PhysRevB.54.4341
31. Wahl A, Hardy V, Warmont F, Maignan A, Delamare MP, Simon Ch (1997) Scaling behavior of conductivity and magnetization in high-temperature superconductors. Phys Rev B 55:3929. https://doi.org/10.1103/PhysRevB.55.3929
32. Castaño O et al (2003) High quality YBa2Cu3O7 thin films grown by trifluoroacetates metalorganic deposition. Supercond Sci Technol 16:45. https://doi.org/10.1088/0953-2048/16/1/309
33. Ruixing Liang; Bonn, D. A. Bonn and W. N. Hardy, (2006) Evaluation of CuO2 plane hole doping in YBa2Cu3O6+x single crystals. Phys Rev B 73(18):180505. https://doi.org/10.1103/physrevb.73.180505
34. Arpaia R, Andersson E, Trabaldo E, Bauch T, Lombardi F (2018) Probing the phase diagram of cuprates with YBa2Cu3O7-δ thin films and nanowires. Phys Rev Materials 2:024804. https://doi.org/10.1103/PhysRevMaterials.2.024804
35. Kirkpatrick S (1973) Percolation and Conduction. Rev Mod Phys 45:4. https://doi.org/10.1103/RevModPhys.45.574

On the dilemma between percolation processes and fluctuating pairs as the origin of the enhanced conductivity above the superconducting transition in cuprates

I. F. Llovo[1,2], J. Mosqueira[1,2,*] and F. Vidal[1]
[1] *QMatterPhotonics Research Group, Departamento de Física de Partículas, Universidade de Santiago de Compostela, 15782 Santiago de Compostela, Spain and*
[2] *Instituto de Materiais (iMATUS), Universidade de Santiago de Compostela, 15706 Santiago de Compostela, Spain*
(Dated: October 24, 2023)

The confrontation between percolation processes and superconducting fluctuations to account for the observed enhanced in-plane electrical conductivity above but near T_c in cuprates is revisited. This dilemma is currently an open and debated question, whose solution would contribute to the phenomenological understanding of the emergence of superconductivity in these compounds. The cuprates studied here, $La_{1.85}Sr_{0.15}CuO_4$, $Bi_2Sr_2CaCu_2O_{8+\delta}$, and $Tl_2Ba_2Ca_2Cu_3O_{10}$, have a different number of superconducting CuO_2 (*ab*)-layers per unit-cell length and different Josephson coupling between them, and are optimally-doped to minimize T_c-inhomogeneities. The excellent chemical and structural quality of these optimally-doped samples also contribute to minimize the effect of extrinsic T_c-inhomogeneities, a crucial aspect when analyzing the possible presence of intrinsic percolative processes. Our analyses also cover the so-called high reduced-temperature region, up to the resistivity rounding onset $\varepsilon_{\rm onset}$. By using the simplest form of the effective-medium theory, we show that possible emergent percolation processes alone cannot account for the measured enhanced conductivity. In contrast, these measurements can be quantitatively explained using the Gaussian-Ginzburg-Landau (GGL) approach for the effect of superconducting fluctuations in layered superconductors, extended to $\varepsilon_{\rm onset}$ by including a total energy cutoff, which takes into account the limits imposed by the Heisenberg uncertainty principle to the shrinkage of the superconducting wavefunction. Our present analysis confirms the adequacy of this cutoff, which was introduced heuristically, and that the effective periodicity length is controlled by the relative Josephson coupling between superconducting layers, two long standing debated aspects of the GGL approaches for multilayered superconductors. These conclusions are reinforced by analyzing, as an example, one of the recent works that allegedly discards the superconducting fluctuations scenario while supporting a percolative scenario for the enhanced conductivity above T_c in cuprates.

I. INTRODUCTION

As early as 1950, Pippard suggested that the electrical resistivity rounding observed around the superconducting transition of low-T_c superconductors could be caused by the interplay between superconducting fluctuations and emergent percolative phenomena associated with chemical and structural inhomogeneities [1]. Later, as stressed in a review article by Hohenberg [2], percolative processes were addressed as alternative to the pioneering theoretical works of Ferrell and Schmid [3] and, mainly, of Aslamazov and Larkin [4]. These authors explained the resistivity rounding observed above T_c, particularly by Shier and Ginsberg [5] and by Glover [6] in amorphous bismuth superconductors, in terms of superconducting fluctuations. The dilemma between superconducting fluctuations and emergent percolation processes was also commented by Kosterlitz and Thouless, when summarizing the studies on the resistivity rounding around T_c in different metallic films [7]. Some recent examples of this confrontation in low-T_c superconductors and of the influence of disorder and inhomogeneities around T_c on different observables can be seen in Refs. 8–17.

In cuprate superconductors, the dilemma between percolation processes and superconducting fluctuations was already posed by Bednorz and Müller in their seminal work [18]. These authors noted that the resistivity decrease observed above but near T_c in their Ba-La-Cu-O samples *results partially from the percolative nature, but possibly also from 2D superconducting fluctuations of double perovskite layers of one of the phases present.* Since then, the relevance of inhomogeneities and percolation processes in the physics of cuprate superconductors was suggested [19–21]. This dilemma was addressed at a quantitative level in Ref. 22 by studying the dc in-plane resistivity, $\rho_{ab}(T)$, of the prototypical optimally-doped $YBa_2Cu_3O_{7-\delta}$ (YBCO). In that work, the simplest version of the mean-field approach of the effective-medium theory (EMT) [23, 24] was used to study possible emergent percolative effects due to T_c inhomogeneities. Additionally, the Lawrence-Doniach (LD) approach for layered superconductors in the Gaussian approximation [25–31] was used to analyze the data in terms of fluctuating superconducting pairs created by the unavoidable thermal agitation energy. Ref. 22 concluded that, in the case of the optimally-doped YBCO, the LD scenario could account for the observed rounding, whereas the possible percolation processes played a negligible role. These conclusions for optimally-doped YBCO have been recently extended to the high reduced-temperature $\varepsilon \equiv \ln(T/T_c)$ region [32] by heuristically introducing a total-energy

* j.mosqueira@usc.es

cutoff, which takes into account the quantum localization energy of the short wavelength fluctuating modes [33–37].

Since the earlier results commented above, a number of studies have addressed the influence of possible chemical, structural and electronic disorder on the behavior of different observables around T_c in cuprate superconductors [38–43]. However, the dilemma between fluctuating superconducting pairs and percolation processes remains at present an open and debated question, despite the relevance of understanding the emergence of the superconductivity in these materials at a phenomenological level [11, 32, 44–63]. To contribute to answering that question, detailed $\rho_{ab}(T)$ data, previously measured in high quality crystals and films of $La_{1.85}Sr_{0.15}CuO_4$, $Bi_2Sr_2CaCu_2O_{8+\delta}$, and $Tl_2Ba_2Ca_2Cu_3O_{10}$, will be analyzed here [43, 64–66]. The studied compounds are also optimally-doped, to minimize the T_c-inhomogeneities associated with chemical disorder, but they have different number of ab-layers in their periodicity length and different Josephson coupling between them.

Even in high quality samples the in-plane resistivity rounding close to T_c may be deeply affected by the presence of T_c inhomogeneities, intrinsic or not, mainly in the case of the underdoped samples studied in Ref. [60] and analyzed also in our present paper. So, a considerable and original improvement from previous confrontations between percolation or superconducting fluctuation scenarios is that our analyses also cover the so-called high reduced-temperature region, up to the reduced-temperature onset of the resistivity rounding, $\varepsilon_{\rm onset} \equiv \ln(T_{\rm onset}/T_c)$. In fact, before any detailed comparison with the two scenarios confronted here, the present analyses quantitatively confirm the coincidence for the three studied compounds, well within the experimental uncertainties, of $\varepsilon_{\rm onset}$. In addition, the experimental $\varepsilon_{\rm onset}$ agrees with an estimation based on the limit imposed by the Heisenberg uncertainty principle to the shrinkage of the superconducting wave function well above T_c [36, 37]. This generalizes the result previously observed in $YBa_2Cu_3O_{7-\delta}$ [32, 35] to other optimally-doped cuprates, supporting the fluctuating superconducting pairs scenario.

In this paper, the EMT approach proposed in Ref. 22 will be used to evaluate the possible presence of emergent percolative processes arising from T_c-inhomogeneities to describe the $\rho_{ab}(T)$ rounding above T_c. In addition, the adequacy of the fluctuating superconducting pairs scenario will also be tested, for which the LD approach for layered superconductors will be used, extended to the high-ε region by heuristically including a total-energy cutoff [33–37]. Another considerable improvement from previous analyses is that both the effective interlayer distance $d_{\rm eff}$ and the total-energy cutoff were estimated independently. In the case of the highly-anisotropic optimally-doped $Bi_2Sr_2CaCu_2O_{8+\delta}$, and $Tl_2Ba_2Ca_2Cu_3O_{10}$, the corresponding analyses could therefore be performed without free parameters.

Our results confirm that the observed $\rho_{ab}(T)$ rounding around T_c in optimally-doped cuprates can be quantitatively explained by taking into account the unavoidable presence superconducting fluctuations. These analyses also strongly support the adequacy of the total-energy cutoff to extend the LD scenario to high ε, and that $d_{\rm eff}$ is controlled by the relative Josephson coupling between ab layers, two long-standing debated aspects of the GGL approaches [31, 35, 67] ($d_{\rm eff}$ was already studied in the extensions of the LD approach to multilayered superconductors by Maki and Thompson [68] and by Klemm [69]). In addition, the inadequacy of possible percolative effects to explain the enhanced conductivity above T_c in optimally-doped cuprates was also shown. These conclusions enhance the interest of section III.D, where we will briefly examine a recent proposal that questions the conventional GGL scenarios, and that instead suggests percolation processes as the origin of the conductivity enhancement observed just above T_c in cuprates [60].

II. METHODS

The $\rho_{ab}(T)$ roundings around T_c analyzed here were previously measured in high-quality samples of three different optimally-doped compounds, $La_{1.85}Sr_{0.15}CuO_4$ (LaSCO/0.15), $Bi_2Sr_2CaCu_2O_{8+\delta}$ (Bi-2212), and $Tl_2Ba_2Ca_2Cu_3O_{10}$ (Tl-2223) [43, 64–66]. These results, presented in Figs. 1 (a-c), have been chosen due to the exceptional structural and stoichiometric quality of the samples, and to the resolution of the measurements ($\sim$ 1 $\mu\Omega$cm for the resistivity and $\sim$ 10 mK for the temperature). The uncertainty in the samples geometry and in the distances between electrical contacts leads to an uncertainty in the absolute ρ_{ab} below 20%. These experimental aspects, as well as the chemical, structural and magnetic characterization of the samples, can be seen in Refs. 43, 64–66 and references therein.

A summary of the main parameters of the samples studied in this work is presented in Table I, where N is the number of ab-layers per periodicity length, d. As shown in Figs. 1 (a-c), the superconducting transition temperature T_c was estimated from the maximum of the

Sample	d (nm)	N	T_c (K)	ΔT_c (K)	$T_{\rm onset}$ (K)	$\varepsilon_{\rm onset}$
LaSCO/0.15	0.66	1	27.2±1.0	2.2±1.0	46.6±2.0	0.54±0.06
Bi-2212	1.54	2	87±2	1.5±0.4	147±13	0.53±0.09
Tl-2223	1.78	3	116±2	3.9±1.6	195±4	0.52±0.03

TABLE I. General characteristics of the studied compounds. d is the ab layers periodicity length and N is the number of layers in d. T_c and ΔT_c are the superconducting transition temperature and transition width (FWHM), calculated from $d\rho_{ab}/dT$. $T_{\rm onset}$ is the temperature at which $d\rho_{ab}/dT$ rises above the normal state contribution beyond the noise level, and $\varepsilon_{\rm onset} \equiv \ln(T_{\rm onset}/T_c)$.

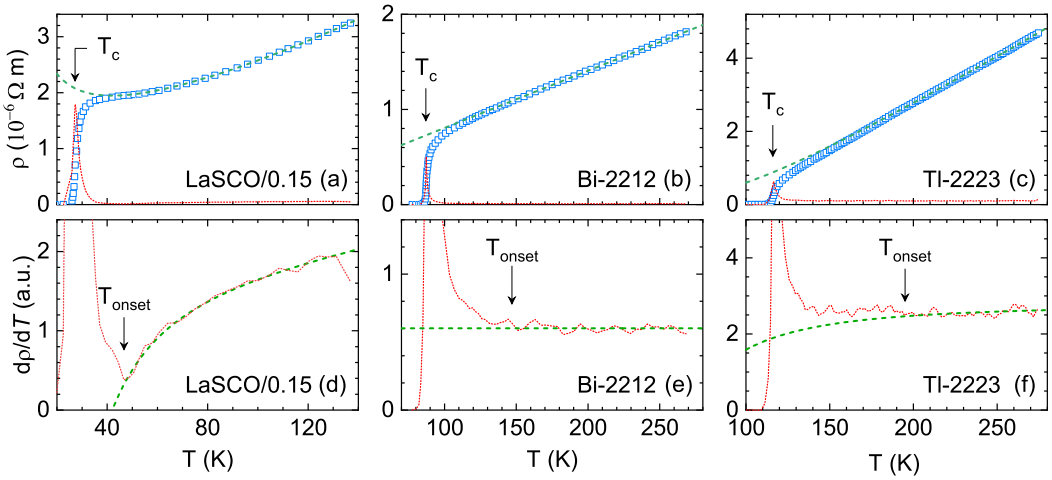

FIG. 1. Resistive characterization of LaSCO/0.15, Bi-2212 and Tl-2223 (captured from Fig. 2 of Ref. 43 and Fig. 1 of Ref. 66). **a, b, c** In-plane resistivity (blue squares), in-plane background resistivity $\rho_{abB}(T)$ (dashed green line), $d\rho_{ab}(T)/dT$ (dotted red line). **d, e, f** Detail of $d\rho_{ab}/dT$ and $d\rho_{abB}/dT$ around $T_{\rm onset}$.

$d\rho_{ab}/dT$ vs. T curve, whereas the transition width ΔT_c corresponds to the full width at half maximum. The ΔT_c values, indicative of the sample homogeneity (see also next section), are within those of the best samples of these compounds [11, 31, 39–65, 68], in particular for LaSCO/0.15, one of the most studied cuprate superconductors [52]. In fact, the c-axis oriented 150 nm thickness thin film used in this work was grown using a procedure specifically aimed at improving its structural and chemical homogeneity [43].

III. RESULTS AND DISCUSSION

A. Resistivity rounding characterization above T_c

The temperature dependence of the in-plane resistivity of the three samples studied here is shown in Figs. 1 (a-c). To characterize the in plane resistivity rounding observed above but near the superconducting transition, we will use the so-called in-plane paraconductivity, already introduced in the pioneering works on these rounding's effects in low T_c superconductors and defined as [1–6, 28–30]

$$\Delta\sigma_{ab} = \frac{1}{\rho_{ab}(\varepsilon)} - \frac{1}{\rho_{abB}(\varepsilon)}. \qquad (1)$$

Here $\varepsilon \equiv \ln(T/T_c)$ is the reduced temperature and ρ_{abB} is the background or bare in-plane resistivity, i.e., the normal in-plane resistivity if the critical phenomena associated with the presence of the superconducting transition were absent. The separation between critical and normal contributions is unavoidable when studying the behavior of most of the observables around any phase transition, and it is a consequence that the corresponding theoretical approaches calculate only the first contributions [70]. A central and general hypothesis in doing such a separation is that the non-critical and the critical behaviors are independent. Therefore, as usual (see e. g., Refs. [2–6, 30, 31] and references therein), $\rho_{abB}(T)$ can be determined by fitting an adequate function to the measured $\rho_{ab}(T)$ in a temperature region well above T_c, well into the normal state, where the critical phenomena are supposed to be absent (obviously, such a sample-dependent background has no direct physical meaning, an irrelevant aspect when extracting the paraconductivity). The procedure to obtain $\rho_{abB}(T)$ in the studied samples (dashed green lines in Fig. 1) is described in detail in Refs. [43, 66]. As illustrated in Fig. 1, the rounding onset temperature $T_{\rm onset}$ is approximated as the temperature at which $d\rho_{abB}/dT$ deviates from $d\rho_{ab}/dT$ beyond the experimental noise level.

The values for each sample of T_{onset}, and of the corresponding ε_{onset}, are indicated in Table I. A relevant result in Table I which is already worth stressing here is the agreement, well within the experimental uncertainties, of the ε_{onset} values for the three optimally doped compounds studied here, which also agree with the one shown by the optimally doped $YBa_2Cu_3O_{7-\delta}$ compound studied elsewhere [32, 35]. The implications of this result on the physical origin of the enhanced in-plane conductivity above T_c in optimally doped cuprates will be analyzed in Section III.C. But we must also already note that these ε_{onset} values are consistent with the predictions of the Gaussian Ginzburg-Landau (GGL) approach under a total-energy cutoff [36, 37], favoring the presence of fluctuating superconducting pairs as the origin of the precursor conductivity in these superconductors.

The data points in Fig. 2 are $\Delta\sigma_{ab}(\varepsilon)$ for the three compounds studied here, calculated from Eq. (1). In the case of Bi-2212 and Tl-2223, for $0.03 \lesssim \varepsilon \lesssim 0.2$, $\Delta\sigma_{ab} \propto \varepsilon^{-1}$, an ε-dependence consistent with 2D superconducting fluctuations as we will see in section III.C. For

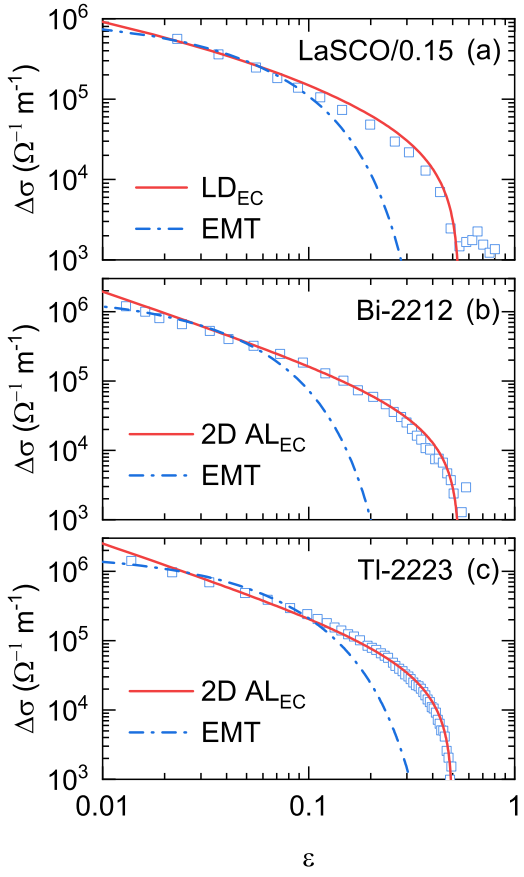

FIG. 2. Analysis of $\Delta\sigma_{ab}$ (blue squares) of the samples studied. The dot-dashed blue lines were obtained by using the EMT approach (the corresponding parameters are summarized in Table II). The solid red curves correspond to the fluctuating superconducting pairs scenario and were obtained by using the GGL approach with a total-energy cutoff (the corresponding parameters are summarized in Table III). The excellent agreement of the GGL curves, obtained without any free parameters for Bi-2212 and Tl-2223, contrasts with the poor results of the percolative model, even at a qualitative level. See the main text for details.

$\varepsilon \lesssim 0.02$ the data may be affected by the so-called full-critical effects [38, 40, 43, 45]. Also, T_c-inhomogeneities could affect the data down to $\varepsilon \approx \Delta T_c/T_c$, that is 0.017 and 0.034 for Bi-2212 and Tl-2223, respectively. In the case of LaSCO/0.15, $\Delta\sigma_{ab}(\varepsilon)$ is affected close to T_c by its much larger $\Delta T_c/T_c \approx 0.09$ (which also complicates its T_c estimation), and also presents a somewhat smoother ε-dependence at higher ε. As stressed before, these behaviors close to T_c further enhance the relevance of extending the analyses to the high reduced temperature region, up to $\varepsilon_{\rm onset}$, as it is done in the next two Subsections.

B. Analysis in terms of percolative processes

To probe if emergent percolative processes associated with the presence of chemical and structural inhomogeneities could be the origin of the paraconductivity, Bruggeman's effective-medium theory (EMT) [23, 24] can be used, as proposed in Ref. 22. The main hypothesis is to assume that doping-level inhomogeneities at long length scales (much larger than the superconducting coherence length amplitudes), cause a spatial T_c-distribution. The effective in-plane electrical conductivity $\langle\sigma_{ab}\rangle$ can be obtained by numerically solving the implicit equation

$$\int_0^\infty \frac{\sigma_{ab}(T,T_c) - \langle\sigma_{ab}(T)\rangle}{\sigma_{ab}(T,T_c) + 2\langle\sigma_{ab}(T)\rangle} G(T_c) dT_c = 0, \qquad (2)$$

where $G(T_c)$ is the volume fraction of domains with T_c as critical temperature. $G(T_c)$ can be approximated by a Gaussian distribution, characterized by an average critical temperature T_c^{EMT} and a full width at half-maximum (FWHM) ΔT_c^{EMT}. The in-plane electrical conductivity of the different domains is assumed to be

$$\sigma_{ab}(T,T_c) \rightarrow \begin{cases} \infty & \text{if } T_c^{\rm EMT} > T \\ 1/\rho_{abB}(T) & \text{if } T_c^{\rm EMT} < T \end{cases} \qquad (3)$$

The best fits of Eq. (2) to the experimental $\Delta\sigma_{ab}(\varepsilon)$ with $\Delta T_c^{\rm EMT}$ and $T_c^{\rm EMT}$ as free parameters are shown in Fig. 2. The resulting values for these two parameters are presented in Table II. The disagreement is dramatic for $\varepsilon > 0.1$, and can also be seen in the $\rho_{ab}(T)$ representation in Fig. 3. Notice also that the seeming agreement observed closer to T_c in Fig. 3 is questioned by the large $\Delta T_c^{\rm EMT}$ values resulting from the EMT fits, a factor ~ 10 larger than the resistive transition widths for Bi-2212 and Tl-2223 (see Table I). The latter are in turn consistent with the diamagnetic transition widths observed in similar samples [31, 35, 51], confirming that they are a reasonable indicative of their actual T_c-inhomogeneities. In fact, previous paraconductivity analyses on the grounds of percolative scenarios also lead to unphysical T_c distributions, with $\Delta T_c^{\rm EMT}$ values comparable to the T_c of the samples [22, 32, 59–61].

Sample	T_c^{EMT} (K)	ΔT_c^{EMT} (K)
LaSCO/0.15	24.5±0.3	8.5±0.6
Bi-2212	80.1±0.7	18.0±1.5
Tl-2223	101.3±1.0	44.2±2.4

TABLE II. Parameters obtained in the percolative scenario by fitting Eq. (2) to the resistivity rounding just above T_c in the studied compounds. The ΔT_c^{EMT} values are particularly high (comparable to T_c^{EMT}) and the fit quality is bad, as it can be seen in Figs. 2 and 3.

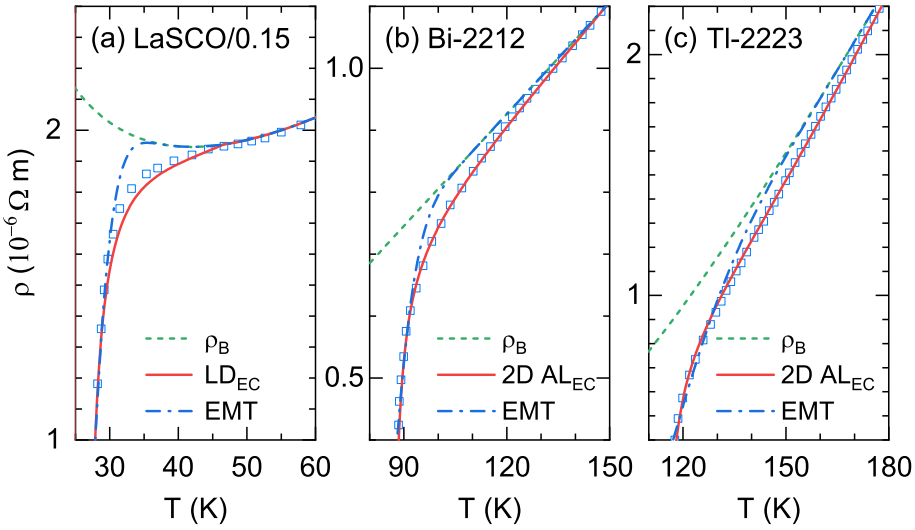

FIG. 3. Comparison of $\rho_{ab}(T)$ with the EMT approach (dot-dashed blue lines), and the GGL approaches (solid red lines) in the extended mean field region above T_c for **a** LaSCO/0.15, **b** Bi-2212 and **c** Tl-2223. The background resistivity ρ_B is also shown for comparison.

C. Analysis in terms of superconducting fluctuations

We will now probe if the presence of fluctuating superconducting pairs, created by the thermal agitation energy, could be the primary cause of the resistivity rounding effects observed just above T_c in the three compounds studied here. For that, we take advantage of the well-established absence of appreciable indirect (Maki-Thompson) fluctuation effects on the in-plane paraconductivity in cuprate superconductors [31, 35]. Therefore, the Lawrence-Doniach (LD) approach of the phenomenological Gaussian-Ginzburg-Landau (GGL) scenario can be used [25–30]. This approach, well adapted to the layered nature of the cuprate superconductors, can be extended to the high-ε region by introducing a total-energy cutoff (see below), which leads to [33–37]

$$\Delta\sigma_{ab}(\varepsilon) = \frac{e^2}{16\hbar d_{\rm eff}}\left[\frac{1}{\varepsilon}\left(1+\frac{B_{LD}}{\varepsilon}\right)^{-\frac{1}{2}} - \frac{1}{\varepsilon^c}\left(1+\frac{B_{LD}}{\varepsilon^c}\right)^{-\frac{1}{2}}\right] \quad (4)$$

Here, $B_{LD} \equiv [2\xi_c(0)/d_{\rm eff}]^2$ is the LD coupling parameter, $\xi_c(0)$ the c-axis coherence length amplitude, ε^c the total energy cutoff constant, and $d_{\rm eff}$ the effective distance between ab-layers, which depends on their relative Josephson coupling (see below). In the highly anisotropic compounds studied here, the Josephson coupling between neighboring layers can be neglected, i.e., $\xi_c(0) \sim 0$ (or $B_{LD} \sim 0$), and Eq. (4) reduces to

$$\Delta\sigma_{ab}(\varepsilon) = \frac{e^2}{16\hbar d_{\rm eff}}\left(\frac{1}{\varepsilon} - \frac{1}{\varepsilon^c}\right). \quad (5)$$

In the absence of cutoff, i. e., $\varepsilon^c \to \infty$, Eq. (4) further reduces to the well-known Aslamazov-Larkin (AL) result for the superconducting fluctuations of layered superconductors (which is the same as the AL result in the 2D limit but with $d_{\rm eff}$ replacing the film thickness, as it is easy to check) [4]. The conventional GGL approach (and so Eqs. (4) and (5)) is applicable in the mean field region, which is limited by ε_{LG}, the Levanyuk-Ginzburg reduced-temperature [28–31, 35, 72]. Below ε_{LG}, the superconducting fluctuations enter in the so-called full-critical (non-Gaussian) region, and theoretical approaches such as the 3D-XY model must be applied [72]. Although ε_{LG} depends on the particular characteristics of each compound, it is of the order of 10^{-2} for those studied here [31, 52, 72]. For Bi-2212 and Tl-2223, this limit is near the $\Delta T_c/T_c$ values shown in Table I, and it is well below the corresponding $\Delta T_c/T_c$ in the case of the LSCO sample. Therefore, to avoid the possible influence of both full-critical fluctuations and T_c-inhomogeneities, the comparison with Eqs. (4) and (5) will be restricted to $\varepsilon \gtrsim 0.02$.

In the high-ε region, for $\varepsilon \gtrsim 0.1$, it is also well known that the GGL approach overestimates the contribution of short-wavelength fluctuation modes [28–31]. Trying to overcome this shortcoming, the so-called kinetic-energy or momentum cutoff was early heuristically proposed when analyzing the superconducting fluctuations in low-T_c superconductors [28, 30, 73], and later in cuprate superconductors [28–31, 74–76]. More recently, this momentum cutoff was recovered by using a microscopic approach based on diagrammatic techniques [29]. However, such a cutoff does not take into account that, when the temperature increases above T_c, the Heisenberg uncertainty principle limits the shrinkage of the superconducting coherence length $\xi(T)$ below ξ_0, the Pippard or BCS characteristic length, representative of the Cooper pairs' size [36, 37]. To solve this problem, the so-called total-

energy cutoff was also heuristically introduced, to include the kinetic energy of the fluctuating modes as well as their quantum localization energy [33, 34, 36]. Up to now, that total-energy cutoff has not been recovered by using microscopic approaches (in fact, the difficulties to extend the microscopic calculations to $\Delta\sigma$ at high-ε were earlier commented, for instance, in Ref. 77). However, the heuristic introduction of the total energy cutoff extends the applicability of Eqs. (4) and (5) up to the temperature onset of the fluctuations [33–37], and for $\varepsilon > \varepsilon^c$ (the total-energy cutoff constant) all the fluctuating modes are correctly suppressed.

As first proposed in Refs. 36 and 37, ε^c can be estimated through the condition $\xi(\varepsilon_{\rm onset}) = \xi_0$. As already stressed therein, and later when analyzing the superconducting fluctuations in optimally-doped YBCO [35], this condition is general and must be applied to any theoretical description in terms of fluctuating superconducting pairs. Assuming the mean-field temperature dependence of the coherence length, $\xi(T) = \xi(0)\varepsilon^{-1/2}$, and the relationship between ξ_0 and $\xi(0)$ proposed in the BCS theory, which in the clean limit is [71] $\xi(0) = 0.74\xi_0$, the above condition leads to $T_{\rm onset} \approx 1.7T_c$, hence $\varepsilon^c \approx 0.55$ (in anisotropic superconductors the above expressions are valid for both ab and c directions). The agreement well within the experimental uncertainty of this ε^c value and the $\varepsilon_{\rm onset}$ observed in the three optimally-doped cuprates studied here is a remarkable result. Such an agreement was also found when analyzing the $\rho_{ab}(T)$ rounding and the precursor diamagnetism above T_c in high-quality YBCO samples [35], and already suggests that fluctuating superconducting pairs are responsible for the precursor electrical conductivity in optimally-doped cuprates.

Considering the above comments, Eqs. (4) and (5) were used to analyze the paraconductivity data in the ε-region between 0.02 and $\varepsilon_{\rm onset}$. In doing so, an appreciable improvement relative to previous works is the independent estimation of ε^c and $d_{\rm eff}$. The origin of ε^c and the $d_{\rm eff}$ estimation are long standing still open issues of the GGL scenario [11, 35–52, 67]. For ε^c, we will use $\varepsilon_{\rm onset} \equiv \ln(T_{\rm onset}/T_c)$. Regarding $d_{\rm eff}$, it is now well established that it is controlled by the relative, not the absolute, Josephson coupling between superconducting layers [31, 35, 68, 69, 72]. Moreover, it was also shown that even for interlayer coupling differences as big as 100, the effective periodicity length can be approximated as d/N, where N is the number of layers per periodicity length d [31, 72]. This conclusion can be then applied to the compounds studied here and we will approximate $d_{\rm eff} = d/N$, as summarized in Table II. Notice that the independent estimations of ε^c and $d_{\rm eff}$ allows the use of Eq. (4) without free parameters to analyze the measurements in Bi-2212 and Tl-2223.

The solid red line in Fig. 3(a) is the best fit of Eq. (4) to the $\Delta\sigma_{ab}(\varepsilon)$ measured in LaSCO/0.15. As previously discussed, this fit was performed in the ε-region between 0.02 and $\varepsilon_{\rm onset} = 0.54$. Moreover, in this single layered compound (with $N = 1$) $d_{\rm eff}$ coincides with the

Sample	$d_{\rm eff}$ (nm)	ε^c	B_{LD}	$\xi_c(0)$ (nm)	$\xi_{ab}(0)$ (nm)
LaSCO/0.15	0.66	0.54	0.048±0.004	0.072±0.006	3.2
Bi-2212	0.77	0.53	0	~ 0	0.9
Tl-2223	0.593	0.52	0	~ 0	1.0

TABLE III. Parameters of the fluctuating superconducting pair's scenario, obtained from the GGL analysis of the resistivity roundings just above T_c in the studied optimally-doped compounds. $d_{\rm eff}$ is the effective interlayer distance and B_{LD} the Lawrence-Doniach parameter. The total-energy cutoff constant ε_c in Eqs. (4) and (5) was set to the value of $\varepsilon_{\rm onset}$ (see Table I). These different parameters were obtained as indicated in the main text. For completeness, values of the in-plane coherence length amplitude taken from Refs. 78–80 are also included.

ab-layers periodicity length, i.e., $d_{\rm eff} = 0.66$ nm, as it is shown in Table III. B_{LD} is then the only free parameter, and the best fit leads to $B_{LD} = 0.048 \pm 0.004$, hence $\xi_c(0) = 0.072 \pm 0.006$ nm. This $\xi_c(0)$ value is much smaller than $d_{\rm eff}$, which is indicative of weak Josephson coupling. Although weak, this interlayer coupling justifies that the critical exponent of the measured in-plane paraconductivity is between -1/2 and -1 for $0.02 \lesssim 0.1$, confirming the 2D-3D behavior of the superconducting fluctuations in this compound [31, 43].

For the multi-layered compounds Bi-2212 ($N = 2$, $d = 1.54$ nm) and Tl-2223 ($N = 3$, $d = 1.78$ nm), the effective interlayer distances are $d_{\rm eff} = d/2 = 0.77$ nm and $d_{\rm eff} = d/3 = 0.593$ nm, respectively. As shown in Figs. 1(e-f), the aforementioned procedure to estimate $\varepsilon_{\rm onset}$ was also followed, obtaining $\varepsilon_{\rm onset} = 0.53$ for Bi-2212, and $\varepsilon_{\rm onset} = 0.52$ for Tl-2223. Moreover, the experimental results in Figs. 3(b-c) shows that for $0.01 \lesssim \varepsilon \lesssim 0.1$, $\Delta\sigma_{ab}(\varepsilon) \propto \varepsilon^{-1}$ well within the experimental uncertainties, corresponding to the 2D limit consistent with a negligibly small $\xi_c(0)$ value [81]. Therefore, when analyzing the corresponding $\Delta\sigma_{ab}(\varepsilon)$ in terms of the GGL approach, Eq. (5) was used. The resulting paraconductivity curves, obtained without free parameters, are shown as solid red lines in Figs. 3(b-c). As it can be seen, the experimental data are remarkably well explained by the extended GGL approach for multilayered superconductors in the ε-range analyzed.

D. Comparison with some recent results

To complement our analyses, here we will analyze one of the recent works that propose a universal percolative scenario for the paraconductivity in cuprate superconductors [57–62], in opposition to the GGL approaches. This example corresponds to Ref. 60, and we will show that the arguments presented therein against the GGL approach and the ones supporting the percolative scenario are unjustified. The interest of this section is enhanced by the fact that our results can also be applied

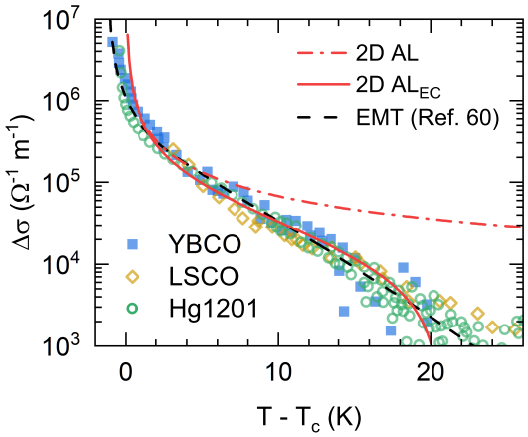

FIG. 4. Paraconductivity data for YBCO, LSCO and Hg1201, captured from Fig. 2 of Ref. 60. The data are compared with the percolative model of Ref. 60 (denoted as EMT, dashed black line), the 2D AL result without cutoff (dot dashed red line), and with a total-energy cutoff (2D AL$_{\rm EC}$, solid red line). All these curves correspond to Hg1201 (see main text for details). Data for $\Delta\sigma_{ab} < 10^3\ \Omega^{-1}{\rm m}^{-1}$ were not considered due to the high dispersion.

to the analyses of other authors questioning the GGL scenarios for the rounding effects observed above T_c in cuprates [59, 61].

The central starting point of the analyses presented in Ref. 60 is the claim that their paraconductivity measurements *demonstrate a remarkable degree of universality*. This conclusion contradicts the GGL scenarios for layered superconductors, which predict a compound-dependent paraconductivity, particularly depending on the relative Josephson coupling between superconducting layers [25–35, 68, 69]. To demonstrate such universality, Fig. 2 of Ref. 60 shows $\Delta\sigma$ vs. $T - T_c$ of three underdoped cuprates: LSCO ($T_c = 28$ K), YBCO $T_c = 47$ K), and $HgBa_2CuO_{4+\delta}$ (Hg1201, $T_c = 80$ K). Here we will show the shortcomings of this analysis. Notice first that the paraconductivity of LSCO was divided by a factor of two to make it scale with the ones of underdoped YBCO and Hg1201. Indeed, $\Delta\sigma$ may be appreciably affected by temperature independent factors, such as the geometrical ones associated to the finite size of the electrical contacts in small or irregular samples. These uncertainties are generally considered by introducing an adjustable, temperature-independent factor in the theory to be probed (see below). However, it is questionable to discard the AL approach (whithout any cutoff, see below) after a comparison with data that has been forced to scale with the percolative approach (as it is done in Fig. 2 of Ref. 60, see also our Fig. 4). In addition, with the amplitude factor for LSCO proposed in Ref. 60, the seeming universality is just a consequence of the data dispersion and the small resolution of the logarithmic representation used. The actual differences concern not only the $\Delta\sigma$ amplitudes but also their ε-behavior, as it can be seen in Fig. 5, where the data sets are shown separately for each compound as a function of both $T - T_c$ and ε. For instance, for $\varepsilon \gtrsim 0.02$, where the data are probably not affected by T_c-inhomogeneities, the YBCO paraconductivity is more than two times larger than for Hg1201 (these two compounds not being affected by any amplitude correction). As it can also be seen in Figs. 5 (b,d,f), the ε-onset of $\Delta\sigma$ varies between 0.23 and 0.65 (see below), beyond the data dispersion.

The non-universality of the scaling proposed in Ref. 60 is further evidenced when other samples are added to the same $\Delta\sigma(T - T_c)$ representation. Figure 6 shows our paraconductivity data for optimally-doped Tl2223, Bi2212 and LSCO, superimposed on the data sets from Fig. 2 of Ref. 60 (shown as a gray area for clarity). The differences between our data sets are well beyond the experimental uncertainties, even if the paraconductivity amplitude of our data were adapted as proposed in Ref. 60. Nevertheless, our LaSCO/0.15 data are compatible with the LSCO data from Ref. 60.

A quantitative analysis shows further difficulties with the EMT model proposed in Ref. 60. In their approach, the only free parameter was the full width at half maximum ΔT_c of the Gaussian T_c distribution (see Ref. 60 for the details). The best fit to their data set is shown in Fig. 2 of Ref. 60 and is reproduced in Fig. 4 here. It leads to $\Delta T_c = 26 \pm 1$ K, which is a significant fraction of the T_c value of the samples studied (28 K for LSCO, 47 K for YBCO, and 80 K for Hg1201). Such a large ΔT_c is inconsistent with the low-field (15 Oe) field-cooled magnetization M^{FC} from Ref. 60, which is temperature independent up to ~ 10 K below T_c. A wide T_c distribution would lead to a temperature dependent M^{FC} well below T_c (some relevant examples from the early times of high-T_c cuprates may be seen in Refs. 82 and 83) In fact, the actual T_c distribution may be estimated from the temperature derivative of M^{FC} (see e.g., Ref. 42). The T_c distribution for Hg1201 obtained with this procedure is shown in Fig. 7, the resulting ΔT_c being ~ 3 K, one order of magnitude smaller than the one resulting from the percolative approach fit of Ref. 60, also represented in Fig. 7.

Another point emphasized in Ref. 60, is that *the exponential temperature dependence* (shown by their paraconductivity data) *is incompatible with standard models of superconducting fluctuations such as Ginzburg-Landau theory*. To arrive to this conclusion, a comparison of data for different compounds with the 2D AL expression without any cutoff [4] was made in Fig. 2 of Ref. 60. However, as we have already stressed in section III.C, the original AL paraconductivity overestimates the short wavelength fluctuating modes, and a momentum cutoff was early introduced to mitigate such a disagreement at high reduced temperatures [28–30, 73]. In addition, a single curve, calculated by using only the Hg1201 effective interlayer distance, was used in Fig. 2 of Ref. 60, even though the 2D AL paraconductivity is dependent on the effective interlayer distance and on T_c.

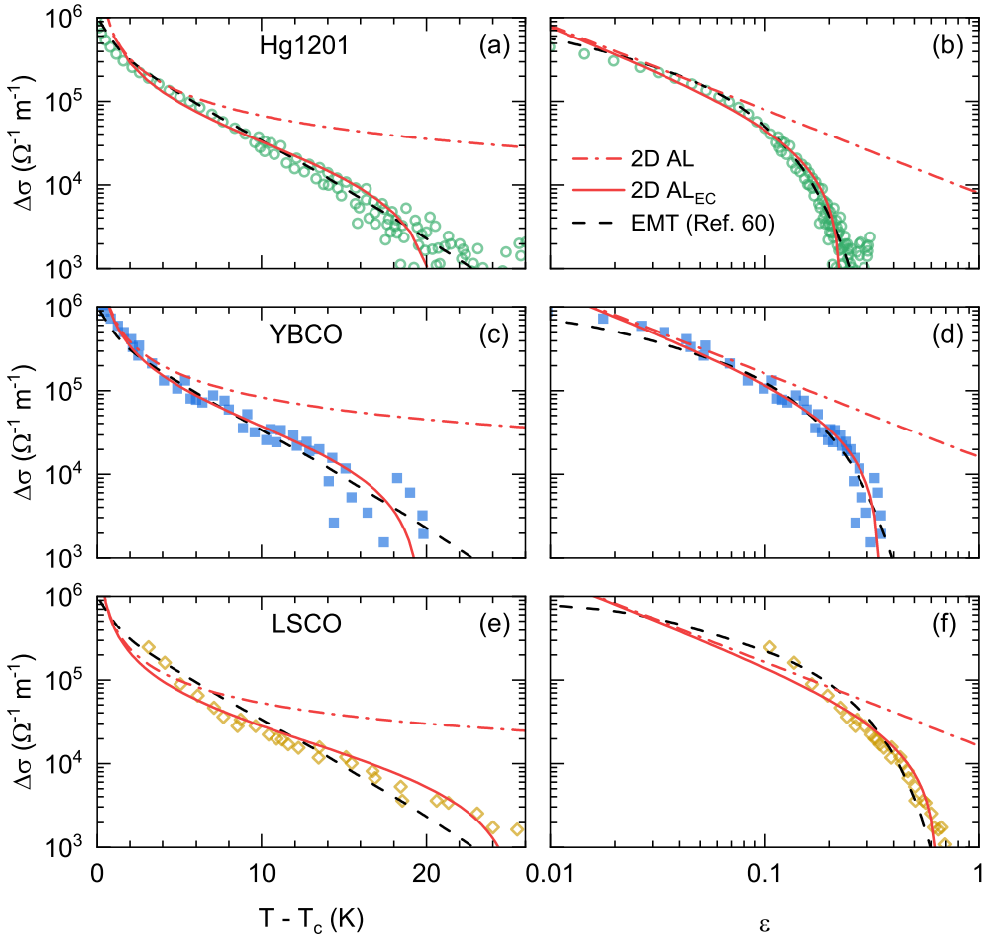

FIG. 5. $\Delta\sigma_{ab}(\varepsilon)$ data from Fig. 4, shown separately for each compound as a function of both $T - T_c$ and ε. Each data set is shown next to curves corresponding to the percolative model of Ref. 60 (denoted as EMT, dashed black line), the 2D AL result (dot dashed red line) and the 2D AL result with a total-energy cutoff (2D AL$_{\rm EC}$, solid red line). Notice the difference between the EMT approach and the LSCO data despite the amplitude adaptation introduced in Ref. 60 (see the main text for details).

For the aforementioned reasons, we will analyze Ref. 60 data in terms of the AL paraconductivity for 2D layered superconductors up to the high-ε region by using the GGL approach with a total energy cutoff [28–31, 43, 73–76]. The possible amplitude indeterminations affecting $\Delta\sigma_{ab}$ from Ref. 60 were considered by including a temperature-independent multiplicative parameter C_g in Eq. (5). Only data above T_c and up to the ε-value at which $\Delta\sigma_{ab}$ falls below the noise level were used, resulting in a $\Delta\sigma_{ab}$ window in Fig. 5 between $10^3\ \Omega^{-1}\mathrm{m}^{-1}$ and $10^6\ \Omega^{-1}\mathrm{m}^{-1}$ (for $\Delta\sigma_{ab}$ below this value the signal-to-noise ratio becomes too low). The cutoff parameters were estimated from Figs. 5 (b,d,f) as the reduced temperatures at which $\Delta\sigma_{ab} \approx 10^3\ \Omega^{-1}\mathrm{m}^{-1}$.

The 2D AL curve for each compound is shown in Fig. 5 as a dot-dashed line, and the curve from Eq. (5) with the C_g values indicated in Table IV as solid red lines (the curves obtained for Hg1201 are also shown in Fig. 4). As it can be seen, the agreement with the experimental data is remarkably good even in the high-ε region. Nevertheless, the observed differences between the ε^c values for the different compounds may be associated with differences in the relationship between the Pippard and the GGL coherence length amplitudes [36, 37], or to uncertainties associated to the background subtraction procedure, as the background determination is particularly difficult in non-optimally-doped compounds [42, 43].

Finally, it is worth noting two points. First, the adequacy of the superconducting fluctuations scenario in cuprates was also earlier supported by the analyses of the behavior above but near T_c of other observables, mainly the in-plane magnetization (see, e.g., Refs. [31, 35, 51, 63, 65]). Second, the $\Delta\sigma_{ab}$ measurements in underdoped LSCO under magnetic fields up to 50 T presented in Ref. [86] are also consistent with the 2D-AL approach near T_c, and show a reduction at high-ε that is related to the total-energy cutoff (see also Ref. [87]). The $\Delta\sigma_{ab}$ data in slightly underdoped YBCO also show a good agreement with the 3D AL approach near T_c, and the seemingly exponential behavior

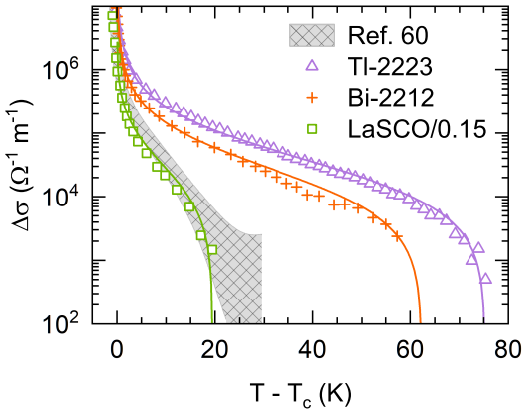

FIG. 6. Comparison of the $\Delta\sigma_{ab}(\varepsilon)$ data for Tl-2223, Bi-2212, and LaSCO/0.15, with the data for all the compounds studied in Ref. 60 (grey area). The lines are the GGL fits to each data set, as described in the main text. LaSCO/0.15 scales with the data from Ref. 60, but the also optimally-doped Bi-2212 and Tl-2223 data do not. This rules out the universal $\Delta\sigma$ behavior proposed in the percolative scenario of Ref. 60.

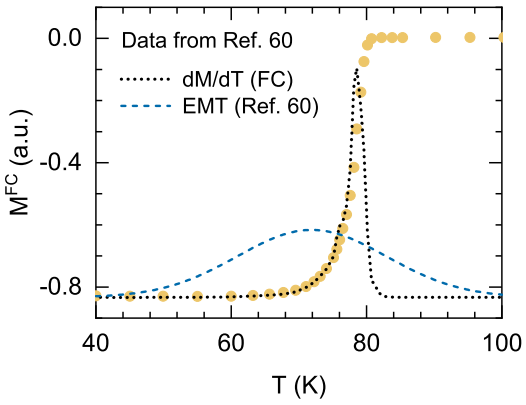

FIG. 7. Field-cooled magnetization of the Hg1201 sample, captured from Fig. 1**c** of Ref. 60. As explained in the main text, dM/dT (black dotted line, a. u.) approximates the actual T_c distribution for this sample. This distribution strongly contrasts with the one resulting from the percolative model proposed in Ref. 60 (blue dashed line, a. u.).

at higher temperatures seems to be a crossover to the cutoff-dominated region[88].

IV. CONCLUSIONS

The $\rho_{ab}(T)$ roundings measured just above T_c in three optimally-doped compounds $La_{1.85}Sr_{0.15}CuO_4$, $Bi_2Sr_2CaCu_2O_{8+\delta}$, and $Tl_2Ba_2Ca_2Cu_3O_{10}$ [43, 64–66], have been used for a throughout confrontation between percolation processes and the unavoidable presence of fluctuating superconducting pairs. The excellent chemical and structural quality of these optimally-doped samples miniimizes the effect of extrinsic T_c-inhomogeneities,

Sample	d (nm)	N	T_c (K)	ΔT_c (K)	$d_{\rm eff}$ (nm)	C_g	ε^c	$\xi_{ab}(0)$ (nm)
Hg1201	0.95	1	80	0.8±0.2	0.95	0.5	0.23	3.0
YBCO	1.17	2	47	2.2±0.2	0.585	0.62	0.35	2.9
LSCO	0.66	1	28	1.8±0.2	0.66	0.71	0.65	3.5

TABLE IV. Parameters corresponding to the analysis of the paraconductivity data of Ref. 60 in terms of the 2D AL approach with a total-energy cutoff, Eq. (5). ΔT_c was estimated as the FWHM of $d\rho_{ab}/dT$. A multiplicative constant parameter C_g was also included to account for the uncertainties in the $\Delta\sigma$ amplitude (due, in particular, to possible uncertainties in the samples geometry). Without the amplitude adaptation introduced in Ref. 60, for the LSCO compound C_g would be ~ 1.4. The resulting curves can be seen in Fig. 4 for Hg1201 and Fig. 5 for all compounds (red solid curves). For completeness, values of the in-plane coherence length amplitude taken from Refs. 50, 84, and 85 are also included.

a crucial aspect when analyzing the possible presence of intrinsic percolative processes. In addition, these compounds have different number of superconducting ab-layers in their periodicity length, and different Josephson coupling between layers, which is particularly relevant to probe the presence of fluctuating superconducting pairs. In our analyses, we have excluded the so-called full-critical region close to T_c (a reduced temperature region also affected, mainly in the case of the LaSCO/0.15 sample, by T_c-inhomogeneities). However, we have covered the high-ε region, up to the resistivity rounding onset.

A remarkable result of our analysis is the agreement between the $\varepsilon_{\rm onset}$ values well within the experimental uncertainties. These $\varepsilon_{\rm onset}$ are also consistent with the value (0.55) predicted by the Gaussian-Ginzburg-Landau approach under a total-energy cutoff for clean superconductors [36, 37]. The latter was introduced heuristically [36, 37], as it also was the classical momentum cutoff [28, 30, 73]. A similar $\varepsilon_{\rm onset}$ was also found when analyzing the $\rho_{ab}(T)$ rounding and the precursor diamagnetism above T_c in optimally-doped YBCO [35]. These results confirm earlier results in different optimally-doped cuprates [36, 37, 43, 66] at a quantitative level, evidencing that the unavoidable fluctuating superconducting pairs must be the origin of the precursor conductivity in optimally-doped cuprates.

Additionally, by using the simplest form of the effective-medium theory we conclude that percolative processes alone cannot account for the measured $\Delta\sigma_{ab}(\varepsilon)$, generalizing previous findings in optimally-doped YBCO [22] (see also the short conference proceedings recently published in SN Applied Science, Ref. 32). In contrast, these measurements have been quantitatively explained using the GGL approach for layered superconductors, extended to high-ε by including the total-energy cutoff. In the case of $Bi_2Sr_2CaCu_2O_{8+\delta}$ and $Tl_2Ba_2Ca_2Cu_3O_{10}$, for which the superconducting fluctuations in the $0.01 < \varepsilon < 0.1$ range are in the 2D limit, the analysis has been done

without adjustable parameters. In the case of optimally-doped cuprates, our results provide an unambiguous conclusion to the question addressed by Bednorz and Müller in their seminal work [18]: The enhanced conductivity observed above but near T_c can be quantitatively accounted for, up to the rounding onset temperature, by the presence of unavoidable superconducting pairs created by the thermal agitation energy. This conclusion is also supported by the analyses of the behavior above but near T_c of other observables, mainly the in-plane magnetization [31, 35, 50, 51, 63, 65].

Finally, we have shown that data from a recent work seemingly supporting a percolative scenario in three underdoped cuprates can in fact be explained on the grounds of conventional thermal fluctuations. This result is not trivial, because these materials are expected to be affected to some extent by T_c inhomogeneities: their T_c is strongly dependent on the doping level, contrary to optimally doped cuprates. On the other hand, the doping level presents a spatial variation due to the random distribution of dopants and to the small ξ_{ab} amplitude (of the order of nm). Our analysis suggests that, in these underdoped samples, T_c inhomogeneities play a non-negligible role only in a restricted temperature range (just a few K around T_c) where the AL approach deviates appreciably from the data. These results reinforce the adequacy of fluctuation models for the conductivity enhancement above but not too close to T_c, and directly address the proposals of other authors questioning the GGL scenarios for the paraconductivity in cuprates, particularly in the high-ε region.

ACKNOWLEDGMENTS

We thank C. Carballeira, J. Maza, and M. V. Ramallo for earlier discussions on the theoretical approaches for the paraconductivity. This work was supported by the Agencia Estatal de Investigación (AEI) through project PID2019-104296GB-I00. I. F. Llovo acknowledges financial support from Xunta de Galicia through grant ED481A-2020/149.

Conflict of interest statement: The authors declare that there is no conflict of interest to disclose.

Data access statement: Data will be made available upon reasonable request.

REFERENCES

[1] A. B. Pippard, Field variation of the superconducting penetration depth. *Proc. Roy. Soc.* (London) A **203,** 210 (1950).

[2] For an earlier review see, P. C. Hohenberg, Critical phenomena and their bearing on the superconducting transition, in *Proceedings of the Conference on Fluctuations in Superconductors*, edited by Goree, W. & Chilton, F. (Stanford Research Institute, 1968), p. 305.

[3] F. A. Ferrel and H. Schmidt, Ideal resistive transition of a superconductor. *Phys. Lett. A* **25,** 544 (1967).

[4] L. G. Aslamazov and A. I. Larkin, The influence of fluctuation pairing of electrons on the conductivity of normal metal. *Phys. Lett. A* **26,** 238 (1968).

[5] J. S. Shier and D. M. Ginsberg, Superconducting Transitions of Amorphous Bismuth Alloys. *Phys. Rev.* **147,** 384 (1966).

[6] R. Glover, Ideal resistive transition of a superconductor. *Phys. Lett. A* **25,** 542 (1967).

[7] M. Kosterlitz and D. J. Thouless, Two-Dimensional Physics, in *Progress in Low temperature Physics*, edited by Brewer, D. F. (North-Holland, Amsterdam, 1978), Vol. VIIB, p.371.

[8] K. Char and A. Kapitulnik, Fluctuation conductivity in inhomogeneous superconductors. *Z. Phys B* **72,** 253 (1988).

[9] B. Sacépé, C. Chapelier, T. I. Baturina, V. M. Vinokur, M. R. Baklanov, and M. Sanquer, Disorder-induced inhomogeneities of the superconducting state close to the superconductor-insulator transition. *Phys. Rev. Lett.* **101,** 157006 (2008).

[10] G. Venketeswara Pai, E. Shimshoni, and N. Andrei, Resistivity of inhomogeneous superconducting wires. *Phys. Rev. B* **77,** 104528 (2008).

[11] S. Caprara, M. Grilli, L. Benfatto, and C. Castellani, Effective medium theory for superconducting layers: A systematic analysis including space correlation effects. *Phys. Rev. B* **84,** 014514 (2011).

[12] O. Cohen, M. Ovadia, and D. Shahar, Electric breakdown effect in the current-voltage characteristics of amorphous indium oxide thin films near the superconductor-insulator transition. *Phys. Rev. B* **84,** 100507(R) (2011).

[13] G. Seibold, L. Benfatto, C. Castellani, and J. Lorenzana, Amplitude, density and current correlations of strongly disordered superconductors. *Phys. Rev B* **92,** 064512 (2015).

[14] M. H. Beutel *et al.*, Microwave study of superconducting Sn films above and below percolation. *Supercond. Sci. Technol.* **29,** 085011 (2016).

[15] C. Carbillet *et al.*, Confinement of superconducting fluctuations due to emergent electronic inhomogeneities. *Phys. Rev. B* **93,** 144509 (2016).

[16] For some recent results which favors the conventional superconducting fluctuations scenario in Al films see, D. Sóñora, C. Carballeira, J. J. Ponte, F. Vidal, T. Grenet, and J. Mosqueira, Paraconductivity of granular Al films at high reduced temperatures and magnetic fields. *Phys. Rev. B* **100,** 104509 (2019).

[17] R. Ganguly, I. Roy, A. Banerjee, H. Singh, A. Ghosal, and P. Raychaudhuri, Magnetic field induced emergent inhomogeneity in a superconducting film with weak and homogeneous disorder. *Phys. Rev. B* **96,** 054509 (2017).

[18] J. G. Bednorz and K. A. Müller, Possible high T_c superconductivity in the Ba-La-Cu-O system. *Z. Phys. B* **64,** 189 (1986).

[19] J. C. Phillips, Quantum percolation in electron cuprate superconductors $Nd_{2-x}Ce_xCuO_{4-y}$. *Phys. Rev. B* **41,**

850R (1990).
[20] J. C. Phillips, A. Saxena, and A. R. Bishop, Pseudogap, dopants, and strong disorder in cuprate high-temperature superconductors. *Rep. Prog. Phys.* **66,** 211 (2003).
[21] V. Z. Kresin, Y. N. Ovchinnikov, and S. A. Wolf, Inhomogeneous superconductivity and the pseudogap state of novel superconductors. *Phys. Rep.* **431,** 231 (2006).
[22] J. Maza and F. Vidal, Critical-temperature inhomogeneities and resistivity rounding in copper oxide superconductors. *Phys. Rev. B* **43,** 10560 (1991).
[23] R. Landauer, Electrical conductivity in inhomogeneous media, in *Proceedings of the first conference on Electrical Transport and Optical Properties in Inhomogeneous Media*, AIP Conf. Proc. Nº 40, edited by Garland, J. C. & Tanner, D. B. (AIP, New York, 1978), p. 2.
[24] S. Kirkpatrick, Percolation and conduction. *Rev. Mod. Phys.* **45,** 574 (1973). See also Ref. 6, p. 99.
[25] W. E. Lawrence and S. Doniach, Theory of layer structure superconductors, in *Proceedings of the Twelve International Conference on Low-Temperature Physics*, Tokyo, 1970, edited by E. Kanda (Keigatu, Tokyo, 1970) p. 361.
[26] T. Tsuzuki, Critical anomalies of superconducting intercalated layer compounds. *Phys. Lett. A* **37,** 159 (1971).
[27] K. Yamaji, Phenomenological theory of the increase in the superconducting transition temperature in thin film layered sandwiches. *Phys. Lett. A* **38,** 43 (1972).
[28] For an introduction to the phenomenological Gaussian-Ginzburg-Landau (GGL) descriptions of the superconducting fluctuations see, e.g., M. Tinkham, *Introduction to Superconductivity* (McGraw-Hill, New York, 1996), Chaps. 8 and 9.
[29] A. I. Larkin and A. A. Varlamov, *Theory of Fluctuations in Superconductors* (Clarendon Press, Oxford, 2005).
[30] W. J. Skocpol and M. Tinkham, Fluctuation near superconducting phase transitions. *Rep. Prog. Phys.* **38,** 1049 (1975).
[31] For a review of early experimental results on the superconducting fluctuations in optimally-doped cuprate superconductors and of their description in terms of the GGL approach for multilayered superconductors, see F. Vidal and M. V. Ramallo, Multilayering effects on the thermal fluctuations of Cooper pairs around the superconducting transition in cuprates, in *The Gap Symmetry and Fluctuations in High-T_c Superconductors*, edited by Bok, J. et al. NATO-ASI Series (Plenum, New York, 1998), p. 443.
[32] I. F. Llovo, J. Mosqueira, C. Carballeira and F. Vidal, Precursor superconducting effects in the optimally-doped $YBa_2Cu_3O_{7-\delta}$ superconductor: The confrontation between superconducting fluctuations and percolative effects revisited. *SN Applied Sciences* **4,** 110 (2022) (proceeding of the communications presented at the ICSM 2021 Conference).
[33] J. Mosqueira, C. Carballeira and F. Vidal, Fluctuation induced diamagnetism in the zero magnetic field limit in a low temperature superconducting alloy. *Phys. Rev. Lett.* **87,** 167009 (2001).
[34] C. Carballeira, J. Mosqueira, M. V. Ramallo, J. A. Veira and F. Vidal, Fluctuation-induced diamagnetism in bulk isotropic superconductors at high reduced temperatures. *J. Phys. Condens. Matter.* **13,** 9271 (2001).
[35] R. I. Rey *et al.*, The conductivity and the magnetization around T_c in optimally-doped $YBa_2Cu_3O_{7-\delta}$ revisited: quantitative analysis in terms of fluctuating superconducting pairs. *Supercond. Sci. Technol.* **32,** 045009 (2019), and references therein.
[36] F. Vidal *et al.*, On the consequences of the uncertainty principle on the superconducting fluctuations well inside the normal state. *Europhys. Lett.* **59,** 754 (2002).
[37] F. Vidal, M. V. Ramallo, J. Mosqueira, and C. Carballeira, Superconducting fluctuations above T_c and the uncertainty principle: How small may the coherence length be? *Int. J. Mod. Phys. B* **17,** 3470 (2003).
[38] J. Mosqueira, A. Pomar, A. Díaz, J. A. Veira, and F. Vidal, Resistivity anomalies above the superconducting transition in $YBa_2Cu_3O_{7-\delta}$ crystals and non-uniformly distributed critical-temperature inhomogeneities. *Physica C* **225,** 34 (1994).
[39] W. Lang, Influence of a distribution of critical temperatures on the paraconductivity and the fluctuation magnetoconductivity in high-temperature superconductors. *Physica C* **226,** 267 (1994).
[40] A. Casaca *et al.*, Model for the broadening of the resistive transition in $YBa_2Cu_3O_{7-\delta}$ thin films. *Supercond. Sci. Technol.* **10,** 75 (1997).
[41] D. V. Shantsev, M. E. Gaevski, R. A. Suris, A. V. Bobyl, V. E. Gasumyants, and O. L. Shalaev, Temperature and magnetic-field dependence of the conductivity of YBaCuO films in the vicinity of superconducting transition: Effect of T_c-inhomogeneity. *Phys. Rev. B* **60,** 12485 (1999).
[42] For a review of earlier results on structural and chemical inhomogeneities and disorder effects, with different spatial distributions, on the resistivity behavior above T_c in cuprate superconductors see, F. Vidal, J. A. Veira, J. Maza, J. Mosqueira, and C. Carballeira, On the interplay between T_c-inhomogeneities at long length scales and thermal fluctuations around the average superconducting transition in cuprates, in *High-T_c Superconductors and Related materials: Material Science, Fundamental Properties and Some Future electronic Applications*, Edited by S. L. Drechsler and T. Mishonov, Nato Science Series 3. High Technology (Kluwer Academic Publisher, The Netherlands, 2001) Vol. 86, pag.289.
[43] S. R. Currás, G. Ferro, M. T. González, M. V. Ramallo, M. Ruibal, J. A. Veira, P. Wagner, and F. Vidal, In-plane paraconductivity in $La_{2-x}Sr_xCuO_4$ thin film superconductors at high reduced temperatures: Independence of the normal-state pseudogap. *Phys. Rev. B* **68,** 094501 (2003).
[44] H. H. Wen *et al.*, Intrinsic percolative superconductivity in heavily overdoped high temperature superconductors. *Europhys. Lett.* **57,** 260 (2002).
[45] E. V. L. de Mello, E. S. Caixeiro, and J. L. González, Is the superconducting state for the cuprates reached through a percolation transition? *Act. Phys. Pol. B* **34,** 563 (2003).
[46] S. H. Naqib, J. R. Cooper, J. L. Tallon, R. S. Islam, and R. A. Chakalov, Doping phase diagram of from transport measurements: Tracking the pseudogap below T_c. *Phys. Rev. B* **71,** 054502 (2005).
[47] R. Seto, R. Botet, and H. Kuratsuji, Excess conductivity in high-T_c superconducting films: Role of smooth doping disorder. *Phys. Rev. B* **73,** 012508 (2006).
[48] U. K. Mohapatra, R. Biswal, D. Behera, and N. C. Mishra, Fluctuation conductivity and inhomogeneity in

granular $YBa_2Cu_3O_{7-y}$/Ag composite thick films. *Supercond. Sci. Technol.* **19,** 635 (2006).

[49] L. Benfatto, C. Castellani, and T. Giamarchi, Broadening of the Berezinskii-Kosterlitz-Thouless superconducting transition by inhomogeneity and finite-size effects. *Phys. Rev. B* **80,** 214506 (2009).

[50] J. Mosqueira, L. Cabo, and F. Vidal, Structural and T_c inhomogeneities inherent to doping in $La_{2-x}Sr_xCuO_4$ superconductors and their effects on the precursor diamagnetism. *Phys. Rev. B* **80,** 214527 (2009).

[51] J. Mosqueira, J. D. Dancausa, and F. Vidal, Diamagnetism above the superconducting transition in underdoped $La_{1.9}Sr_{0.1}CuO_4$: Chemical disorder versus phase incoherent superconductivity. *Phys. Rev. B* **84,** 174518 (2011).

[52] N. Cotón, B. Mercey, J. Mosqueira, M. V. Ramallo, and F. Vidal, Synthesis from separate oxide targets of high quality $La_{2-x}Sr_xCuO_4$ thin films and dependence with doping of their superconducting transition width. *Supercond. Sci. Technol.* **26,** 075011 (2013).

[53] G. Campi, A. Ricci, N. Poccia, and A. Bianconi, Two-dimensional nano-granularity of the oxygen chains in the $YBa_2Cu_3O_{6.33}$ superconductor. *J. Supercond. Nov. Magn.* **29**, 3023 (2016).

[54] N. Cotón, M. V. Ramallo, and F. Vidal, Critical temperatures for superconducting phase-coherence and condensation in $La_{2-x}Sr_xCuO_4$. Preprint at `https://doi.org/10.48550/arXiv.1309.5910` (2013).

[55] G. Campi *et al.*, Inhomogeneity of charge density wave order and quenched disorder in a high T_c superconductor. *Nature* **525,** 359 (2015).

[56] S. H. Naqib and R. S. Islam, In-plane paraconductivity of optimally-doped and slightly overdoped cuprates: implications and origin of the pseudogap. *Supercond. Sci. Technol.* **28,** 065004 (2015).

[57] N. Zaki, H. B. Yang, J. D. Rameau, P. D. Johnson, H. Claus, and D. G. Hinks, The cuprate phase diagram and the influence of nanoscale inhomogeneities. *Phys. Rev. B* **96,** 195163 (2017).

[58] S. S. Seidov, K. K. Kesharpu, P. I. Karpov, and P. D. Grigoriev, Conductivity of anisotropic inhomogeneous superconductors above critical temperature. *Phys. Rev. B* **98,** 014515 (2018).

[59] D. Pelc *et al.*, Emergence of superconductivity in cuprates via a universal percolation process. *Nat. Commun.* **9,** 4327 (2018).

[60] P. Popcevic *et al.*, Percolative nature of the direct current paraconductivity in the cuprate superconductors. *npj Quantum Mater.* **3,** 42 (2018).

[61] D. Pelc, M. J. Veit, C. J. Dorow, Y. Ge, N. Barišić, and M. Greven, Resistivity phase diagram of cuprates revisited. *Phys. Rev. B* **102,** 075114 (2020).

[62] H. Richter it et al., Resistivity, Hall effect, and anisotropic superconducting coherence lengths of $HgBa_2CaCu_2O_6$ thin films with different morphology. *Supercond. Sci. Technol.* **34,** 035031 (2021).

[63] A. S. Borna, R. S. Islam, and S. H. Naqib, Hole content dependent fluctuation diamagnetism in $YBa_2Cu_3O_{7-\delta}$: possible role of the pseudogap. *J. Supercond. Nov. Magn.* **35,** 49 (2022).

[64] J. A. Campá, E. Gutiérrez-Puebla, M. A. Monge, I. Rasines, and C. Ruiz-Valero, Single-crystal growth of superconducting $Bi_2Sr_2CaCu_2O_8$ using rotary crucibles. *J. Cryst. Growth* **125,** 17 (1992).

[65] A. Maignan *et al.*, A crystal study of the 128 K superconductor $Tl_2Ba_2Ca_2Cu_3O_{10-\delta}$ synthesis and anisotropic magnetic properties. *Physica C* **219,** 407 (1994).

[66] J. Viña *et al.*, Universal behavior of the in-plane paraconductivity of cuprate superconductors in the short-wavelength fluctuation regime. *Phys. Rev. B* **65,** 212509 (2002).

[67] B. Leridon *et al.*, Protected superconductivity at the boundaries of charge-density-wave domains. *New J. Phys.* **22,** 073025 (2020).

[68] K. Maki and R. S. Thompson, Fluctuation conductivity in high T_c superconductors. *Phys. Rev. B* **39,** 2767 (1989).

[69] R. A. Klemm, Phenomenological model of the cooper oxide superconductors. *Phys. Rev. B* **41,** 2073 (1990).

[70] See e.g., K. G. Wilson, The renormalization group and critical phenomena, Rev. Mod. Phys. **55**, 583 (1983), and referenced therein.

[71] P. G. De Gennes, *Superconductivity of Metals and Alloys* (New York: W. A. Benjamin, 1999). Chap. 1-4.

[72] M. V. Ramallo, A. Pomar, and F. Vidal, In-plane paraconductivity and fluctuation-induced magnetoconductivity in biperiodic layered superconductors: Application to $YBa_2Cu_3O_{7-\delta}$. *Phys. Rev. B* **54,** 4341 (1996).

[73] W. L. Johnson, C. C. Tsuei, and P. Chaudhari, Paraconductivity of three-dimensional amorphous superconductors: evidence for a short-wavelength cutoff in the fluctuation spectrum. *Phys. Rev. B* **17,** 2884 (1978).

[74] P. P. Freitas, C. C. Tsuei, and T. S. Plaskett, Thermodynamic fluctuations in the superconductor $Y_1Ba_2Cu_3O_{7-\delta}$: Evidence for three-dimensional superconductivity. *Phys. Rev. B* **36,** R833 (1987).

[75] W. C. Lee, R. A. Klemm, and D. C. Johnston, Superconducting Fluctuation Diamagnetism above T_c in $YBa_2Cu_3O_7$, $La_{1.8}Sr_{0.2}CuO_4$ and $Bi_{2-x}Pb_xSr_2CaCu_2O_{8+\delta}$. *Phys. Rev. Lett.* **63,** 1012 (1989).

[76] A. Gauzzi and D. Pavuna, Evidence for nonuniversal behavior of paraconductivity caused by predominant shot-wavelength Gaussian fluctuations in $YBa_2Cu_3O_{6.9}$. *Phys. Rev. B* **51,** 15420 (1995). The non-universality observed by these authors in different almost optimally YBCO samples with the same nominal composition may be caused by non-intrinsic chemical and structural inhomogeneities (see Refs. 38–43).

[77] B. R. Patton and J. W. Wilkins, Problems in constructing a proper theory for fluctuation-induced diamagnetism in a superconductor. *Phys. Rev. B* **6,** 4349 (1972).

[78] M. Suzuki and M. Hikita, Resistive transition, magnetoresistance, and anisotropy in $La_{2-x}Sr_xCuO_4$ single-crystal thin films. *Phys. Rev. B* **44,** 249 (1991).

[79] J. Mosqueira, E. G. Miramontes, C. Torrón, J. A. Campá, I. Rasines, and F. Vidal, F. Thermal fluctuation effects on the magnetization above and below the superconducting transition in $Bi_2Sr_2CaCu_2O_8$ crystals in the weak magnetic field limit. *Phys. Rev. B* **53,** 15272 (1996).

[80] J. Mosqueira, L. Cabo, F. Vidal, Diamagnetism around the Meissner transition in a homogeneous cuprate single crystal. *Phys. Rev. B* **76,** 064521 (2007).

[81] 2D superconducting fluctuations were first observed in cuprate superconductors in Bi-2212 compounds, see, F. Vidal *et al.*, Excess electrical conductivity in polycrystalline Bi-Ca-Sr-Cu-O compounds and thermodynamic fluctuations of the amplitude of the superconducting or-

der parameter. *Physica C* **156,** 807 (1988).
[82] X. Obradors, A. Labarta, J. Tejada, M. Vallet, and J. M. González-Calbet, Meissner effect and critical fields in an inhomogeneous $Ba_2HoCu_3O_{7-x}$ high T_c superconductor, Phys. Rev. B **38**, 2455 (1988).
[83] A. Schilling, M. Cantoni, J. D. Guo, and H. R. Ott, Superconductivity above 130K in the Hg-Ba-Ca-Cu-O system, Nature **363**, 56 (1993).
[84] J. Hofer *et al.*, Doping dependence of superconducting parameters in $HgBa_2CuO_{4+\delta}$ single crystals. *Physica C* **297,** 103 (1998).
[85] K. E. Gray, D. H. Kim, B. W. Veal, G. T. Seidler, T. F. Rosenbaum, and D. E. Farrell, High anisotropy and a dimensionality crossover in the irreversibility behavior of oxygen-deficient $YBa_2Cu_3O_{7-y}$. *Phys. Rev. B* **45,** 10071 (1992).
[86] B. Leridon, J. Vanacken, T. Wambecq, and V. V. Moshchalkov, Paraconductivity of underdoped $La_{2-x}Sr_xCuO_4$ thin-film superconductors using high magnetic fields, Phys. Rev. B **76**, 012503 (2007).
[87] S. Caprara, M. Grilli, B. Leridon, and J. Lesueur, Extended paraconductivity regime in underdoped cuprates, Phys. Rev. B **72**, 104509 (2005).
[88] B. Leridon, A. Défossez, J. Dumont, and J. Lesueur, Conductivity of Underdoped $YBa_2Cu_3O_{7-\delta}$: Evidence for Incoherent Pair Correlations in the Pseudogap Regime, Phys. Rev. Lett. **87**, 197007 (2001).

Chapter 4

Discussion

4.1 Results on iron-based superconductors

4.1.1 On the multiband structure of $Ba(Fe_{1-x}Co_x)_2As_2$

The issue of the anomalous anisotropic dependency of the upper critical field in 122 family IBS and our proposal to solve this problem on the basis of multiple bands which contribute to superconductivity in these materials was developed in Ref. [88], *Multiband effects on the upper critical field angular dependence of 122family iron pnictide superconductors*. In this paper, we firstly analyzed the $\rho(T)_{H,\theta}$ curves near the superconducting transition temperature, where θ is the angle formed between the applied magnetic field H and the crystal c–axis. The experimental $\rho(T)_{H,\theta}$ curves can be seen in Fig. 1 of Ref. [88]. For $H = 0$, we could estimate the transition temperature $T_c = 22.7 \pm 0.5$ K from the maximum of the temperature derivative of ρ. However, this transition temperature $T_c(H)$ is displaced to lower temperatures with increasing field. This effect can be observed for all θ, and due to the anisotropy of the samples, the displacement observed is larger for $\theta \to 0°$. For 5 and 9 T, extensive magnetoresistance measurements were made, with θ ranging from 0° to 90° in 3° steps, while for 0.5, 1, 2, 3 and 7 T, the spacing between data series is 15°.

Let us first comment that, while a rough estimation of $H_{c2}(T,\theta)$ can indeed be extracted from the displacement of the superconducting transition, this estimation is strongly dependent on the criterion used to determine $H_{c2}(T,\theta)$, as explained in Section 2.1. For this reason, a criterion-independent analysis based on the resistivity rounding above $T_c(H,\theta)$ is desirable instead. We have proposed one such method, which has allowed us to extract $H_{c2}(T,\theta)$ from the paraconductivity data and which significantly reduces the uncertainty of $H_{c2}(T,\theta)$ compared to the usual criterion method. As a consistency test, we have also shown that the data obtained with our method is compatible with the usual procedure to obtain $H_{c2}(T,\theta)$.

In order to obtain the paraconductivity data, a background subtraction process was first followed. The sample used for this work has a strongly linear normal state

background resistivity, which made background subtraction more streamlined. In this case, the background resistivity was obtained as a linear fit above 35 K ($\sim 1.5T_c$). The fluctuation effects above this temperature have been previously observed to be negligible in other iron pnictides. [106–110] This procedure was repeated for each magnetic field intensity and orientation data series, from which the paraconductivity $\Delta\sigma(T)_{H,\theta}$ was obtained by subtracting the calculated background conductivity $1/\rho_B(T)_{H,\theta}$ from the experimental conductivity $1/\rho(T)_{H,\theta}$. Some examples of the procedure followed for background subtraction are provided in Figs. 2 (a – c) of Ref. [88].

From the extracted paraconductivity data, a first analysis using $\theta = 0$ data series was made, to obtain the superconducting parameters of the sample. The data series for $\mu_0 H = 2 - 9$ T were fit to a model of superconducting fluctuations developed in Ref. [106], which extended the 3D-Gaussian-Ginzburg-Landau model to finite magnetic fields based and includes the aforementioned total energy cutoff. The final expression for the paraconductivity with $H \perp ab$ reads

$$\Delta\sigma(\varepsilon, h) = \frac{e^2}{32\hbar\pi\xi_c(0)}\sqrt{\frac{2}{h}}\int_0^{\sqrt{\frac{c-\varepsilon}{2h}}} \mathrm{d}x \left[\psi^1\left(\frac{\varepsilon+h}{2h}+x^2\right) - \psi^1\left(\frac{c+h}{2h}+x^2\right)\right], \tag{4.1}$$

where $\varepsilon \equiv \ln(T/T_c)$ is the reduced temperature, $h \equiv H/H_{c2}^{\perp}$ is the reduced magnetic field, $H_{c2}^{\perp}$ is the linear extrapolation to $T = 0$ K of the upper critical field for $H \perp ab$, e is the electron charge, $\xi_c(0)$ is the c–axis coherence length amplitude and c is the cutoff constant, which corresponds to the reduced temperature where the superconducting fluctuations vanish. The classical Aslamazov-Larkin expression is recovered from Eq. (4.1) when $c \to \infty$ and $h \ll \varepsilon$. As shown in Figs. 2 (a – c) of Ref. [88], we observed that the resistivity data curves begin to deviate from the background linear fits when $T < 30 - 31$ K, from which we calculated that the cutoff constant in this system is $c \approx 0.3$, which is consistent with the values obtained in other iron-based superconductors. [106–110] With the cutoff constant set to $c = 0.3$, we performed a simultaneous fit of Eq. (4.1) to all the $\theta = 0$ data for $\mu_0 H = 2$, 3, 5, 7 and 9 T. It is worth mentioning that the data at small magnetic fields show a discrepancy with the paraconductivity predicted by the Gaussian-Ginzburg-Landau approach, a phenomenon that has been previously observed in other IBS, and which has been attributed to diverse causes such as T_c distributions [106, 107] or phase fluctuations. [188–190] For this reason, data with $\mu_0 H < 2$ T were not included in our analysis. The free parameters of this fit are just two, the coherence length in the c direction ξ_c, and the upper critical field with $\theta = 0$, $H_{c2}^{\perp}$, implicit in h. As shown in Fig. 2 (d) of Ref. [88], where the solid lines represent the best fit of Eq. (4.1) for $\xi_c(0) = 6.89 \pm 0.15$ Å and $\mu_0 H_{c2}^{\perp} = 39.9 \pm 0.4$ T, the agreement of this model with our data is excellent.

After this preliminary analysis, a more in-depth analysis of the angular anisotropy was made for the highest measured magnetic field, 9 T, which shows the maximum displacement with θ of our data. The paraconductivity $\Delta\sigma(\varepsilon, \theta)$ of each orientation series was obtained with the aforementioned procedure, so Eq. (4.1) could

be compared with the experimental data by setting $h = H/H_{c2}(\theta)$, where $H_{c2}(\theta)$ is the upper critical field extrapolated to 0 K for a given θ field orientation. [111] The values of $\xi_c(0)$ and c were fixed from the previous analysis, so only one parameter per data series was kept free, $H_{c2}(\theta)$. Fig. 3 of Ref. [88] shows the result of the fits for $\mu_0 H = 9$ T, along with the obtained values of $H_{c2}(\theta)$. The values of $\mu_0 H_{c2}(\theta)$ obtained from the fit range from 43 T for $H \perp ab$ and 120 T for $H \parallel ab$, and the corresponding slopes at T_c, -1.9 T/K for $H \perp ab$ and -5.3 T/K for $H \parallel ab$, are close to the ones found in the literature. [191–196] The $\mu_0 H_{c2}(\theta)$ curve obtained, represented in Fig. 3 (b) of Ref. [88], is well behaved and monotonically increases with θ, and the orange line shown in this figure corresponds to the 3D-aGL model, Eq. (2.1), which was directly evaluated with the experimental values of $H_{c2}^{\perp}$ and $H_{c2}^{\parallel}$. For comparison, Tinkham's calculation in the 2D limit, which is also only dependent on the experimental data for $H_{c2}^{\perp}$ and $H_{c2}^{\parallel}$, is also shown as a green line, given by [197, 198]

$$\left|\frac{H_{c2}(\theta)\cos\theta}{H_{c2}^{\perp}}\right| + \left(\frac{H_{c2}(\theta)\sin\theta}{H_{c2}^{\parallel}}\right)^2 = 1 \ . \tag{4.2}$$

As shown, the experimental data are not well explained by either the 3D and 2D calculations. However, the best fit to a quasi-2D calculation by Mineev, [199]

$$\frac{H_{c2}^2(\theta)\sin^2\theta}{H_{c2}^{\parallel 2}}\left(1 - \frac{H_{c2}^{\parallel}}{\gamma H_{c2}^{\perp}}\right) + \frac{H_{c2}(\theta)}{H_{c2}^{\perp}}\sqrt{\cos^2\theta + \frac{\sin^2\theta}{\gamma^2}} = 1 \ , \tag{4.3}$$

does fit the data in the whole range of data, shown as a grey line. In this calculation, the anisotropy factor $\gamma = (m_c^*/m_{ab}^*)^{1/2}$ differs from the experimental anisotropy factor $H_{c2}^{\parallel}/H_{c2}^{\perp}$. Fig. 3 (c) of Ref. [88] shows the obtained $H_{c2}(\theta)$ in linealized form $[H_{c2}(\theta = 0)/H_{c2}(\theta)]^2$ vs $\sin^2(\theta)$, which helps visualize the results in the medium range, with the aforementioned models for 3D-aGL, 2D-aGL and Mineev's result for 2D layered superconductors. Nevertheless, the value of $\gamma = 16.5$ required to fit the data is unjustifiably large for the phenomenology of these superconductors, which is not consistent with fully 3D nature of $\Delta\sigma$ at all temperatures above T_c. For comparison, optimally doped $YBa_2Cu_3O_{7-\delta}$ has a rather large anisotropy factor of $\gamma \approx 10$, and this system shows crossover dimensionality at temperatures close to T_c. [7] This suggests that the agreement of the layered quasi-2D calculation with the data may be spurious.

However, all previous analyses of the angular dependency of $Ba(Fe_{1-x}Co_x)_2As_2$ have not considered that multiple bands may be contributing to the superconductivity in these materials, [200] evidenced in experiments such as angle-resolved photoemission spectroscopy (ARPES) [201] and point-contact Andreev reflection. [202] Moreover, models based on two-band superconductivity have been shown to be able to explain anomalous experimental dependencies with temperature of the magnetic penetration depth [55, 203–209] and of the specific heat. [55, 56] Nevertheless, the seeming agreement with a quasi-2D approach has precedents as well, as the appearance of multiple superconducting gaps has been shown to affect certain observables similarly. [210]

Our main contribution in this paper is that, for the first time, we showed that two-band models can account for the anomalous $H_{c2}(\theta)$. Even before the discovery of IBS, Gurevich calculated the angular dependency of two-band superconductors to describe the angular anisotropy of superconductors such as MgB_2 [103,104] in both the dirty [113] and clean limits. [58,114] The criterion to decide if our superconductor is closer to the dirty ($\xi_0 >> l$) or clean ($\xi_0 << l$) limit can be obtained from the BCS expression $\xi_0/v_F \equiv \hbar/\pi\Delta(0)$, where $\Delta(0)$ is one half of the energy gap at $T = 0$ K and v_F the Fermi. [7] This expression can be directly compared with the the quasiparticle relaxation time $\tau = l/v_F$, where l is the mean free path and v_F the Fermi velocity. As an estimation, we can use that the system has been reported to present two superconducting gaps of $\Delta_1(0) \sim 3k_BT_c$ and $\Delta_2(0) \sim 6k_BT_c$. [56, 201–203, 205, 207, 208] So, with these values of $\Delta(0)$, we obtain $\hbar/\pi\Delta(0) \sim (7 - 3.5) \times 10^{-14}$ s, while $\tau \sim (1 - 2) \times 10^{-14}$ s near T_c. [211, 212]. Therefore, our system is closer to the dirty limit, [113] in which the expression for $H_{c2}(\theta)/H_{c2}(0)$ can be expressed in simple terms (see Ref. [88] for details) as

$$\frac{H_{c2}(\theta)}{H_{c2}(0)} = \frac{1+\delta}{\sqrt{\cos^2\theta + \gamma_1^{-2}\sin^2\theta} + \delta\sqrt{\cos^2\theta + \gamma_2^{-2}\sin^2\theta}}\,, \tag{4.4}$$

with $\gamma_{1,2}$ the anisotropy of each band and δ the relative contribution of the second band. The resulting curve of the best fit of Eq. (4.4) to our $H_{c2}(\theta)$ data, with $\delta = 0.61 \pm 0.21$, $\gamma_1 = 8.7 \pm 2.2$ and $\gamma_2 = 1.28 \pm 0.16$ is shown as a solid red line in Fig. 3 (d) of Ref. [88]. The agreement is excellent for all θ. These results seem to indicate that one band may be almost isotropic, while the other band may be significantly more anisotropic, causing the overall angular anisotropy of the sample, and that both bands contribute similarly to the superconductivity. However, as we have already discussed, OP-BaFeCoAs is not strictly in the dirty limit, so the $\gamma_{1,2}$ values we have obtained may not be accurate to the actual band anisotropies. As a consistency check, the usual method used by most authors to obtain $H_{c2}(T)(\theta)$, obtaining percentual cuts of the resistive transition and extrapolating the data linearly to $T = 0$ K, was also used. As shown in Fig. 4 of Ref. [88], the H_{c2} amplitude obtained from this method is strongly dependent on the percent chosen, although the results obtained for small percentages (15-50%) are similar to the ones obtained from our method based on fluctuation effects, with slight deviations at high θ but well within the high uncertainty of the procedure.

Another part of our study centers on the temperature dependence of the anisotropy factor γ found in multiple studies in IBS. [213–217] In these works, γ is often obtained using a 3D-aGL scaling of $\rho(T)_{H,\theta}$ versus $H(\cos^2\theta + \sin^2\theta/\gamma^2)^{1/2}$. We argue this scaling may be flawed, as our analysis shows that the 3D-aGL dependency is not applicable to this system. As shown in Fig. 5 (b) of Ref. [88], an almost linear, strong dependency of $\gamma(T)$ is required to make the data scale. However, restricting the scaling to $\theta < 60°$, where the 3D-aGL calculation is a good approximation, shows much better results with a constant γ (see Fig. 5 (c) of Ref. [88]). A similar result was found in $Ba_{1-x}Na_xFe_2As_2$ ($x = 0.35 - 0.4$), after excluding θ data close to 90°, [217] which the authors attributed to a crossover from 3D to 2D behavior.

However, we have shown that our paraconductivity data are strongly consistent with an almost 3D system with the experimental data for all θ.

Finally, the irreversibility field $H_{irr}(\theta)$ was also studied in this paper. In this case, $H_{irr}(\theta)$ was obtained from the 1% cuts of $\rho_B(T_c)$, and the resulting $H_{irr}(T)$ data are shown in Fig. 6 (a) of Ref. [88], next to the best (simultaneous) fits of the power law $H_{irr} = A(\theta)(T_c - T)^n$ to all the data series (θ in 15° intervals) with $A(\theta)$ and n as free parameters. From these fits, we obtained $n = 1.30 \pm 0.14$, a result that is close to the value found in other IBS, [218, 219] as well as in cuprates. [220, 221] Having reduced this degree of freedom, we applied the same fits to the data series for which we had much smaller θ–intervals of 3°, 5 T and 9 T by fixing the value of n previously obtained, as shown in Fig. 6 (b) of Ref. [88]. From this last analysis, we obtained the angular dependency of H_{irr} for various temperatures, represented in Fig. 6 (c) of Ref. [88]. Unlike the results for H_{c2}, the irreversibility field does not show an anomalous dependency versus θ, following instead the 3D-aGL dependency closely. Fig. 6 (d) of Ref. [88] shows the excellent scaling of the $H_{irr}(\theta)$ data with the 3D-aGL model, which was obtained for $\gamma = H_{irr}^{\parallel}/H_{irr}^{\perp} = 3.27$. Although the discrepancy with the $H_{c2}(\theta)$ behavior is notorious, one possible explanation is that the vortex pinning is not appreciably affected by the band structure of the material.

4.1.2 On the vortex dynamics of $Ca_{0.82}La_{0.18}Fe_{0.96}Ni_{0.04}As_2$

To investigate the origin of the second magnetization peak in the more anisotropic $Ca_{0.82}La_{0.18}Fe_{0.96}Ni_{0.04}As_2$, we studied the magnetization hysteresis curves $M(H)$ of this system as a function of temperature and applied magnetic field, and the magnetic relaxation as a function of time. The results of this study are published in Ref. [89], titled *Vortex dynamics and second magnetization peak in the iron-pnictide superconductor* $Ca_{0.82}La_{0.18}Fe_{0.96}Ni_{0.04}As_2$.

Firstly, the isothermal magnetic hysteresis $M(H)$ was measured at multiple constant temperatures. Fig. 1 of Ref. [89] shows the $M(H)$ curves obtained for (a) $H \parallel c$ and (b) $H \parallel ab$, where our data display a pronounced SMP with $H \parallel c$ at all temperatures, even for $T \to T_c$. However, with $H \parallel ab$, the SMP could only be observed in the temperature region above 7.5 K. Additionally, $M(t)_{H,T}$ measurements were taken for span times up to 80 min (only for $H \parallel c$, as our signal-to-noise ratio was too low for $H \parallel ab$). The resulting curves can be observed in Fig. 2 of Ref. [89] for different T and H values.

From the isothermal relaxation measurements, a change in the curvature of the relaxation rate $R(H) = d\ln(M(H))/d\ln(t)$ could be observed near H_{on} and H_p, the onset and peak of the SMP, respectively, suggesting changes in the pinning behavior may be taking place in these regions. [123, 125, 222] For a first study of this change in behavior, collective pinning theory can be used to try to shed light into the change of pinning mechanism. According to this theory, the activation energy U_0 can be roughly described by

$$U_0 \approx (1/J_c)^{\mu}\ , \tag{4.5}$$

where J_c is the critical current and μ is a critical exponent. [151,223] This exponent contains information about the pinning collective behavior: $\mu = 1/7$ corresponds to the pinning of single vortices, $\mu = 3/2$ to small bundles of vortices and $\mu = 7/9$ to large bundles. Using Beans critical-state model, the $J_c(H)$ curves were estimated for our sample with $H \parallel c$. [224–226] The resulting $J_c(H)$ and $U_0(1/J_c)$ curves can be seen in Fig. 3 of Ref. [89], revealing a pronounced peak near H_p. We found two different behaviors occurring for all isofield curves. Below H_p, the exponent $\mu \approx 1$ for $H = 10, 15$ kOe and $\mu = 0.63$ for $H = 20$ kOe, suggesting that the vortex lattice was pinned as small and large bundles. However, above H_p we observed $\mu \sim -0.4$, which cannot be explained in terms of collective pinning theory. This behavior has instead been associated with plasticity of the vortex lattice, with -0.5 as the characteristic exponent, indicating that the mechanism responsible for the SMP in our sample could be a crossover from collective to plastic pinning. [124, 128] It is worth mentioning that this behavior has also been observed in systems that do not present a SMP. [140]

From the temperature dependencies of H_p, H_{on} and the irreversibility magnetic field H_{irr}, some additional information regarding the dimensionality of this system can also be inferred. These curves are shown together in the phase diagram represented in Fig. 4 of Ref. [89]. Both the $H_p(T)$ and $H_{irr}(T)$ curves were observed to be well described by a power law behavior $(1 - (T/T_c))^n$, with $n = 2$ for $H_p(T)$ and $n = 1.3$ for $H_{irr}(T)$ respectively. [221] However, for $H_{on}(T)$ this is not true, observing that the curve followed opposite curvature to that of H_p at low T. This opposite curvature may eventually lead to the merging of H_p and H_{on} lines below 2 K (not achievable with our experimental setup); such merging at high fields would imply the disappearance of the SMP, which in the present case of a highly anisotropic system, could be associated to a possible field-induced crossover to a 2D vortex system.

A more in-detail analysis of the activation energy can be obtained by analyzing the isofield $M(t)$ curves with the method developed by Maley et al. [152, 154] The determination of the activation energy $U(M)$ for each isofield curve can be then made by assuming that the activation energy must be a smooth function of the hysteresis $M - M_{eq}$, being the equilibrium magnetization M_{eq} the average of the two branches $M(H) > 0$ and $M(H) < 0$ at a given H. In our system, $M - M_{eq} \approx M$, so $U(M)$ can be obtained as

$$U(M) = -T \ln(dM/dt) + CT \,, \tag{4.6}$$

where T is the temperature, dM/dt the relaxation rate of M, and C is a constant which makes the data scale. However, McHenry et al. suggested that, to make $U(M)$ scale in some systems, it must be divided by a suitable scaling function $g(T/T_c)$; a usual choice being $g(T/T_c) = (1 - T/Tc)^{3/2}$ which accounts for the dependency of the coherence length, and has been shown to describe the behavior of both IBS and cuprates. [126, 153] After performing this scaling, $C = 15$ was selected to obtain a smooth curve, as shown in Fig. 5 of Ref. [89]. With this value of C, $U(M)$ can then be obtained for isothermal $M(H)$ both below and above H_p. This analysis allowed

us to observe two clearly different behaviors for $U(M)$ across H_p, as shown in Fig. 6 of Ref. [89] for $T = 12$ K data. This evidences that the mechanism behind H_p is indeed a change in pinning behavior, from collective to plastic pinning, similarly to what has been observed in $Ba(Fe_{1-x}Co_x)_2As_2$. [123, 130, 227]

For vortex pinning analysis, another useful observable is the remanent critical current $J_c(H = 0)$. This magnitude can be obtained by subtracting the negative branch of the isothermal curves $M(H)^-$ from the positive branch $M(H)^+$ and introducing the resulting $\Delta M = M(0)^+ - M(0)^-$ to the calculation of Beans critical current. The normalized remanent critical current density $J_c(H = 0, T)/J_c(H = 0, T = 0\text{ K})$, where $J_c(0)$ is the value extrapolated to $T = 0$ K, can be then compared to theoretical calculations for different types of pinning. For δl pinning, $J_c(H = 0, T)/J_c(H = 0, T = 0\text{ K}) \sim (1 - t^2)^{5/2}(1 + t^2)^{-1/2}$, while for δT_c pinning, $J_c(H = 0, T)/J_c(H = 0, T = 0\text{ K}) \sim (1 - t^2)^{7/6}(1 + t^2)^{5/6}$ where $t = T/T_c$. [228] Fig. 7 (a) of Ref. [89] evidences that, as observed in other pnictides, the pinning mechanism cannot be explained by the two aforementioned dependencies, a behavior that has been attributed to weak and strong pinning occurring at low and high magnetic fields respectively. [124, 228, 229]

Our findings are reinforced by a scaling analysis of the normalized pinning force density $F_p(H)/F_p^{max}$ vs reduced field $h = H/H_{irr}$, where $F_p = H \times J_c$, [230–232] as shown in Fig. 7 (b) of Ref. [89]. From this scaling analysis, the magnetic field at which maximum of the pinning force density occurs, h_{max}, could be obtained. All curves were found to scale well, so the data were fit to Dew-Hughes expression, $F_p(H)/F_p^{max} \sim h^p(1 - h)^q$, where the critical exponents p and q are associated to the type of pinning. [230, 231] This model predicts $p = 1$, $q = 2$ for δl pinning due to point disorder, leading to $h_{max} = 0.33$. We obtained $p = 2$ and $q = 5.5$ for our sample, and $h_{max} = p/(p + q) \sim 0.27$, consistent with the h_{max} expected for δl pinning. However, the higher values of p and q and slightly lower h_{max} may suggest an additional pinning contribution, perhaps caused by surface defects. [125, 233–235]

4.1.3 On the increased surface pinning of $BaFe_2(As_{1-x}P_x)_2$

The effect of an increment of surface rugosity in two crystals of $BaFe_2(As_{1-x}P_x)_2$, close to the optimally doped P content, was studied in Ref. [92], titled *Enhancement of the critical current by surface irregularities in Fe-based superconductors*.

In this paper, the crystals were first characterized by x-ray diffraction, to prove their structural quality, as shown in Fig. 1 of Ref. [92]. Their magnetic susceptibility vs temperature $\chi(T)$ curves were also measured at very low fields (~ 0.3 mT), to show their diamagnetic properties, evidencing a sharp transition with $T_c \approx 27$ K. Both samples have almost rectangular shape, which facilitated the data treatment. The diamagnetic transition of both samples, as well as an inset with the pictures taken to estimate their dimensions, are shown in Fig. 2 of Ref. [92]. As can be seen, the ΔT_c widths are under 1 K, demonstrating their stoichiometric purity.

Following the initial characterization, the isothermal magnetic moment hyster-

esis $m(H)$ of the pristine crystals was measured at multiple temperatures, ranging 5 K to 27 K and up to applied magnetic fields $\mu_0 H = 7$ T with $H \parallel c$, after which the samples were subject to a process of abrasive sandblasting with silica sand at low pressure (1 bar), inducing rugosity in the sample surface. AFM micrographs of the surface of the samples are shown Fig. 3 of Ref. [92], where the pristine crystals in (a) are shown to be very flat down to the ~ 50 nm scale, and a notoriously more rough surface can be observed after the sandblasting process in (b), with peaks and valleys with typical dimensions ~ 5 µm width and ~ 1 µm depth (notice the change in z scale). Crystal 2 was subject to the process on both of its faces, while only one of the surfaces on crystal 1 was sandblasted. After the sandblasting processs, the $m(H)$ curves were measured again at the same temperatures and fields, and compared with the pristine results. A change in hysteresis amplitude could be directly observed from the raw data for all temperatures and at all fields, as can be seen in Fig. 4 of Ref. [92]. By subracting the positive branch from the negative branch of $m(H)$ to estimate the paramagnetic contribution, and removing this contribution from the raw data, the magnetization curves $M(H) = m(H)/V$ were obtained, as shown in Fig. 5 of Ref. [92]. The effect of surface rugosity is dramatic, and for temperatures close to T_c the increase in magnetization reaches a factor ~ 2. An increase of the irreversibility field H_{irr} was also observed, which suggests that stronger pinning may also be taking place.

From the $m(H)$ hysteresis data obtained with pristine samples, the critical current density in the *ab*–layers was estimated using a Bean-like surface current distribution in the critical-state [224–226] when $H \parallel c$, which for a crystal of dimensions $L_a > L_b > L_c$ can be estimated as

$$J_c = \frac{2m_h/V}{L_b\,(1 - L_b/3L_a)}\,, \tag{4.7}$$

where $V = L_a L_b L_c$. [226] The increased hysteresis amplitude after sandblasting Δm_h can be understood to arise from non-dissipative currents which occur at the surface and which are sustained by the surface irregularities. [70] This is caused by the multiple ways that vortices can bend in a region near the surface, of typical length λ_L, the London penetration length. Therefore, each sandblasted surface perpendicular to the magnetic field of the sample can support an additional non-dissipative current, which cannot occur in flat samples. The magnetic moment m_s due to these currents is given by

$$m_s = \frac{1}{2}\int_{surface} (\vec{r} \times \vec{K})\, d\vec{S}\,, \tag{4.8}$$

where $\vec{K}$ is the surface current density. In the critical state (i.e., when the superconductor carries the maximum current it can withstand), this corresponds to $\vec{K}_c$, the critical surface current density. Therefore, the increased hysteresis amplitude due to the surface Δm_h can be obtained as

$$\Delta m_h = \left| \int_{surface} (\vec{r} \times \vec{K}_c)\, d\vec{S} \right|\,. \tag{4.9}$$

This equation can be evaluated with a Bean-like current distribution $\vec{K}_c$, resembling the expected bulk distribution (as shown in the inset of Fig. 2 (b) of Ref. [92]), obtaining the m_h contribution of each of the sandblasted surfaces,

$$\Delta m_h = \frac{K_c L_b^3}{2}\left(\frac{L_a}{L_b} - \frac{1}{3}\right) . \tag{4.10}$$

The resulting J_c and K_c curves from Eqs. (4.7) and (4.10) respectively are shown in Fig. 6 of Ref. [92]. At low temperatures, both of these two critical currents follow a decreasing trend with temperature. However, there are significant differences which are worth mentioning, and which suggest that the mechanics of the increased pinning can be truly attributed to a surface effect instead of just an increase of bulk pinning. Firstly, J_c decreases substantially faster than K_c at lower temperatures, which in turn shows an almost linear tendency. Also, while the J_c data present the characteristic wide critical current bump corresponding to the SMP, the calculated K_c data evidences a sharp peak instead, much closer to the irreversibility temperature T_{irr}. This so-called *peak effect*, which has also been observed in both low-T_c superconductors [236, 237] and high-T_c cuprates, [238] has been attributed to the different T–dependence of pinning and elastic forces near the upper critical field line $H_{c2}(T)$. [239]

To complete our analysis, a calculation was made using Mathieu-Simon continuum theory of the mixed state for the non-dissipative surface current that a rough surface can withstand with $H \parallel c$. [168] Assuming that our samples are in the intermediate magnetic fields range (i.e., in the region between H_{c_1} and H_{c2}, the two critical fields of a type-II superconductor, and far from both these two fields), [240] the dependence of $K_c(T)$ is

$$K_c = \frac{\phi_0}{16\pi\mu_0\gamma\lambda_\perp^2} W\left(\frac{2e^2\eta^2}{b^2}\right)\left[1 - \frac{2}{W\left(\frac{2e^2\eta^2}{b^2}\right)}\right]^{3/2} , \tag{4.11}$$

where ϕ_0 is the magnetic flux quantum, μ_0 is the vacuum magnetic permeability, $\lambda_\perp$ is the London penetration depth perpendicular to the ab layers, $b \equiv B/B_{c2}$ is the reduced magnetic field, $\eta \sim 1$ is a geometric constant, $W(x)$ is Lambert's function, the inverse of xe^x, and e is Euler's constant (see details in Ref. [92]). Similar results were obtained in Ref. [70] in the high magnetic field approximation (i.e., close to H_{c2}). However, the high magnetic field approximation is not applicable for most IBS, as $H_{irr}(T) \sim 0.5H_{c2}(T)$, making the high-field regime not experimentally accessible. For the superconducting parameters necessary for the model, we used data from Ref. [241] for optimally doped $BaFe_2(As_{1-x}P_x)_2$, and we set $\eta = 1$. The calculated $K_c(T)$, shown in Fig. 7 of Ref. [92], roughly follows a similar dependence to our data, monotonically decreasing with temperature. However, this model does not predict the appearance of the *peak effect* that our data show. We also observe a difference in amplitude (about a factor ~ 2), which may be due to the uncertainty of the superconducting parameters used.

Finally, an increase of the irreversibility field H_{irr} was also observed after sandblasting. The H_{irr} curves were estimated from the isothermal $m(H)$ positive branch as the magnetic field above which the magnetic moments $m(H^{\uparrow})$ and $m(H^{\downarrow})$, obtained by increasing and decreasing H respectively coincide within the experimental resolution. As shown in the phase diagram in Fig. 8 of Ref. [92], the effect of sandblasting the surface is to shift the $H_{irr}(T)$ line to ~ 0.5 K higher temperature, which was observed for both samples. The critical-state model we used to estimate K_c predicts that the surface critical current should vanish at the $H_{c2}(T)$ line, which is not observed due to the effect of thermal fluctuations on the vortices, which play a non negligible role in these materials. [105, 107, 111, 242, 243]

4.2 Results on precursor effects of cuprate superconductors

The study of the origin of precursor effects on cuprate superconductors was conducted in two related articles. Firstly, we focused our analysis on the precursor effects of optimally doped YBCO. This study was published in *Precursor superconducting effects in the optimally doped $YBa_2Cu_3O_{7-\delta}$ superconductor: the confrontation between superconducting fluctuations and percolative effects revisited*, which corresponds to Ref. [90]. In *On the dilemma between percolation processes and fluctuating pairs as the origin of the enhanced conductivity above the superconducting transition in cuprates*, which corresponds to Ref. [91], we extended the results of Ref. [90] to other other optimally doped cuprates with different number of interlayer CuO_2 planes, LaSCO, Bi2212 and Tl2223, with 1, 2 and 3 CuO_2 layers in the periodicity length respectively.

4.2.1 Percolative analysis

Bruggeman's effective medium theory (EMT) was used in Refs. [90] and [91] to analyze if emergent percolative effects arising from chemical or structural inhomogeneities at length scales larger than the coherence length in the sample could be the single source of paraconductivity in cuprates, due to a distribution of T_c. The EMT effective in-plane electrical conductivity $\langle\sigma_{ab}\rangle$ can be obtained in this model by numerically solving the implicit equation [85–87]

$$\int_0^{\infty} \frac{\sigma_{ab}(T,T_c) - \langle\sigma_{ab}(T)\rangle}{\sigma_{ab}(T,T_c) + 2\langle\sigma_{ab}(T)\rangle} G(T_c) dT_c = 0 \ , \tag{4.12}$$

where $G(T_c)$ is the volume fraction of domains with T_c as critical temperature. $G(T_c)$ can be approximated by a Gaussian distribution, characterized by an average critical temperature T_c^{EMT} and a full width at half-maximum (FWHM) ΔT_c^{EMT}. The in-plane electrical conductivity of the different domains is then

$$\sigma_{ab}(T,T_c) \rightarrow \begin{cases} \infty & \text{if } T_c^{\text{EMT}} > T \ , \\ 1/\rho_B(T) & \text{if } T_c^{\text{EMT}} < T \ . \end{cases} \tag{4.13}$$

Sample	T_c (K)	ΔT_c (K)	T_c^{EMT} (K)	ΔT_c^{EMT} (K)
YBCO [90]	91.1 ± 0.2	0.6 ± 0.1	55.4 ± 0.8	57.7 ± 1.1
LaSCO [91]	27.2 ± 1.0	2.2 ± 1.0	24.5 ± 0.3	8.5 ± 0.6
Bi2212 [91]	87 ± 2	1.5 ± 0.4	80.1 ± 0.7	18.0 ± 1.5
Tl2223 [91]	116 ± 2	3.9 ± 1.6	101.3 ± 1.0	44.2 ± 2.4

Table 4.1: T_c^{EMT} and ΔT_c^{EMT} obtained in Refs. [90, 91] from the percolative analysis by fitting Eq. (4.12) to the paraconductivity $\Delta\sigma_{ab}$ data, compared with the experimental values T_c and ΔT_c. Notice the large discrepancy between both sets of parameters, which is not observed in other observables which are not susceptible to percolative effects, such as magnetization data (see, e.g., Refs. [105, 170, 176]).

The best fits of Eq. (4.12) were obtained leaving T_c^{EMT} and $\Delta T_c^{\mathrm{EMT}}$ as free parameters for optimally doped YBCO paraconductivity data in Ref. [90], and for LaSCO, Bi2212 and Tl2223 paraconductivity data in Ref. [91], obtaining the values shown in Table 4.1. For comparison, the experimental T_c and ΔT_c parameters, obtained from the derivative of the $\rho(T)$ curves are also shown in this table. The resulting curves are shown in Fig. 2 (in $\Delta\sigma(\varepsilon)$ representation) and Fig. 3 (in $\rho(T)$ representation) of both Ref. [90] for YBCO (dotted blue lines) and Ref. [91] for LaSCO, Bi2212 and Tl2223 data (dashed blue lines).

For all compounds, the EMT model failed to reconstruct the experimental paraconductivity for values of $\varepsilon > 0.1$, albeit more notoriously for the more anisotropic compounds. However, even though the EMT model seems to explain the data close to T_c, the resulting T_c^{EMT} and $\Delta T_c^{\mathrm{EMT}}$ are very far from the experimental T_c and ΔT_c. We must remark it is expected that a percolative model must necessarily lead to an average domain T_c^{EMT} below the experimental T_c due to percolation eventually taking place. However, T_c^{EMT} and ΔT_c^{EMT} must be consistent with the diamagnetic transition width, as this observable is not subject to percolative phenomena and each domain with a different T_c must contribute individually to the total magnetic moment. Nevertheless, this is not the case, being the calculated T_c^{EMT} significantly lower and ΔT_c^{EMT} at least an order of magnitude higher than the T_c and ΔT_c observed in the diamagnetic transition of similar samples, [105, 170, 176] which are instead very close to the experimental values observed in our resistive transition. As an example, the distribution of T_c predicted by the EMT model for the YBCO data is shown as a dashed green line in Fig. 3 of Ref. [90]. As can be seen, the T_c distributions required to explain the data are extremely wide, as other authors have found for underdoped compounds. [74, 244, 245]

4.2.2 Fluctuation analysis

Additionally, our data were analyzed in the framework of Gaussian-Ginzburg-Landau (GGL) superconducting fluctuations. Given the layered nature of cuprate superconductors, the Lawrence-Doniach (LD) approach of the phenomenological GGL scen-

Sample	d_{eff} (nm)	c	B_{LD}	$\xi_c(0)$ (nm)
YBCO [90, 176]	0.59	0.55 ± 0.15	0.14 ± 0.03	0.11 ± 0.02
LaSCO [91]	0.66	0.54 ± 0.06	0.048 ± 0.004	0.072 ± 0.006
Bi2212 [91]	0.77	0.53 ± 0.09	0	~ 0
Tl2223 [91]	0.593	0.52 ± 0.03	0	~ 0

Table 4.2: Parameters used in Refs. [90,91] for the fluctuation analysis of optimally doped YBCO, LaSCO, Bi2212 and Tl2223. d_{eff} is the effective interlayer distance and B_{LD} the Lawrence-Doniach parameter. The parameters for YBCO were obtained from Ref. [176].

ario is well suited to describe the contribution of fluctuations to the conductivity above T_c. [7, 76, 169, 246, 247] The calculation with the inclusion of a total energy cutoff leads to [174–178]

$$\Delta\sigma_{ab}(\varepsilon) = \frac{e^2}{16\hbar d_{\text{eff}}}\left[\frac{1}{\varepsilon}\left(1+\frac{B_{LD}}{\varepsilon}\right)^{-\frac{1}{2}} - \frac{1}{c}\left(1+\frac{B_{LD}}{c}\right)^{-\frac{1}{2}}\right], \tag{4.14}$$

where $B_{LD} \equiv [2\xi_c(0)/d_{\text{eff}}]^2$ is the Lawrence-Doniach coupling parameter, $\xi_c(0)$ the c–axis coherence length amplitude, c the total energy cutoff constant, and d_{eff} the effective distance between ab–layers. Eq. (4.14) was previously used by Rey et al. [176] to study the optimally doped YBCO thin-film analyzed in Ref. [90]. To prove if this model was applicable to other cuprates with different number of CuO_2 layers per unit cell N, we applied the same methodology in Ref. [91] to the LaSCO ($N = 1$), Bi2212 ($N = 2$) and Tl2223 ($N = 3$) paraconductivity data. However, as Bi2212 and Tl2223 are very anisotropic and $\xi_c(0) \ll d_{\text{eff}}$, we can approximate $B_{LD} \approx 0$ in Eq. (4.14), reducing to

$$\Delta\sigma_{ab}(\varepsilon) = \frac{e^2}{16\hbar d_{\text{eff}}}\left(\frac{1}{\varepsilon} - \frac{1}{c}\right). \tag{4.15}$$

which in the absence of a total energy cutoff (i.e., $c \to \infty$) reduces to the well-known 2-dimensional Aslamazov-Larkin (AL2D) calculation. [248] For the fluctuation analysis, d_{eff} was set to d/N, [170, 176, 249–251] and the cutoff parameter was selected following the criterion $c \equiv \log(T_{\text{onset}}/T_c)$, being T_{onset} the temperature at which the derivative $d\rho_{\text{bkg}}/dT$ deviated from the $d\rho/dT$ data beyond the noise level. The selection of c with this criterion made the direct computation of Eq. (4.15) without any free parameters possible for Bi2212 and Tl2223.

Figs. 1(d −− f) of Ref. [91] illustrate the procedure used to select T_{onset}, and therefore, c, for the LaSCO, Bi2212 and Tl2223 samples. As shown, the deviation of the derivative of the background resistivity from the experimental data is clear. A best fit of Eq. (4.14) was performed for LaSCO in the range $0.02 \leq \varepsilon \leq 0.54$ with B_{LD} as the only free parameter, leading to $B_{LD} = 0.048 \pm 0.004$, or $\xi_c(0) = 0.072 \pm 0.006$ nm. The obtained result $\xi_c(0) \ll d_{\text{eff}}$ is indicative of weak Josephson

coupling, which justifies the interdimensional 2D–3D critical exponent between $-1/2$ and -1, far from the full critical region and the short wavelength fluctuation regime, $0.02 \lesssim \varepsilon \lesssim 0.1$. [170, 252]. For comparison, the values found for optimally doped YBCO in Ref. [176] were $B_{LD} = 0.14 \pm 0.03$ and $\xi_c(0) = 0.11 \pm 0.02$ nm. Additionally, the computed value of Eq. (4.15) was compared directly with the Bi2212 and Tl2223 data, with no free parameters. The values of c, B_{LD} and $\xi_c(0)$ obtained from our analysis for all the compounds analyzed in Ref. [91], and for the YBCO crystal used in Ref. [90], are compiled in Table 4.2. As shown, the experimental data are well explained by the extended GGL approach for multilayered superconductors in the ε–range analyzed. The resulting curves of this analysis are included as solid red lines in Figs. 2 and 3 (in $\Delta\sigma(\varepsilon)$ representation and $\rho(T)$ representation, respectively) of both Refs. [91] (LaSCO, Bi2212, Tl2223) and [90] (YBCO), next to our EMT calculation.

4.2.3 Comparison with recent results

In this section, we will discuss a recent proposal, Ref. [74], where a percolative model for cuprates was suggested. The proposed percolative model was introduced to explain paraconductivity data in three different underdoped compounds, LaSCO ($T_c = 28$ K), YBCO $T_c = 47$ K), and $HgBa_2CuO_{4+\delta}$ (Hg1201, $T_c = 80$ K), and as a result, the authors conclude that thermal fluctuations should not be the cause of paraconductivity in underdoped cuprates. Their main argument is that these data scale in the representation $\Delta\sigma(T - T_c)$, and so *"demonstrate a remarkable degree of universality"*. The proposed scaling of the underdoped data was reconstructed in Fig. 4 of Ref. [91]. However, this conclusion is far from universal – as we will show, it cannot explain data from optimally doped cuprates, while the fluctuation models used in the previous section, which predict a different dependency based on the relative Josephson coupling between superconducting layers, [76, 169, 170, 174–176, 246–250] can indeed explain data from both underdoped and optimally doped cuprates. As a first criticism, Ref. [74] claim that *the exponential temperature dependence is incompatible with standard models of superconducting fluctuations such as Ginzburg-Landau theory*. However, the calculation used to support these claims is the classical AL2D result without any type of cutoff, even though a momentum cutoff was early introduced to mitigate the disagreement caused by the overestimation of the short wavelength fluctuating modes at high reduced temperatures, [7, 76, 247, 253] and only a single curve is shown, corresponding to Hg1201, even though fluctuation models predict a dependency on d_{eff} and T_c (hence, different behaviors would be expected for LaSCO and YBCO).

Fig. 5 of Ref. [91] shows the data of the three underdoped cuprates separatedly, in both $\Delta\sigma(T-T_c)$ (a, c, e) and $\Delta\sigma(\varepsilon)$ (b, d, f) representations. In order to tackle the possible amplitude uncertainty of the paraconductivity from Ref. [74], acknowledged by the authors of Ref. [74] a temperature-independent multiplicative parameter C_g was added to Eq. (4.15), which does not change the functional dependence of the

Sample	d (nm)	N	T_c (K)	ΔT_c (K)	d_{eff} (nm)	C_g	c
Hg1201	0.95	1	80	0.8 ± 0.2	0.95	0.5	0.23
YBCO	1.17	2	47	2.2 ± 0.2	0.585	0.62	0.35
LaSCO	0.66	1	28	1.8 ± 0.2	0.66	0.71	0.65

Table 4.3: Parameters corresponding to the analysis of the paraconductivity data of the underdoped compounds from Ref. [74] using the GGL calculation with total energy cutoff, Eq. (4.16). ΔT_c was estimated as the FWHM of $d\rho_{ab}/dT$. The amplitude of LaSCO was already adapted by a factor 2 in Ref. [74] to make the data scale so C_g would be 1.4 from the raw data.

GGL model used (see Table 4.3), leading to

$$\Delta\sigma_{ab}(\varepsilon) = \frac{C_g\, e^2}{16\hbar d_{\text{eff}}} \left(\frac{1}{\varepsilon} - \frac{1}{c}\right) . \tag{4.16}$$

The comparison of the fluctuation model in Eq. (4.16) with Ref. [74] data is shown in Fig. 5 of Ref. [91]. The resulting curves correspond to the solid red lines. The classical AL2D calculation (i.e., setting $c \to \infty$ in Eq. (4.16)) and the EMT calculation from Ref. [74] are also shown for each compound as dot-dashed red lines and dashed black lines, respectively. Only data for $T > T_c$ and above $\Delta\sigma = 10^3\ \Omega^{-1}\text{m}^{-1}$ are shown, as the SNR below that paraconductivity value was too low, and the c values were estimated from the ε at which the paraconductivity plummets below the noise level, obtaining $c = 0.23$ for Hg1201, $c = 0.35$ for YBCO and $c = 0.65$ for LaSCO. As evidenced, the agreement of the fluctuation models with the experimental data of underdoped cuprates is good up to the cutoff region, $\varepsilon \to c$. However, the dispersion of the cutoff parameter c is larger than in optimally doped cuprates (well beyond the data dispersion), which could be related to uncertainties related to the background extraction, knowingly more challenging in non-optimally doped compounds. [252, 254]

However, this percolative model cannot in any case explain the optimally doped samples. To demonstrate this, Fig. 6 of Ref. [91] shows the optimally doped Tl2223, Bi2212 and LaSCO paraconductivity data in $\Delta\sigma(T - T_c)$ representation, superimposed on the scaling of the data from Ref. [74] (grey area, for clarity). As shown, the differences between optimally doped cuprates and underdoped cuprates go beyond the experimental uncertainties even if the amplitude was adapted, and no scaling is observed whatsoever. Interestingly, as a sanity check, we observed that the paraconductivity of the optimally doped LaSCO used in our analysis is still compatible with the not strongly underdoped LaSCO used in Ref. [74].

More importantly, the strongest argument against the percolative scenario in general and Ref. [74] in particular is that the T_c distributions necessary to explain the data with these models are quantitatively unphysical. The analysis by Popcevic et al., shown in Fig. 4 of Ref. [91], leads to $\Delta T_c = 26 \pm 1$ K, which is a significant fraction of the T_c value of the samples studied (28 K for LSCO, 47 K

for YBCO, and 80 K for Hg1201), and is of the same order of magnitude of the ΔT_c values obtained in our percolative analysis of optimally doped YBCO, LaSCO, Bi2212 and Tl2223 data. However, this wide T_c distribution is not verified from other observables such as the field-cooled magnetization. As no percolation effects take place in magnetization, an inhomogeneous material must evidence a widened transition below T_c, [255, 256] and given that magnetic domains with a given T_c contribute independently to the total magnetization, a transition temperature T_c^{FC} and width ΔT_c^{FC} can be directly obtained from the $dM^{FC}(T)/dT$ curve. [254] Nevertheless, in the data from Ref. [74] for field cooled magnetization, $M^{FC}(T)$ turns temperature-independent only 10 K below the transition. The comparison between the T_c distribution obtained in Ref. [74] and the $dM^{FC}(T)/dT$ curve for the same compound are shown in Fig. 7 of Ref. [91] as dashed blue and dotted black lines, respectively. As shown, the T_c distributions obtained from the percolative model are in complete disagreement with the curves obtained from magnetization measurements.

Chapter 5

General conclusion

In the first part of this thesis, critical phenomena and the vortex dynamics of iron-based superconductors (IBS) single crystals were studied, particularly iron-pnictides $Ba(Fe_{1-x}Co_x)_2As_2$ and $BaFe_2(As_{1-x}P_x)_2$ of the 122 family, and the more anisotropic $Ca_{1-x}La_xFe_{1-y}Ni_yAs_2$ of the 112 family. Firstly, the anomalous upper critical field angular dependency of $Ba(Fe_{1-x}Co_x)_2As_2$ [68,69] was studied by measuring its electrical resistivity with different orientations of an applied magnetic field. The excess magnetoconductivity data were interpreted in terms of the Aslamazov-Larkin (AL) calculation for fluctuation phenomena in the 3D limit (given the small anisotropy of the system), generalized to the finite magnetic field regime. [106] From these results, a criterion-free determination of $H_{c2}(\theta)$ could be made, obtaining a profile that deviates significantly from the one predicted by the Ginzburg-Landau calculation for anisotropic materials close to the 3D limit (3D-aGL), but which nevertheless agrees with the $H_{c2}(\theta)$ data obtained by the conventional percentage cuts method while greatly reducing the uncertainty. The profile of $H_{c2}(\theta)$ was then successfully explained by a theoretical calculation for dirty two-band superconductors, [113] in which one band is roughly isotropic ($\gamma \approx 1$) and another band is highly anisotropic ($\gamma \approx 9$). From these results, we suggest that the temperature-dependent γ that other authors introduce to account for the $\rho(T, H, \theta)$ behavior [213–217] is an artifact associated to the use of the 3D-aGL calculation. We also found that the irreversibility field does not show such anomalous behavior and fully agrees with the 3D anisotropic calculation, which can be understood as if the pinning mechanism were not strongly affected by the the multiband electronic structure. Secondly, to study the $Ca_{1-x}La_xFe_{1-y}Ni_yAs_2$ vortex dynamics, the magnetization hysteresis curves $M(H)$ were measured for $H \parallel ab$ and $H \parallel c$. Our results suggest a crossover from plastic to collective pinning across H_p as the cause for the secondary magnetization peak (SMP) observed in the $H \parallel c$ direction. [124,128] At low temperatures, the H_{on} and H_p lines close in following inverse curvatures and may eventually merge, which would imply a change in the pinning structure to 2D Josephson-coupled vortices. However, this merging could not be measured at temperatures above 2 K. Additional pinning analysis by fitting the normalized pinning force vs reduced mag-

netic field $h = H/H_{irr}$ curves to the Dew-Hughes model points towards a δl–type pinning caused by point disorder and surface defects. [230–232] Thirdly, the effect of surface irregularities on the critical properties of $BaFe_2(As_{1-x}P_x)_2$ was also explored by studying the amplitude increase of the isothermal $m(H)$ hysteresis curves with $H \parallel c$ before and after sandblasting the crystal surfaces. A significant critical current increase was observed for all samples and for all isothermal curves (i.e., at all temperatures), following temperature and magnetic field dependenc appreciably different from the bulk critical current before sandblasting. From these data, an estimated surface critical current density $K_c(T, H)$ was obtained, which was subsequently compared with a theoretical calculation for the maximum non-dissipative current that a rough surface can withstand, based on Mathieu-Simon continuum theory for the mixed state, and which can qualitatively explain the hysteresis increase. [168, 240] From the hysteresis curves, the irreversiblity field H_{irr} was also obtained for temperatures close to T_c. An increase of the $H_{irr}(T)$ line could also be observed after the treatment. Additionally, a sharp increase of $K_c(T)$ was observed right next to the $H_{irr}(T)$ line, an effect that is not present in the bulk critical current density curves $J_c(T)$, which could help shed light on the origin of its appearance in other superconductors.

In the second part of this thesis, the adequacy of both percolative and superconducting fluctuation models to describe the paraconductivity of cuprates above T_c was studied. The resistivity in the ab–direction ρ_{ab} was analyzed for four optimally doped cuprate systems, namely $YBa_2Cu_3O_{7-\delta}$ (YBCO), $La_{2-x}Sr_xCuO_4$ (LaSCO), $Bi_2Sr_2CaCu_2O_{8+\delta}$ (Bi2212) and $Tl_2Ba_2Ca_2Cu_3O_{10}$ (Tl2223). Being in the optimal doped regime makes the effect of extrinsic T_c–inhomogeneities less pronounced, as the variation of T_c in domains close to the maximum is small. This allowed us to probe whether intrinsic inhomogeneities i.e., the small chemical composition variations in the nanostructure of the material which should appear even in perfect crystals, could explain the paraconductivity $\Delta\sigma_{ab}$. [71–73] Our analyses covered the region of reduced temperature $\varepsilon = \log(T/T_c)$ up to the onset of the paraconductivity, i.e., where the extrapolated normal-state resistivity begins to deviate from the experimental data. On the one hand, our results show that effective-medium-theory (EMT) cannot explain the measured $\Delta\sigma_{ab}(\varepsilon)$ of the optimally doped compounds. Moreover, the EMT best fits predict extreme distributions of T_c, including very low values of the average critical temperature T_c^{EMT} and large ΔT_c^{EMT} (comparable to T_c^{EMT} itself), which is not supported by other observables not susceptible to percolative effects such as the magnetic susceptibility, which shows sharp diamagnetic transitions. On the other hand, our work extends the results found for the optimally doped YBCO system, previously analyzed in detail in Ref. [176], to the more anisotropic LaSCO, Bi2212 and Tl2223 compounds. We provided an explanation of the paraconductivity data of these materials in terms of the GGL approach for superconducting fluctuations, extended to high ε with the introduction of a total energy cutoff in the fluctuation modes. Additionally, the GGL fluctuation models were also successfully used to explain the paraconductivity data from Ref. [74] of underdoped YBCO, LaSCO and $HgBa_2CuO_{4+\delta}$ (Hg1201), which were previously

used to support a model based on the percolative scenario.

List of publications and quality metrics

- I. F. Llovo, C. Carballeira, D. Sóñora, A. Pereiro, J. J. Ponte, S. SalemSugui Jr., A. S. Sefat and J. Mosqueira, Multiband effects on the upper critical field angular dependence of 122family iron pnictide superconductors, Sci. Rep. **11**, 11526 (2021).

  i. I. F. Llovo contribution: sample preparation, measurement and data analysis with D. Sóñora and A. Pereiro; theoretical calculations, drawing of figures and redaction of the manuscript with J. Mosqueira

  ii. Quality metrics:

  - Number of times cited (as of November 2023, Google Scholar): 3
  - Journal Citation Reports (2021) JIF 4.997, JCI 1.05
    - Multidisciplinary Sciences: JIF 19/74, 75% (Q2); JCI 19/135, 86.30% (Q1)
  - Scopus CiteScore (2021) 6.9
    - Multidisciplinary: 11/120, 91% (Q1)

  iii. Copyright declaration from the journal (from www.nature.com/srep/open-access, accessed 09 November 2023):

  > *Scientific Reports articles are published OA under a CC BY license (Creative Commons Attribution 4.0 International license). The CC BY license is the most open license available, and is considered the industry 'gold standard' for open access; it is also preferred by many funders. This license allows readers to copy and redistribute the material in any medium or format, and to alter, transform, or build upon the material, including for commercial use, providing the original author is credited.*

  iv. Affiliations:

  - I. F. Llovo, C. Carballeira, D. Sóñora, A. Pereiro and J. Mosqueira: QMatterPhotonics Research Group, Departamento de Física de Par-

tículas, Universidade de Santiago de Compostela, 15782 Santiago de Compostela, Spain.

- J. J. Ponte: Unidade de Magnetosusceptibilidade, RIAIDT, Universidade de Santiago de Compostela, 15782 Santiago de Compostela, Spain.
- S. Salem-Sugui Jr.: Instituto de Fisica, Universidade Federal do Rio de Janeiro, Rio de Janeiro, RJ 21941972, Brazil.
- A. S. Sefat: Oak Ridge National Laboratory, Oak Ridge, TN 87831, USA.

- I. F. Llovo, D. Sóñora, J. Mosqueira, S. Salem-Sugui Jr., S. Sundar, A. D. Alvarenga, Tao Xie, Chang Liu, Shiliang Li and Huiqian Luo, Vortex dynamics and second magnetization peak in the iron-pnictide superconductor $Ca_{0.82}La_{0.18}Fe_{0.96}Ni_{0.04}As_2$, Supercond. Sci. Technol., **34**, 115010 (2021). I IOP Publishing. Reproduced with permission. All rights reserved.

  i. I. F. Llovo contribution: data analysis with D. Sóñora, S. Sundar; drawing of figures 1-4; drawing of figure 7 and redaction of the manuscript with J. Mosqueira, S. Salem-Sugui and S. Sundar

  ii. Quality metrics:

  - Number of times cited (as of November 2023, Google Scholar): 10
  - Journal Citation Reports (2021) JIF 3.464, JCI 0.60
    - Physics, Applied: JIF 60/161, 63.04% (Q2); JCI 73/178, 59.27% (Q2)
    - Physics, Condensed Matter: JIF 30/69, 57.25% (Q2); JCI 25/79, 68.99% (Q2)
  - Scopus CiteScore (2021) 5.5
    - Materials Science, Metals and Alloys: 22/155, 85% (Q1)
    - Materials Science, Materials Chemistry: 66/298, 77% (Q1)
    - Physics and Astronomy, Condensed Matter Physics: 94/415, 76% (Q1)
    - Engineering, Electrical and Electronic Engineering: 173/708, 75% (Q1)
    - Materials Science, Ceramics and Composites: 35/115, 70% (Q2)

  iii. Copyright declaration from the journal (from publishingsupport.iopscience.iop.org/author-rights-policies, accessed 09 November 2023):

  Preprints
  IOP supports the sharing of article preprints. Our authors can share

a preprint of their article anywhere and at any time. For full details, please refer to our preprint policy. The policy applies to all articles submitted to or published by IOP, whether on a subscription or gold open access basis.

Articles published on a subscription basis
Our policy grants authors the rights to:

Immediately: [...] include the Final Published Version in a research thesis or dissertation, provided it is not then shared online [...]

After a 12-month embargo period: share the Accepted Manuscript on any non-commercial institutional or subject repository.

iv. Affiliations:

- I. F. Llovo, D. Sóñora, and J. Mosqueira: QMatterPhotonics Research Group, Departamento de Física de Partículas, Universidade de Santiago de Compostela, 15782 Santiago de Compostela, Spain.
- S. Salem-Sugui Jr. and S. Sundar: Instituto de Fisica, Universidade Federal do Rio de Janeiro, Rio de Janeiro, RJ 21941972, Brazil.
- A. D. Alvarenga: Instituto Nacional de Metrologia Qualidade e Tecnologia, 25250-020 Duque de Caxias, RJ, Brazil.
- Tao Xie and Chang Liu: Beijing National Laboratory for Condensed Matter Physics, Institute of Physics, Chinese Academy of Sciences, Beijing 100190, Peoples Republic of China.
- Shiliang Li and Huiqian Luo: Beijing National Laboratory for Condensed Matter Physics, Institute of Physics, Chinese Academy of Sciences, Beijing 100190, Peoples Republic of China; Songshan Lake Materials Laboratory, Dongguan, Guangdong 523808, Peoples Republic of China.

- I. F. Llovo, J. Mosqueira, C. Carballeira and F. Vidal, Precursor superconducting effects in the optimally doped $YBa_2Cu_3O_{7-\delta}$ superconductor: the confrontation between superconducting fluctuations and percolative effects revisited, SN Appl. Sci., **4**, 110 (2022).

  i. I. F. Llovo contribution: data analysis with J. Mosqueira, drawing of figures, all authors contributed equally to the redaction of the manuscript

  ii. Quality metrics:

  - Number of times cited (as of November 2023, Google Scholar): 1
  - Journal Citation Reports (2022) JCI 0.43
    - Multidisciplinary Sciences: JCI 53/133, 57.52% (Q2)
  - Scopus CiteScore (2022) 5.3

  - Engineering, General Engineering: 55/302, 81% (Q1)
  - Earth and Planetary Sciences, General Earth and Planetary Sciences: 39/192, 79% (Q1)

iii. Copyright declaration from the journal (from www.springer.com/journal/42452/how-to-publish-with-us, accessed 09 November 2023):

> *SN Applied Sciences articles are published open access under a CC BY licence (Creative Commons Attribution 4.0 International licence). The CC BY licence is the most open licence available and considered the industry 'gold standard' for open access; it is also preferred by many funders. This licence allows readers to copy and redistribute the material in any medium or format, and to alter, transform, or build upon the material, including for commercial use, providing the original author is credited.*

iv. Affiliations:

- I. F. Llovo and J. Mosqueira: QMatterPhotonics Research Group, Departamento de Física de Partículas, Universidade de Santiago de Compostela, 15782 Santiago de Compostela, Spain; iMATUS, Universidade de Santiago de Compostela, 15706 Santiago de Compostela, Spain.
- C. Carballeira and F. Vidal: QMatterPhotonics Research Group, Departamento de Física de Partículas, Universidade de Santiago de Compostela, 15782 Santiago de Compostela, Spain.

- I. F. Llovo, J. Mosqueira and F. Vidal. On the dilemma between percolation processes and fluctuating pairs as the origin of the enhanced conductivity above the superconducting transition in cuprates. *Supercond. Sci. Technol.*, **36**, 125004 (2023). © IOP Publishing. Reproduced with permission. All rights reserved.

  i. I. F. Llovo contribution: data analysis with J. Mosqueira, drawing of figures, all authors contributed equally to the redaction of the manuscript

  ii. Quality metrics:

  - Journal Citation Reports (2022, latest available) JIF 3.464, JCI 0.63
    - Physics, Applied: JIF 51/159, 68.2% (Q2); JCI 66/176, 62.78% (Q2)
    - Physics, Condensed Matter: JIF 24/66, 64.4% (Q2); JCI 25/75, 67.33% (Q2)
  - Scopus CiteScore (2022, latest available) 6.0
    - Materials Science, Metals and Alloys: 29/164, 82% (Q1)
    - Physics and Astronomy, Condensed Matter Physics: 100/423,

76% (Q1)

· Engineering, Electrical and Electronic Engineering: 182/738, 75% (Q1)

· Materials Science, Materials Chemistry: 82/306, 73% (Q2)

· Materials Science, Ceramics and Composites: 39/123, 68% (Q2)

iii. Copyright declaration from the journal (from publishingsupport.iopscience.iop.org/author-rights-policies, accessed 09 November 2023):

> ***Preprints***
> *IOP supports the sharing of article preprints. Our authors can share a preprint of their article anywhere and at any time. For full details, please refer to our preprint policy. The policy applies to all articles submitted to or published by IOP, whether on a subscription or gold open access basis.*
>
> ***Articles published on a subscription basis***
> *Our policy grants authors the rights to:*
>
> *Immediately: [...] include the Final Published Version in a research thesis or dissertation, provided it is not then shared online [...]*
>
> *After a 12-month embargo period: share the Accepted Manuscript on any non-commercial institutional or subject repository.*

iv. Affiliations:

- I. F. Llovo: QMatterPhotonics Research Group, Departamento de Física de Partículas, Universidade de Santiago de Compostela, 15782 Santiago de Compostela, Spain; iMATUS, Universidade de Santiago de Compostela, 15706 Santiago de Compostela, Spain; Centro de Supercomputación de Galicia (CESGA), 15705 Santiago de Compostela, Spain.
- J. Mosqueira: QMatterPhotonics Research Group, Departamento de Física de Partículas, Universidade de Santiago de Compostela, 15782 Santiago de Compostela, Spain; iMATUS, Universidade de Santiago de Compostela, 15706 Santiago de Compostela, Spain.
- F. Vidal: QMatterPhotonics Research Group, Departamento de Física de Partículas, Universidade de Santiago de Compostela, 15782 Santiago de Compostela, Spain.

- (In peer review) I. F. Llovo, J. Mosqueira, Ding Hu, Huiqian Luo and Shiliang Li, Enhancement of the critical current by surface irregularities in Fe-based superconductors.

  i. I. F. Llovo contribution: sample preparation, measurement, drawing of

figures, data analysis and writing of the manuscript with J. Mosqueira

ii. Quality metrics: N/A

iii. Copyright declaration: N/A

iv. Affiliations:

- I. F. Llovo and J. Mosqueira: QMatterPhotonics Research Group, Departamento de Física de Partículas, Universidade de Santiago de Compostela, 15782 Santiago de Compostela, Spain.
- Ding Hu: School of Physics, Hangzhou Normal University, Hangzhou 311121, China.
- Shiliang Li and Huiqian Luo: Beijing National Laboratory for Condensed Matter Physics, Institute of Physics, Chinese Academy of Sciences, Beijing 100190, PR China

References

[1] Kamerlingh Onnes, H. Experiments on the condensation of helium by expansion. *KNAW, Proceedings, 10 II* 744–747 (1908). URL dwc.knaw.nl/DL/publications/PU00013699.pdf.

[2] van Delft, D. & Kes, P. The discovery of superconductivity. *Europhys. News* **42**, 21–25 (2011). URL dx.doi.org/10.1051/epn/2011104.

[3] Kamerlingh Onnes, H. On the sudden change in the rate at which the resistance of mercury disappears. *Commun. Phys. Lab. Univ. Leiden, c* **124** (1911). URL physics.ucf.edu/~rep/EDII/Onnes1911.pdf.

[4] Meissner, W. & Ochsenfeld, R. Ein neuer Effekt bei Eintritt der Supraleitfähigkeit. *Naturwissenschaften* **21**, 787–788 (1933). URL dx.doi.org/10.1007/BF01504252.

[5] Forrest, A. M. Meissner and Ochsenfeld revisited. *Euro. J. Phys.* **4**, 117 (1983). URL dx.doi.org/10.1088/0143-0807/4/2/011.

[6] London, F., London, H. & Lindemann, F. A. The electromagnetic equations of the supraconductor. *Proceedings of the Royal Society of London. Series A - Mathematical and Physical Sciences* **149**, 71–88 (1935). URL dx.doi.org/10.1098/rspa.1935.0048.

[7] Tinkham, M. *Introduction to Superconductivity.* International series in pure and applied physics (McGraw Hill, New York, 1996), 2nd edn. URL books.google.es/books?id=XP_uAAAAMAAJ.

[8] Drude, P. Zur Elektronentheorie der Metalle. *Annalen der Physik* **306**, 566–613 (1900). URL dx.doi.org/10.1002/andp.19003060312.

[9] Drude, P. Zur Elektronentheorie der Metalle; ii. Teil. Galvanomagnetische und thermomagnetische Effecte. *Annalen der Physik* **308**, 369–402 (1900). URL dx.doi.org/10.1002/andp.19003081102.

[10] De Gennes, P. *Superconductivity of Metals and Alloys* (CRC Press, Boca Raton, 1999), 1st edn. URL dx.doi.org/10.1201/9780429497032.

[11] Landau, L. D. 30 - On the Theory of Superconductivity. In Ter Haar, D. (ed.) *Collected Papers of L.D. Landau*, 193–216 (Pergamon, 1965). URL dx.doi.org/10.1016/B978-0-08-010586-4.50035-3.

[12] Ginzburg, V. L. & Landau, L. D. *On Superconductivity and Superfluidity: A Scientific Autobiography*, 113–137 (Springer Berlin Heidelberg, Berlin, Heidelberg, 2009). URL dx.doi.org/10.1007/978-3-540-68008-6_4.

[13] Maxwell, E. Isotope effect in the superconductivity of mercury. *Phys. Rev.* **78**, 477–477 (1950). URL dx.doi.org/10.1103/PhysRev.78.477.

[14] Reynolds, C. A., Serin, B., Wright, W. H. & Nesbitt, L. B. Superconductivity of isotopes of mercury. *Phys. Rev.* **78**, 487–487 (1950). URL dx.doi.org/10.1103/PhysRev.78.487.

[15] Fröhlich, H. Theory of the superconducting state. I. The ground state at the absolute zero of temperature. *Phys. Rev.* **79**, 845–856 (1950). URL dx.doi.org/10.1103/PhysRev.79.845.

[16] Bardeen, J., Cooper, L. N. & Schrieffer, J. R. Theory of superconductivity. *Phys. Rev.* **108**, 1175–1204 (1957). URL dx.doi.org/10.1103/PhysRev.108.1175.

[17] Cooper, L. N. Bound electron pairs in a degenerate Fermi gas. *Phys. Rev.* **104**, 1189–1190 (1956). URL dx.doi.org/10.1103/PhysRev.104.1189.

[18] Gorkov, L. P. Microscopic derivation of the Ginzburg-Landau equations in the theory of superconductivity. *Sov. Phys. - JETP (Engl. Transl.)* **9**, 1364–1367 (1959). URL www.osti.gov/biblio/7264935.

[19] Josephson, B. Possible new effects in superconductive tunnelling. *Phys. Lett.* **1**, 251–253 (1962). URL dx.doi.org/10.1016/0031-9163(62)91369-0.

[20] Gallop, J. SQUIDs, the Josephson effects and measurement. *Meas. Sci. Technol.* **2**, 485 (1991). URL dx.doi.org/10.1088/0957-0233/2/6/001.

[21] Nakamura, Y., Pashkin, Y. A. & Tsai, J. S. Coherent control of macroscopic quantum states in a single-Cooper-pair box. *Nature* **398**, 786–788 (1999). URL dx.doi.org/10.1038/19718.

[22] Paraoanu, G. S. Microwave-induced coupling of superconducting qubits. *Phys. Rev. B* **74**, 140504 (2006). URL dx.doi.org/10.1103/PhysRevB.74.140504.

[23] Likharev, K. & Semenov, V. RSFQ logic/memory family: a new Josephson-junction technology for sub-terahertz-clock-frequency digital systems. *IEEE Trans. Appl. Supercond.* **1**, 3–28 (1991). URL dx.doi.org/10.1109/77.80745.

[24] Takeuchi, N., Ozawa, D., Yamanashi, Y. & Yoshikawa, N. An adiabatic quantum flux parametron as an ultra-low-power logic device. *Supercond. Sci. Technol.* **26**, 035010 (2013). URL dx.doi.org/10.1088/0953-2048/26/3/035010.

[25] Bednorz, J. G. & Müller, K. A. Possible high-T_c superconductivity in the Ba-La-Cu-O system. *Z. Phys. B Condens. Matter* **64**, 189–193 (1986). URL dx.doi.org/10.1007/BF01303701.

[26] Wu, M. K. *et al.* Superconductivity at 93 K in a new mixed-phase Y-Ba-Cu-O compound system at ambient pressure. *Phys. Rev. Lett.* **58**, 908–910 (1987). URL dx.doi.org/10.1103/PhysRevLett.58.908.

[27] Dai, P. *et al.* Synthesis and neutron powder diffraction study of the superconductor $HgBa_2Ca_2Cu_3O_{8+\delta}$ by Tl substitution. *Physica C* **243**, 201–206 (1995). URL dx.doi.org/10.1016/0921-4534(94)02461-8.

[28] Deng, S., Simon, A. & Köhler, J. Pairing mechanisms viewed from physics and chemistry. In Müller, K. A. & Bussmann-Holder, A. (eds.) *Superconductivity in Complex Systems: -/-*, 103–141 (Springer Berlin Heidelberg, Berlin, Heidelberg, 2005). URL dx.doi.org/10.1007/b101018.

[29] OMahony, S. M. *et al.* On the electron pairing mechanism of copper-oxide high temperature superconductivity. *PNAS* **119**, e2207449119 (2022). URL dx.doi.org/10.1073/pnas.2207449119.

[30] Namburi, D. K., Shi, Y. & Cardwell, D. A. The processing and properties of bulk (RE)BCO high temperature superconductors: current status and future perspectives. *Supercond. Sci. Technol.* **34**, 053002 (2021). URL dx.doi.org/10.1088/1361-6668/abde88.

[31] Fujikura high temperature superconductors. URL www.fujikura.co.uk/products/fel2ghts_high-temperature-superconductors. (Online) Accessed: 2023-10-03.

[32] Schneider, T. Universal properties of cuprate superconductors. *Physica B* **326**, 289–295 (2003). URL dx.doi.org/10.1016/S0921-4526(02)01635-6.

[33] Chien, T. *et al.* Dimensional crossover and oxygen deficiency in $YBa_2Cu_3O_\chi$ single crystals. *Physica C* **229**, 273–279 (1994). URL dx.doi.org/10.1016/0921-4534(94)90507-X.

[34] Hosono, H., Yamamoto, A., Hiramatsu, H. & Ma, Y. Recent advances in iron-based superconductors toward applications. *Mater. Today* **21**, 278–302 (2018). URL dx.doi.org/10.1016/j.mattod.2017.09.006.

[35] Kamihara, Y., Watanabe, T., Hirano, M. & Hosono, H. Iron-based layered superconductor $La[O_{1-x}F_x]FeAs$ (x = 0.05-0.12) with Tc = 26 k. *J. Am. Chem. Soc.* **130**, 3296–3297 (2008). URL dx.doi.org/10.1021/ja800073m.

[36] Miura, M. *et al.* Strongly enhanced flux pinning in one-step deposition of $BaFe_2(As_{0.66}P_{0.33})_2$ superconductor films with uniformly dispersed $BaZrO_3$ nanoparticles. *Nat. Commun.* **4**, 2499 (2013). URL dx.doi.org/10.1038/ncomms3499.

[37] Ishida, S. *et al.* Doping-dependent critical current properties in K, Co, and P-doped $BaFe_2As_2$ single crystals. *Phys. Rev. B* **95**, 014517 (2017). URL dx.doi.org/10.1103/PhysRevB.95.014517.

[38] Mohan, S. *et al.* Transport and magnetic properties of Co-doped $BaFe_2As_2$ epitaxial thin films grown on MgO substrate. *Supercond. Sci. Technol.* **23**, 105016 (2010). URL dx.doi.org/10.1088/0953-2048/23/10/105016.

[39] Sakoda, M., Iida, K. & Naito, M. Recent progress in thin-film growth of Fe-based superconductors: superior superconductivity achieved by thin films. *Supercond. Sci. Technol.* **31**, 093001 (2018). URL dx.doi.org/10.1088/1361-6668/aabddb.

[40] Talantsev, E. F. Evaluation of a practical level of critical current densities in pnictides and recently discovered superconductors. *Supercond. Sci. Technol.* **32**, 084007 (2019). URL dx.doi.org/10.1088/1361-6668/ab1a16.

[41] Katase, T. *et al.* Advantageous grain boundaries in iron pnictide superconductors. *Nat. Commun.* **2**, 409 (2011). URL dx.doi.org/10.1038/ncomms1419.

[42] Yao, C. & Ma, Y. Recent breakthrough development in iron-based superconducting wires for practical applications. *Supercond. Sci. Technol.* **32**, 023002 (2019). URL dx.doi.org/10.1088/1361-6668/aaf351.

[43] Pyon, S. *et al.* Enhancement of critical current density in $(Ba,Na)Fe_2As_2$ round wires using high-pressure sintering. *Supercond. Sci. Technol.* **33**, 065001 (2020). URL dx.doi.org/10.1088/1361-6668/ab804c.

[44] Weiss, J. D. *et al.* Demonstration of an iron-pnictide bulk superconducting magnet capable of trapping over 1 T. *Supercond. Sci. Technol.* **28**, 112001 (2015). URL dx.doi.org/10.1088/0953-2048/28/11/112001.

[45] Johnston, D. C. The puzzle of high temperature superconductivity in layered iron pnictides and chalcogenides. *Adv. Phys.* **59**, 803–1061 (2010). URL dx.doi.org/10.1080/00018732.2010.513480.

[46] Stewart, G. R. Superconductivity in iron compounds. *Rev. Mod. Phys.* **83**, 1589–1652 (2011). URL dx.doi.org/10.1103/RevModPhys.83.1589.

[47] Ishida, K., Nakai, Y. & Hosono, H. To what extent iron-pnictide new superconductors have been clarified: A progress report. *J. Phys. Soc. Jpn.* **78**, 062001 (2009). URL dx.doi.org/10.1143/JPSJ.78.062001.

[48] Wang, F. & Lee, D.-H. The electron-pairing mechanism of iron-based superconductors. *Science* **332**, 200–204 (2011). URL dx.doi.org/10.1126/science.1200182.

[49] Paglione, J. & Greene, R. L. High-temperature superconductivity in iron-based materials. *Nat. Phys.* **6**, 645–658 (2010). URL dx.doi.org/10.1038/nphys1759.

[50] Hirschfeld, P. J., Korshunov, M. M. & Mazin, I. I. Gap symmetry and structure of Fe-based superconductors. *Rep. Prog. Phys.* **74**, 124508 (2011). URL dx.doi.org/10.1088/0034-4885/74/12/124508.

[51] Chen, X., Dai, P., Feng, D., Xiang, T. & Zhang, F.-C. Iron-based high transition temperature superconductors. *Natl. Sci. Rev.* **1**, 371–395 (2014). URL dx.doi.org/10.1093/nsr/nwu007.

[52] Rey, R. I. *et al.* Direct measurement of the temperature dependence of the magnetic penetration depth in $Ba(Fe_{1-x}Ni_x)_2As_2$ superconductors. *Supercond. Sci. Technol.* **27**, 055015 (2014). URL dx.doi.org/10.1088/0953-2048/27/5/055015.

[53] R., P. & Kogan, V. G. London penetration depth in iron-based superconductors. *Rep. Prog. Phys.* **74**, 124505 (2011). URL dx.doi.org/10.1088/0034-4885/74/12/124505.

[54] Pallecchi, I., Caglieris, F. & Putti, M. Thermoelectric properties of iron-based superconductors and parent compounds. *Supercond. Sci. Technol.* **29**, 073002 (2016). URL dx.doi.org/10.1088/0953-2048/29/7/073002.

[55] Maksimov, E. G. *et al.* Two-band Bardeen-Cooper-Schrieffer superconducting state of the iron pnictide compound $Ba(Fe_{0.9}Co_{0.1})_2As_2$. *Phys. Rev. B* **83**, 140502 (2011). URL dx.doi.org/10.1103/PhysRevB.83.140502.

[56] Hardy, F. *et al.* Calorimetric evidence of multiband superconductivity in $Ba(Fe_{0.925}Co_{0.075})_2As_2$ single crystals. *Phys. Rev. B* **81**, 060501 (2010). URL dx.doi.org/10.1103/PhysRevB.81.060501.

[57] Hunte, F. *et al.* Two-band superconductivity in $LaFeAsO_{0.89}F_{0.11}$ at very high magnetic fields. *Nature* **453**, 903–905 (2008). URL dx.doi.org/10.1038/nature07058.

[58] Gurevich, A. Iron-based superconductors at high magnetic fields. *Rep. Prog. Phys.* **74**, 124501 (2011). URL dx.doi.org/10.1088/0034-4885/74/12/124501.

[59] Xing, X. *et al.* Two-band and Pauli-limiting effects on the upper critical field of 112-type iron pnictide superconductors. *Sci. Rep.* **7**, 45943 (2017). URL dx.doi.org/10.1038/srep45943.

[60] Huang, H.-L., Wu, D., Fan, D. & Zhu, X. Superconducting quantum computing: a review. *Sci. China Inf. Sci.* **63**, 180501 (2020). URL dx.doi.org/10.1007/s11432-020-2881-9.

[61] Gambetta, J. IBM Quantum Roadmap to build quantum-centric supercomputers (2022). URL research.ibm.com/blog/ibm-quantum-roadmap-2025.

[62] Alam, S., Hossain, M. S., Srinivasa, S. R. & Aziz, A. Cryogenic memory technologies. *Nat. Electron.* **6**, 185–198 (2023). URL dx.doi.org/10.1038/s41928-023-00930-2.

[63] Smirnov, K. *et al.* NbN single-photon detectors with saturated dependence of quantum efficiency. *Supercond. Sci. Technol.* **31**, 035011 (2018). URL dx.doi.org/10.1088/1361-6668/aaa7aa.

[64] You, L. Superconducting nanowire single-photon detectors for quantum information. *Nanophotonics* **9**, 2673–2692 (2020). URL dx.doi.org/10.1515/nanoph-2020-0186.

[65] Reddy, D. V., Nerem, R. R., Nam, S. W., Mirin, R. P. & Verma, V. B. Superconducting nanowire single-photon detectors with 98% system detection efficiency at 1550 nm. *Optica* **7**, 1649–1653 (2020). URL dx.doi.org/10.1364/OPTICA.400751.

[66] Shibata, H. Review of superconducting nanostrip photon detectors using various superconductors. *IEICE Trans. Electron.* **E104.C**, 429–434 (2021). URL dx.doi.org/10.1587/transele.2020SUI0001.

[67] Charaev, I. *et al.* Single-photon detection using high-temperature superconductors. *Nat. Nanotechnol.* **18**, 343–349 (2023). URL dx.doi.org/10.1038/s41565-023-01325-2.

[68] Murphy, J. *et al.* Angular-dependent upper critical field of overdoped $Ba(Fe_{1-x}Ni_x)_2As_2$. *Phys. Rev. B* **87**, 094505 (2013). URL dx.doi.org/10.1103/PhysRevB.87.094505.

[69] Hänisch, J. *et al.* High field superconducting properties of $Ba(Fe_{1-x}Co_x)_2As_2$ thin films. *Sci. Rep.* **5**, 17363 (2015). URL dx.doi.org/10.1038/srep17363.

[70] Lazard, G. *et al.* Critical currents in the anisotropic superconductor $2H - NbSe_2$: evidence for an upper bound of the surface critical-current density. *Phys. Rev. B* **65**, 064518 (2002). URL dx.doi.org/10.1103/PhysRevB.65.064518.

[71] Phillips, J. C. Quantum percolation in electron cuprate superconductors $Nd_{2-x}Ce_xCuO_{4-y}$. *Phys. Rev. B* **41**, 850–852 (1990). URL dx.doi.org/10.1103/PhysRevB.41.850.

[72] Phillips, J. C., Saxena, A. & Bishop, A. R. Pseudogaps, dopants, and strong disorder in cuprate high-temperature superconductors. *Rep. Prog. Phys.* **66**, 2111 (2003). URL dx.doi.org/10.1088/0034-4885/66/12/R02.

[73] Kresin, V. Z., Ovchinnikov, Y. N. & Wolf, S. A. Inhomogeneous superconductivity and the pseudogap state of novel superconductors. *Phys. Rep* **431**, 231–259 (2006). URL dx.doi.org/10.1016/j.physrep.2006.05.006.

[74] Popčević, P. *et al.* Percolative nature of the direct-current paraconductivity in cuprate superconductors. *npj Quantum Materials* **3**, 42 (2018). URL dx.doi.org/10.1038/s41535-018-0115-2.

[75] Borna, A. S., Islam, R. S. & Naqib, S. H. Hole content dependent fluctuation diamagnetism in $YBa_2Cu_3O_{7-\delta}$: Possible role of the pseudogap. *J. Supercond. Nov. Magn.* **35**, 49–55 (2022). URL dx.doi.org/10.1007/s10948-021-06035-1.

[76] Larkin, A. & Varlamov, A. *Theory of Fluctuations in Superconductors* (Oxford University Press, 2005). URL https://academic.oup.com/book/6617.

[77] Serbyn, M. N., Skvortsov, M. A., Varlamov, A. A. & Galitski, V. Giant Nernst effect due to fluctuating Cooper pairs in superconductors. *Phys. Rev. Lett.* **102**, 067001 (2009). URL dx.doi.org/10.1103/PhysRevLett.102.067001.

[78] Alloul, H., Rullier-Albenque, F., Vignolle, B., Colson, D. & Forget, A. Superconducting fluctuations, pseudogap and phase diagram in cuprates. *Europhys. Lett.* **91**, 37005 (2010). URL dx.doi.org/10.1209/0295-5075/91/37005.

[79] Rullier-Albenque, F., Alloul, H. & Rikken, G. High-field studies of superconducting fluctuations in high-T_c cuprates: Evidence for a small gap distinct from the large pseudogap. *Phys. Rev. B* **84**, 014522 (2011). URL dx.doi.org/10.1103/PhysRevB.84.014522.

[80] Ramallo, M. V., Carballeira, C., Rey, R. I., Mosqueira, J. & Vidal, F. Comment on "High-field studies of superconducting fluctuations in high-T_c cuprates: Evidence for a small gap distinct from the large pseudogap". *Phys. Rev. B* **85**, 106501 (2012). URL dx.doi.org/10.1103/PhysRevB.85.106501.

[81] Grbić, M. S. *et al.* Temperature range of superconducting fluctuations above T_c in $YBa_2Cu_3O_{7-\delta}$ single crystals. *Phys. Rev. B* **83**, 144508 (2011). URL dx.doi.org/10.1103/PhysRevB.83.144508.

[82] Caprara, S. The ancient Romans route to charge density waves in cuprates. *Condens. Matter* **4** (2019). URL dx.doi.org/10.3390/condmat4020060.

[83] Sóñora, D., Mosqueira, J. & Vidal, F. Comment on "Temperature range of superconducting fluctuations above T_c in $YBa_2Cu_3O_{7-\delta}$ single crystals". *Phys. Rev. B* **102**, 176501 (2020). URL dx.doi.org/10.1103/PhysRevB.102.176501.

[84] Wahlberg, E. *et al.* Restored strange metal phase through suppression of charge density waves in underdoped $YBa_2Cu_3O_{7-\delta}$. *Science* **373**, 1506–1510 (2021). URL dx.doi.org/10.1126/science.abc8372.

[85] Maza, J. & Vidal, F. Critical-temperature inhomogeneities and resistivity rounding in copper oxide superconductors. *Phys. Rev. B* **43**, 10560–10567 (1991). URL dx.doi.org/10.1103/PhysRevB.43.10560.

[86] Landauer, R. Electrical conductivity in inhomogeneous media. *AIP Conf. Proc.* **40**, 2–45 (1978). URL dx.doi.org/10.1063/1.31150.

[87] Kirkpatrick, S. Percolation and conduction. *Rev. Mod. Phys.* **45**, 574–588 (1973). URL dx.doi.org/10.1103/RevModPhys.45.574.

[88] Llovo, I. F. *et al.* Multiband effects on the upper critical field angular dependence of 122-family iron pnictide superconductors. *Sci. Rep.* **11**, 11526 (2021). URL dx.doi.org/10.1038/s41598-021-90858-4.

[89] Llovo, I. F. *et al.* Vortex dynamics and second magnetization peak in the iron-pnictide superconductor $Ca_{0.82}La_{0.18}Fe_0.96Ni_{0.04}As_2$. *Supercond. Sci. Technol.* **34**, 115010 (2021). URL dx.doi.org/10.1088/1361-6668/ac2556.

[90] Llovo, I. F., Mosqueira, J., Carballeira, C. & Vidal, F. Precursor superconducting effects in the optimally doped $YBa_2Cu_3O_{7-\delta}$ superconductor: the confrontation between superconducting fluctuations and percolative effects revisited. *SN Appl. Sci* **4**, 110 (2022). URL dx.doi.org/10.1007/s42452-022-04995-0.

[91] Llovo, I. F., Mosqueira, J. & Vidal, F. On the dilemma between percolation processes and fluctuating pairs as the origin of the enhanced conductivity above the superconducting transition in cuprates. *Supercond. Sci. Technol.* **36**, 125004 (2023). URL dx.doi.org/10.1088/1361-6668/acff8a.

[92] Llovo, I. F., Mosqueira, J., Hu, D., Luo, H. & Li, S. Enhancement of the critical current by surface irregularities in Fe-based superconductors. (Preprint).

[93] Sarangan, A. *Physical and Chemical Vapor Deposition*, chap. 3 (CRC Press, Boca Raton, 2016). URL dx.doi.org/10.1201/9781315370514-4.

[94] Nakajima, M. *et al.* Growth of BaFe2($As_{1-x}P_x$)$_2$ single crystals (0≤x≤1) by Ba_2As_3/Ba_2P_3-flux method. *J. Phys. Soc. Jpn.* **81**, 104710 (2012). URL dx.doi.org/10.1143/JPSJ.81.104710.

[95] Webster, J. & Eren, H. *Measurement, Instrumentation, and Sensors Handbook: Two-Volume Set*. Electrical Engineering Handbook (CRC Press, Boca Raton, 2018). URL https://books.google.es/books?id=t0BZDwAAQBAJ.

[96] Myeongkyu, L. *X-Ray Diffraction for Materials Research: From Fundamentals to Applications* (Apple Academic Press, New York, 2016), 1st edn. URL dx.doi.org/10.1201/b19936.

[97] Voigtländer, B. *Scanning Probe Microscopy* (Springer-Verlag, Berlin Heidelberg, 2015). URL dx.doi.org/10.1007/978-3-662-45240-0.

[98] Convens, E. *Sandblasting Basics* (Gaelic Victors, 2017). URL https://books.google.es/books?id=OegGtAEACAAJ.

[99] Terashima, T. *et al.* Resistivity and upper critical field in KFe_2As_2 single crystals. *J. Phys. Soc. Jpn.* **78**, 063702 (2009). URL dx.doi.org/10.1143/JPSJ.78.063702.

[100] Yuan, H. Q. *et al.* Nearly isotropic superconductivity in (Ba,K)Fe_2As_2. *Nature* **457**, 565–568 (2009). URL dx.doi.org/10.1038/nature07676.

[101] Su, T. S., Yin, Y. W., Teng, M. L., Zhang, M. J. & Li, X. G. Angular dependence of vortex dynamics in $BaFe_{1.9}Ni_{0.1}As_2$ single crystal. *Mater. Res. Express* **1**, 016003 (2014). URL dx.doi.org/10.1088/2053-1591/1/1/016003.

[102] Hao, F. X. *et al.* Angle-resolved vortex glass transition and pinning properties in $BaFe_{1.8}Co_{0.2}As_2$ single crystals. *J. App. Phys.* **117** (2015). URL dx.doi.org/10.1063/1.4919776.

[103] Shi, Z. X. *et al.* Out-of-plane and in-plane anisotropy of upper critical field in MgB_2. *Phys. Rev. B* **68**, 104513 (2003). URL dx.doi.org/10.1103/PhysRevB.68.104513.

[104] Kim, H.-J. *et al.* Comparison of temperature and angular dependence of the upper critical field in $Mg_{1-x}Al_xB_2$ single crystals in dirty-limit two-gap theory. *Phys. Rev. B* **73**, 064520 (2006). URL dx.doi.org/10.1103/PhysRevB.73.064520.

[105] Mosqueira, J. *et al.* Observation of anisotropic diamagnetism above the superconducting transition in iron pnictide $Ba_{1-x}K_xFe_2As_2$ single crystals due to thermodynamic fluctuations. *Phys. Rev. B* **83**, 094519 (2011). URL dx.doi.org/10.1103/PhysRevB.83.094519.

[106] Rey, R. I. *et al.* Measurements of the fluctuation-induced in-plane magnetoconductivity at high reduced temperatures and magnetic fields in the iron arsenide $BaFe_{2-x}Ni_xAs_2$. *Supercond. Sci. Technol.* **26**, 055004 (2013). URL dx.doi.org/10.1088/0953-2048/26/5/055004.

[107] Ramos-Álvarez, A. *et al.* Superconducting fluctuations in isovalently substituted $BaFe_2(As_{1-x}P_x)_2$: Possible observation of multiband effects. *Phys. Rev. B* **92**, 094508 (2015). URL dx.doi.org/10.1103/PhysRevB.92.094508.

[108] Sóñora, D. *et al.* Quasi-two-dimensional behavior of 112-type iron-based superconductors. *Phys. Rev. B* **96**, 014516 (2017). URL dx.doi.org/10.1103/PhysRevB.96.014516.

[109] Ahmad, D. *et al.* Effect of proton irradiation on the fluctuation-induced magnetoconductivity of $FeSe_{1-x}Te_x$ thin films. *New J. Phys.* **19**, 093004 (2017). URL dx.doi.org/10.1088/1367-2630/aa76ad.

[110] Ahmad, D. *et al.* Anisotropy dependence of the fluctuation spectroscopy in the critical and gaussian regimes in superconducting $NaFe_{1-x}Co_xAs$ single crystals. *Sci. Rep.* **8**, 8556 (2018). URL dx.doi.org/10.1038/s41598-018-26939-8.

[111] Rey, R. I. *et al.* Measurements of the superconducting fluctuations in optimally doped $BaFe_{2-x}Ni_xAs_2$ under high magnetic fields: probing the 3D-anisotropic Ginzburg-Landau approach. *Supercond. Sci. Technol.* **27**, 075001 (2014). URL dx.doi.org/10.1088/0953-2048/27/7/075001.

[112] Mosqueira, J., Cabo, L. & Vidal, F. Structural and T_c inhomogeneities inherent to doping in $La_{2-x}Sr_xCuO_4$ superconductors and their effects on the precursor diamagnetism. *Phys. Rev. B* **80**, 214527 (2009). URL dx.doi.org/10.1103/PhysRevB.80.214527.

[113] Gurevich, A. Enhancement of the upper critical field by nonmagnetic impurities in dirty two-gap superconductors. *Phys. Rev. B* **67**, 184515 (2003). URL dx.doi.org/10.1103/PhysRevB.67.184515.

[114] Gurevich, A. Upper critical field and the Fulde-Ferrel-Larkin-Ovchinnikov transition in multiband superconductors. *Phys. Rev. B* **82**, 184504 (2010). URL dx.doi.org/10.1103/PhysRevB.82.184504.

[115] Rosenstein, B. & Li, D. Ginzburg-Landau theory of type II superconductors in magnetic field. *Rev. Mod. Phys.* **82**, 109–168 (2010). URL dx.doi.org/10.1103/RevModPhys.82.109.

[116] Lortz, R., Musolino, N., Wang, Y., Junod, A. & Toyota, N. Origin of the magnetization peak effect in the Nb_3Sn superconductor. *Phys. Rev. B* **75**, 094503 (2007). URL dx.doi.org/10.1103/PhysRevB.75.094503.

[117] Stamopoulos, D., Speliotis, A. & Niarchos, D. From the second magnetization peak to peak effect. a study of superconducting properties in Nb films and MgB_2 bulk samples. *Supercond. Sci. Technol.* **17**, 1261 (2004). URL dx.doi.org/10.1088/0953-2048/17/11/006.

[118] Rosenstein, B. *et al.* Peak effect and square-to-rhombic vortex lattice transition in $La_{2-x}Sr_xCuO_4$. *Phys. Rev. B* **72**, 144512 (2005). URL dx.doi.org/10.1103/PhysRevB.72.144512.

[119] Salem-Sugui, S. *et al.* Vortex dynamics and phase diagram in the electron-doped cuprate superconductor $Pr_{0.87}LaCe_{0.13}CuO_4$. *Phys. Rev. B* **102**, 064509 (2020). URL dx.doi.org/10.1103/PhysRevB.102.064509.

[120] Cheng, W., Lin, H., Shen, B. & Wen, H.-H. Comparative study of vortex dynamics in $CaKFe_4As_4$ and $Ba_{0.6}K_{0.4}Fe_2As_2$ single crystals. *Sci. Bull.* **64**, 81–90 (2019). URL dx.doi.org/10.1016/j.scib.2018.12.024.

[121] Wang, C. *et al.* Novel sample-thickness-dependent flux pinning behaviors of KFe_2As_2 intercalations in $CaKFe_4As_4$ single crystals. *Supercond. Sci. Technol.* **34**, 055001 (2021). URL dx.doi.org/10.1088/1361-6668/abecd0.

[122] Shen, B. *et al.* Flux dynamics and vortex phase diagram in $Ba(Fe_{1-x}Co_x)_2As_2$ single crystals revealed by magnetization and its relaxation. *Phys. Rev. B* **81**, 014503 (2010). URL dx.doi.org/10.1103/PhysRevB.81.014503.

[123] Sundar, S. *et al.* Study of the second magnetization peak and the pinning behaviour in $Ba(Fe_{0.935}Co_{0.065})_2As_2$ pnictide superconductor. *Supercond. Sci. Technol.* **30**, 125007 (2017). URL dx.doi.org/10.1088/1361-6668/aa90b4.

[124] Sundar, S. *et al.* Plastic pinning replaces collective pinning as the second magnetization peak disappears in the pnictide superconductor $Ba_{0.75}K_{0.25}Fe_2As_2$. *Phys. Rev. B* **95**, 134509 (2017). URL dx.doi.org/10.1103/PhysRevB.95.134509.

[125] Sundar, S. *et al.* Doping dependence of the second magnetization peak, critical current density, and pinning mechanism in $BaFe_{2-x}Ni_xAs_2$ pnictide superconductors. *ACS Appl. Electron. Mater.* **1**, 179–188 (2019). URL dx.doi.org/10.1021/acsaelm.8b00014.

[126] Salem-Sugui, S. *et al.* Flux dynamics associated with the second magnetization peak in the iron pnictide $Ba_{1-x}K_xFe_2As_2$. *Phys. Rev. B* **82**, 054513 (2010). URL dx.doi.org/10.1103/PhysRevB.82.054513.

[127] Ahmad, D. *et al.* Doping dependence of the vortex dynamics in single-crystal superconducting $NaFe_{1-x}Co_xAs$. *Supercond. Sci. Technol.* **30**, 105006 (2017). URL dx.doi.org/10.1088/1361-6668/aa7ec3.

[128] Zhou, W., Xing, X., Wu, W., Zhao, H. & Shi, Z. Second magnetization peak effect, vortex dynamics and flux pinning in 112-type superconductor $Ca_{0.8}La_{0.2}Fe_{1-x}Co_xAs_2$. *Sci. Rep.* **6**, 22278 (2016). URL dx.doi.org/10.1038/srep22278.

[129] Galluzzi, A. *et al.* Pinning energy and anisotropy properties of a Fe(Se,Te) iron based superconductor. *Nanotechnology* **30**, 254001 (2019). URL dx.doi.org/10.1088/1361-6528/ab0c23.

[130] Kopeliansky, R. *et al.* Possibility of vortex lattice structural phase transition in the superconducting pnictide $Ba(Fe_{0.925}Co_{0.075})_2As_2$. *Phys. Rev. B* **81**, 092504 (2010). URL dx.doi.org/10.1103/PhysRevB.81.092504.

[131] Pramanik, A. K. *et al.* Fishtail effect and vortex dynamics in LiFeAs single crystals. *Phys. Rev. B* **83**, 094502 (2011). URL dx.doi.org/10.1103/PhysRevB.83.094502.

[132] Salem-Sugui Jr., S. *et al.* Observation of an anomalous peak in isofield M(T) curves in $BaFe_2(As_{0.68}P_{0.32})_2$ suggesting a phase transition in the irreversible regime. *Supercond. Sci. Technol.* **28**, 055017 (2015). URL dx.doi.org/10.1088/0953-2048/28/5/055017.

[133] Miu, L. *et al.* Second magnetization peak, rhombic-to-square Bragg vortex glass transition, and intersecting magnetic hysteresis curves in overdoped $BaFe_2(As_{1-x}P_x)_2$ single crystals. *Sci. Rep.* **10**, 17274 (2020). URL dx.doi.org/10.1038/s41598-020-74156-z.

[134] Zehetmayer, M. How the vortex lattice of a superconductor becomes disordered: a study by scanning tunneling spectroscopy. *Sci. Rep.* **5**, 9244 (2015). URL dx.doi.org/10.1038/srep09244.

[135] Miu, D., Noji, T., Adachi, T., Koike, Y. & Miu, L. On the nature of the second magnetization peak in $FeSe_{1-x}Te_x$ single crystals. *Supercond. Sci. Technol.* **25**, 115009 (2012). URL dx.doi.org/10.1088/0953-2048/25/11/115009.

[136] Ionescu, A. M., Miu, D., Crisan, A. & Miu, L. Pinning-induced vortex-system disordering at the origin of the second magnetization peak in superconducting

single crystals. *J. Supercond. Nov. Magn.* **31**, 2329–2337 (2018). URL dx.doi.org/10.1007/s10948-017-4487-5.

[137] Song, D. *et al.* Distinct doping dependence of critical temperature and critical current density in $Ba_{1-x}K_xFe_2As_2$ superconductor. *Sci. Rep.* **6**, 26671 (2016). URL dx.doi.org/10.1038/srep26671.

[138] Wang, C. *et al.* Flux dynamics and vortex phase diagram of the new superconductor $(Li_{1-x}Fe_x)$OHFeSe single crystals. *Supercond. Sci. Technol.* **30**, 085004 (2017). URL dx.doi.org/10.1088/1361-6668/aa742e.

[139] Jung, S.-G. *et al.* Effects of magnetic impurities on upper critical fields in the high-T_c superconductor La-doped $CaFe_2As_2$. *Supercond. Sci. Technol.* **30**, 085009 (2017). URL dx.doi.org/10.1088/1361-6668/aa766c.

[140] Sundar, S. *et al.* Strong pinning in the hole-doped pnictide superconductor $La_{0.34}Na_{0.66}Fe_2As_2$. *J. Appl. Phys.* **125** (2019). URL dx.doi.org/10.1063/1.5088823.

[141] Weyeneth, S. *et al.* Anisotropy of superconducting single crystal $SmFeAsO_{0.8}F_{0.2}$ studied by torque magnetometry. *J. Supercond. Nov. Magn.* **22**, 325–329 (2009). URL dx.doi.org/10.1007/s10948-008-0413-1.

[142] Prozorov, R., Tillman, M. E., Mun, E. D. & Canfield, P. C. Intrinsic magnetic properties of the superconductor $NdFeAsO_{0.9}F_{0.1}$ from local and global measurements. *New J. Phys.* **11**, 035004 (2009). URL dx.doi.org/10.1088/1367-2630/11/3/035004.

[143] Yakita, H. *et al.* A new layered iron arsenide superconductor: (Ca,Pr)$FeAs_2$. *J. Am. Chem. Soc.* **136**, 846–849 (2014). URL dx.doi.org/10.1021/ja410845b.

[144] Zhou, W. *et al.* Anisotropic superconductivity of $Ca_{1-x}La_xFeAs_2$ ($x \sim 0.18$) single crystal. *Appl. Phys. Express* **7**, 063102 (2014). URL dx.doi.org/10.7567/APEX.7.063102.

[145] Xing, X. *et al.* Anisotropic GinzburgLandau scaling of H_{c_2} and transport properties of 112-type $Ca_{0.8}La_{0.2}Fe_{0.98}Co_{0.02}As_2$ single crystal. *Supercond. Sci. Technol.* **29**, 055005 (2016). URL dx.doi.org/10.1088/0953-2048/29/5/055005.

[146] Xie, T. *et al.* Crystal growth and phase diagram of 112-type iron pnictide superconductor $Ca_{1-y}La_yFe_{1-x}Ni_xAs_2$. *Supercond. Sci. Technol.* **30**, 095002 (2017). URL dx.doi.org/10.1088/1361-6668/aa7994.

[147] Moll, P. J. W. *et al.* Transition from slow Abrikosov to fast moving Josephson vortices in iron pnictide superconductors. *Nat. Mater.* **12**, 134–138 (2013). URL dx.doi.org/10.1038/nmat3489.

[148] Salem-Sugui Jr., S. *et al.* Fishtail and vortex dynamics in the Ni-doped iron pnictide $BaFe_{1.82}Ni_{0.18}As_2$. *Phys. Rev. B* **84**, 052510 (2011). URL dx.doi.org/10.1103/PhysRevB.84.052510.

[149] Salem-Sugui Jr., S. *et al.* Vortex dynamics as a function of field orientation in $BaFe_{1.9}Ni_{0.1}As_2$. *Supercond. Sci. Technol.* **26**, 025006 (2012). URL dx.doi.org/10.1088/0953-2048/26/2/025006.

[150] Sharma, S., Vinod, K., Sundar, C. S. & Bharathi, A. Critical current density and magnetic phase diagrams of $BaFe_{1.29}Ru_{0.71}As_2$ single crystals. *Supercond. Sci. Technol.* **26**, 015009 (2012). URL dx.doi.org/10.1088/0953-2048/26/1/015009.

[151] Feigel'man, M. V., Geshkenbein, V. B., Larkin, A. I. & Vinokur, V. M. Theory of collective flux creep. *Phys. Rev. Lett.* **63**, 2303–2306 (1989). URL dx.doi.org/10.1103/PhysRevLett.63.2303.

[152] Maley, M. P., Willis, J. O., Lessure, H. & McHenry, M. E. Dependence of flux-creep activation energy upon current density in grain-aligned $YBa_2Cu_3O_{7-x}$. *Phys. Rev. B* **42**, 2639–2642 (1990). URL dx.doi.org/10.1103/PhysRevB.42.2639.

[153] McHenry, M. E. *et al.* Dependence of the flux-creep activation energy on the magnetization current for a $La_{1.86}Sr_{0.14}CuO_4$ single crystal. *Phys. Rev. B* **44**, 7614–7624 (1991). URL dx.doi.org/10.1103/PhysRevB.44.7614.

[154] Abulafia, Y. *et al.* Plastic vortex creep in $YBa_2Cu_3O_{7-x}$ Crystals. *Phys. Rev. Lett.* **77**, 1596–1599 (1996). URL dx.doi.org/10.1103/PhysRevLett.77.1596.

[155] Eisterer, M. Radiation effects on iron-based superconductors. *Supercond. Sci. Technol.* **31**, 013001 (2017). URL dx.doi.org/10.1088/1361-6668/aa9882.

[156] Maiorov, B. *et al.* Competition and cooperation of pinning by extrinsic point-like defects and intrinsic strong columnar defects in $BaFe_2As_2$ thin films. *Phys. Rev. B* **86**, 094513 (2012). URL dx.doi.org/10.1103/PhysRevB.86.094513.

[157] Taen, T., Nakajima, Y., Tamegai, T. & Kitamura, H. Enhancement of critical current density and vortex activation energy in proton-irradiated Co-doped $BaFe_2As_2$. *Phys. Rev. B* **86**, 094527 (2012). URL dx.doi.org/10.1103/PhysRevB.86.094527.

[158] Nakajima, Y. *et al.* Critical current densities and flux creep rate in Co-doped $BaFe_2As_2$ with columnar defects introduced by heavy-ion irradiation. *Physica C Supercond.* **470**, 1103–1105 (2010). URL dx.doi.org/10.1016/j.physc.2010.05.047. Proceedings of the 22nd International Symposium on Superconductivity (ISS 2009).

[159] Otabe, E. S. *et al.* Condensation energy density properties of Ba-122 pnictide superconductor with columnar defects introduced by heavy-ion irradiation. *Phys. Procedia* **36**, 693–697 (2012). URL dx.doi.org/10.1016/j.phpro.2012.06.269. Superconductivity Centennial Conference 2011.

[160] Tarantini, C. *et al.* Artificial and self-assembled vortex-pinning centers in superconducting $Ba(Fe_{1-x}Co_x)_2As_2$ thin films as a route to obtaining very

high critical-current densities. *Phys. Rev. B* **86**, 214504 (2012). URL dx.doi.org/10.1103/PhysRevB.86.214504.

[161] Lee, S. *et al.* Artificially engineered superlattices of pnictide superconductors. *Nat. Mater.* **12**, 392–396 (2013). URL dx.doi.org/10.1038/nmat3575.

[162] Aburas, M., Pautrat, A. & Bellido, N. Change of surface critical current in the surface superconductivity and mixed states of superconducting niobium. *Supercond. Sci. Technol.* **30**, 015009 (2016). URL dx.doi.org/10.1088/0953-2048/30/1/015009.

[163] Casalbuoni, S. *et al.* Surface superconductivity in niobium for superconducting RF cavities. *Nucl. Instrum. Methods Phys. Res.* **538**, 45–64 (2005). URL dx.doi.org/10.1016/j.nima.2004.09.003.

[164] Sung, Z.-H., Dzyuba, A., Lee, P. J., Larbalestier, D. C. & Cooley, L. D. Evidence of incomplete annealing at 800 řC and the effects of 120 řC baking on the crystal orientation and the surface superconducting properties of cold-worked and chemically polished Nb. *Supercond. Sci. Technol.* **28**, 075003 (2015). URL dx.doi.org/10.1088/0953-2048/28/7/075003.

[165] Cubero, A. *et al.* Effects of laser-induced periodic surface structures on the superconducting properties of niobium. *Appl. Surf. Sci.* **508**, 145140 (2020). URL dx.doi.org/10.1016/j.apsusc.2019.145140.

[166] Cubero, A. *et al.* Surface superconductivity changes of niobium sheets by femtosecond laser-induced periodic nanostructures. *Nanomaterials* **10**, 2525 (2020). URL dx.doi.org/10.3390/nano10122525.

[167] Hu, D. *et al.* Structural and magnetic phase transitions near optimal superconductivity in $BaFe_2(As_{1-x}P_x)_2$. *Phys. Rev. Lett.* **114**, 157002 (2015). URL dx.doi.org/10.1103/PhysRevLett.114.157002.

[168] Mathieu, P. & Simon, Y. Phenomenological theory of vortex motion in type-II superconductors. *Europhys. Lett.* **5**, 67 (1988). URL dx.doi.org/10.1209/0295-5075/5/1/012.

[169] Lawrence, W. E. & Doniach, S. Theory of layer structure superconductors. In Kanda, E. (ed.) *Proceedings of the 12th International Conference on Low Temperature Physics*, 361 (Academic Press of Japan, Keigatu, Tokyo, 1970). URL books.google.es/books?id=6ryyXwAACAAJ.

[170] Vidal, F. & Ramallo, M. V. Multilayering effects on the thermal fluctuations of Cooper pairs around the superconducting transition in cuprates. In Bok, J., Deutscher, G., Pavuna, D. & Wolf, S. A. (eds.) *The Gap Symmetry and Fluctuations in High-T_c Superconductors*, 443–464 (Springer US, Boston, MA, 1998). URL dx.doi.org/10.1007/0-306-47081-0_24.

[171] Lang, W. Influence of a distribution of critical temperatures on the paraconductivity and the fluctuation magnetoconductivity in high-temperature super-

conductors. *Physica C Supercond.* **226**, 267–278 (1994). URL dx.doi.org/10.1016/0921-4534(94)90205-4.

[172] Casaca, A. *et al.* Model for the broadening of the resistive transition in $YBa_2Cu_3O_{7-\delta}$ thin films. *Supercond. Sci. Technol.* **10**, 75 (1997). URL dx.doi.org/10.1088/0953-2048/10/2/001.

[173] Ghosh, A. K., Bandyopadhyay, S. K. & Basu, A. N. Generalization of fluctuation induced conductivity in polycrystalline $Y_{1-x}Ca_xBa_2Cu_3O_y$ and $Bi_2Sr_2Ca_1Cu_2O_{8+\delta}$ superconductors. *J. Appl. Phys.* **86**, 3247–3252 (1999). URL dx.doi.org/10.1063/1.371197.

[174] Mosqueira, J., Carballeira, C. & Vidal, F. Fluctuation induced diamagnetism in the zero magnetic field limit in a low temperature superconducting alloy. *Phys. Rev. Lett.* **87**, 167009 (2001). URL dx.doi.org/10.1103/PhysRevLett.87.167009.

[175] Carballeira, C., Mosqueira, J., Ramallo, M. V., Veira, J. A. & Vidal, F. Fluctuation-induced diamagnetism in bulk isotropic superconductors at high reduced temperatures. *J. Phys. Condens. Matter* **13**, 9271 (2001). URL dx.doi.org/10.1088/0953-8984/13/41/316.

[176] Rey, R. I. *et al.* The conductivity and the magnetization around T_c in optimally-doped $YBa_2Cu_3O_{7-\delta}$ revisited: quantitative analysis in terms of fluctuating superconducting pairs. *Supercond. Sci. Technol.* **32**, 045009 (2019). URL dx.doi.org/10.1088/1361-6668/aafe93.

[177] Vidal, F. *et al.* On the consequences of the uncertainty principle on the superconducting fluctuations well inside the normal state. *Europhys. Lett.* **59**, 754 (2002). URL dx.doi.org/10.1209/epl/i2002-00190-3.

[178] Vidal, F., Ramallo, M. V., Mosqueira, J. & Carballeira, C. Superconducting fluctuations above T_c and the uncertainty principle: How small may the coherence length be? *Int. J. Mod. Phys. B* **17**, 3470–3472 (2003). URL dx.doi.org/10.1142/S0217979203021228.

[179] Luo, C. W. *et al.* Comment on "Conductivity of underdoped $YBa_2Cu_3O_{7-\delta}$: Evidence for incoherent pair correlations in the pseudogap regime". *Phys. Rev. Lett.* **90**, 179703 (2003). URL dx.doi.org/10.1103/PhysRevLett.90.179703.

[180] Cabo, L., Mosqueira, J. & Vidal, F. Comment on "Field-enhanced diamagnetism in the pseudogap state of the cuprate $Bi_2Sr_2CaCu_2O_{8+\delta}$ superconductor in an intense magnetic field". *Phys. Rev. Lett.* **98**, 119701 (2007). URL dx.doi.org/10.1103/PhysRevLett.98.119701.

[181] Podolsky, D., Raghu, S. & Vishwanath, A. Nernst effect and diamagnetism in phase fluctuating superconductors. *Phys. Rev. Lett.* **99**, 117004 (2007). URL dx.doi.org/10.1103/PhysRevLett.99.117004.

[182] Mosqueira, J., Ramallo, M. V. & Vidal, F. Comment on "Phase fluctuation superconductivity in overdoped $La_{2-x}Sr_xCuO_4$." Preprint at dx.doi.org/10.48550/arXiv.1112.6104 (2011). URL dx.doi.org/10.48550/arXiv.1112.6104.

[183] Rey, R. I., Ramos-Álvarez, A., Mosqueira, J., Ramallo, M. V. & Vidal, F. Comment on "Diamagnetism and Cooper pairing above T_c in cuprates". *Phys. Rev. B* **87**, 056501 (2013). URL dx.doi.org/10.1103/PhysRevB.87.056501.

[184] Kokanović, I., Hills, D. J., Sutherland, M. L., Liang, R. & Cooper, J. R. Diamagnetism of $YBa_2Cu_3O_{6+x}$ crystals above T_c: Evidence for gaussian fluctuations. *Phys. Rev. B* **88**, 060505 (2013). URL dx.doi.org/10.1103/PhysRevB.88.060505.

[185] Cyr-Choinière, O. *et al.* Pseudogap temperature T^* of cuprate superconductors from the Nernst effect. *Phys. Rev. B* **97**, 064502 (2018). URL dx.doi.org/10.1103/PhysRevB.97.064502.

[186] Sóñora, D., Mosqueira, J. & Vidal, F. Comment on "Temperature range of superconducting fluctuations above T_c in $YBa_2Cu_3O_{7-\delta}$ single crystals". *Phys. Rev. B* **102**, 176501 (2020). URL dx.doi.org/10.1103/PhysRevB.102.176501.

[187] Leridon, B. *et al.* Protected superconductivity at the boundaries of charge-density-wave domains. *New J. Phys.* **22**, 073025 (2020). URL dx.doi.org/10.1088/1367-2630/ab976e.

[188] Bernardi, E. *et al.* Superconducting diamagnetic fluctuations in Sm-based underdoped cuprates studied via SQUID magnetometry. *Phys. Rev. B* **81**, 064502 (2010). URL dx.doi.org/10.1103/PhysRevB.81.064502.

[189] Prando, G. *et al.* Superconducting phase fluctuations in $SmFeAsO_{0.8}F_{0.2}$ from diamagnetism at a low magnetic field above T_c. *Phys. Rev. B* **84**, 064507 (2011). URL dx.doi.org/10.1103/PhysRevB.84.064507.

[190] Bossoni, L., Romanó, L., Canfield, P. C. & Lascialfari, A. Non-conventional superconducting fluctuations in $Ba(Fe_{1-x}Rh_x)_2As_2$ iron-based superconductors. *J. Phys. Cond. Matter* **26**, 405703 (2014). URL dx.doi.org/10.1088/0953-8984/26/40/405703.

[191] Ni, N. *et al.* Effects of Co substitution on thermodynamic and transport properties and anisotropic H_{c2} in $Ba(Fe_{1-x}Co_x)_2As_2$ single crystals. *Phys. Rev. B* **78**, 214515 (2008). URL dx.doi.org/10.1103/PhysRevB.78.214515.

[192] Sun, D. L., Liu, Y. & Lin, C. T. Comparative study of upper critical field H_{c2} and second magnetization peak H_{sp} in hole- and electron-doped $BaFe_2As_2$ superconductor. *Phys. Rev. B* **80**, 144515 (2009). URL dx.doi.org/10.1103/PhysRevB.80.144515.

[193] Tanatar, M. A. *et al.* Anisotropy of the iron pnictide superconductor $Ba(Fe_{1-x}Co_x)_2As_2$ ($x = 0.074$, $T_c = 23$ K). *Phys. Rev. B* **79**, 094507 (2009).

URL dx.doi.org/10.1103/PhysRevB.79.094507.

[194] Yamamoto, A. *et al.* Small anisotropy, weak thermal fluctuations, and high field superconductivity in Co-doped iron pnictide $Ba(Fe_{1-x}Co_x)_2As_2$. *Appl. Phys. Lett.* **94**, 062511 (2009). URL dx.doi.org/10.1063/1.3081455.

[195] Kim, S. H. *et al.* Fluctuation conductivity of single-crystalline $BaFe_{1.8}Co_{0.2}As_2$ in the critical region. *J. Appl. Phys.* **108**, 063916 (2010). URL dx.doi.org/10.1063/1.3478716.

[196] Vinod, K., Satya, A. T., Sharma, S., Sundar, C. S. & Bharathi, A. Upper critical field anisotropy in $BaFe_{2-x}Co_xAs_2$ single crystals synthesized without flux. *Phys. Rev. B* **84**, 012502 (2011). URL dx.doi.org/10.1103/PhysRevB.84.012502.

[197] Tinkham, M. Effect of fluxoid quantization on transitions of superconducting films. *Phys. Rev.* **129**, 2413–2422 (1963). URL dx.doi.org/10.1103/PhysRev.129.2413.

[198] Harper, F. E. & Tinkham, M. The mixed state in superconducting thin films. *Phys. Rev.* **172**, 441–450 (1968). URL dx.doi.org/10.1103/PhysRev.172.441.

[199] Mineev, V. General expression for the angular dependence of the critical field in layered superconductors. *Phys. Rev. B* **65**, 012508 (2001). URL dx.doi.org/10.1103/PhysRevB.65.012508.

[200] Miloevi, M. V. & Perali, A. Emergent phenomena in multicomponent superconductivity: an introduction to the focus issue. *Supercond. Sci. Technol.* **28**, 060201 (2015). URL dx.doi.org/10.1088/0953-2048/28/6/060201.

[201] Terashima, K. *et al.* Fermi surface nesting induced strong pairing in iron-based superconductors. *Proc. Natl. Acad. Sci.* **106**, 7330–7333 (2009). URL dx.doi.org/10.1073/pnas.0900469106.

[202] Tortello, M. *et al.* Multigap superconductivity and strong electron-boson coupling in Fe-based superconductors: A point-contact Andreev-reflection study of $Ba(Fe_{1-x}Co_x)_2As_2$ single crystals. *Phys. Rev. Lett.* **105**, 237002 (2010). URL dx.doi.org/10.1103/PhysRevLett.105.237002.

[203] Williams, T. J. *et al.* Muon spin rotation measurement of the magnetic field penetration depth in $Ba(Fe_{0.926}Co_{0.074})_2As_2$: Evidence for multiple superconducting gaps. *Phys. Rev. B* **80**, 094501 (2009). URL dx.doi.org/10.1103/PhysRevB.80.094501.

[204] Choi, K.-Y. *et al.* Two s-wave gap symmetry for single crystals of the superconductor $BaFe_{1.8}Co_{0.2}As_2$. *Physica C Supercond.* **470**, S506–S507 (2010). URL dx.doi.org/10.1016/j.physc.2009.11.150. Proceedings of the 9th International Conference on Materials and Mechanisms of Superconductivity.

[205] Fischer, T. *et al.* Highly anisotropic energy gap in superconducting $Ba(Fe_{0.9}Co_{0.1})_2As_2$ from optical conductivity measurements. *Phys. Rev. B* **82**, 224507 (2010). URL dx.doi.org/10.1103/PhysRevB.82.224507.

[206] Gordon, R. T. *et al.* Doping evolution of the absolute value of the London penetration depth and superfluid density in single crystals of $Ba(Fe_{1-x}Co_x)_2As_2$. *Phys. Rev. B* **82**, 054507 (2010). URL dx.doi.org/10.1103/PhysRevB.82.054507.

[207] Luan, L. *et al.* Local measurement of the penetration depth in the pnictide superconductor $Ba(Fe_{0.95}Co_{0.05})_2As_2$. *Phys. Rev. B* **81**, 100501 (2010). URL dx.doi.org/10.1103/PhysRevB.81.100501.

[208] Luan, L. *et al.* Local measurement of the superfluid density in the pnictide superconductor $Ba(Fe_{1-x}Co_x)_2As_2$ across the superconducting dome. *Phys. Rev. Lett.* **106**, 067001 (2011). URL dx.doi.org/10.1103/PhysRevLett.106.067001.

[209] Yong, J. *et al.* Superfluid density measurements of $Ba(Fe_{1-x}Co_x)_2As_2$ films near optimal doping. *Phys. Rev. B* **83**, 104510 (2011). URL dx.doi.org/10.1103/PhysRevB.83.104510.

[210] Bekaert, J. *et al.* Anisotropic type-I superconductivity and anomalous superfluid density in OsB_2. *Phys. Rev. B* **94**, 144506 (2016). URL dx.doi.org/10.1103/PhysRevB.94.144506.

[211] Cherpak, N. T., Barannik, A. A., Prozorov, R., Tanatar, M. & Velichko, A. V. On the determination of the quasiparticle scattering rate in unconventional superconductors by microwave surface impedance. *Low Temp. Phys.* **39**, 1110–1112 (2013). URL dx.doi.org/10.1063/1.4830422.

[212] Barannik, A. *et al.* Millimeter-wave surface impedance of optimally-doped $Ba(Fe_{1-x}Co_x)_2As_2$ single crystals. *Phys. Rev. B* **87**, 014506 (2013). URL dx.doi.org/10.1103/PhysRevB.87.014506.

[213] Wang, Z.-S., Luo, H.-Q., Ren, C. & Wen, H.-H. Upper critical field, anisotropy, and superconducting properties of $Ba_{1-x}K_xFe_2As_2$ single crystals. *Phys. Rev. B* **78**, 140501 (2008). URL dx.doi.org/10.1103/PhysRevB.78.140501.

[214] Yi, X. *et al.* Vortex phase transition and anisotropy behavior of optimized $(Li_{1-x}Fe_xOH)FeSe$ single crystals. *Supercond. Sci. Technol.* **29**, 105015 (2016). URL dx.doi.org/10.1088/0953-2048/29/10/105015.

[215] Yuan, F. F. *et al.* Anisotropy of iron-platinum-arsenide $Ca_{10}(Pt_nAs_8)(Fe_{2-x}Pt_xAs_2)_5$ single crystals. *Appl. Phys. Lett.* **107**, 012602 (2015). URL dx.doi.org/10.1063/1.4926486.

[216] Jia, Y. *et al.* Angular dependence of resistivity in the superconducting state of $NdFeAsO_{0.82}F_{0.18}$ single crystals. *Supercond. Sci. Technol.* **21**, 105018 (2008). URL dx.doi.org/10.1088/0953-2048/21/10/105018.

[217] Kalenyuk, A. A. *et al.* Unusual two-dimensional behavior of iron-based superconductors with low anisotropy. *Phys. Rev. B* **96**, 134512 (2017). URL dx.doi.org/10.1103/PhysRevB.96.134512.

[218] Bendele, M. *et al.* Anisotropic superconducting properties of single-crystalline $FeSe_{0.5}Te_{0.5}$. *Phys. Rev. B* **81**, 224520 (2010). URL dx.doi.org/10.1103/PhysRevB.81.224520.

[219] Prando, G. *et al.* Vortex dynamics and irreversibility line in optimally doped $SmFeAsO_{0.8}F_{0.2}$ from ac susceptibility and magnetization measurements. *Phys. Rev. B* **83**, 174514 (2011). URL dx.doi.org/10.1103/PhysRevB.83.174514.

[220] Malozemoff, A. P., Worthington, T. K., Yeshurun, Y., Holtzberg, F. & Kes, P. H. Frequency dependence of the ac susceptibility in a Y-Ba-Cu-O crystal: A reinterpretation of H_{c2}. *Phys. Rev. B* **38**, 7203–7206 (1988). URL dx.doi.org/10.1103/PhysRevB.38.7203.

[221] Yeshurun, Y. & Malozemoff, A. P. Giant flux creep and irreversibility in an Y-Ba-Cu-O crystal: An alternative to the superconducting-glass model. *Phys. Rev. Lett.* **60**, 2202–2205 (1988). URL dx.doi.org/10.1103/PhysRevLett.60.2202.

[222] Polichetti, M. *et al.* A precursor mechanism triggering the second magnetization peak phenomenon in superconducting materials. *Sci. Rep.* **11**, 7247 (2021). URL dx.doi.org/10.1038/s41598-021-86728-8.

[223] Beasley, M. R., Labusch, R. & Webb, W. W. Flux creep in type-II superconductors. *Phys. Rev.* **181**, 682–700 (1969). URL dx.doi.org/10.1103/PhysRev.181.682.

[224] Bean, C. P. Magnetization of hard superconductors. *Phys. Rev. Lett.* **8**, 250–253 (1962). URL dx.doi.org/10.1103/PhysRevLett.8.250.

[225] Bean, C. P. Magnetization of high-field superconductors. *Rev. Mod. Phys.* **36**, 31–39 (1964). URL dx.doi.org/10.1103/RevModPhys.36.31.

[226] Poole Jr., C. P., Farach, H. A., Creswick, R. J. & Prozorov, R. *Superconductivity* (Academic Press, London, 2007), 2nd edn. URL shop.elsevier.com/books/superconductivity/poole/978-0-12-088761-3.

[227] Prozorov, R. *et al.* Vortex phase diagram of $Ba(Fe_{0.93}Co_{0.07})_2As_2$ single crystals. *Phys. Rev. B* **78**, 224506 (2008). URL dx.doi.org/10.1103/PhysRevB.78.224506.

[228] Griessen, R. *et al.* Evidence for mean free path fluctuation induced pinning in $YBa_2Cu_3O_7$ and $YBa_2Cu_4O_8$ films. *Phys. Rev. Lett.* **72**, 1910–1913 (1994). URL dx.doi.org/10.1103/PhysRevLett.72.1910.

[229] Galluzzi, A. *et al.* Second magnetization peak effect in a Fe(Se,Te) iron based superconductor. *J. Phys. Conf. Ser.* **1226**, 012012 (2019). URL dx.doi.org

/10.1088/1742-6596/1226/1/012012.

[230] Dew-Hughes, D. Flux pinning mechanisms in type II superconductors. *Phil. Mag.* **30**, 293–305 (1974). URL dx.doi.org/10.1080/14786439808206556.

[231] Koblischka, M. R. & Muralidhar, M. Pinning force scaling analysis of Fe-based high-Tc superconductors. *Int. J. Mod. Phys. B* **30**, 1630017 (2016). URL dx.doi.org/10.1142/S0217979216300176.

[232] Zhang, Q. *et al.* Enhanced transport critical current density in Sn-added $SmFeAsO_{1-x}F_x$ tapes prepared by the pit method. *Supercond. Sci. Technol.* **30**, 065004 (2017). URL dx.doi.org/10.1088/1361-6668/aa6850.

[233] Shahbazi, M., Wang, X. L., Dou, S. X., Fang, H. & Lin, C. T. The flux pinning mechanism, and electrical and magnetic anisotropy in $Fe_{1.04}Te_{0.6}Se_{0.4}$ superconducting single crystal. *J. Appl. Phys.* **113**, 17E115 (2013). URL dx.doi.org/10.1063/1.4794134.

[234] Shahbazi, M., Wang, X. L., Choi, K. Y. & Dou, S. X. Flux pinning mechanism in $BaFe_{1.9}Ni_{0.1}As_2$ single crystals: Evidence for fluctuation in mean free path induced pinning. *Appl. Phys. Lett.* **103**, 032605 (2013). URL dx.doi.org/10.1063/1.4813113.

[235] Van Gennep, D., Hassan, A., Luo, H. & Abdel-Hafiez, M. Sharp peak of the critical current density in $BaFe_{2-x}Ni_xAs_2$ at optimal composition. *Phys. Rev. B* **101**, 235163 (2020). URL dx.doi.org/10.1103/PhysRevB.101.235163.

[236] Bhattacharya, S. & Higgins, M. J. Peak effect and anomalous flow behavior of a flux-line lattice. *Phys. Rev. B* **49**, 10005–10008 (1994). URL dx.doi.org/10.1103/PhysRevB.49.10005.

[237] Xiao, Z. L., Andrei, E. Y., Shuk, P. & Greenblatt, M. Equilibration and dynamic phase transitions of a driven vortex lattice. *Phys. Rev. Lett.* **85**, 3265–3268 (2000). URL dx.doi.org/10.1103/PhysRevLett.85.3265.

[238] Kwok, W. K., Fendrich, J. A., van der Beek, C. J. & Crabtree, G. W. Peak effect as a precursor to vortex lattice melting in single crystal $YBa_2Cu_3O_{7-\delta}$. *Phys. Rev. Lett.* **73**, 2614–2617 (1994). URL dx.doi.org/10.1103/PhysRevLett.73.2614.

[239] Xu, X. B. *et al.* Peak effect in the critical current of type II superconductors with strong magnetic vortex pinning. *Phys. Rev. Lett.* **101**, 147002 (2008). URL dx.doi.org/10.1103/PhysRevLett.101.147002.

[240] Kogan, V. G., Fang, M. M. & Mitra, S. Reversible magnetization of high-T_c materials in intermediate fields. *Phys. Rev. B* **38**, 11958–11961 (1988). URL dx.doi.org/10.1103/PhysRevB.38.11958.

[241] Chaparro, C. *et al.* Doping dependence of the specific heat of single-crystal $BaFe_2(As_{1-x}P_x)_2$. *Phys. Rev. B* **85**, 184525 (2012). URL dx.doi.org/10.1103/PhysRevB.85.184525.

[242] Salem-Sugui, S. *et al.* Superconducting fluctuations in the reversible magnetization of the iron-pnictide $Ba_{1-x}K_xFe_2As_2$. *Phys. Rev. B* **80**, 014518 (2009). URL dx.doi.org/10.1103/PhysRevB.80.014518.

[243] Rey, R. I. *et al.* Measurements of the fluctuation-induced in-plane magnetoconductivity at high reduced temperatures and magnetic fields in the iron arsenide $BaFe_{2-x}Ni_xAs_2$. *Supercond. Sci. Technol.* **26**, 055004 (2013). URL dx.doi.org/10.1088/0953-2048/26/5/055004.

[244] Pelc, D. *et al.* Emergence of superconductivity in the cuprates via a universal percolation process. *Nat. Commun.* **9**, 4327 (2018). URL dx.doi.org/10.1038/s41467-018-06707-y.

[245] Pelc, D. *et al.* Resistivity phase diagram of cuprates revisited. *Phys. Rev. B* **102**, 075114 (2020). URL dx.doi.org/10.1103/PhysRevB.102.075114.

[246] Tsuzuki, T. Critical anomalies of superconducting intercalated layer compounds. *Phys. Lett. A* **37**, 159–160 (1971). URL dx.doi.org/10.1016/0375-9601(71)90105-8.

[247] Skocpol, W. J. & Tinkham, M. Fluctuations near superconducting phase transitions. *Rep. Prog. Phys.* **38**, 1049–1097 (1975). URL dx.doi.org/10.1088/0034-4885/38/9/001.

[248] Aslamasov, L. & Larkin, A. The influence of fluctuation pairing of electrons on the conductivity of normal metal. *Phys. Lett. A* **26**, 238–239 (1968). URL dx.doi.org/10.1016/0375-9601(68)90623-3.

[249] Maki, K. & Thompson, R. S. Fluctuation conductivity of high-T_c superconductors. *Phys. Rev. B* **39**, 2767–2770 (1989). URL dx.doi.org/10.1103/PhysRevB.39.2767.

[250] Klemm, R. A. Phenomenological model of the copper oxide superconductors. *Phys. Rev. B* **41**, 2073–2097 (1990). URL dx.doi.org/10.1103/PhysRevB.41.2073.

[251] Ramallo, M. V., Pomar, A. & Vidal, F. In-plane paraconductivity and fluctuation-induced magnetoconductivity in biperiodic layered superconductors: Application to $YBa_2Cu_3O_{7-\delta}$. *Phys. Rev. B* **54**, 4341–4356 (1996). URL dx.doi.org/10.1103/PhysRevB.54.4341.

[252] Currás, S. R. *et al.* In-plane paraconductivity in $La_{2-x}Sr_xCuO_4$ thin film superconductors at high reduced temperatures: Independence of the normal-state pseudogap. *Phys. Rev. B* **68**, 094501 (2003). URL dx.doi.org/10.1103/PhysRevB.68.094501.

[253] Johnson, W. L., Tsuei, C. C. & Chaudhari, P. Paraconductivity of three-dimensional amorphous superconductors-evidence for a short-wavelength cutoff in the fluctuation spectrum. *Phys. Rev. B* **17**, 2884–2891 (1978). URL dx.doi.org/10.1103/PhysRevB.17.2884.

[254] Vidal, F., Veira, J. A., Maza, J., Mosqueira, J. & Carballeira, C. On the interplay between T_c-inhomogeneities at long length scales and thermal fluctuations around the average superconducting transition in cuprates. In Drechsler, S. L. & T. Mishonov, N. S. S. . H. T. (eds.) *High-T_c Superconductors and Related materials: Material Science, Fundamental Properties and Some Future electronic Applications*, vol. 86, 289 (Kluwer Academic Publisher, The Netherlands, 2001). URL sauls.lsu.edu/publications/jas106/NATO-ASI_High-Tc-Superconductivity.pdf.

[255] Obradors, X., Labarta, A., Tejada, J., Vallet, M. & González-Calbet, J. M. Meissner effect and critical fields in an inhomogeneous $Ba_2HoCu_3O_{7-x}$ high-T_c superconductor. *Phys. Rev. B* **38**, 2455–2459 (1988). URL dx.doi.org/10.1103/PhysRevB.38.2455.

[256] Schilling, A., Cantoni, M., Guo, J. D. & Ott, H. R. Superconductivity above 130 K in the Hg-Ba-Ca-Cu-O system. *Nature* **363**, 56–58 (1993). URL dx.doi.org/10.1038/363056a0.

This thesis focuses on several open questions of high-Tc superconductors. Firstly, we study the vortex state of iron-based superconductors (IBS), particularly the anomalous angular dependence of the upper critical field, the second magnetization peak in the critical state of highly anisotropic IBS, and the less studied vortex pinning induced by surface irregularities. Secondly, we investigate the highly debated nature of precursor superconducting effects on cuprate superconductors. Our findings deepen our understanding of the impact of nano-structuration and dimensionality on superconducting properties, with implications on the technological applications of superconductors, by exploring mechanisms to enhance the critical current and the irreversibility magnetic field.